Oscillations, synchronization and waves in neuronal networks

Ling Kang

PSL UNIVERSITÉ PARIS

THÈSE DE DOCTORAT

DE L'UNIVERSITÉ PSL

Préparée au Laboratoire de Physique de l'Ecole normale supérieure

Dans le cadre d'une cotutelle avec

East China normal university

Oscillations, synchronization and waves in neuronal networks

Soutenue par

Ling KANG

Le 25 Novembre 2022

École doctorale n°564

Physique en Ile-de-France

Spécialité

Physique

Composition du jury :

Boris GUTKIN The Laboratoire de Neurosciences Cognitives Computationnelles	*Président du jury*
Gemma HUGUET Departament de Matemàtiques, Universitat Politècnica de Catalunya	*Rapporteur*
Tatjana TCHUMATCHENKO University Medical Center of the Johannes Gutenberg-University Mainz	*Rapporteur*
Alexa RIEHLE Institut de Neurosciences de la Timone - Aix-Marseille Université	*Examinateur*
Jonas RANFT IBENS	*Examinateur*
Zonghua LIU ECNU	*Co-Directeur de thèse*
Vincent HAKIM LPENS	*Directeur de thèse*

ENS | PSL

Acknowledgments

First and foremost, I would like to express my deepest gratitude to my supervisor Prof.Vincent Hakim. For my Ph.D., without your assistance and dedicated involvement in every step throughout the process, this thesis would have never been accomplished. Thank you for kindly assisting me with the theoretical analysis and being very patient with my knowledge gaps in the area. Thank you very much for your support, understanding, and encouragement over these past three years. Your rational, calm and serious attitude will inspire me in my academic research and life.

I'm extremely grateful to my supervisor Prof.Zonghua Liu, whose office's door was always open whenever I ran into a trouble spot or had a question about my research. Thank you for sharing expertise, and sincere and valuable guidance and encouragement to me. Your confident and optimistic attitude will always infect me.

I would like to express my appreciation for Jonas Ranft, your guidance, support and encouragement have been invaluable throughout the research project. Thank you for every time, step by step explanation, page after page of notes help me to fill my gaps in neuroscience. Your teaching style and enthusiastic attitude made a strong influence on me. By the way, your Chinese is excellent.

I would also like to show gratitude to my committee, Boris Gutkin, who is also in my thesis committee and followed by my Ph.D. process, Tatjana Tchumatchenko and Gemma Huguet as my thesis reviewers, and Alexa Riehle, whose group provided us with a lot of practical advice about the experimental data. Thank you.

It was an amazing experience in Paris, I am also grateful to the different people I met: Anna, Xiaoshuang, Shun, Dan, Lexuan, Mingfeng, Yuxiu, Ting, Elie, Marco, Simone, Kevin, Trang-Ahn, Betsy..., thank for listening to and helping me over the past three years. Because of you, I have many beautiful memories. I cannot express my gratitude and appreciation for your friendship.

I take this opportunity to express gratitude to all of the department faculty members for their help and support.

I am also grateful to the financial support from CSC.

Finally, I must express my very profound gratitude to my parents and to my brother and his wife for providing me with unconditional love and encouragement, thank you and love you forever.

Résumé

Les oscillations neuronales sont un élément essentiel de la dynamique cérébrale. L'activité synchrone de réseaux de neurones et l'activité séquentielle de groupes de neurones en différents point de l'espace sont considérées comme des mécanismes importants reliant l'activité des neurones individuels aux fonctions cérébrales et au comportement. Dans cette thèse, je me concentre d'abord sur les mécanismes donnant lieu au rythmes neuronaux, spécialement au rythme beta qui est observé dans le cortex moteur des primates. J'étudie, ensuite la synchronisation partielle, comme les états "chimériques" ou la synchronisation "à distance", en utilisant le réseau de connexions entres aires corticales du cerveau humain.

Les oscillations beta ($13-30Hz$), enregistrées, par exemple, en utilisant des singes entrainés à une tâche de préhension avec délai, sont prépondérantes durant la préparation du mouvement. Elles apparaissent sproradiquement et sont spatialement organisées de façon complexe (par ex. en ondes plane, radiale ou spirale). Pour étudier l'origine et les caractéristiques des oscillations beta, nous proposons un modèle simple du cortex moteur consistant en des populations neuronales excitatrices et inhibitrices locales, couplées par des connexions excitatrices à plus longue portée. Ces modules reçoivent aussi des entrées stochastisques provenant d'autres structures neurales. Ces entrées stochastiques sont de deux types : un premier consistant en des entrées locales qui varient de module à module et un second correspondant à une entrée globale, identique sur tous les modules. Nous avons montré que ce modèle reproduit la statistique des données d'enrégistrement quand le temps de corrélation des entrées externes est court ($\sim 25ms$) et le poids respectif des deux types d'entrée est choisi de façon appropriée. Le modèle reproduit la distribution de la durée des bouffées d'oscillation beta, les proportions des différents types d'ondes et leurs vitesses. Il permet aussi d'analyser théoriquement les oscillations beta.

Les états chimériques correspondent à la coexistence de dynamiques cohérente et incohérente. Ils sont reliés au sommeil mono-hémisphérique de certains oiseaux ou mammifères marins et à l'effet 'première nuit" chez les humains. Nous proposons un réseau de neurones couplées à deux couches (chaque couche représente un hémisphère et les liens entres les deux couches représente leur couplage par le corps calleux) pour étudier les patrons d'activité du réseau cérébral. Ce modèle réduit nous permet de trouver des états chimériques. De plus, nous étudions plus généralement ce réseau à deux couches pour déterminer comment les paramètres structuraux influent sur sa dynamique. Nous considérons aussi l'effet de délai dans la transmission des signaux en distinguant les connections inter-couches, décrites par des synapses chimiques, des synapses intra-couches décrites comme des synapses électriques.

La synchronisation à distance est caractérisée par la synchronisation de la dynamique de paires de noeuds non physiquement connectés et non connectés par une chaine de noeuds syn-

chronisés. Elle est considérée comme un mécanisme important de ségrégation et d'intégration des fonctions cérébrales. En se fondant sur le réseau réel des connections cérébrales, nous montrons que la synchronisation à distance peut être observée dans un réseau d'oscillateurs identiques. pourvu que des délais appropriés soient pris en compte. Nous proposons un cadre nouveau, consistant en de multiples réseaux en étoile connectés par des "feuilles" communes, pour comprendre la synchronisation à distance. Nous montrons, de plus, que ces feuilles partagées jouent un rôle essentiel dans la synchronisation à distance.
Mots clés : oscillations synchronisation ondes neurosciences réseau complexe

Abstract

Neuronal oscillations are an essential characteristic of the brain dynamics. The synchronous activity of oscillating networks and the sequential movement in space of oscillating networks are thought to be important mechanisms linking single-neuron activity to functions and behaviors. In this thesis, first, I focus on the mechanisms of neuronal rhythms, particularly the beta rhythm observed in the primate motor cortex. Then, I investigate partial synchronization such as chimera states and remote synchronization based on the human cerebral cortex network.

Beta oscillations ($13 - 30Hz$), which are observed in monkeys when they are trained to perform a delayed reach-to-grasp task, are prominent during movement preparation. Beta oscillations are sporadic and organized into complex patterns (e.g in planar, radial, spiral waves). In order to study the origin and characteristics of beta oscillations, we propose a simple model of the motor cortex based on local excitatory-inhibitory neuronal populations coupled by longer range excitation. These modules also receive additional stochastic inputs from other neural structures. We separate the stochastic inputs into two parts: one is local and varies from module to module, and the other is global and consistent across all modules. We have shown that this model can accurately reproduce the statistics of recording data when these external inputs are correlated on a short time scale ($\sim 25ms$) and the two different components of external inputs are appropriately weighted. The model reproduces the distribution of beta burst durations, the proportion of the different observed wave types, and wave speeds. It also serves to provide a theoretical analysis of beta oscillations.

Chimera states represent the coexistence of coherent and incoherent dynamics. They are thought to be related to the unihemispheric sleep of some birds and marine mammals and to the first-night effect of human beings. We present a two-layered network of coupled neurons (each layer represents the left and right hemispheres of the cerebral cortex, respectively, and the links between the two layers represent the inter-couplings through the corpus callosum) to study the collective patterns of the brain network. This simplified model allows us to find chimera states for brain networks. Further, we investigate the general two-layered network and study how structural parameters shape the dynamics of the network. We also consider the effect of delay due to the limited speed of signal transmission by distinguishing the inter- and intra-couplings as chemical synapse couplings and electrical synapse couplings, respectively.

Remote synchronization is characterized by the synchronization of pairs of nodes that are not directly connected via a physical link or any sequence of synchronized nodes. It is thought to take a key role in supporting the segregation and integration of brain functions. Based on the real network of the human cerebral cortex, we show that remote synchronization can be observed in networks of identical oscillators, provided that an appropriate time delay is

considered. We propose a new framework of multiple star-like graphs connected by common leaf nodes to understand the mechanism of remote synchronization. We further show that the common leaf nodes take a key role for the emergence of remote synchronization.
Keywords : oscillations synchronization waves neuroscience complex network

Contents

CHAPTER I

Introduction

1 Research background

For centuries, scientists and philosophers have been fascinated by the brain. It is one of the most complex systems made up of interconnected neurons. It controls our intelligence, sense, movement and behavior, all of which define our humanity. Until now, the underlying operation of the brain has remained a mystery and may continue to be so due to its extreme complexity. However, the recent confluence of neuroscience and network science opens up a number of new avenues for understanding brain functions from different perspectives. One important area of research focuses on structure-function relationships in the brain, aiming to lead a better understanding how structural networks give rise to rich and flexible neural dynamics. Another promising area involves the mechanisms of neuronal activities. Neuronal oscillations, synchronization, and propagating waves are three fundamental mechanisms for understanding brain functions by coordinating neural activity within and between neuronal structures [1, 2, 3, 4].

Neuronal oscillations were firstly observed in human electroencephalogram (EEG) by Berger who discovered the alpha rhythm ($8-13Hz$). More recently, the new high-resolution optical and electrophysiological recording technologies led to the observation of neural oscillations at both the macroscopic and mesoscopic scales in the developing and in the mature brain. The oscillatory frequencies in the brain, which range from approximately 0.02 Hz to 600 Hz, are widely observed at a variety of spatial and temporal scales and are thought to be related to a variety of brain states and functions. Beta oscillations [5] have captured much attention in recent years. The available data from experiments demonstrate that beta-band oscillations are associated with a broad range of processes, including top-down mechanisms involved in cognitive and perceptual processing, attention maintenance, sensorimotor integration, movement preparation and the pathophysiology of movement disorders.

Neuronal synchronization is a fundamental mechanism to understand human cognition that emerges from the coordinated activity of distributed large-scale brain networks operating at different spatiotemporal scales. One of the most studied synchronization regimes in recent years is partial synchronization including chimera states, remote synchronization and cluster synchronization [6, 7, 8]. Significant progress has been achieved on understanding chimera states, which involve the coexistence of synchronized and unsynchronized states. This counterintuitive phenomenon is closely related to the unihemispheric sleep in some marine mammals and birds and has recently gotten hot attention in neural systems. Remote synchronization is characterized by the synchronization of pairs of nodes that are not directly connected via a physical link or any sequence of synchronized nodes. It is thought to take a key role in supporting the segregation and integration of brain functions.

Propagating waves reflecting phase offsets in spatiotemporal scales were noticed with the advent of simultaneous multichannel recordings. They can be spontaneously generated by recurrent currents or evoked by external stimuli and form complex spatiotemporal patterns (including planar, radial and spiral waves). Propagating waves are thought to serve many functions in normal behavior states and pathological brain states.

My Ph.D. research concentrated on neuronal oscillations, synchronization, and wave prop-

agation in neuronal networks. My first project was to investigate partial synchronization in the human network. We studied chimera states based on a two-layered human cerebral cortex network and investigated how network characteristics shape the dynamics. This was followed by a work about remote synchronization in the human cerebral cortex network, which aims to understand the underlying mechanism of remote synchronization in brain functioning. Then I focused on the mechanisms of neuronal rhythms, particularly the beta rhythm observed in the primate motor cortex.

The organization of this manuscript is as follows:

- Chapter I covers a basic introduction to complex networks, a rich variety of single neuron models and how to use mathematical tools to analyze the dynamical behavior of the system.
- Chapter II introduces the experimental data we rely on to study beta oscillations in the motor cortex of monkeys. It proposes a basic mechanism underlying the generation of beta oscillations and presents a theoretical framework for describing this beta generation mechanism.
- Chapter III is devoted to our work on partial synchronization, first with an emphasis on chimera states based on a two-layered human network. Then, remote synchronization associated with possible network structure is discussed.
- Chapter IV finally, summarize the general insights that have been gained and make a brief discussion of envisioned future studies.

2 Complex networks

We are surrounded by networks, such as the biological network of cellular interactions between genes, proteins, and metabolites; the neuronal network which captures the connections between neurons and is helpful to understand brain functions; the social communication networks such as Google and Facebook which construct our interpersonal relationships; the virus networks that control the spread of viruses such as Covid which has made devastating effects; the power grid networks, the traffic networks and so on. Uncovering the structure of these networks, the interplay between network components, as well as how dynamics affect the whole network is crucial for us to address the problems of life. Studies of networks have a long history. Their roots go back at least to 1736, when the Swiss mathematician Leonhard Euler published the solution to the Königsberg bridge problem [9]. This new subfield of mathematics was called graph theory [10]. In addition to the development in mathematical graph theory, the study of networks has seen important achievements in the social sciences. At the dawn of the 21st century, a new movement of interest and research in network science was triggered by Watts and Strogatz with their study on small-world network [11], and the work of Barabási and Alberts on scale-free network [12, 13]. Later, massive and comparative analysis of networks from different fields has produced a new discipline, which we call network science today. It aims to understand the common basic structures and the unifying principles behind the diverse complex networks.

In this section, we will introduce how to describe a network as a graph, as well as the basic features of networks, such as degree, degree distribution, adjacency matrix, path, distance, clustering coefficient and so on. Network science aims to build models that reproduce the properties of real networks, so we also introduce some typical network models such as random network, small-network, and scale-free network. Finally, we will give a special emphasis on the study and modeling of brain networks.

2.1 Basic description of networks

To understand a complicated system, we must first understand how its components interact with one another.

Node and Link

In network science, a network is a collection of a system's components. The components are typically referred to as nodes, and the direct connections between them are referred to as links. The links can be distinguished as directed or undirected depending on whether the direction is required. Here, we focus on undirected networks. Fig.2.1(a) provides an example of a network with $N = 6$ nodes and $L = 6$ links. It will serve to illustrate the different quantities introduced below.

Degree and degree distribution

An important property of each node is its degree, representing the number of links it has to other nodes. We use k_i to represent the degree of node i in the network. In an undirected

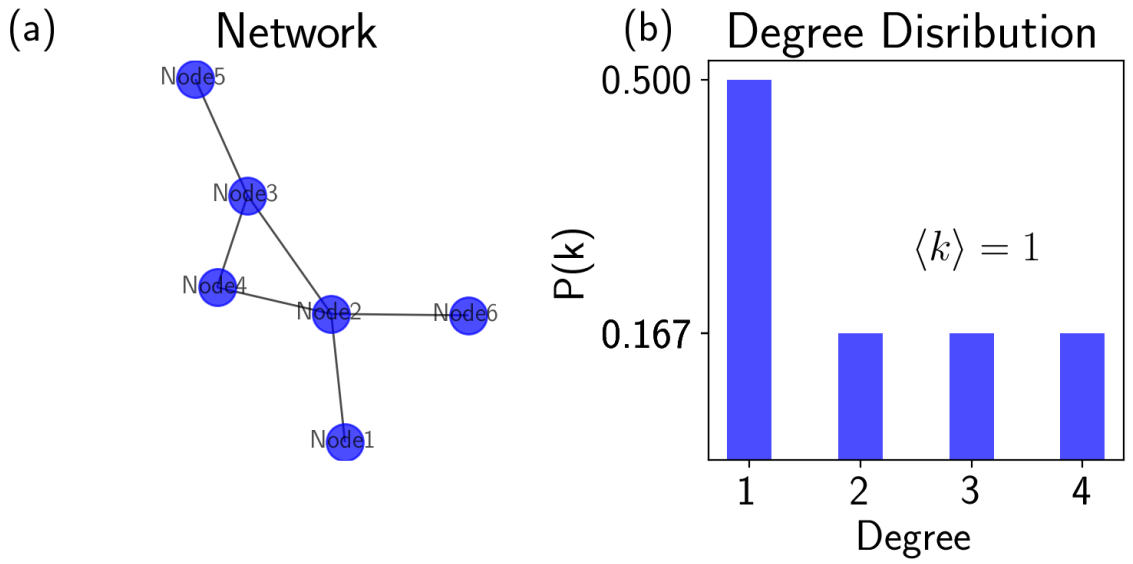

(c) Adjacency Matrix

$$A_{ij} = \begin{pmatrix} 0 & 1 & 0 & 0 & 0 & 0 \\ 1 & 0 & 1 & 1 & 0 & 1 \\ 0 & 1 & 0 & 1 & 1 & 0 \\ 0 & 1 & 1 & 0 & 0 & 0 \\ 0 & 0 & 1 & 0 & 0 & 0 \\ 0 & 1 & 0 & 0 & 0 & 0 \end{pmatrix}$$

(d) Clustering Coefficient

$$C_1 = 0 \quad C_2 = \tfrac{1}{6}$$
$$C_3 = \tfrac{1}{3} \quad C_4 = 1$$
$$C_5 = 0 \quad C_6 = 0$$
$$\langle C \rangle = \tfrac{1}{4}$$

Figure 2.1: **Network description.** (a) Network structure. (b) Degree distribution. (c) Adjacency matrix. (d) Clustering coefficient.

network, the total number of links L, can be expressed as the sum of the node degrees of the N nodes,

$$L = \frac{1}{2} \sum_{i=1}^{N} k_i. \tag{2.1}$$

- Average degree

The average degree in an undirected network is

$$\langle k \rangle = \frac{1}{N} \sum_{i=1}^{N} k_i = \frac{2L}{N}. \tag{2.2}$$

- Degree distribution

The likelihood that a randomly picked node in the network has degree k is given by the degree distribution p_k,

$$p_k = \frac{N_k}{N} \tag{2.3}$$

where N_k is the number of the nodes with a degree equal to k. p_k is a probability, and it is normalized $\sum_{k=1}^{\infty} p_k = 1$. The relationship between average degree and degree distribution is

$$\langle k \rangle = \sum_{k=0}^{\infty} k p_k. \tag{2.4}$$

The degree distribution of the network (Fig.2.1(a)) is shown in Fig.2.1(b), the average degree is $\langle k \rangle = 2$.

Adjacency matrix

In order to represent the connectivity of a network, it is useful to introduce the network adjacency matrix. The adjacency matrix of an undirected network of N nodes has N rows and N columns, its elements $A_{ij} = 1$ if there is a link between node j to node i, $A_{ij} = 0$ if there is no link between node j to node i. The adjacency matrix of an undirected network is symmetric $A_{ij} = A_{ji}$. The relationship between adjacency matrix and degree is

$$k_i = \sum_{i=1}^{N} A_{ij} = \sum_{j=1}^{N} A_{ij}. \tag{2.5}$$

The adjacency matrix of the network in Fig.2.1(a) is shown in Fig.2.1(c).

Path and distance

In network science, distance is represented by path length. A path between nodes i_1 and i_n is an ordered list of $n-1$ links $P = (i_1, i_2), (i_2, i_3), ..., (i_{n-1}, i_n)$, the length of this path is $n-1$. The path between $node1$ and $node6$ shown in Fig.2.1(a) follows the route $node1 \rightarrow node2 \rightarrow node6$, hence its length is $n = 2$.

- Shortest path

The shortest path between nodes i and j is the path with the fewest number of links, denoted by d_{ij}.

- Average path length

The average distance of a network is given by $\langle d \rangle$, which is the average of the shortest path length between all pairs of nodes,

$$\langle d \rangle = \frac{1}{N(N-1)} \sum_{i \neq j} d_{ij}. \tag{2.6}$$

- Network diameter

The diameter of a network is the maximum shortest path in the network, denoted by d_{max}.

- Connectedness

In an undirected network nodes i and j are connected if there is a path between them, otherwise they are disconnected and the distance $d_{ij} = \infty$. A network is connected if all pairs of nodes in the network are connected. If there is at least one pair with $d_{ij} = \infty$, it is unconnected.

In Fig.2.1(a), there are two paths from $node1$ to $node3$: $node1 \rightarrow node2 \rightarrow node3$ or $node1 \rightarrow node2 \rightarrow node4 \rightarrow node3$, so the shortest path from $node1$ to $node3$ has length 2. The network shown in Fig.2.1(a) is a connected network.

Clustering coefficient

The clustering coefficient captures the degree to which the neighbors of a given node are connected to each other, which measures the network's local link density. For a node i with degree k_i, the local clustering coefficient is defined by

$$C_i = \frac{2L_i}{k_i(k_i - 1)} \tag{2.7}$$

where L_i represents the number of links between the k_i neighbors of node i. If $C_i = 0$, there is no link between neighbors; if $C_i = 1$, all neighbors of node i are connected to each other and form a complete graph. The clustering coefficient for a network is the average of C_i over all nodes, $\langle C \rangle = \frac{1}{N} \sum_{i=1}^{N} C_i$. It represents the probability that two neighbors of a randomly selected node are connected to each other. The clustering coefficients of the network Fig.2.1(a) are shown in Fig.2.1(d).

Communities

If there is a locally dense and connected subgraph in a network, the network has a community structure. For example, in a social network, people who have the same hobbies are more likely to interact with each other; in a biological network, cells that carry out a specific cellular function tends to be active together, which was firstly identified by Ravasz and collaborators [14]. Community structures are important because they allow us to rescale a large network into a smaller network since the same communities often conduct the same functions or have similar properties. However, finding the communities in a real network can be a difficult task. Several methods for community finding have been developed such as Hierarchical clustering, Girvan–Newman algorithm [15], Modularity maximization [16] and so on. In Fig.2.1(a), the $node2 - 4$ can be seen as a community.

2.2 Topology of real networks

From the above, we know how to describe a network, but the majority of the networks we encounter in reality do not have the reassuring regularity that we could have hoped for. Instead, they possess complicated and disparate topological properties. However, despite their inherent differences, most real networks are characterized by the same topological properties such as short path length, high clustering coefficients, fat tailed shapes in the degree distribution, community structures and so on. Understanding the common basic topology underneath these complex architectures, and revealing the unifying principles behind these sophisticated networks, are

helpful for learning and controlling the dynamics of the network. During the last decades, people have developed several typical network models to help us understand real networks. In the following, we will introduce several classical network models.

Regular network

In network science, a regular network is a graph where each node has the same number of links, like a ring network or a star network.

Random network

The systematic study of random graphs was initiated by Erdös and Rényi in 1959 [17]. Their model is one of the best studied graph models. A random network as defined by Erdös and Rényi is made up of N nodes with the links randomly drawn between these nodes. Each pair of nodes is connected with a probability of p. There are two different definitions of a random network:

Fixed link Model: N labeled nodes are connected with L randomly placed links.

Fixed probability Model: Each pair of N labeled nodes is connected with probability p.

We choose the fixed probability model. So one can construct a random network with the following steps:

First, begin with N separated nodes and sets the probability p; then, choose a node pair and produce a number between 0 and 1 at random, connect the selected node pair with a link if the number exceeds p, else, leave them disconnected; finally, repeat step two for each of the $N(N-1)/2$ node pairs.

In order to honor Pál Erdós and Alfréd Rényi, who have played an important role in understanding the properties of these networks, such a random network is also called an Erdós-Rényi network. The degree distribution of a random network follows the binomial distribution

$$P_k = \binom{N-1}{k} p^k (1-p)^{N-1-k}. \tag{2.8}$$

When $N \gg \langle k \rangle$, the degree distribution (Eq.2.8) is well approximated by the *Poisson* distribution

$$P_k = e^{-\langle k \rangle} \frac{\langle k \rangle^k}{k!}. \tag{2.9}$$

The expected number of links in a random network is

$$\langle L \rangle = p \frac{N(N-1)}{2}. \tag{2.10}$$

The average degree of a random network is

$$\langle k \rangle = p(N-1). \tag{2.11}$$

The diameter of a random network is approximately given for $N \gg N$ by,

$$d_{max} \approx \frac{\ln N}{\ln \langle k \rangle}. \tag{2.12}$$

The clustering coefficient for a random network is

$$C = p = \frac{\langle k \rangle}{N - 1}. \tag{2.13}$$

Small-word network

In most real networks, in spite of their large size, there is a relatively short path between any two nodes. This feature is known as the small-world phenomenon, also known as six degrees of separation.

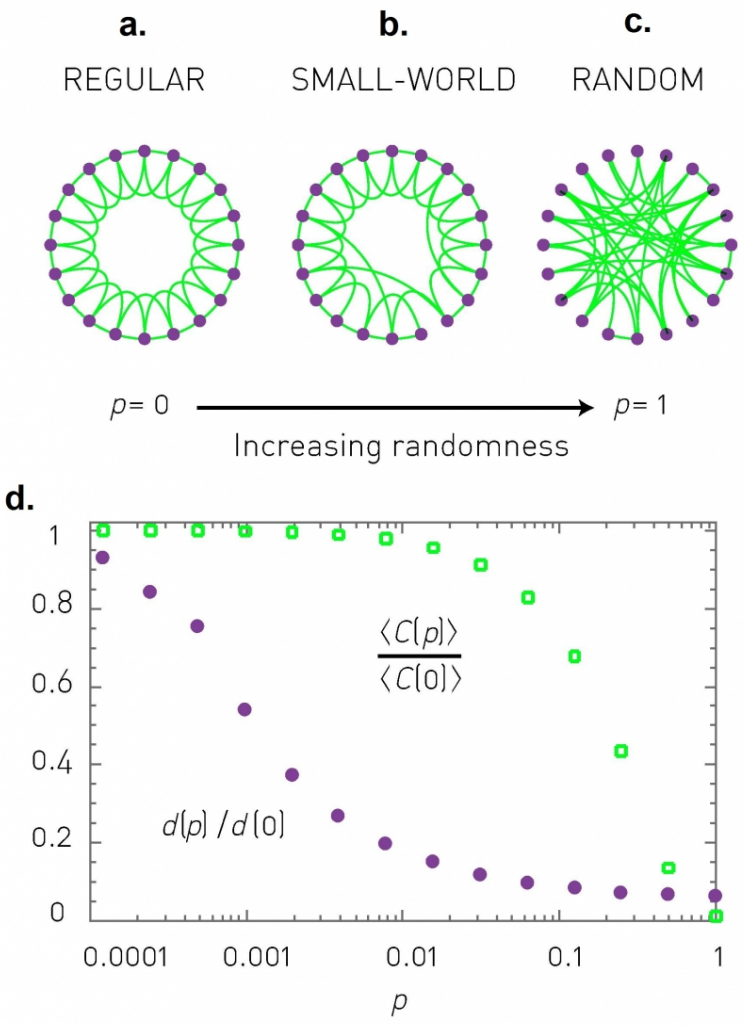

Figure 2.2: **The WS small-world model.** (a-c) The network changes with probability p. (d) The average path length $d(p)$ (purple) and the clustering coefficient $\langle C(p) \rangle$ (green) change with parameter p, $d(0)$ and $\langle C(0) \rangle$ are got from the regular network (a). Taken from [11].

Duncan Watts and Steven Strogatz proposed the small-world network model in 1998 [11]. They constructed the small-world network with the following steps:

First, they began with a ring of nodes N (N is even). Each node is connected to its imme-

diate and next nearest neighbors (high cluster coefficient), also known as a regular network (Fig.2.2(a)). Then, with probability p, each link is rewired to a randomly chosen node (one endpoint is kept unchanged, the other is chosen at random while preventing self-connection and reconnection), this produces a small-world network (Fig.2.2(b)). If $p = 1$, all links are rewired and one obtains a random network (Fig.2.2(c)).

Following the quantities we introduced before, a small-world network has relatively high clustering coefficient and also displays short paths, the small-world property. The evolution of network properties among regular, small world and random networks are shown in Fig.2.2. The random network (for $p = 1$) displays the small-world property but with low clustering coefficient, the regular network (for $p = 0$) has high clustering coefficient but lacks the small-world phenomenon.

Scale-free network

The networks we introduced above are homogeneous networks, which means that almost all nodes are topologically equivalent. When studying the available datasets of real networks, researchers have found that most real networks are heterogeneous and follow a power law shaped degree distribution as shown in Fig.2.3. This kind of network is called a scale-free network, and γ is the degree exponent,

$$p_k \sim k^{-\gamma} (log p_k \sim -\gamma log k). \tag{2.14}$$

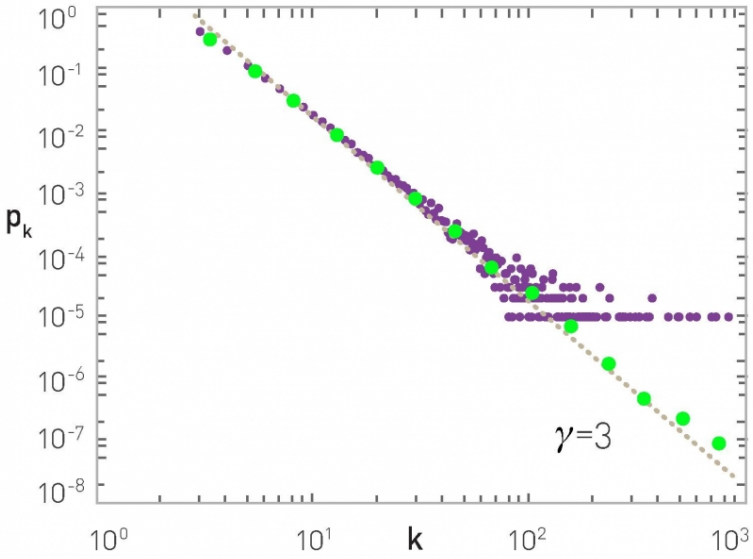

Figure 2.3: **The degree distribution of a network is generated by the Barabási-Albert model.** The figure shows p_k (linearly-binned (purple), log-binned version (green)) for a single network of size N=100,000 and γ=3. The straight line is added to guide the eyes and has a slope γ=3. Taken from [18].

A model created by Albert-László Barabási and Réka Albert, can generate scale-free networks. The BA model or the scale-free model [12] is defined as follows:
First, one starts from a network with m_0 isolated nodes; then, at each time step $t = 1, 2, 3, ..., N - m_0$ a new node j with m ($\leq m_0$) links is added to the network. The probability $\prod(k_i)$ that a link will connect j to an existing node i with degree k_i is linearly proportional to the actual degree of i,

$$\prod(k_i) = \frac{k_i}{\sum_j k_j}. \tag{2.15}$$

The evolution of the BA model is illustrated in Fig.2.4.

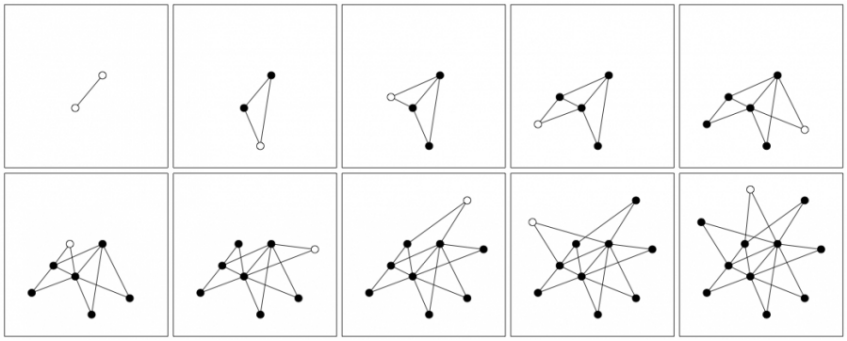

Figure 2.4: **Evolution of the Barabási-Albert model.** The image shows nine subsequent steps to produce a Barabási-Albert network. Empty circles denotes the newly added node to the network connecting its two links ($m = 2$) using a preferential attachment. Taken from [18].

In real networks, new nodes tend to link to the more connected nodes. This phenomenon is called preferential attachment and can create nodes with a large number of links. These nodes are called hub nodes. Hub nodes represent the most striking difference between a random network and a scale-free network.

Because of the existence of the hub nodes, the diameter in the Barabási-Albert network, for $m > 1$ and large N [19, 20] is

$$d_{max} \sim \frac{\ln N}{\ln \ln N} \tag{2.16}$$

which is smaller than the random network (Eq.2.12).

The clustering coefficient for scale-free network is small [21, 22]

$$\langle C \rangle \sim \frac{(lnN)^2}{N}. \tag{2.17}$$

The existence of the hub nodes and the fat power law make the network "robust yet fragile" which is an important characteristic of real networks [23].

2.3 Brain network

The human cerebral cortex consists of approximately 10^{11} neurons and 10^{14} synapses that are organized into a complex network of local circuits and long-range fiber pathways. Experimental studies have shown that the interactions of these neurons and synapses form the structural substrate that supports brain functions. For example, the firing rate of spontaneously active neurons in cortical areas strongly depends on the cortical networks in which they are embedded [24]. Several studies indicate that despite the huge number of neurons and their interconnections, the human cerebral cortex is governed by the optimizing principles of resource allocation and constraint minimization [25]. So a main goal is to figure out the core connectivity structure of the human cortex. However, it is controversial when one considers the different species, different spatial and temporal scales if a unifying connectivity skeleton exists. One usually refers to three different types of connectivity [26] according to the different methods used to measure it:

- Structural connectivity

It is the description of the physical connections, generally referring to white matter projections linking cortical and subcortical regions. Structural connectivity is thought to be relatively stable, and is commonly measured as a set of undirected links due to the fact that the projection directions are not easy to discern.

- Functional connectivity

It is often defined as the temporal correlation (cross-correlation, mutual information, or spectral coherence) between spatially distant points measured from neurophysiological activity data like electroencephalography (EEG) and magnetoencephalography (MEG), local field potentials (LFP), functional magnetic resonance imaging (fMRI) and positron emission tomography (PET). It is highly time-dependent and can exhibit non-stationary fluctuations.

- Effective connectivity

It describes networks of causal influences between neural elements based on the identification of graph models that best explain empirical data [27, 28, 29].

Both human and non-human brain networks exhibit a broad degree distribution [30]. The distribution of the degree follows the exponential or power-law characteristic as we introduced in the scale-free network. A high clustering coefficient and a short path length prosperity as the small-world network can also be found in brain networks [31]. Closer analyses of brain networks have shown that brain networks also have "communities" property across multiple scales, resulting in a hierarchical organization of nested "modules-within-modules" organizations [32]. These rich topology characteristics lead to a better understanding of how structural networks give rise to rich and flexible neural dynamics.

Relatively complete information on neuroanatomical connectivity is now available for large-scale networks at the level of segregated brain regions for some animals and mammalian species [33, 34]. The Caenorhabditis elegans has a compact nervous system of 302 identified neurons,

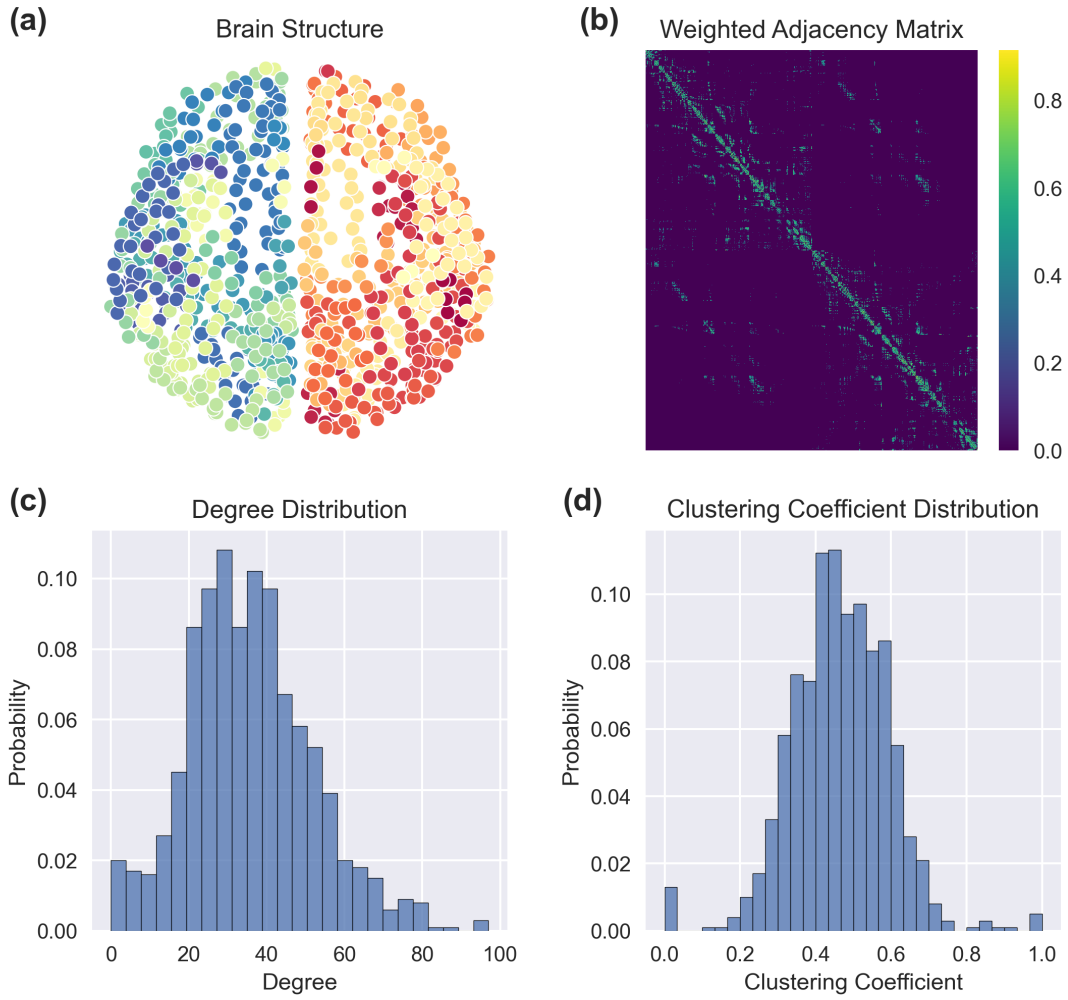

Figure 2.5: **Human cerebral cortex.** (a) Network structure. (b) Weighted adjacency matrix. (c) Degree distribution. (d) Clustering coefficient distribution.

whose connectivity has been fully mapped [35]. The connectivity of the cortico–cortical system in the macaque monkey [36], and of the cortico–thalamic system in the cat [37] have also been well mapped.

Fig.2.5 shows the statistical property of the human cerebral cortex measured by the diffusion imaging and tractography method, which is a noninvasive mapping of white matter cortico-cortical projections at high spatial resolution. In this network, a node represents a cortical region of interest (ROI in neuroimaging refers to selecting a cluster of voxels or brain region a priori when investigating a region for effects). A link represents the connection between two ROIs, and the weight of each link represents the fiber density between the two connected ROIs. The network consists of 998 nodes and 17,865 weighted links [38, 39].

Motor system

The motor system is functionally segregated and hierarchical organized. This means that it is divided into a number of different areas that control different aspects of movement, and that these areas are organized in a hierarchical manner. Specifically, the motor system can be separated into four parts: the spinal cord, the brain stem, the motor cortex, and the association cortex. It also contains two side loops: the basal ganglia and the cerebellum. They interact with each other through connections with the thalamus as Fig.2.6 shows.

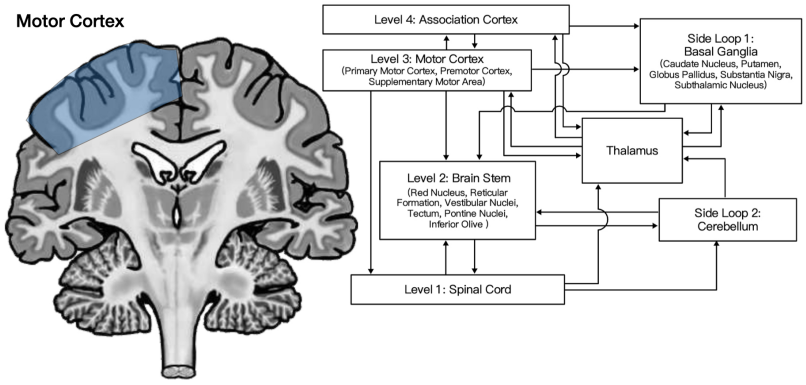

Figure 2.6: **Schematic representation of the different levels and interconnections of the motor system hierarchy.** Taken from [40].

The motor cortex is an area that is involved in the planning, control, and execution of voluntary movements. It includes the primary motor cortex, the premotor cortex, and the supplementary motor area. Experiments with animals performing different motor tasks have shown that the primary motor cortex is usually involved in the execution of movement and has information or quantities like the force, the direction and the speed of a movement; the premotor cortex appears to be involved in the selection of appropriate motor plans for voluntary movements and the supplementary motor area (SMA) is involved in programming complex sequences of movements and coordinating bilateral movements [41, 40, 42].

The generation of a voluntary movement, does not only involved the motor cortex, the basal ganglia and the cerebellum also play important roles. The basal ganglia includes the caudate

nucleus, the putamen, the globus pallidus, and the subthalamic nucleus. The basal ganglia is involved in a complex loop that connects to various areas of the cortex. The information from different areas of the cortex passes through the basal ganglia, then returns to the supplementary motor area via the thalamus. Thus, they are thought to facilitate movement by integrating information. The cerebellum receives information from other parts of the brain and relays it to the motor cortex via the thalamus. It is thought to participate in fine- tuning and coordination of movements.

The first step to initiate a voluntary movement is to select an appropriate response. It is accompanied by increased electrical activity in the frontal region of the cortex and the motor cortex is activated. Then, the motor cortex set the ideal plan for the movement with the information offered by other parts of the cortex. The second step is to plan the movement in physical terms. During this process, the motor cortex calls on other parts of the brain (such as the central grey nuclei and the cerebellum) to help initiate and coordinate the sequential activation of the muscles. The third step is to execute the movement, the axons of neurons in the motor cortex carry the expected movement information to the spinal cord, which connects directly to the muscles and causes the movement [43].

3 Neuroscience

The term "computational neuroscience" was coined by Eric L. Schwartz in 1985 when he organized a conference in Carmel, California, to better understand the principles that govern the development, structure, physiology, and cognitive abilities of the nervous system at many different structural scales, including the biophysical, the circuit, and the systems levels [44]. Theoretical neuroscience models aim to capture the essential features of the biological system at multiple spatio-temporal scales. Computational models frame hypotheses that can be directly tested by biological or psychological experiments. The main fields of computational neuroscience include single-neuron modeling, memory and synaptic plasticity, cognition, discrimination, learning, and network behavior [45].

In this section, we will introduce the structure and electrical properties of a neuron. We focus on simplified models for the dynamics of a single neuron, like the Hodgkin-Huxley model, the Fizhugo-nagumo model, the Integrated-and-fire model, and also on some network models.

3.1 Introduction to neurons

Neurons (which are electrically excitable cells) are frequently referred to as "fundamental units" of the nervous system, forming the foundation of the nervous system alongside glial cells (non-neuronal cells) that provide structural and metabolic support [46]. They communicate with each other via synapses. There are approximately 8.6×10^{10} neurons in the human brain. Each neuron has 7,000 synaptic connections to other neurons on average [47].

Components of the neuron

A typical neuron is divided into three functionally distinct parts known as cell body (soma), one or more dendrites, and a single axon [45], as shown in Fig.3.1. The cell body contains at least one nucleolus and serves as the "central processing unit", performing an important nonlinear processing step; the dendrites serve as the "receiver", collecting signals from other neurons and transmitting them to the soma; and the axon serves as the "launcher", transmitting information away from the soma to different neurons.

The synapse is a structure that permits a neuron (the presynaptic neuron) to pass a signal to another neuron or to a target effector cell (the postsynaptic cell). It is widely assumed to also play a role in memory formation. The word "synapse" was introduced in 1897 by the English neurophysiologist Charles Sherrington [49] and its existence was demonstrated in 1956 by Sanford Palay [50]. Based on the type of signals, synapses can be divided into two main types: electrical synapses and chemical synapses (see Fig.3.2).

The existence of electrical synapses was first demonstrated between escape-related giant neurons in the crayfish in the late 1950s. An electrical synapse is an electrically conductive contact between two nearby neurons. It forms a gap junction, which is a short gap between the pre- and postsynaptic neurons, separated by about 3.8 nanometers. Each gap junction comprises several channels that allow ions and even medium-sized molecules to move from one cell to the

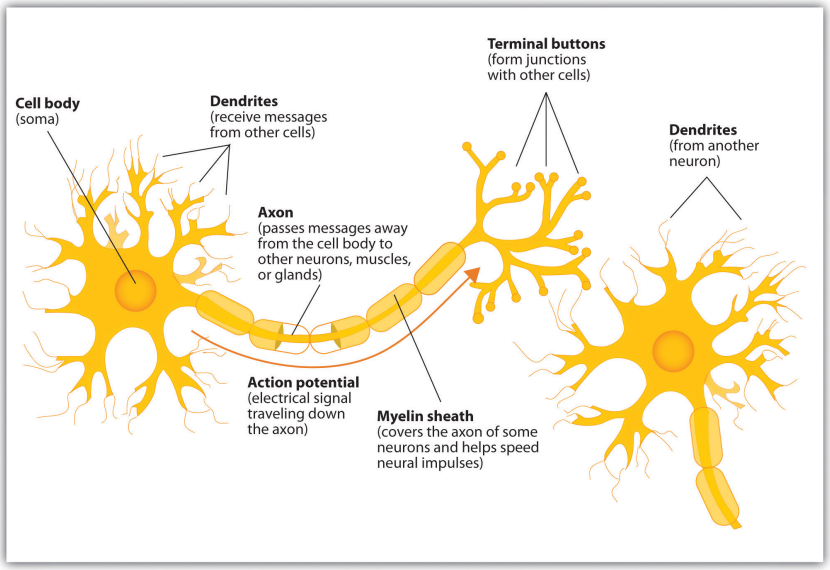

Figure 3.1: **Structure of a typical neuron.** Taken from [48].

next, forming the information transmission process (see Fig.3.2(b)).

Chemical synapses transmit information by releasing neurotransmitter molecules from presynaptic vesicles into a tiny region (the synaptic cleft, about 20 to 40 nanometer wide), where neurotransmitter molecules bind to neurotransmitter receptors on postsynaptic cells. As compared with electrical synapses, due to the involvement of neurotransmitters, chemical synapses produce slower changes in the membrane potential of postsynaptic neuron. Signals produced via chemical synapses are also more modifiable than electrical synapses. Another important characteristic of chemical synapses is that they pass information directionally while the electrical synapses are mostly bidirectional.

Action potential

Because of the maintenance of a voltage gradient across its membrane, a neuron can generate an all-or-none electrochemical pulse. In this so-called "action potential", the voltage changes significantly over a short interval, due to the movement of specific types of ions controlled by the voltage-gated channels on the neuron membrane. The process of the action potential can be separated into four steps as Fig.3.3 shows:

(1) Resting state. The ability of sodium and potassium ions to pass through the membrane is maintained in dynamic equilibrium, and the cell has a net negative charge on the inside.

(2) Depolarization. The neuron sodium channels open when the action potential is triggered, causing a large influx of sodium ions into the cell, resulting in a net positive charge in the neuron relative to the extracellular fluid.

(3) Repolarization. The sodium channels close and the potassium channels open when the action potential peak is reached, increasing the potassium flux into the extracellular fluid and decreasing the membrane potential to a negative value.

(4) Refractory period. After an action potential is generated, this is the period when the excitable cell cannot produce another action potential.

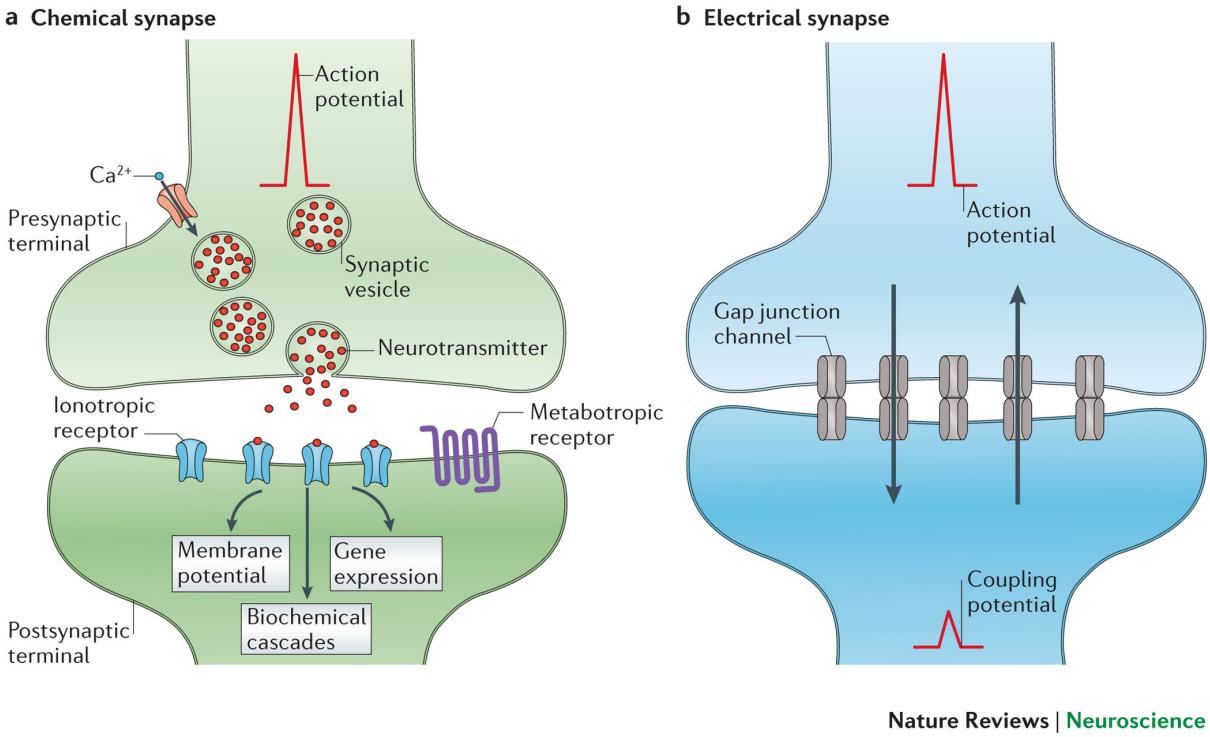

Figure 3.2: **The structure of synapses.** (a) Chemical synapse, (b) Electrical synapse, taken from [51].

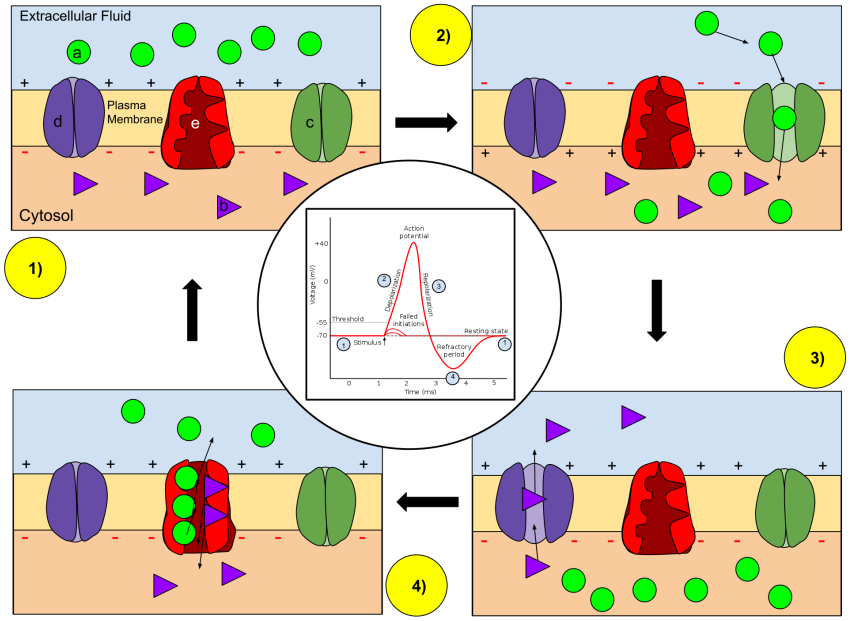

Figure 3.3: **Ions movement during an action potential.** Key: (a) Sodium (Na+) ion. (b) Potassium (K+) ion. (c) Sodium channel. (d) Potassium channel. (e) Sodium-potassium pump. Taken from [52].

A synapse can be classified as an excitatory synapse or an inhibitory synapse based on the distinct possible consequences on a postsynaptic cell. Excitatory synapses release neurotransmitters that increase the likelihood of an action potential in a postsynaptic cell, while inhibitory synapses have the opposite effect.

Spike train

If one ignores the brief duration of an action potential, a spike train is a recorded sequence of

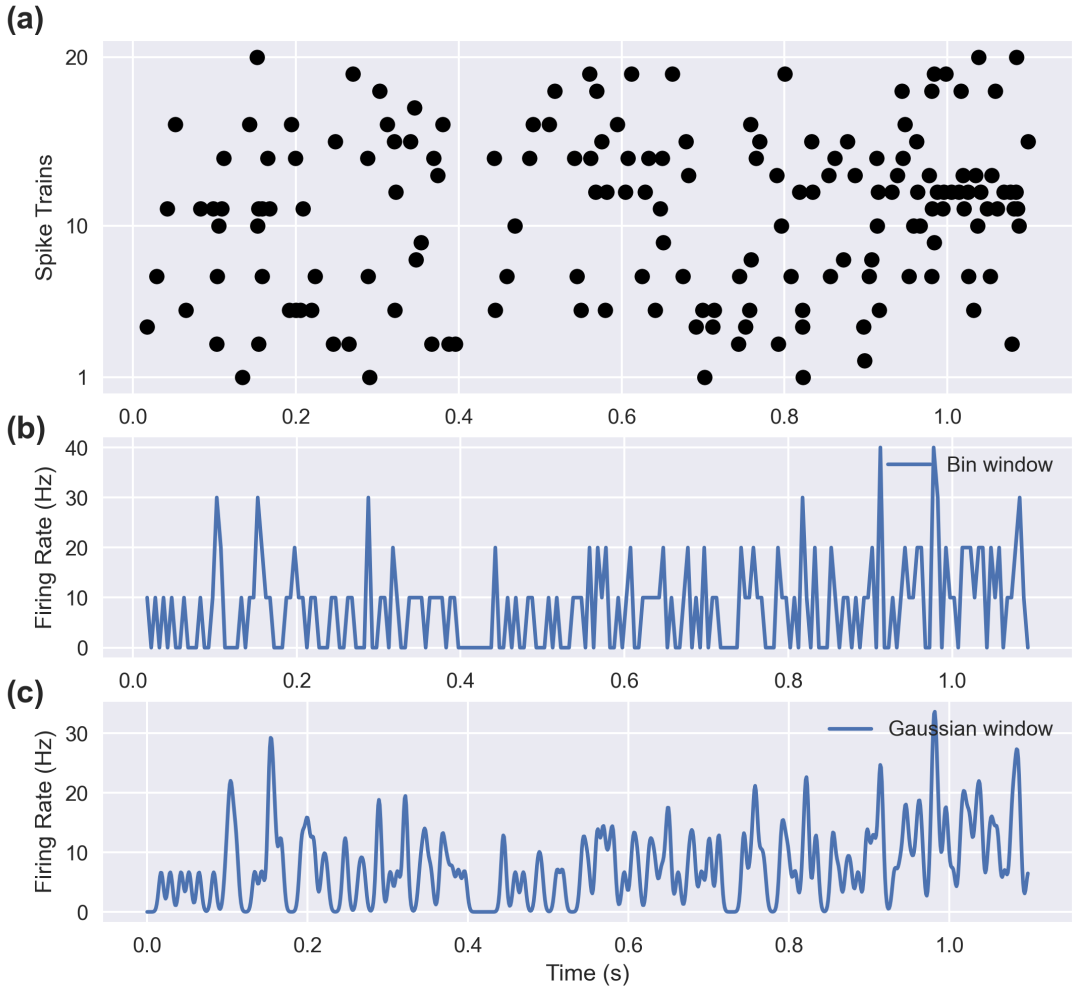

Figure 3.4: **Firing rates are approximated by different procedures.** (a) Spike trains of 20 units from experiment data when a monkey is trained to do an instructed delayed reach-to-grasp task [53]. (b) Discrete-time firing rate are obtained by binning time and counting spikes with $T = 5ms$. (c) Computed firing rate using a Gaussian window function with $\sigma = 3ms$.

times when a neuron fires an action potential. It can be described by

$$p(t) = \sum_{i=1}^{n} \delta(t - t_i) \tag{3.1}$$

where δ is Dirac function. The pattern of spike times varies as the stimulus changes, and it is often typically described statistically or probabilistically. One can define the firing rate

$$r = \frac{n}{T} = \frac{1}{T}\int_0^T d\tau p(\tau) \tag{3.2}$$

where n is the total number of spikes over a time interval of length T. Since spike counts can only take integer values, the rates computed by this method will always be integer multiples of $\frac{1}{T}$ and take discrete values as Fig.3.2(b) shows. In order to avoid this, one usually uses sliding windows or continuous windows functions like Gaussian windows to make the firing rate smoother as shown in Fig.3.2(c).

The Gaussian window is defined by

$$w(\tau) = \frac{1}{\sqrt{2\pi}\sigma}\exp(-\frac{\tau^2}{2\sigma^2}) \tag{3.3}$$

where σ controls the temporal resolution of the resulting rate, playing a role analogous to T.

3.2 Single neuron models

In this section, we will introduce some biological neuron models, such as the Hodgkin-Huxley model, which describes the membrane voltage as a function of the input current and the activation of ion channels; the Fitzhugh-Nagumo model, which is a simplification of the Hodgkin–Huxley model; the Integrate-and-Fire models which describes the membrane voltage as a function of the input current and predicts the spike times.

Hodgkin-Huxley model

Biological neuron models seek to explain the mechanisms underlying nervous system function. The Hodgkin-Huxley model [54] was proposed by Alan Hodgkin and Andrew Huxley in 1952 to explain the ionic mechanisms underlying the initiation and propagation of action potentials in the squid giant axon with data obtained from the voltage-clamp technique. It is widely regarded as one of the most significant conceptual breakthroughs in computational neuroscience. This achievement earned Alan Hodgkin and Andrew Huxley the Nobel Prize in Physiology on Medicine in 1963.

The Hodgkin–Huxley model is a conductance-based model that represents the biophysical characteristic of cell membranes as shown in Fig.3.5.

The mathematical model is described by the following equations:

$$\begin{aligned}
I &= C_m\frac{dV_m}{dt} - \bar{g}_K n^4(E_K - V_m) - \bar{g}_{Na}m^3h(E_{Na} - V_m) - \bar{g}_L(E_L - V_m),\\
\frac{dn}{dt} &= \alpha_n(V_m)(1-n) - \beta_n(V_m)n,\\
\frac{dm}{dt} &= \alpha_m(V_m)(1-m) - \beta_m(V_m)m,\\
\frac{dh}{dt} &= \alpha_h(V_m)(1-h) - \beta_h(V_m)h.
\end{aligned} \tag{3.4}$$

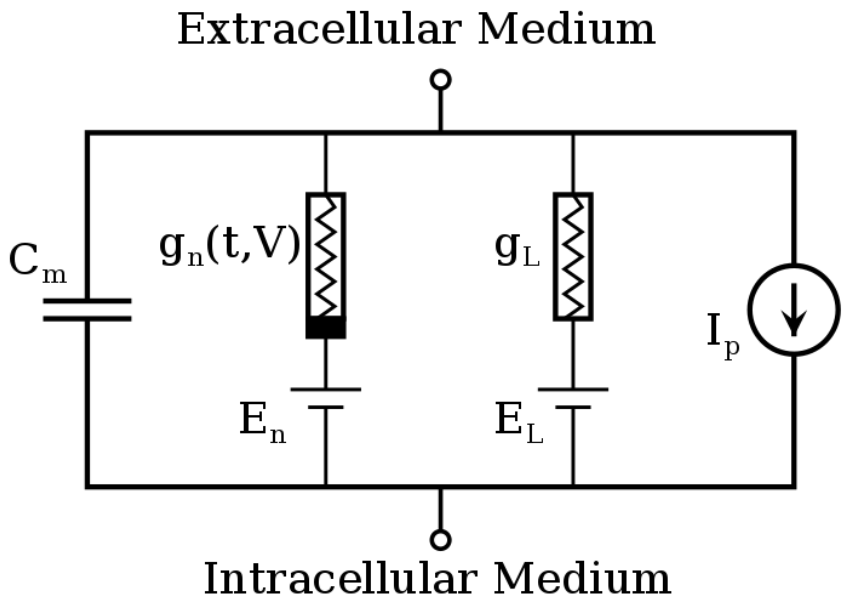

Figure 3.5: **Basic components of Hodgkin–Huxley-type models.** C_m is the membrane capacitance, $g_n(n = Na, K), g_L$ are ion channels and leak conductances, respectively; E_n, E_L are batteries that drive the flow of ions of ion channels and leak channel, respectively; I_p is the current input. Taken from [55].

where I is the total membrane current, C_m is the membrane capacitance, V_m is the membrane potential, E_K, E_{Na} and E_L are the potassium, sodium, and leak reversal potentials, respectively; $\bar{g}_p$ $(p = (n, m, h))$ is the maximal value of the conductance, n, m, and h are associated with potassium channel activation, sodium channel activation, and sodium channel inactivation, respectively. The functions α_p, β_p with $p = (n, m, h)$ take the form:

$$\begin{aligned} \alpha_p(V_m) &= p_\infty(V_m)/\tau_p, \\ \beta_p(V_m) &= (1 - p_\infty(V_m))/\tau_p. \end{aligned} \tag{3.5}$$

where p_∞ is the steady state value for activation. The specific expressions are:

$$\begin{aligned} \alpha_n(V_m) &= \frac{0.01(V_m + 55)}{1 - \exp(\frac{-(V_m+55)}{10})}, \\ \beta_n(V_m) &= 0.125 \exp(\frac{-(V_m + 65)}{80}), \\ \alpha_m(V_m) &= \frac{0.1(V_m + 40)}{1 - \frac{\exp(-(V_m+40))}{10}}, \\ \beta_m(V_m) &= 4 \exp(\frac{-(V_m + 65)}{18}), \\ \alpha_h(V_m) &= 0.07 \exp(\frac{-(V_m + 65)}{20}), \\ \beta_h(V_m) &= \frac{1}{1 + \frac{\exp(-(V_m+35))}{10}}. \end{aligned} \tag{3.6}$$

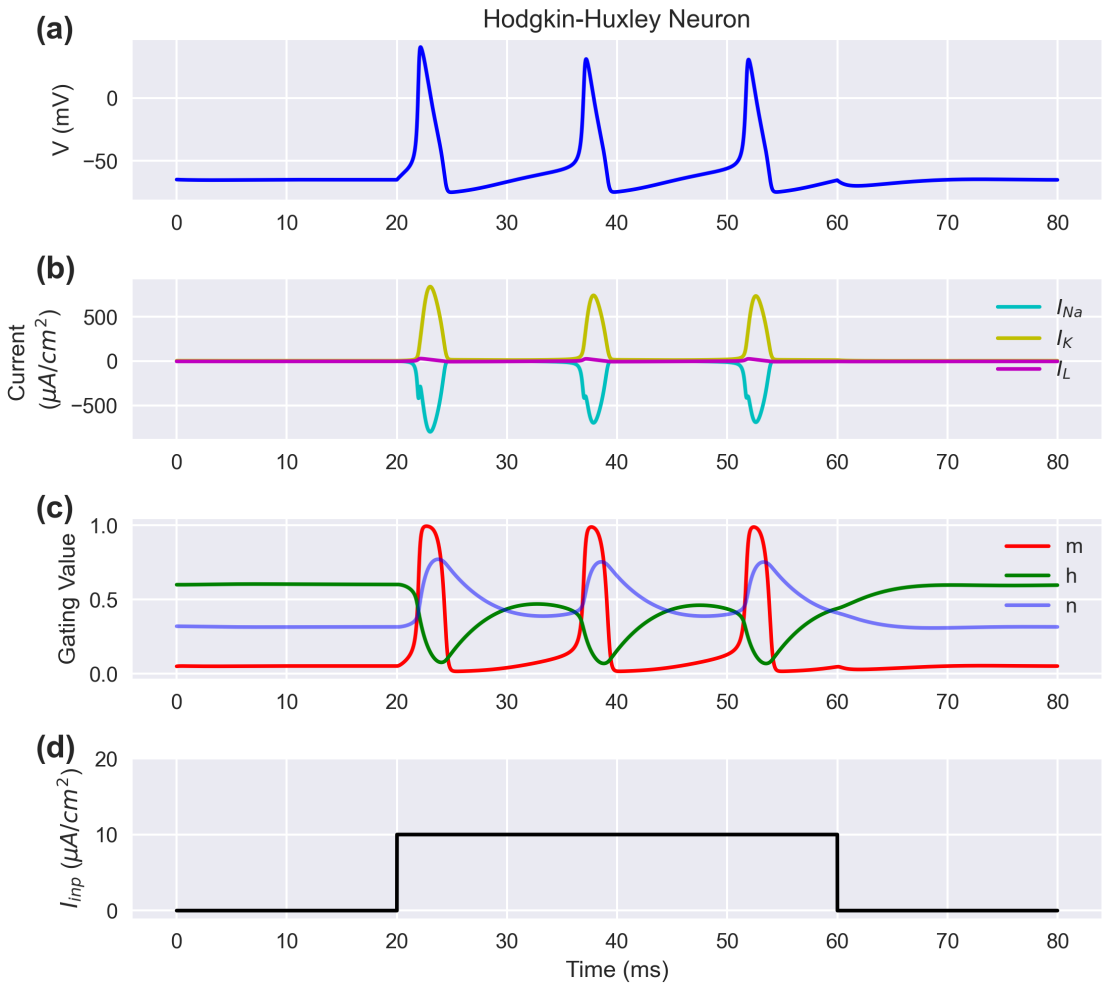

Figure 3.6: **The dynamics of the Hodgkin-Huxley model with different stimulus current I.** (a) Membrane voltage. (b) Ion channel currents. (c) Potassium channel activation n, sodium channel activation m, and sodium channel inactivation h. (d) Input current.

The ion channel kinetics in Eq.3.4 can be written in another useful form by dividing by $(\alpha_p(V_m) + \beta_p(V_m))$,

$$\begin{aligned} \tau_p(V_m)\frac{dp}{dt} &= p_\infty(V_m) - p, \\ \tau_p(V_m) &= \frac{1}{\alpha_p(V_m) + \beta_p(V_m)}, \\ p_\infty &= \frac{\alpha_p(V_m)}{\alpha_p(V_m) + \beta_p(V_m)}. \end{aligned} \tag{3.7}$$

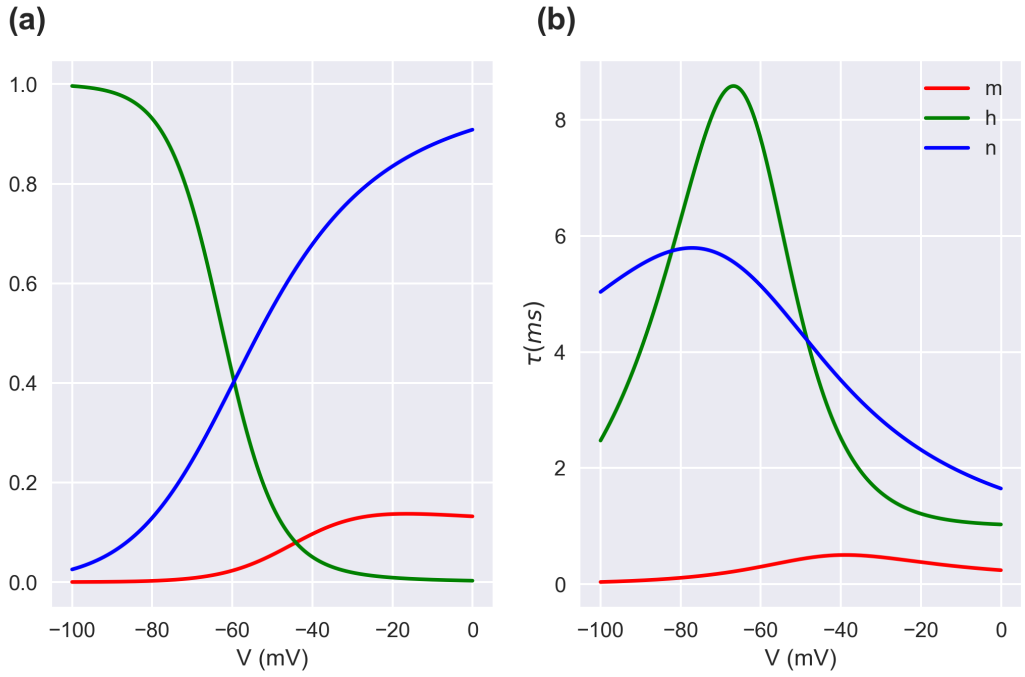

Figure 3.7: **The voltage-dependent functions of the Hodgkin-Huxley model.** (a) The steady-state levels of activation and inactivation of the Na conductance m_∞, h_∞, and activation of the K conductance n_∞. (b) The voltage-dependent time constants that control the rates at which these steady-state levels are approached for the three gating variables.

Parameters			
Symbol	Definition	Value	unit
I	Total membrane current	-	$\mu A/cm^2$
C_m	Membrane capacitance	1.0	$\mu F/cm^2$
E_K	Potassium reversal potential	-77	mV
E_{Na}	Sodium reversal potential	50	mV
E_L	Leak reversal potential	-55	mV
$\bar{g}_K$	Maximal potassium conductance	36	mS/cm^2
$\bar{g}_{Na}$	Maximal sodium conductance	120	mS/cm^2
$\bar{g}_L$	Maximal leak conductance	0.3	mS/cm^2
n	Potassium gating variable		
m	Sodium activation gating variable		
h	Sodium inactivation gating variable		

Table 3.1: **Hodgkin-Huxley model parameters**

Fig.3.6 shows the dynamic trace of the Hodgkin-Huxley model. Fig.3.7 shows the voltage-dependent functions of the Hodgkin-Huxley model for m, h, n. The parameters used in HH model are given in Table.3.1.

Fitzhugh-Nagumo model

The Hodgkin-Huxley model is a realistic and biophysical model for studying the dynamic behav-

ior of neural networks, but due to the many variables in its equations, the amount of calculation required in numerical simulation is large. So simplified models have been proposed for large-scale network calculations. The simplified Fitzhugh-Nagumo model was proposed by Richard FitzHugh in 1961 and then tested by the equivalent electric circuit (shown in Fig.3.8) in the following year by J. Nagumo *et al.* [56, 57]. It is successful to explain the basic properties of excitability as exhibited by the more complex Hodgkin-Huxley model.

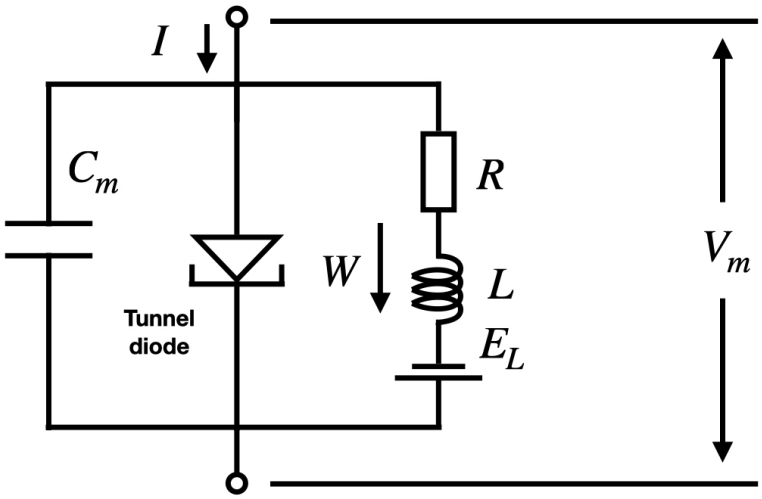

Figure 3.8: **Equivalent circuit diagram of the Fitzhugh-Nagumo model.** C is the membrane capacitance, L is the induction coil, R is the resistance, I is the current inputs. Taken from [57].

The equations for this model are:

$$\begin{aligned} \frac{dv}{dt} &= v - \frac{v^3}{3} - w + I, \\ \frac{dw}{dt} &= \phi(v + a - bw). \end{aligned} \tag{3.8}$$

where v is the membrane potential, w is a recovery variable, I is the magnitude of the stimulus current, and a, b, ϕ are constant number with values $a = 0.7$, $b = 0.8$,$\phi = 0.08$. Although this model is not biological, it is useful as a didactic tool to introduce the dynamics of spike generation through phase plane analysis. When the external stimulus exceeds a certain threshold value, the system exhibits a characteristic excursion in phase space which is typical for spike generation.

The dynamics of the Fitzhugh-Nagumo model is shown in Fig.3.9.

Integrate-and-Fire model

Although the Fitzhugh-Nagumo model reduces computation from four variables to two variables, the numerical integration of the equations of the Fitzhugh–Nagumo model is still computationally expensive when considering complex systems of neurons. So further simplifications of these models need to be considered.

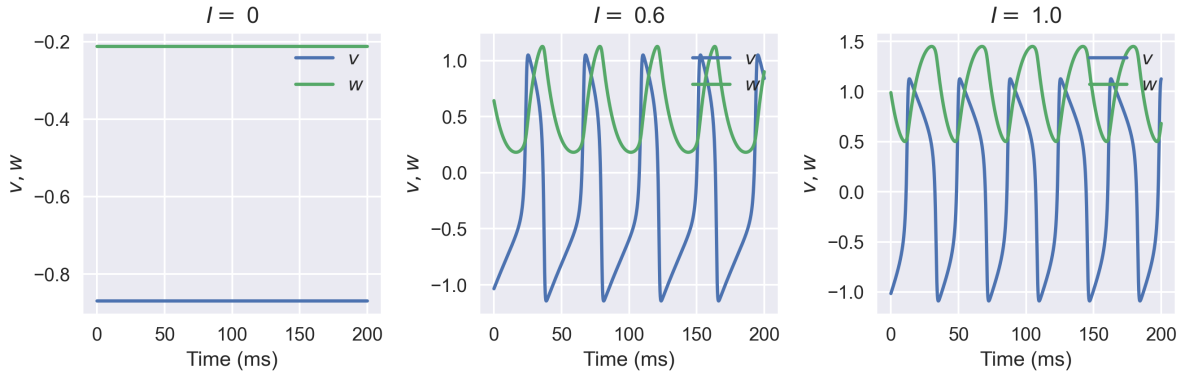

Figure 3.9: **The dynamics of the Fitzhugh-Nagumo model with different stimulus current I.** The other parameters are: $a = 0.7$, $b = 0.8$, $\phi = 0.08$.

- Integrate-and-Fire model:

The Integrate-and-fire model, first described by Louis Lapicque in 1907 [58], is one of the earliest simple models of a neuron. The equation for this model reads

$$I = C_m \frac{dV_m}{dt} \tag{3.9}$$

where C_m is the membrane capacitance, V_m is the membrane voltage, I is the input current. When the input current causes the membrane voltage to reach the threshold V_{th}, one spike occurs and the voltage is reset to the resting potential. Then, Eq.3.9 is used until the next spike occurs. As the input current increases, the firing frequency of the model increases linearly without bound, which is not biologically realistic, so further extensions are considered necessary.

- Leaky integrate-and-fire model (LIF):

As compared with the Integrate-and-fire model, this model considers the diffusion of ions through the membrane as a "leak" term as shown in Fig.3.10.

The equation of this model is

$$C_m \frac{dV_m}{dt} = g_L(E_L - V_m) + I \tag{3.10}$$

or

$$\tau_m \frac{dV_m}{dt} = (E_L - V_m) + IR_m \tag{3.11}$$

where V_m is the membrane potential, g_L is the leak conductance, E_L is the resting potential, I is the external input current, and $\tau_m = \frac{C_m}{g_L}$ ($\tau_m = R_m C_m$) is the membrane time constant.

The dynamics of the leaky integrate-and-fire model is shown in Fig.3.11.

When the input current is constant, the relationship between the firing rate and the input current is

$$r = \begin{cases} [\tau_{ref} + \tau_m ln(\frac{R_m I + E_L - V_{reset}}{R_m I + E_L - V_{th}})]^{-1} & if I > I_{th} = \frac{V_{th} - E_L}{R_m} \\ 0 & if I < I_{th} = \frac{V_{th} - E_L}{R_m} \end{cases} \tag{3.12}$$

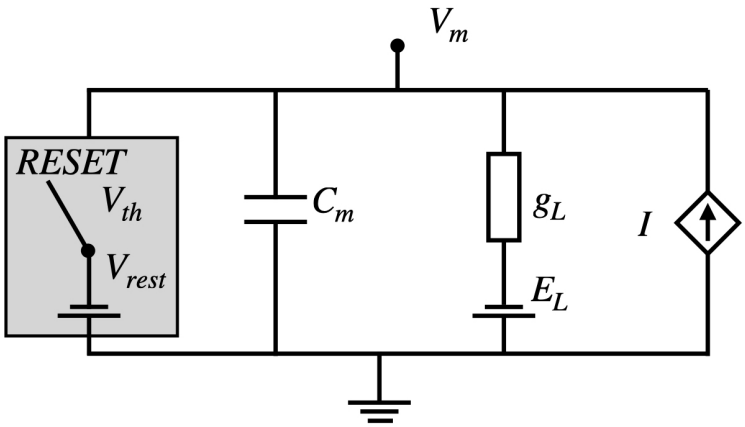

Figure 3.10: **Equivalent circuit diagram of the Integrate-and-fire model.**

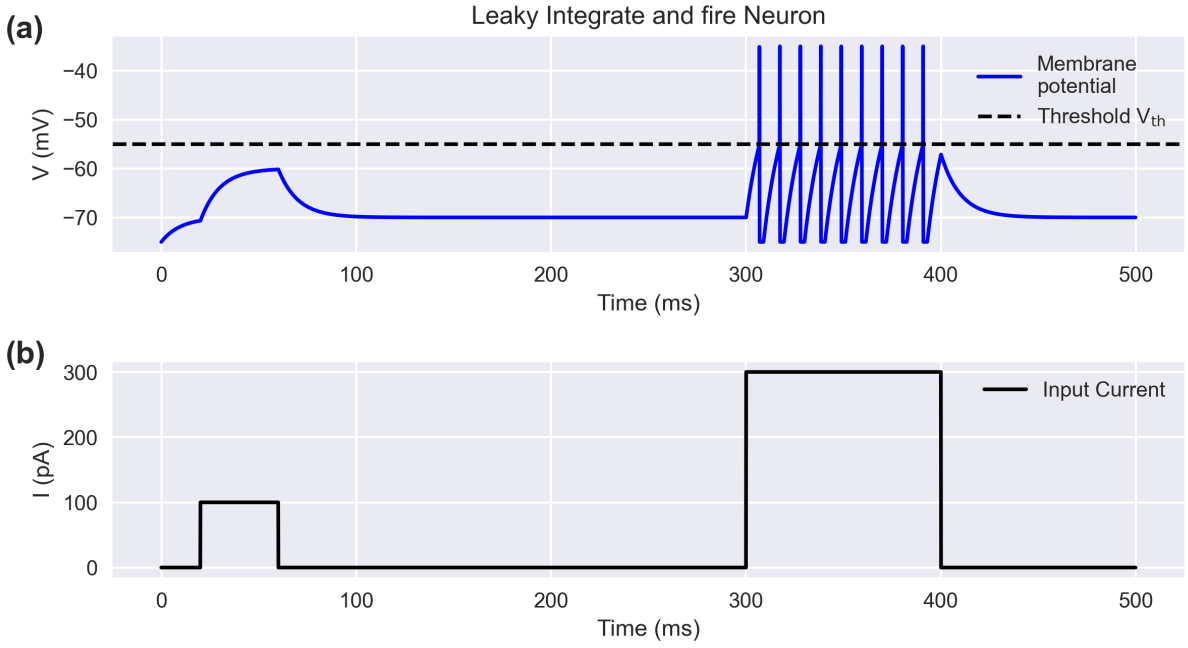

Figure 3.11: **The dynamics of the leaky Integrate-and-fire model with different stimulus current I.** (a) Membrane voltage. (b) Input current. The other parameters are: V_{th} = -55.0 mV, V_{reset}= -75.0 mV, τ_m = 10.0 ms, g_L = 10.0 nS, E_L = -70.0 mV, t_{ref} = 2.0 ms.

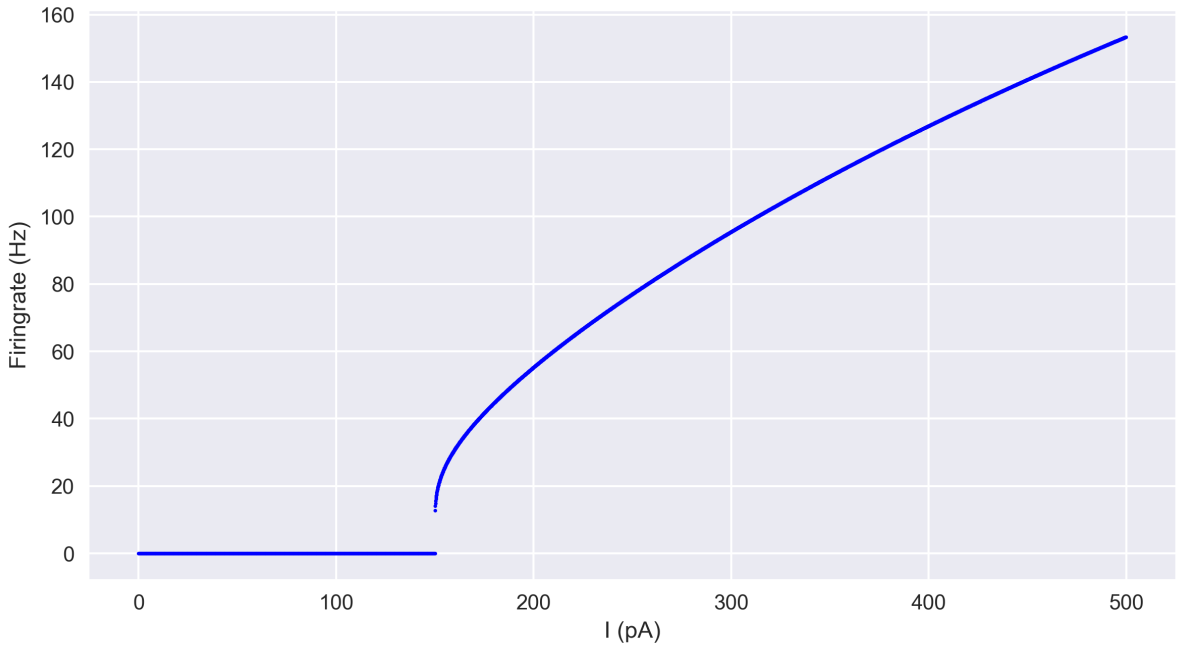

Figure 3.12: **The theoretical (green) and simulated (blue) firing rates of the leaky Integrate-and-fire model with different stimulus current I.** The parameters are: V_{th} = -55.0 mV, V_{reset}= -75.0 mV, τ_m = 10.0 ms, g_L = 10.0 nS, E_L = -70.0 mV, t_{ref} = 2.0 ms.

Fig.3.12 shows the theoretical firing rate (Eq.3.12) and the firing rate measured in simulation as a function of the input current for the LIF model. This type of relation between the firing rate and the input current is called the $f - I$ curve of the neuron.

- Exponential integrate-and-fire model (EIF):

In comparison to the leaky integrate-and-fire model, the exponential integrate-and-fire model modifies how neurons generate action potentials [59]. The threshold for the spike initiation is replaced in the EIF by a depolarizing non-linear term, mimicking the sodium conductance activation. The equation of this model is

$$\tau_m \frac{dV_m(t)}{dt} = (E_L - V_m) + IR_m + \Delta_T \exp(\frac{V_m - V_{th}}{\Delta_T}) \tag{3.13}$$

where V_m is the membrane potential, V_{th} is the intrinsic membrane potential threshold, τ_m is the membrane time constant, E_m is the resting potential, and Δ_T is the sharpness of action potential initiation, usually around 1 mV for cortical pyramidal neurons.

Fig.3.13(a) shows the dynamics of the EIF model, Fig.3.13(b) shows the $f - I$ curve of the EIF model.

Natural inputs are usually complex, and time-varying. In order to mimic this, one can consider different models of input currents:

- Gaussian white noise (GWN)

Gaussian white noise is a zero-mean, stable and ergodic random process described by the following essential property: any two GWN values, no matter how close in time, are statistically

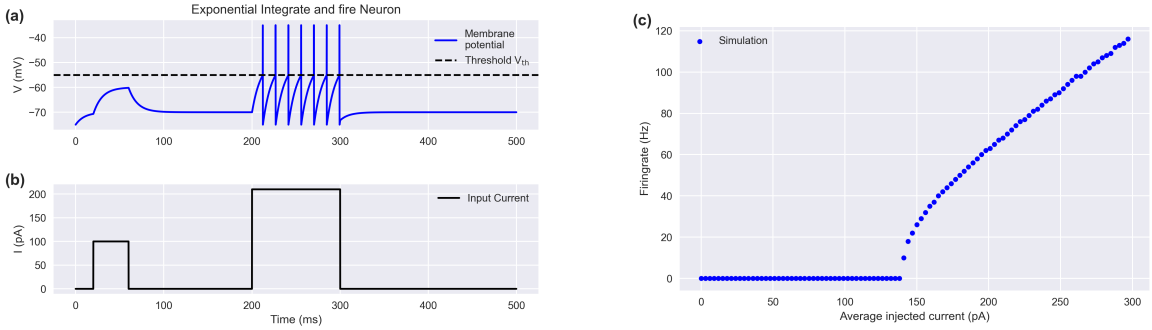

Figure 3.13: **The dynamics of the EIF model.** (a) The membrane potential. (b) The input current. (c) The firing rate VS input current from simulation. The parameters are: $V_{th} = -55.0mV$, $V_{reset} = -75.0mV$, $\tau_m = 10.0ms$, $g_L = 10.0nS$, $E_L = -70.0mV$, $t_{ref} = 2.0ms$, $\Delta_T = 1mV$.

independent, which means that the autocorrelation function of a GWN process is zero for nonzero lags. The dynamics of the EIF model with a constant mean current and fluctuations described by GWN is shown in Fig.3.14.

One can note that the spike train is not regular anymore. It can be described by introducing statistical measures such as the coefficient of variation (CV) of the interspike interval (ISI)

$$CV_{ISI} = \frac{std_{ISI}}{mean_{ISI}}. \tag{3.14}$$

For regular inputs, CV_{ISI}=0, larger CV values mean that the spikes are more irregular as shown in Fig.3.15.

- Ornstein-Uhlenbeck process (OU)

Another noise input that is often used is the *Ornstein-Uhlenbeck* (OU) process. It corresponds to filtered white noise and it can be described by

$$\tau_\eta \frac{d\eta(t)}{dt} = \mu - \eta(t) + \sqrt{2\sigma_\eta \tau_\eta}\xi(t) \tag{3.15}$$

one has for the mean of η, $E[\eta(t)] = \mu$ and for its autocovariance $[\eta(t)\eta(t+\tau)] = \sigma_\eta e^{-|t-\tau|/\tau_\eta}$. σ_η is the variance of the process in its stationary state, τ_η is the time scale controlling the decay of the OU process autocorrelation. Fig.3.16 shows the dynamics of the EIF with OU process input current.

3.3 Synaptic current

Mathematical models for different kinds of synapses can be described as follows.

Electrical synapses

Ions can flow between two neurons via gap junctions, according to the properties of electrical synapses discussed previously. A mathematical model of electrical synapses can be established

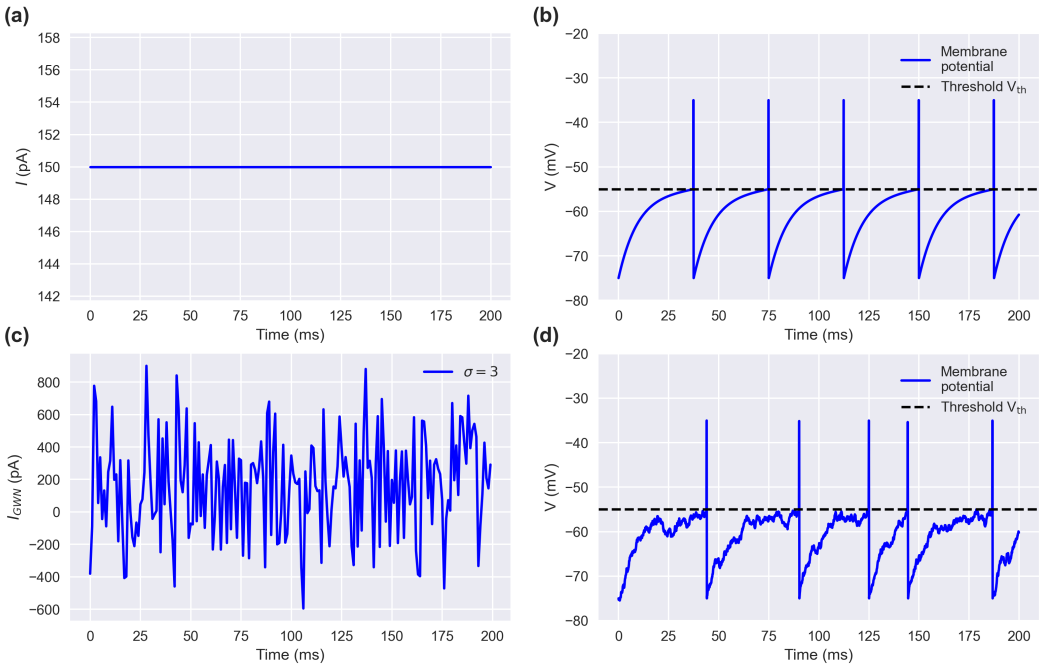

Figure 3.14: **The dynamics of the exponential integrate-and-fire model with Gaussian white noise ($\mu = 150pA$, $\sigma = [0, 3]$) Input I.** (a, c) Input currents. (b, d)Membrane voltages. The other parameters are: $V_{th} = -55.0mV$, $V_{reset} = -75.0mV$, $\tau_m = 10.0ms$, $g_L = 10.0nS$, $E_L = -70.0mV$, $t_{ref} = 2.0ms$, $\Delta T = 1mV$.

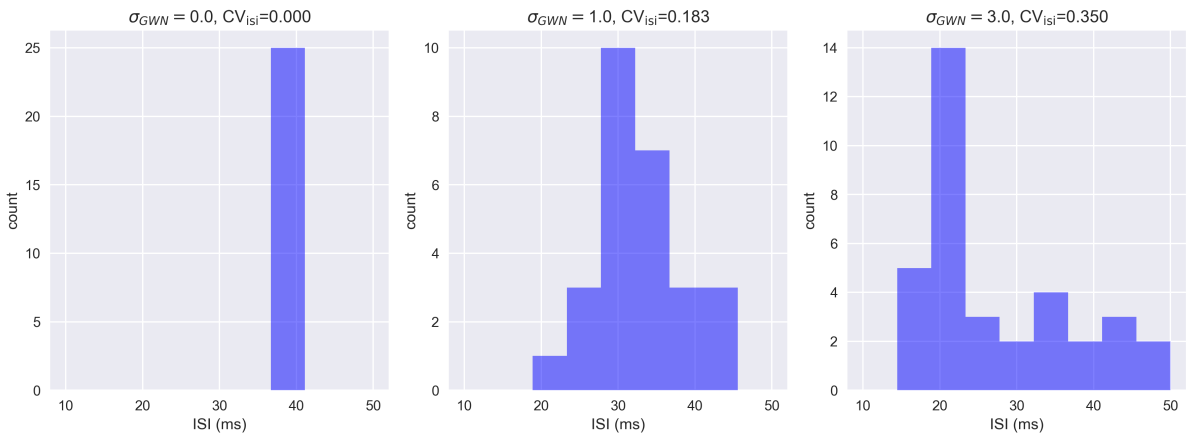

Figure 3.15: **The ISI distribution with different σ for GWN of the EIF model.**

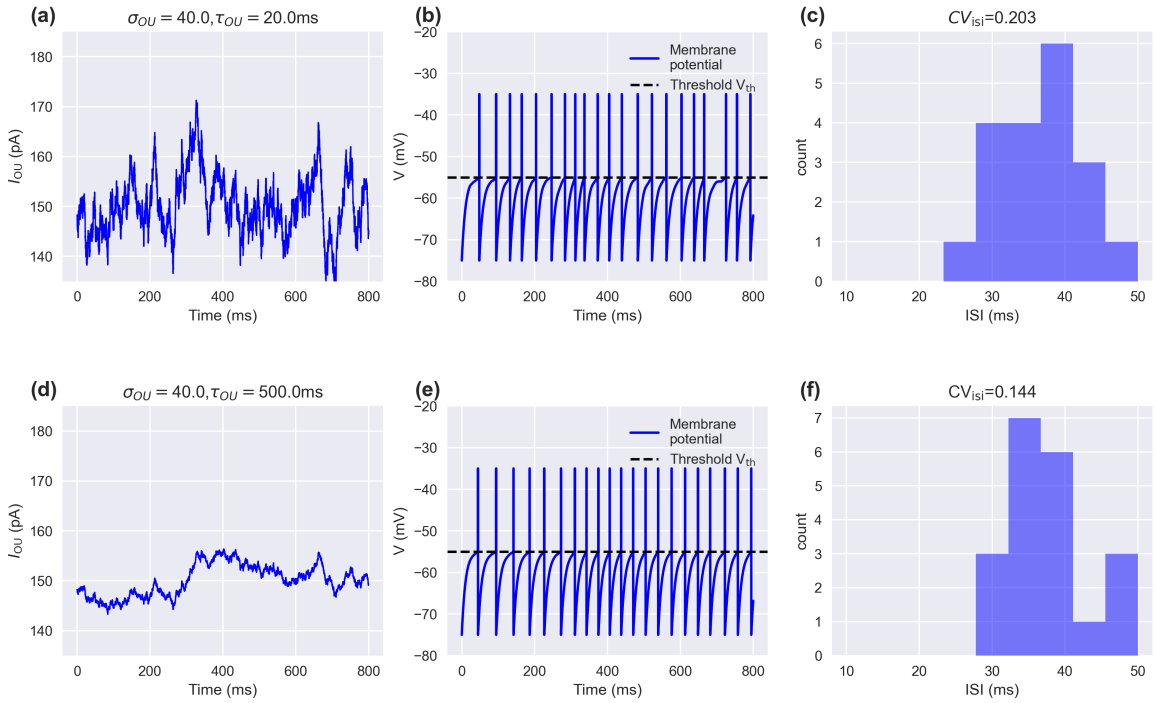

Figure 3.16: **The dynamics of EIF model with OU noise of different τ_η ($\tau_\eta = [20, 500]ms$).** (a, d) Input Currents. (b, d) Membrane voltage. (c, e) The distribution of ISI. The other parameters are: $\mu = 150pA$, $\sigma_\eta = 40$, $V_{th} = -55.0mV$, $V_{reset} = -75.0mV$, $\tau_m = 10.0ms$, $g_L = 10.0nS$, $E_L = -70.0mV$, $t_{ref} = 2.0ms$, $\Delta T = 1mV$.

using Ohm's law as [60]

$$I_{ij}(t) = g_{ij}(V_j(t) - V_i(t)) \tag{3.16}$$

where I_{ij} is the current from synapse j to synapse i, and g_{ij} is the conductance between them.

Chemical synapses

For chemical synapses, the presynaptic cell releases neurotransmitter moleculars into the synapse. Some bind to receptors on the postsynaptic cell surface, directly influencing the state of an associated ion channel, thus forming an excitatory or an inhibitory postsynaptic transmembrane current (EPSC or IPSC). A mathematical description of chemical synapses can be established as:

$$I_{syn}(t) = g_{syn}(t)(V(t) - E_{syn}) \tag{3.17}$$

where E_{syn} and g_{syn} are the synapse reversal potential and time-dependent conductance, respectively. For inhibitory synapses $E_{syn} = -75mV$, whereas for excitatory synapses $E_{syn} \approx 0mV$. An exponential decay is a simple choice for the time course of the synaptic conductance in

Eq.3.17,

$$g_{syn}(t) = \sum_f \bar{g}_{syn} e^{-(t-t^f)/\tau} \Theta(t - t^f) \tag{3.18}$$

where τ is the decay time constant, $\bar{g}_{syn}$ is the maximum conductivity, t^f denotes the arrival time of a presynaptic action potential and Θ is the *Heaviside* step function. For some synapses, the postsynaptic current is more complex and made up of two different components, a fast one with a decay time constant of a few milliseconds, and a slower one with a decay time often ten times slower than the fast one. If one also considers the smooth rise of the synaptic response, the postsynaptic conductance can be described by [45],

$$\begin{aligned} g_{syn}(t) = \sum_f \bar{g}_{syn}(1 - e^{-(t-t^f)/\tau_{rise}}) \\ (ae^{-(t-t^f)/\tau_{fast}} + (1-a)e^{-(t-t^f)/\tau_{slow}})\Theta(t - t^f) \end{aligned} \tag{3.19}$$

where a is the relative weight of the fast component, and τ_{rise} is the rise time of the synaptic conductance.

An excitatory postsynaptic potential (EPSP) is a postsynaptic potential that increases the likelihood of a postsynaptic neuron to fire an action potential, whereas an inhibitory postsynaptic potential (IPSP) has the inverse effect. The neurotransmitter often associated with EPSP in the brain is the amino acid glutamate. AMPA receptors and NMDA receptors are the most common types of excitatory receptor channels in the brain. AMPA receptors lead to a fast EPSC whereas NMDA receptors lead to a slower EPSC. GABA (gamma-Aminobutyric acid) receptors are the most common inhibitory receptors.

The dynamics of postsynaptic current for different kinds of synapses are shown in Fig.3.17. The corresponding parameters are provided in Table.3.2

Parameters						
Type	$\bar{g}_{syn}$	$E_{syn}(mV)$	$\tau_{rise}(ms)$	$\tau_{fast}(ms)$	$\tau_{slow}(ms)$	a
$GABA_A$	40	-75	1	6	100	1
$GABA_B$	40	-75	50	300	500	0.8
$AMPA$	8	0	1	6	100	1
$NMDA$	8	0	50	50	100	0.8

Table 3.2: **Postsynaptic current parameters.**

Synapses on the exponential integrate-and-firing rate model

We consider a synaptic input current I_{syn} which includes both excitatory and inhibitory components. Then, the total synaptic current can be described by

$$I_{syn}(V_m, t) = g_E(t)(E_E - V_m) + g_I(t)(E_I - V_m) \tag{3.20}$$

where g_E, g_I are the excitatory and inhibitory conductances, respectively. We simply modeled

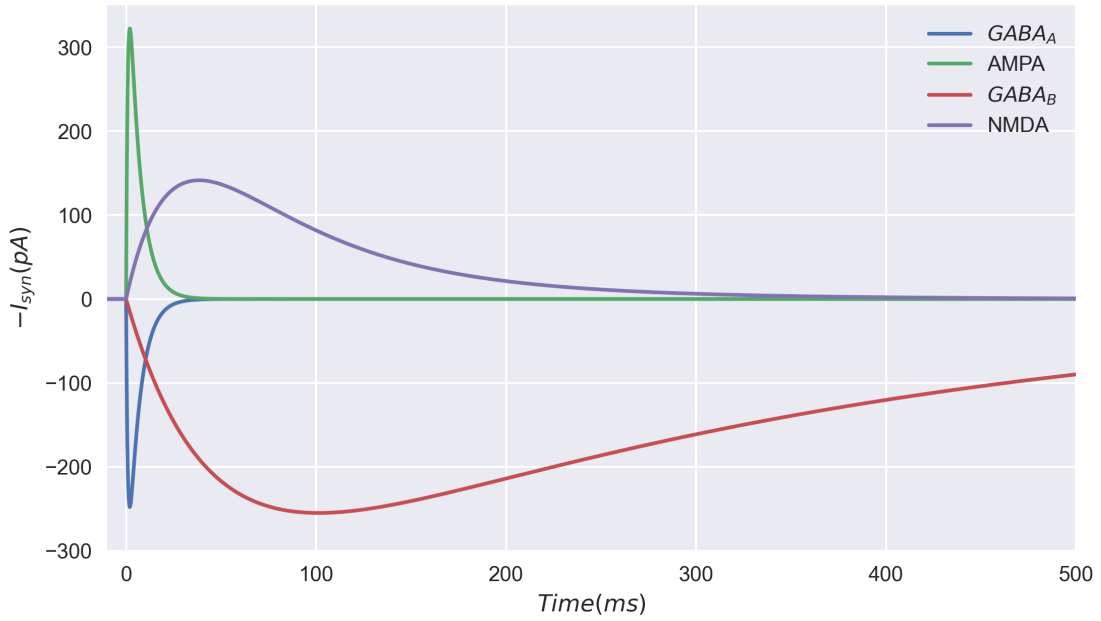

Figure 3.17: **Dynamics of postsynaptic current after a single presynaptic spike of $\mathbf{GABA}_A$, $\mathbf{GABA}_B$, AMPA, NMDA.** The parameters are given in Table.3.2.

them as exponential functions,

$$\frac{dg_A(t)}{dt} = \bar{g}_A \sum_k \delta(t - t_k) - \frac{g_A(t)}{\tau_A}, A \in \{E,\ I\}. \tag{3.21}$$

So the membrane potential dynamics of the EIF neuron under synaptic current drive can be described by:

$$\begin{aligned}\tau_m \frac{dV_m(t)}{dt} &= (E_L - V_m(t)) + (g_E(t)(E_E - V_m(t)) + g_I(t)(E_I - V_m(t)) + I)R_m \\ &+ \Delta_T \exp(\frac{V_m(t) - V_{th}}{\Delta_T}).\end{aligned} \tag{3.22}$$

We assume that the input spikes are *Poissonian* spike trains. An example of the membrane potential trace of this model is shown in Fig .3.18 (a). The presynaptic spike trains are generated with average rates is $5Hz$, $10Hz$ for the excitatory and inhibitory inputs, respectively. Here, The model with 80 independent excitatory synapses and 20 inhibitory ones (see Fig .3.18 (b, c)).

The "Free membrane potential" describes the membrane potential of the neuron when its spike generation mechanism is removed.

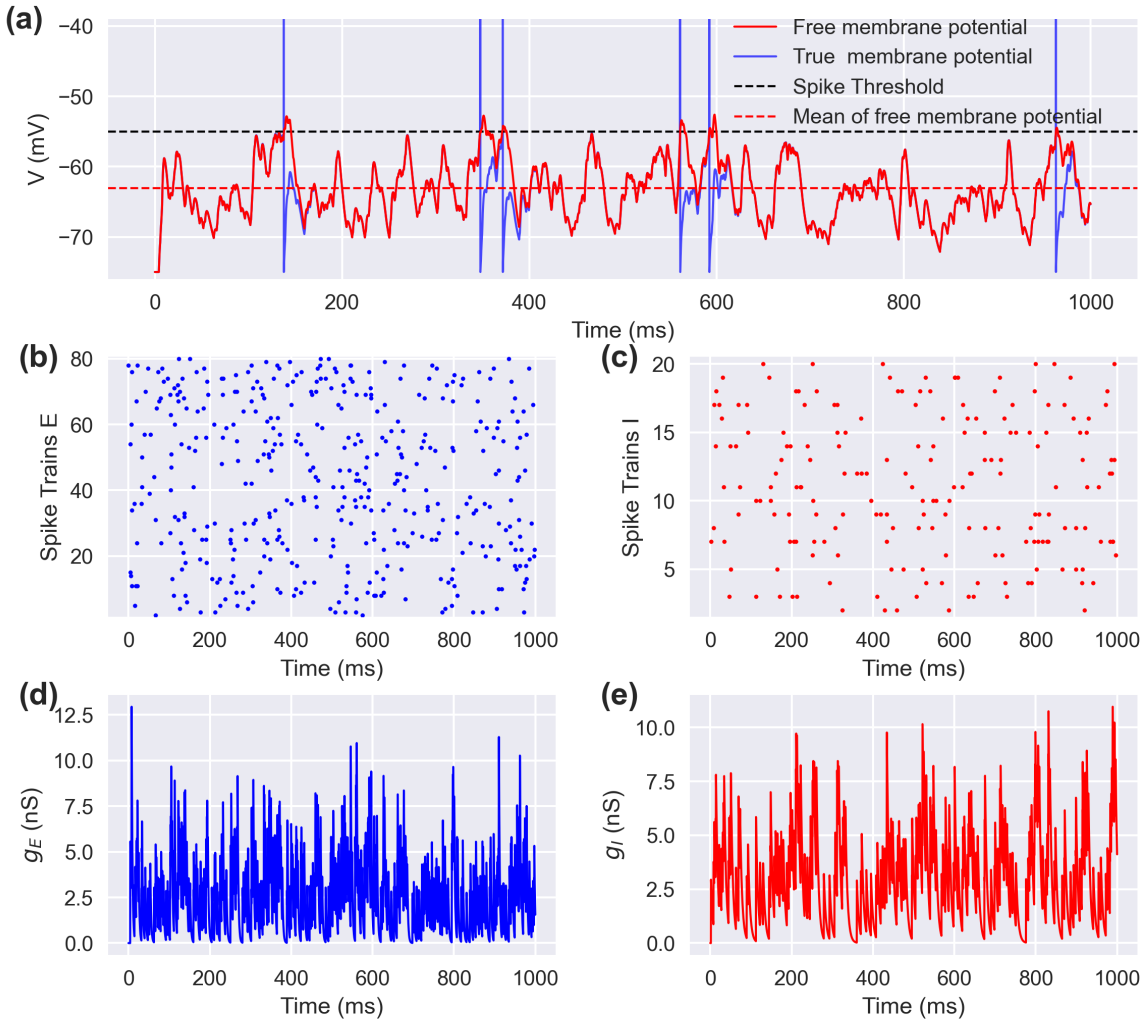

Figure 3.18: **The membrane potential of the EIF model with *Poissonian* spike trains.** (a) The membrane potentials. (b) The excitatory spike trains ($N_E = 80$, $r_E = 5Hz$). (c) The inhibitory spike trains ($N_I = 20$, $r_I = 10Hz$). (d, e) The traces of the excitatory and inhibitory conductances. The other parameters are given in Table.3.3.

Parameters			
Symbol	Definition	Value	unit
τ_m	Membrane time constant	10	ms
τ_E	Excitatory synapse time constant	2	ms
τ_I	Inhibitory synapse time constant	5	ms
E_E	Excitatory synapse reversal potential	0	mV
E_I	Inhibitory synapse reversal potential	-75	mV
E_L	Leak reversal potential	-70	mV
$\bar{g}_E$	Maximal excitatory synapse conductance	3	nS
$\bar{g}_I$	Maximal inhibitory synapse conductance	3	nS
$\bar{g}_L$	Leak conductance	10	nS
V_{th}	Spike threshold potential	-55	mV
Δ_T	Sharpness of action potential initiation	1	mV

Table 3.3: **Synapse current on the EIF model parameters**

3.4 Network models

Understanding how individual neurons release action potentials in response to time-varying inputs is critical for understanding how information is encoded in the brain. A typical neuron receives thousands of synaptic inputs. The membrane potential dynamics in response to such time-varying inputs are extremely complicated. As a result, simplified phenomenological models that ignore biophysical aspects are frequently used to depict the input-output transformation of individual neurons. For example, building networks with firing rates rather than action potentials is a simple and widely used approach. This firing rate model description has been used in many studies since the seminal ones [61, 62]. Firing-rate models are much easier to simulate on computers and to develop analytic calculations. In this section, we will introduce the basic of the firing rate model descriptions.

Firing rate model

- Feedforward network

We consider the feedforward network shown in Fig.3.19(a)), where $\mathbf{v}$ denotes the activity of the postsynaptic neurons, $\mathbf{u}$ is the activity of the presynaptic neurons, and $\mathbf{M}$ is the synaptic weight matrix between them. The firing rate description is

$$\tau \frac{d\mathbf{v}}{dt} = -\mathbf{v} + \Phi(I^{ext}),\ I^{ext} = \mathbf{M} \cdot \mathbf{u} \tag{3.23}$$

τ is the time constant that determines how rapidly the firing rate approaches its steady-state value for a constant I^{ext}. Φ is the $f - I$ curve. It can be the threshold linear function $\Phi(I) = [I - I_{th}]_+$, or the sigmoidal function, $\Phi(I, a, \theta) = \frac{1}{1+\exp[-a(I-\theta)]} + \frac{1}{1+\exp(a\theta)}$, with a, θ is the gain and threshold of the $f - I$ curve respectively. Φ can also be the $f - I$ curve from a specific neuron model like Fig.3.12 or from a real neuron coming from experimental data.

The firing rate model can also be used for recurrent networks, such as excitatory-and-inhibitory network[63]:

- Recurrent network

For the recurrent network shown in Fig.3.19 (b), the description of the output layer firing rate is

$$\tau \frac{d\mathbf{v}}{dt} = -\mathbf{v} + \mathbf{\Phi}(\mathbf{W} \cdot \mathbf{u} + \mathbf{M} \cdot \mathbf{v}). \tag{3.24}$$

It can also be written in terms of the dynamics of the current,

$$\tau \frac{d\mathbf{I}}{dt} = -\mathbf{I} + \mathbf{I}^{\mathbf{ext}} + \mathbf{M} \cdot \mathbf{\Phi}(\mathbf{I}). \tag{3.25}$$

- Excitatory-Inhibitory network

It is convenient to describe a network structure of excitatory and inhibitory neurons (Fig.3.19 (c)) by separating the two neuronal populations,

$$\begin{aligned} \tau_E \frac{d\mathbf{I_E}}{dt} &= -\mathbf{I_E} + \mathbf{I_E^{ext}} + \mathbf{M_{EE}} \cdot \mathbf{\Phi}(\mathbf{I_E}) + \mathbf{M_{EI}} \cdot \mathbf{\Phi}(\mathbf{I_I}), \\ \tau_I \frac{d\mathbf{I_I}}{dt} &= -\mathbf{I_I} + \mathbf{I_I^{ext}} + \mathbf{M_{IE}} \cdot \mathbf{\Phi}(\mathbf{I_E}) + \mathbf{M_{II}} \cdot \mathbf{\Phi}(\mathbf{I_I}). \end{aligned} \tag{3.26}$$

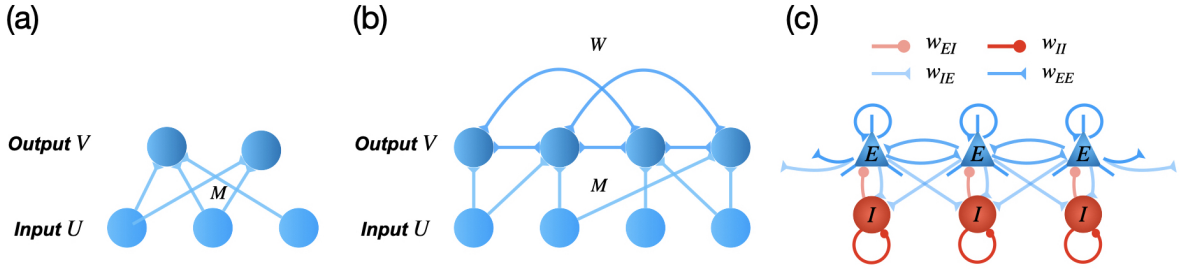

Figure 3.19: **Network models.** (a)Feedfoward network. (b) Recurrent network. (c) Excitatory-Inhibitory network.

Adaptive timescale firing rate model

Recently, Ostojic and Brunel (OB) [64] introduced a model in which the timescale τ depends on the firing rate. This "adaptive" rate model successfully produced an accurate description of firing rate dynamics of an EIF neuron model with relatively strong time-varying inputs (see Fig.3.20. OB called this model the "adaptive timescale firing rate model" .

OB considered that the mapping between input current and output firing rate can be represented with the linear-nonlinear (LN) cascade, which means that the input current is first filtered by a linear filter and then followed by a static non-linear transformation to get the firing

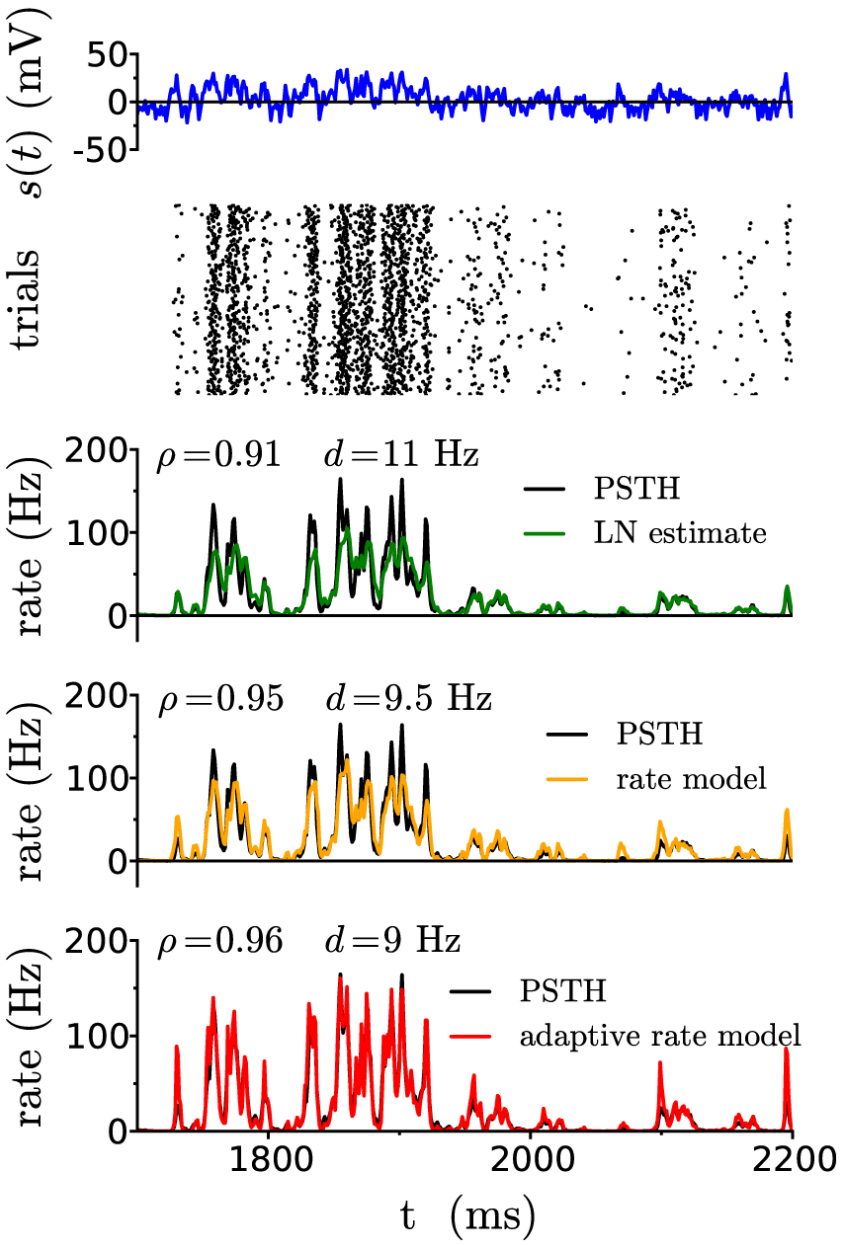

Figure 3.20: **Comparison between PSTH and LN cascade, rate model, adaptive time scale firing model for the EIF model (The Peri-stimulus time histogram (PSTH) is the time dependent firing rate that is calculated by averaging the neuron spike rate over trials).** Taken from [64].

rate. This LN models provide a good approximation of the input-output transform of spiking neurons.

OB considered an input current $I(t)$ to the neuron, divided into a signal and a noise parts:

$$\begin{aligned} I(t) &= I_{signal}(t) + I_{noise}(t), \\ I_{noise}(t) &= I_0 + \sigma\xi(t), \langle\xi(t)\xi(t')\rangle = \delta(t-t'). \end{aligned} \tag{3.27}$$

The input signal I_{signal} is identical across trials. It is taken to be a specific realization of an O-U process with a standard deviation I_s and correlation time τ_s; I_{noise} is an uncorrelated background noise given by a *Gaussian* process, with a mean I_0 and a standard deviation σ. I_{noise} varies from trial to trial.

The firing rate $r(t)$ of the neuron can be described by using a linear-nonlinear cascade

$$\begin{aligned} r(t) &= F(D * s(t)), \\ D * s(t) &= \int_0^\infty d\tau D(\tau)s(t-\tau),\ \ s(t) = I_s n(t). \end{aligned} \tag{3.28}$$

where s is the input signal, D is a temporal linear filter, F is a static non-linearity, $n(t)$ is a *Gaussian* process of zero mean, unit variance and correlation time τ_s.

OB considered two extreme situations:

- The signal amplitude is small enough $I_s \to 0$.

In this situation, Eq.3.28 can be linearized as

$$r(t) = F(0) + F'(0)I_s D * n(t), F(0) = r_0. \tag{3.29}$$

The firing rate of a spiking neuron is given by

$$r(t) = r_0 + I_s R_n * n(t) \tag{3.30}$$

with $R_n(t)$ is the rate response function of the neuron in presence of white noise [65]. By comparing with Eq.3.29 and Eq.3.30, we can identify that the function $F'(0)D$ is equivalent to $R_n(t)$, with $R_n(t)$ is dependent on r_0 and σ.

- The correlation time $\tau_s \to \infty$.

In the LN cascade approximation,

$$r(t) = F(D_0 s(t)). \tag{3.31}$$

And the above equation resembles the response function of the $f - I$ curve:

$$r(t) = \Phi(I_0 + s(t)) \tag{3.32}$$

with Φ is a transfer function that depends on the variance σ of background noise. By comparing Eq.3.31 and Eq.3.32, OB obtained

$$F(L) = \Phi(I_0 + L/D_0). \tag{3.33}$$

Then OB extended the formula to the full parameter space with $F'(0) = 1, D_0 = \Phi'(I_0)$ and got

$$\begin{aligned} D(t) &= R_n(t), \\ F(L) &= \Phi(I_0 + L/\Phi'(I_0)). \end{aligned} \tag{3.34}$$

For EIF models, the linear filter is exponential with a single, effective timescale τ_{eff}

$$\begin{aligned} D_{eff} &= A\exp(-t/\tau_{eff}), \\ A &= \Phi'(r_0)/\tau_{eff}. \end{aligned} \tag{3.35}$$

And the LN cascade (Eq.3.28) can be rewritten as (see [64] for a detailed explanation):

$$\begin{aligned} r(t) &= \Phi(I), \\ \tau_{eff}\frac{dI}{dt} &= -I + I_0 + s(t), \\ \tau_{eff} &= \tau_m \Delta_T \frac{\Phi'(I)}{r}. \end{aligned} \tag{3.36}$$

The timescale τ_{eff} is dependent on the instantaneous firing rate r. This is the reason why OB called this model, the adaptive time scale firing rate model.

Fitted adaptive timescale firing rate model

More recently, Anirudh et al. [66] modeled the adaptive timescale model by taking the exponential kernel that best fitted the firing rate response to an oscillating current at different frequencies based on [67]. They computed the response function for the EIF neuron for frequencies from 1 Hz to 1000 Hz with a linear spacing of 1 Hz and input currents I with step size $0.1mV$. Then, they fitted the firing-rate response by the *Fourier* transform of an exponential decay in the time domain with $\frac{A}{\sqrt{1+(i2\pi f\tau_{eff})^2}}$ for each value. They fit one which gave the minimum squared error between the original data to get the time constant. Fig.3.21(a, b) shows the $f - I$ curve and $\tau^{FAT}(I)$ and $\tau^{OB}(I)$ (see [64]). This fit function more accurately describes population-level oscillations of an E–I spiking neuron module than the adaptive time scale model (see Fig.3.21(c)). Anirudh *et al.* called this model, the fitted adaptive timescale rate model.

$$\begin{aligned} \tau^{FAT}\frac{dI}{dt} &= -I + I_0 + s(t), \\ r(t) &= \Phi(I). \end{aligned} \tag{3.37}$$

Firing rate models have been actively used to model the activity of large populations of neurons and synapses using interval distribution, autocorrelation, noise spectrum, and other mea-

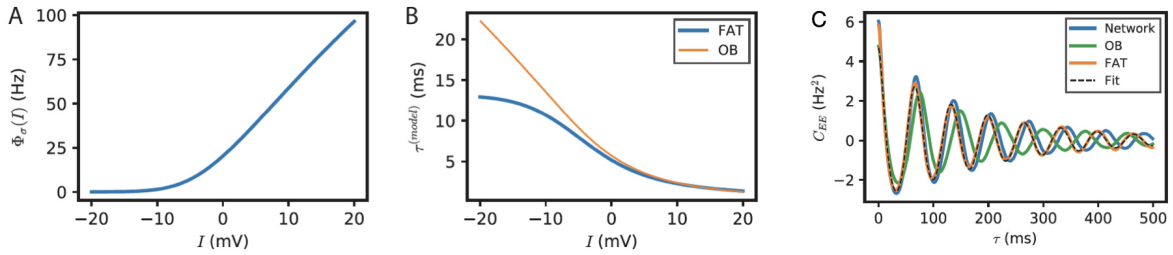

Figure 3.21: **The FAT rate model for the EIF model.** (a) The f-I curve . (b) The fitted adaptive timescale $\tau^{FAT}(I)$ and the adaptive timescale $\tau^{OB}(I)$. (c) Comparison of autocorrelation of the excitatory activity between the spiking EIF module and estimates of different models. Adapted from [66].

surement methods. They have been particularly useful to understand brain rhythms, synaptic-based working memory, and to account for experimental data such as LPFs in monkeys and EEGs in humans.

The successful application of the rate concept to neural data has also facilitated the study of how the neuron type, the network structure, the synaptic current model, and the external inputs influence the dynamics. In the next chapter, we will base on the FAT model to study beta oscillations in the motor cortex of monkeys.

4 Dynamics

In the previous sections, we showed how to characterize neural systems using mathematical equations. In this section, we will recall how to utilize fundamental analysis techniques to get insight into the evolution of such systems. We particularly focus on the possible long-term behaviors of the system dynamics near some particular points.

4.1 Dynamical systems

The temporal evolutions of a system consisting of n variables are given by ordinary differential equations of the first order

$$\begin{cases} \frac{dX_1}{dt} & = f_1(X_1, X_2, \cdots, X_n, t) \\ \frac{dX_2}{dt} & = f_2(X_1, X_2, \cdots, X_n, t) \\ & \vdots \\ \frac{dX_n}{dt} & = f_n(X_1, X_2, \cdots, X_n, t) \end{cases}$$

A vectorial formulation is used for the set of quantities, so that the system can be written as:

$$\frac{d\mathbf{X}}{dt} = \mathbf{F}(\mathbf{X}, t). \tag{4.1}$$

The vector $\mathbf{X}$ belongs to the space R^n, called phase space, the dimension of the space is n, also called the number of degrees of freedom of the system. Given the initial condition $\mathbf{X_0}$, the path followed by the system in the phase space during time is called the trajectory or orbit of the system. $\mathbf{F}$ is a vector field, function of $R^n \times R$ in R. The map ϕ associated to each initial condition of the subsequent trajectory $\mathbf{X}(t)$ is called the flow of the field vector. If $\mathbf{F}$ has no explicit dependence on t, the system is called autonomous, otherwise, the system is called non-autonomous. A non-autonomous system can be transformed into an autonomous one by adding t as one more dimension of the system. If $\mathbf{F}$ is a linear function of $\mathbf{X}$, then the system is a linear system, otherwise, it is a nonlinear system. When the initial conditions are given, the solution of the equation is determined. A linear system is easy to solve. The linear superposition of different solutions of the equation is still a solution of the equation, that is, the superposition principle is satisfied. In general, natural systems are nonlinear, and analytical solutions to nonlinear equations are difficult to obtain. Thanks to the rapid development of computer technology, one can use computers to perform numerical calculations and obtain approximate solutions to equations.

When studying a dynamical system, if we are only interested in its long-term behavior, we must study the stable attractors of the system. In the following section, we will introduce mathematical methods for studying the simpler attractors named the fixed points of the system.

4.2 Attractors

The definition of an attractor [68] is a set of the phase space invariants under the action of the flow, which means that if one chooses a point on the attractor as an initial condition, the system's trajectory will follow the attractor and stay on it indefinitely. Each attractor has an attraction basin that contains all of the initial conditions that will yield asymptotically joining trajectories. The most common attractors are stable fixed points, limit cycles (a closed isolated trajectory in the phase space, which is periodic), the limit torus (quasiperiodic), and strange attractors (chaotic).

4.3 Linear stability analysis

Fixed points are the particular points of the phase space which satisfy

$$\mathbf{F}(\mathbf{X}^*) = 0. \tag{4.2}$$

This means that, for a given initial condition, if the dynamical system does not depend on time, it is a fixed point. Fixed points can be stable or unstable.

To get an idea of what the trajectories look like near a fixed point $\mathbf{X}^*$, we can linearize the equations around the fixed point. Considering $\mathbf{X}$ near $\mathbf{X}^*$: $\mathbf{X}= \mathbf{X}^* + \delta X$ with δX small, we have

$$\frac{d\mathbf{X}^*}{dt} + \frac{d(\delta\mathbf{X})}{dt} = \mathbf{F}(\mathbf{X}^* + \delta\mathbf{X}). \tag{4.3}$$

Then consider the Taylor expansion of each function

$$\frac{d(\delta\mathbf{X})}{dt} = f(\mathbf{X}^*) + \frac{\partial f_1}{\partial X_1}|_{\mathbf{X}^*}\delta X_1 + \frac{\partial f_2}{\partial X_2}|_{\mathbf{X}^*}\delta X_2 + \cdots + \frac{\partial f_n}{\partial X_n}|_{\mathbf{X}^*}\delta X_n. \tag{4.4}$$

The equation can be written as:

$$\frac{d(\delta\mathbf{X})}{dt} \simeq \mathbf{F}(\mathbf{X}^*) + \mathcal{L}|_{\mathbf{X}^*}\delta\mathbf{X} \tag{4.5}$$

$\mathcal{L}$ is jacobian matrix of $\mathbf{F}$, and with $\mathbf{F}(\mathbf{X}^*) = 0$, we obtain

$$\frac{d(\delta\mathbf{X})}{dt} = \mathcal{L}|_{\mathbf{X}^*}\delta\mathbf{X}. \tag{4.6}$$

The solutions to this equation are the form of $\delta\mathbf{X}(t) = e^{(t\mathcal{L}|_{\mathbf{X}^*})}\delta\mathbf{X}(0)$. For the eigenvalues with strictly positive real parts, the system will go away from $\mathbf{X}(0)$, the corresponding eigenvectors are unstable; when the eigenvalues have strictly negative real parts, the system will go to $\mathbf{X}(0)$, the corresponding eigenvectors are stable; if the eigenvalues have imaginary parts, it will lead to an oscillating behavior which is superimposed on the trend given by the real part.

To gain a better understanding, we consider a bidimensional dynamical system of the form

$$\begin{cases} \frac{dX_1}{dt} = f_1(X_1, X_2) \\ \frac{dX_2}{dt} = f_2(X_1, X_2) \end{cases}$$

We consider a small perturbation in the vicinity of a fixed point,

$$\mathbf{X} = \mathbf{X}^* + \delta\mathbf{X} = \begin{pmatrix} x_1^* + \delta x_1 \\ x_2^* + \delta x_2 \end{pmatrix} \tag{4.7}$$

We linearize the system around the fixed point $\mathbf{X}^*$ and using $L_{ij} = \frac{\partial f_i}{\partial X_j}|_{\mathbf{X}^*}$, we obtain

$$\begin{cases} \frac{d\delta x_1}{dt} = L_{11}\delta x_1 + L_{12}\delta x_2 \\ \frac{d\delta x_2}{dt} = L_{21}\delta x_1 + L_{22}\delta x_2 \end{cases}$$

we rewrite it as:

$$\frac{d}{dt}\begin{pmatrix} \delta x_1 \\ \delta x_2 \end{pmatrix} = \begin{pmatrix} L_{11} & L_{12} \\ L_{21} & L_{22} \end{pmatrix}\begin{pmatrix} \delta x_1 \\ \delta x_2 \end{pmatrix}. \tag{4.8}$$

Then, we compute the characteristic polynomial $P(\lambda)$,

$$Det(L - \lambda 1) = \begin{vmatrix} L_{11} - \lambda & L_{12} \\ L_{21} & L_{22} - \lambda \end{vmatrix} \tag{4.9}$$

$$= \lambda^2 - Tr(L)\lambda + Det(L) \tag{4.10}$$

where 1 denotes the identity matrix, $Tr(L) = (L_{11} + L_{22})$, $Det(L) = (L_{11}L_{22} - L_{12}L_{21})$. The eigenvalues are the zeros of $P(\lambda)$:

$$\lambda_{1,2} = \frac{Tr(L) \pm \sqrt{(Tr(L))^2 - 4Det(L)}}{2}. \tag{4.11}$$

When $Tr(L)^2 - 4Det(L) \geq 0$: $\lambda_{1,2}$ are real, and the fixed points can be classified as:

- Stable nodes: $\lambda_1 < 0$, $\lambda_2 < 0$
- Unstable nodes: $\lambda_1 > 0$, $\lambda_2 > 0$
- Saddle points: $\lambda_1\lambda_2 < 0$

When $Tr(L)^2 - 4Det(L) < 0$: $\lambda_{1,2}$ have complex part $\sigma \pm i\omega$, the fixed points can be classified as:

- Stable spiral: $\sigma < 0$
- Unstable spiral: $\sigma > 0$
- Center: $\sigma = 0$

Fig.4.1 shows the summary of the above cases.

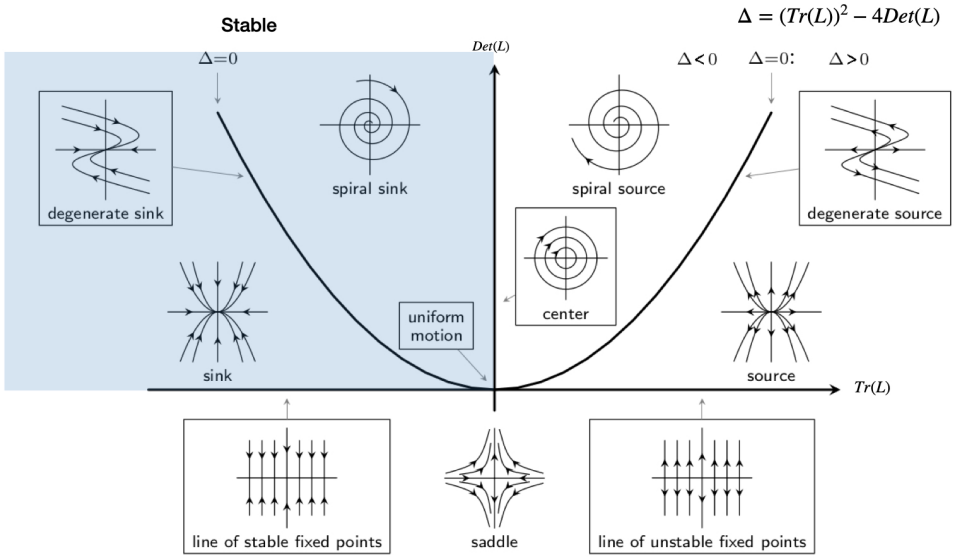

Figure 4.1: **Stability diagram of 2D dynamic system.**

4.4 Bifurcations

In general, the vector field **F** is dependent on parameters, and the system's behavior is affected by the values of those parameters. This means that fixed points can be created or destroyed, or the stability of those fixed points can be changed. This is referred to as bifurcation [68], and the parameters where this type of change occurs are referred to as bifurcation points. Common example of bifurcations include saddle-node bifurcations, transcritical bifurcations, pitchfork bifurcations and Hopf bifurcations. The bifurcation diagram depicts the fixed points as a function of the parameter value. Typically, the set of stable fixed points is represented by a solid line, while the set of unstable fixed points is represented by a dashed line, as shown in Fig.4.2.

In the following, we will recall several classical bifurcations of a vector field **F** depending only on one parameter.

Saddle-node bifurcation

This kind of bifurcation corresponds to the apparition or annihilation of a pair of fixed points. Its normal form is

$$\dot{x} = r - x^2. \tag{4.12}$$

- When $r < 0$, the system has no real solutions;

- When $r > 0$, the system has two fixed points $\pm\sqrt{r}$, one is stable and the other one is unstable, $r = 0$ is the bifurcation point as shown in Fig.4.2(a).

Transcritical bifurcation

This bifurcation corresponds to an exchange of stability between two fixed points. Its normal form is

$$\dot{x} = rx - x^2. \tag{4.13}$$

The fixed points are $x^* = 0$ and $x^* = r$, which gives:

- When $r < 0$, $x^* = 0$ is stable and $x^* = r$ is unstable;
- When $r > 0$, $x^* = 0$ is unstable and $x^* = r$ is stable, $r = 0$ is bifurcation point as shown in Fig.4.2(b).

Pitchfork bifurcation

Supercritical bifurcation:
The normal form of the supercritical pitchfork bifurcation is

$$\dot{x} = rx - x^3. \tag{4.14}$$

The system has one or three fixed points $(x^* = 0, \pm\sqrt{r})$ which depend on the sign of parameter r,

- When $r < 0$, the system has one fixed point $x^* = 0$ which is stable;
- When $r > 0$, the system has three fixed points, $x^* = 0$ is unstable, $x^* = \pm\sqrt{r}$ are stable, as shown in Fig.4.2(c).

Subcritical bifurcation:
The normal form of the subcritical pitchfork bifurcation is:

$$\dot{x} = rx + x^3 \tag{4.15}$$

The stability of fixed points is the inverse of the supercritical bifurcation case, as shown in Fig.4.2(d).

Hopf bifurcation

Supercritical case:
This bifurcation corresponds to the emergence of a periodic solution from a stationary solution. The normal form of the Hopf bifurcation is

$$\dot{z} = z((\mu + i\gamma) - |z|^2) \tag{4.16}$$

where z is complex and μ, γ is real and $\gamma \neq 0$. To do the linear stability analysis, we write

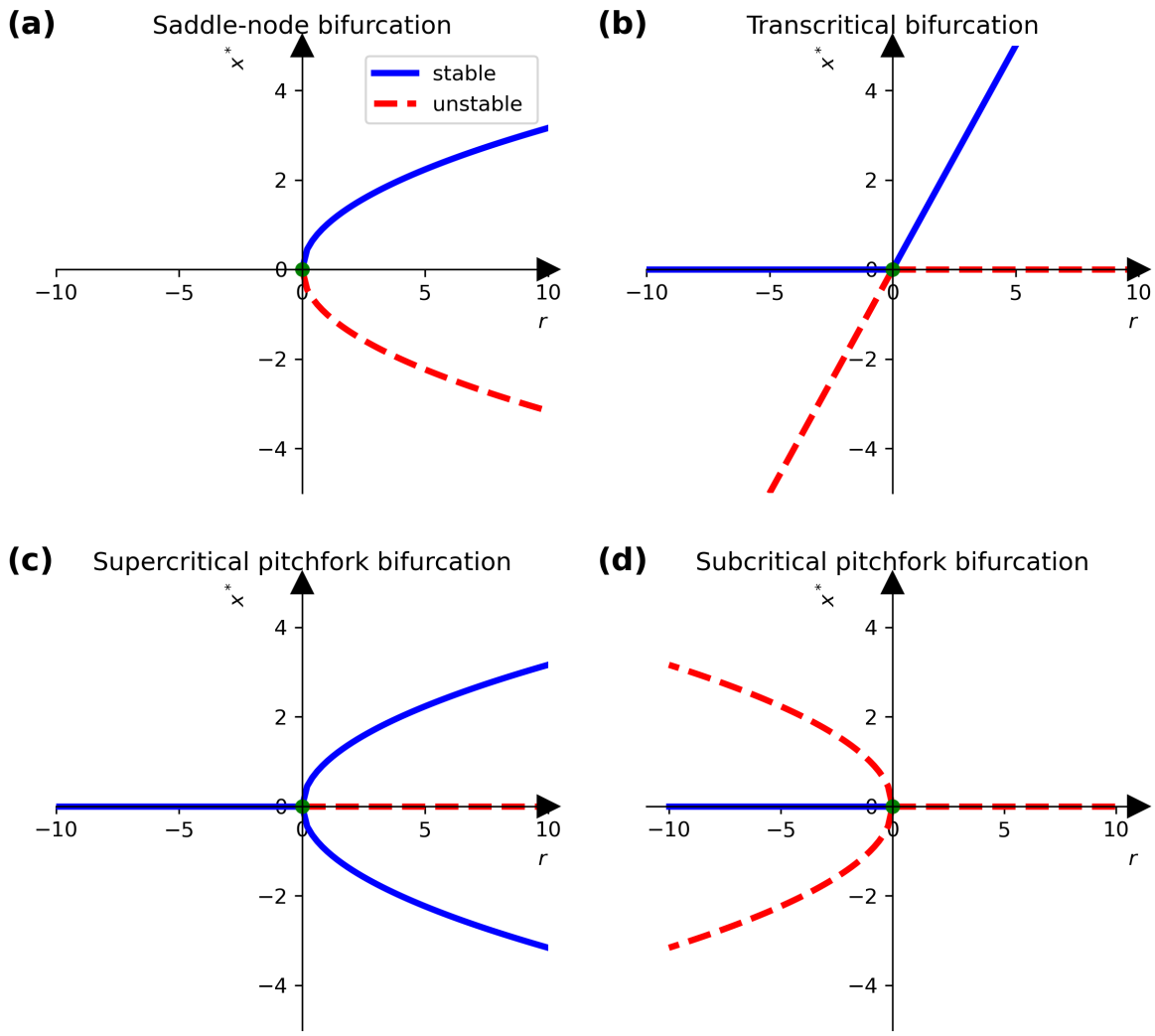

Figure 4.2: **Bifurcation diagram (blue real line is fixed, red dashed line is unstable).** (a) Saddle-node bifurcation. (b) Transcritical bifurcation. (c) Supercritical pitchfork bifurcation. (d) Subcritical pitchfork bifurcation.

$z = x + iy$, then,

$$\begin{cases} \dot{x} = \mu x - \gamma y - x(x^2 + y^2) \\ \dot{y} = \gamma x + \mu y - y(x^2 + y^2) \end{cases}$$

The jacobian matrix at $(0, 0)$ is

$$\mathcal{L}|_{(0,0)} = \begin{pmatrix} \mu & -\gamma \\ \gamma & \mu \end{pmatrix}. \tag{4.17}$$

- When $\mu < 0$,the fixed point $(0, 0)$ is stable
- When $\mu > 0$, the fixed point $(0, 0)$ is unstable. To understand what happens to the trajectories when $\mu > 0$, we use the other decomposition of a complex number with

modulus and phase: $z = re^{i\theta}$ which gives

$$\begin{cases} \dot{r} = \mu r - r^3 \\ \dot{\theta} = \gamma \end{cases}$$

which is the form of supercritical pitchfork bifurcation, the fixed point $r = \sqrt{\mu}$ is stable and $\theta = \gamma t + \theta_0$

Subcritical case:

$$\dot{z} = z((\mu + i\gamma) + |z|^2) \tag{4.18}$$

Leading to unstable limit cycles solution for $\mu < 0$. The Hopf bifurcation diagram as shown in Fig.4.3.

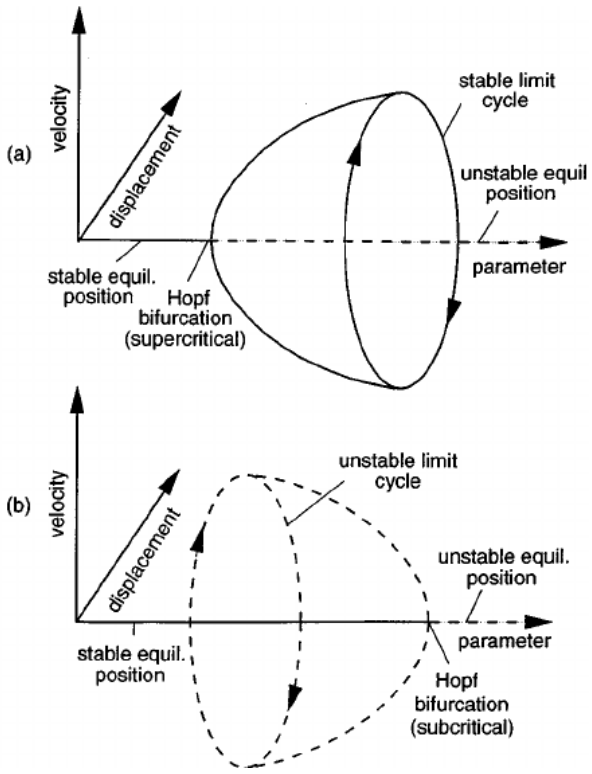

Figure 4.3: **Hopf bifurcation.** (a) supercritical Hopf bifurcation; (b)subcritical Hopf bifurcation. Adapted from [69].

4.5 Stability analysis of the fitted adaptive timescale (FAT) rate model

We consider the rate-model description of an E-I module. It is obtained by coupling an excitatory and an inhibitory neuronal population, each described as:

$$\begin{aligned}\tau_E(I_E)\frac{dI_E}{dt} &= -I_E + w_{EE}r_E - w_{EI}r_I + I_E^{ext}\\ \tau_I(I_E)\frac{dI_I}{dt} &= -I_I + w_{IE}r_E - w_{II}r_I + I_I^{ext}\end{aligned} \tag{4.19}$$

where r_E, r_I are the firing rates of the excitatory and inhibitory populations, $r_E = \Phi(I_E), r_I = \Phi(I_I)$. τ_E, τ_I are the response times and depend on the current I as shown in Fig.4.4. w_{EE}, w_{EI}, w_{IE}, w_{II} are the synaptic weights between the excitatory and the inhibitory neuronal populations. I_E^{ext}, I_I^{ext} represent the external inputs. We choose the steady firing rates: $r_E^s, r_I^s = [5, 10]Hz$, thus,

$$\begin{aligned}I_E^{ext} &= I_E^s - w_{EE}r_E^s + w_{EI}r_I^s,\\ I_I^{ext} &= I_I^s - w_{IE}r_E^s + w_{II}r_I^s.\end{aligned} \tag{4.20}$$

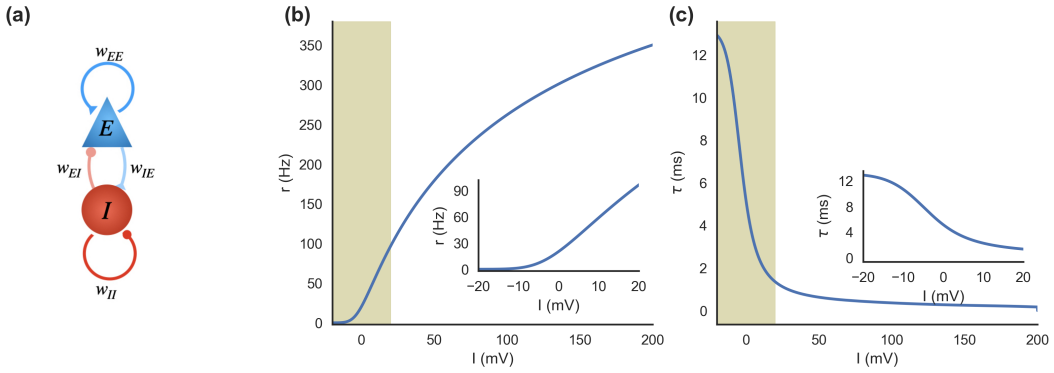

Figure 4.4: **Fitted adaptive timescale (FAT) rate model.** (a) E-I model. (b) Firing rate current f-I curve. (c) Fitted adaptive timescale current τ -I curve.

We consider two different sets of values for the synaptic weights:

- A: $w_{EE} = 2.06mV \cdot s$, $w_{EI} = 1.0mV \cdot s$, $w_{IE} = 2.0mV \cdot s$, $w_{II} = 0.43mV \cdot s$
- B: $w_{EE} = 2.46mV \cdot s$, $w_{EI} = 1.0mV \cdot s$, $w_{IE} = 2.0mV \cdot s$, $w_{II} = 0.43mV \cdot s$

Examples of trajectories for I_E, I_I are shown in Fig.4.5.

In order to analyze the stability of these two cases, we first find the equations of the null-isoclines for I_E and I_I, That is the parameter values such that $\frac{dI_E}{dt} = 0$, $\frac{dI_I}{dt} = 0$. The equilibria are found as the crossing between the null-isoclines as Fig.4.6 shows.

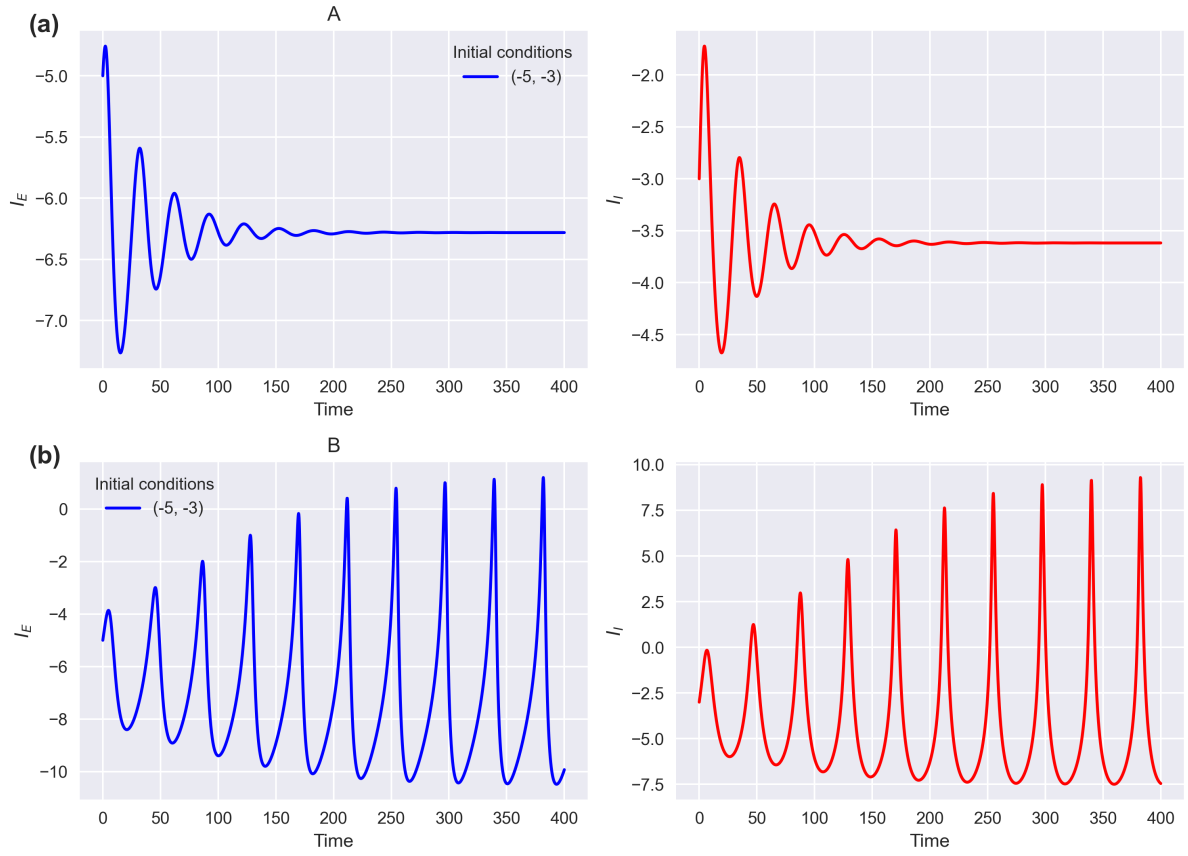

Figure 4.5: **The trajectories of the fitted adaptive timescale (FAT) rate model with different synaptic weights.** A: $w_{EE} = 2.06mV \cdot s$, $w_{EI} = 1.0mV \cdot s$, $w_{IE} = 2.0mV \cdot s$, $w_{II} = 0.43mV \cdot s$; B: $w_{EE} = 2.46mV \cdot s$, $w_{EI} = 1.0mV \cdot s$, $w_{IE} = 2.0mV \cdot s$, $w_{II} = 0.43mV \cdot s$. The blue line corresponds to the excitatory current, the red line corresponds to the inhibitory current.

The Jacobian matrix of the model is

$$L_{|(E^*I^*)} = \begin{pmatrix} (-1 + w_{EE}\Phi'(I_E^*)/\tau_E^* & -w_{EI}\Phi'(I_I^*)/\tau_I^* \\ w_{IE}\Phi'(I_E^*)/\tau_E^* & (-1 - w_{II}\Phi'(I_I^*))/\tau_I^* \end{pmatrix}. \tag{4.21}$$

The corresponding eigenvalues for these two cases are shown in Fig.4.7.

- A: $\lambda_{Re} < 0$, $\lambda_{Im} \neq 0$, the trajectory is a stable spiral
- B: $\lambda_{Re} > 0$, $\lambda_{Im} \neq 0$, the trajectory is an unstable spiral

So, as introduced before, this corresponds to a Hopf bifurcation.

In order to see how the stability of the FAT model changes when we vary the synaptic weights, we take the solutions of Eq.4.21 as linear combinations of two exponentials in time, $\exp(\lambda t)$. The two arguments λ are solutions of

$$\tau_E\tau_I\lambda^2 + ((\gamma+1)\tau_E + (1-\alpha)\tau_I)\lambda + (1-\alpha)(\gamma+1) + \beta = 0 \tag{4.22}$$

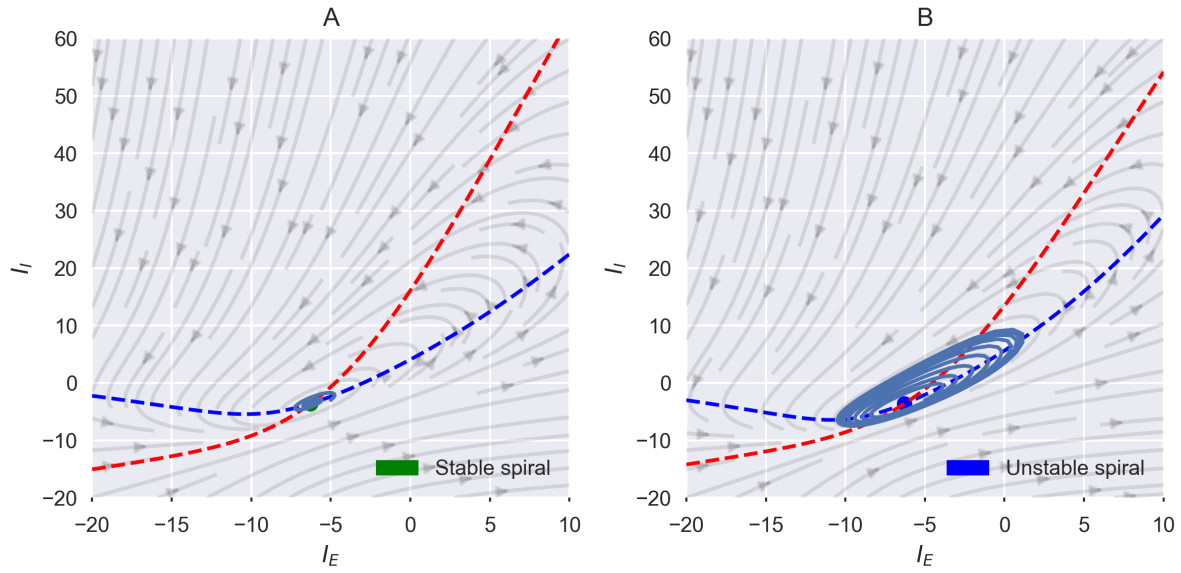

Figure 4.6: **The null-isoclines and vector field of the FAT rate model for different synaptic weights.** The dotted lines are null-isoclines, the grey lines are trajectories, the colored points represent equilibrium points, the dark blue lines are trajectories near the equilibrium points.

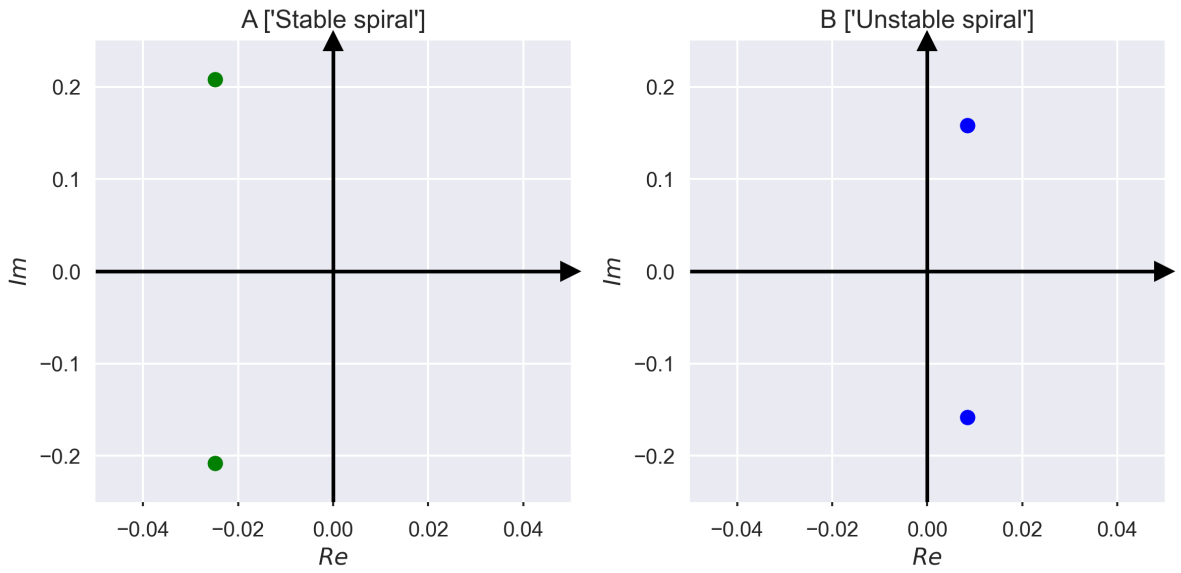

Figure 4.7: **The eigenvalues of FAT rate model for different synaptic weights.**

with

$$\begin{aligned}\alpha &= \Phi'(I_E^*)w_{EE},\\ \beta &= \Phi'(I_E^*)\Phi'(I_I^*)w_{IE}w_{EI},\\ \gamma &= \Phi'(I_I^*)w_{II}.\end{aligned} \tag{4.23}$$

We now use the stability analysis that we introduced before. The real parts of the roots are negative when the two following conditions hold,

$$\begin{aligned}\alpha &< 1 + (\gamma+1)\frac{\tau_E}{\tau_I},\\ \beta &> (\alpha-1)(\gamma+1).\end{aligned} \tag{4.24}$$

The roots have imaginary parts when

$$\beta < \frac{((\gamma+1)\tau_E + (1-\alpha)\tau_I)^2}{4\tau_E\tau_I} + (\alpha-1)(\gamma+1). \tag{4.25}$$

The corresponding stability phase diagram of the FAT rate model is shown in Fig.4.8, for the stationary state values, $r_E^s, r_I^s = [5, 10]Hz$, and for $w_{II} = 0.43mV \cdot s$.

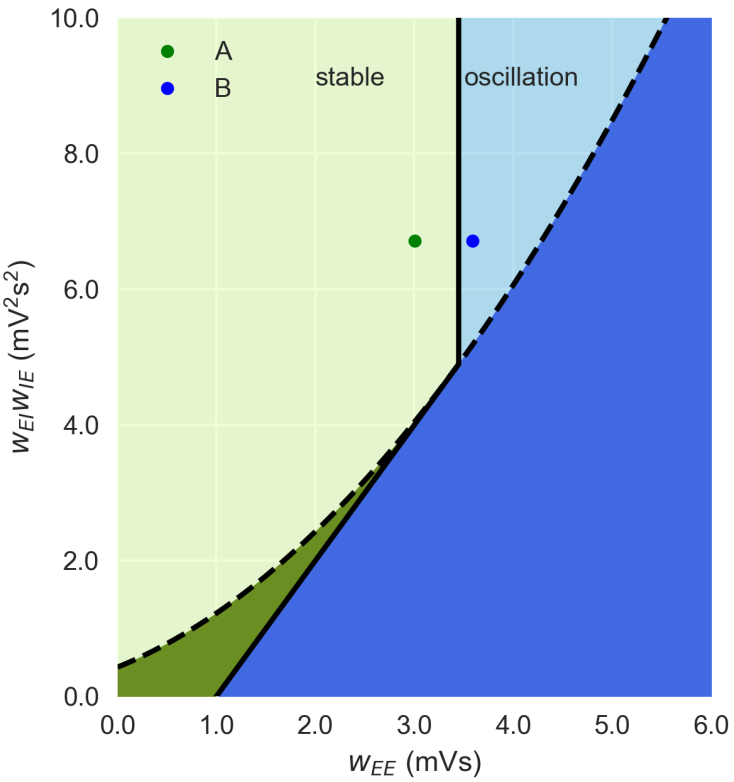

Figure 4.8: **The stability phase diagram of the FAT rate model as a function of synaptic weights.** Stable regions with complex eigenvalues (light green) and real eigenvalues (dark green) as well as unstable regions with complex eigenvalues (light blue) and real eigenvalues (dark blue) are shown for the stationary state $r_E^s, r_I^s = [5, 10]Hz$, $w_{II} = 0.43mV \cdot s$. The parameters for the points A and B are: A: $w_{EE} = 2.06mV \cdot s$, $w_{EI} = 1.0mV \cdot s$, $w_{IE} = 2.0mV \cdot s$; B: $w_{EE} = 2.46mV \cdot s$, $w_{EI} = 1.0mV \cdot s$, $w_{IE} = 2.0mV \cdot s$.

CHAPTER II

Beta oscillation in the motor cortex

5 Basic introduction of neuronal oscillations

5.1 Neural rhythms

Synchronous rhythms are a key mechanism for shaping the temporal coordination of neural activity across the brain, covering more than four orders of magnitude in frequency, from approximately 0.02 to 600 Hz [70]. Neural oscillations in humans were originally observed by Hans Berger in 1924 [71]. More recently, the new high-resolution optical and electrophysiological (EEG) recording technologies led to the observation of neural oscillations at both the macroscopic and mesoscopic scales of the cortex. Oscillatory activity in the brain is widely observed at a variety of spatial and temporal scales and is thought to play different roles in neural information processing. A plethora of experimental studies support a functional role for the variety of neural oscillations [72], which are briefly described below.

Theta rhythm (4-8 Hz)

It is mainly observed in the hippocampus and several other brain regions connected to the hippocampus [73]. Studies have suggested that these rhythms are correlated to some short-memory tasks [74] and various voluntary behaviors, such as exploration, spatial navigation and alert states in rats, which suggests that it may reflect the integration of sensory information with motor output [75, 76]. A lot of evidence indicates that theta rhythm in the neocortex is associated with REM sleep, the transition from sleep to waking [77], and human meditation [78].

Alpha rhythm (8-13 Hz)

It was first discovered by German neurologist Hans Berger who also is the inventor of the EEG [71]. Recent studies have found that the alpha rhythm is present at different stages of the wake-sleep cycle [79] mainly centered in the occipital lobe. Another study has found that the appearance of the alpha rhythm with open eyes can be a predictor of visual information processing in working memory.

Beta rhythm (13-30 Hz)

It was initially observed in the primary motor cortex [71]. Then with the help of the electroencephalogram (EEG) and local field potentials (LFPs) technology, it was observed across the sensorimotor cortex of both human and non-human primates. Studies have shown that beta power increases during movement planning or steady postural configurations and attenuates as movement begins [80, 81, 82, 83]. More recently, it has been observed using multi-electrode arrays that beta oscillations can come as planar or more complex waves propagating horizontally on the motor cortex [84, 85, 86].

Gamma rhythm (30-80 Hz)

One of the earliest reports described gamma activity in the visual cortex of awake monkeys [87]. Later the gamma rhythm has been extensively studied in the visual cortex [88, 89]. It is thought to correlate with large scale brain network activity and cognitive phenomena such as working memory, attention[90], perceptual grouping, and can be increased in amplitude via meditation or neurostimulation [91]. The gamma rhythm is observed as neural synchrony induced by both

conscious and subliminal visual stimuli. It has also shed light on how neural synchrony may explain stochastic resonance in the nervous system [92, 93].

High-frequency rhythm (>80 Hz)

The high-frequency rhythm that occurs in physiological state during immobility and sleep is thought to be involved in memory consolidation [94]. Studies have shown that it is also associated with pathophysiology of the brain like epileptic seizures and schizophrenia [95, 96].

These and other rhythms are bound by a hierarchical relationship, and can temporally coexist in the same or in different structures and interact with each other. They are associated with brain state changes, facilitating the effectiveness of message exchange between brain areas.

Many neurological and mental disorders are associated with rhythm alteration. For example, enhanced beta oscillations in motor areas are a symptom of Parkinson's disease [97, 98, 99], gamma oscillations are diminished in schizophrenia [100, 101], depression is characterized by changes in sleep spindles and hypersynchrony is a sign of epilepsy [102]. So understanding how these neural rhythms are formed and which cognitive behaviors they reflect on is critical for us.

5.2 Network synchronization mechanisms

What is the underlying basis of synchronous cortical rhythms? Thanks to the confluence of computational neuroscience and experimental development, their mechanisms are being revealed. Depending on the source of the inputs, the mechanisms behind the rhythms which synchronize neurons can be divided into two types: oscillatory synaptic recurrent inputs and correlated but random external inputs [72].

Oscillatory synaptic interaction inputs

We consider two types of neurons: excitatory pyramidal neurons and inhibitory interneurons. So the synaptic interactions can be classified as:

- Recurrent excitation between pyramidal neurons. Experiments and modeling have revealed that AMPA receptor mediated excitatory synapses are adequate for synchronizing the low frequency (5–10 Hz) rhythmic bursting carbachol induced rhythm in *vitro* [103], but insufficiently to account for the synchronized oscillations at high frequency.

- Reciprocal inhibition between interneurons. Many studies have shown that inhibition can improve neural synchrony in a broad frequency range[104, 105, 106]. Wang and Buzsaki discovered synchrony in the gamma frequency band with GABAergic interneurons [107], and experiments conducted by Whittington, Traub and collaborators have been the first to report experimentally synchronous oscillations around $40Hz$ in the rat hippocampus in *vitro* [108].

- Reciprocal interactions between excitatory and inhibitory neurons. Wilson and Cowan [62] proposed a firing rate model of reciprocal interactions between excitatory and inhibitory neural populations and this model was successfully used to explain gamma oscillations in the olfactory bulb and hippocampus [109, 110]. The oscillatory cycle dynamics begin as the fast excitation drives up neural firing with positive feedback until the inhibition catches

up and brings the population activity down, as the excitatory drive to interneurons fades, the network recovers from inhibition, and the cycle begins again. At the macroscopic scale of the cortex, both the inhibitory interneuronal network mechanism and the excitatory-inhibitory feedback loop mechanism are present [111].

Recent studies have also shown that electrical synapses with gap junctions contribute to neural synchrony. Compared with chemical synapses, electrical synapses are faster and bidirectional so they are especially important for synchronizing the fast rhythms [112, 113].

Correlated stochastic input

When the intrinsic oscillation frequencies of the neurons are roughly the same and the correlated stochastic input is broad-band and faster than the period of the intrinsic neuronal oscillation, the network will exhibit synchronous oscillation even though the neurons do not directly interact [114, 115], Galán *et al.* [116, 117] successfully used this correlation-induced stochastic synchrony to model the olfactory bulb dynamics.

Studies that combined LFPs and single-unit (or multi-unit) recordings discovered that coherent oscillation exists with units in the LFPs with irregular spike trains. For example, high $CV_{ISI}s$ (the CV of the ISI) are recorded from the primary visual cortex of cat and monkey during anesthetised and awake states[118, 119, 120, 121], and from behaving monkeys prefrontal cortex [122, 123], and motor cortex [124]. Computational models of spiking neuron networks have shown how synchrony could emerge in recurrent networks with noisy units. Brunel and Hakim [125, 126, 127] have shown that a network oscillation can be produced with sparse synchronization in pyramidal cells and interneurons under strong noise and strong recurrent inhibition. Interestingly, studies have shown that the oscillation frequency produced by I-I loop is generally higher than that produced by E-I loop. When inhibition is sufficiently strong, the frequencies are mainly controlled by the kinetics of synaptic transmission and tend to be in the upper gamma range or higher[128, 129, 130].

5.3 Propagating waves in the brain

Studies have shown that the neural rhythms that we introduced above are not always fully synchronized with zero phase lag, but that their organization into traveling waves is widespread in non-human primates and the human brain at multiple scales. They are related to cognition. For example, the gamma waves found in primary visual cortical are thought to reflect the dynamic of stimulus-modulated information transfer [131, 132], the hippocampal theta oscillations are found to be strongly related to memory and spatial navigation [133], the beta waves were associated with movement preparation [84]. In addition, Studies of computational and theoretical neuroscientists have shown that these waves can be generated by computational models [134, 135]. See Ref. [4] for a review of propagating waves in different brain areas like the thalamus, the cortex and the thalamocortical system under different brain states (anesthetized and awake) from both experimental and computational points of view.

6 Beta oscillation in motor cortex

Beta frequency oscillations (13–30 Hz) in sensorimotor cortices [136] and basal ganglia structures have been studied in both humans [137, 138, 139] and animals, including monkeys [80, 86, 140], and cats [141] with electroencephalography (EEG), magnetoencephalography (MEG) and local field potential (LFP) tools. These oscillations occur during stable postures and decrease during active states. Many classical studies have shown that beta oscillations are pronounced during the movement preparatory period and are attenuated as the beginning of movements [80, 84, 85, 142, 86, 143]. The beta rhythm may correspond to an "idling rhythm" in the motor system [144] or it may correspond to a "status quo" of the sensorimotor system. Instead of reflecting a mere lack of movement, studies have shown that beta oscillations may promote existing motor set and posture while compromising processing related to new movements [83, 145, 146]. For example, Gilbertson *et al.* [83] have shown that reinforced beta oscillations are associated with impaired new movement in the cerebral cortical motor areas in healthy subjects. So beta oscillations may be compatible with an "active-akinetic" process [5]. Interestingly, Roelfsema *et al.* have found that beta oscillation occurs when cats expect the upcoming of a predicted event [147] and may reflect anticipatory processes.

Studies have shown that beta oscillations are related to the top-down mechanisms involved in cognitive and perceptual processing [148, 149, 150, 151]. For example, Buschman *et al.* [148] found prominent beta oscillations during a search regime which corresponds to a strong endogenous top-down processing when they trained monkeys to detect an object either in a pop-out regime or a serial search regime. Several studies using the attentional blink paradigm also support this hypothesis [152, 153].

In some reports, beta oscillations are considered as a repeated cycle of oscillatory activity sustained over time. However, many studies have shown that beta oscillations occur sporadically in bursts that last less than 150 ms [154, 155]. The timing and duration of these bursts are critical for normal functioning of the motor system [99, 156, 157]. Beta oscillations are also found related to pathological movements, like those of patients with Parkinson's disease who have trouble initiating movements [158, 159, 160].

So understanding how beta oscillations are generated will promote a better understanding of their functional roles. However, the underlying mechanism of beta oscillations and how they reflect underlying neural population dynamics have remained elusive. Several lines of evidence point to beta rhythms as being generated in basal ganglia and thalamic structures [161, 162, 163] and as a reflection of external inputs to the motor cortex. Alternatively, beta rhythms may originate independently in each area. This is supported by transcranial magnetic stimulation (TMS) perturbation studies which show that different cortical regions have intrinsic oscillation frequencies [164, 165, 166]. Recently Sherman *et al.* [157, 167] proposed that beta oscillations can emerge from the combination of these two mechanisms.

Rubino *et al.* [84] found that the beta oscillations in the motor cortex, when monkeys are trained to do an instructed delay task, can organize into traveling waves. The propagating speeds

are around 30 cm/s along one dominant direction (anterior–posterior in primary motor cortex; medio-lateral in dorsal pre-motor cortex). The amplitudes and the phases of beta oscillations encode information about monkey's behaviors. This supports the hypothesis that the beta oscillations do not just represent an "idling rhythm" but suggest that they could perform useful computation. Rule *et al.* and Denker *et al.*[85, 86] have shown that LFP beta oscillations in the motor cortex also travel across the cortex with more complex patterns (radial, spiral waves). Several methods have been developed to detect and analyze these patterns [168, 85, 86].

Here, we first describe the experimental data published by [53] to analyze the beta oscillation in motor cortex. Then we develop a model to explain the origin of beta oscillations.

6.1 Experimental data introduction

The data published in Ref. [53] includes two electrophysiological datasets recorded by 10-by-10 Utah electrode arrays (96 active electrodes and 4 non-active electrodes) implanted in the motor cortex of two macaque monkeys (N and L) which were are trained to do an instructed delayed reach-to-grasp task. The datasets contain: the raw neural signals (sampled at 30 kHz, broadly band-pass filtered to $0.3Hz$-$7.5kHz$); the local field potential (a downsampled and filtered version of the raw neural signals sampled at 1 kHz, and broadly band-pass filtered to $0.3Hz$-$250Hz$); time stamps and spike waveforms of offline sorted single and multi units (93/49 and 156/19 (SUA/MUA) for the two monkeys, respectively); as well as the specific time of tasks and behavioral events recorded along with the electrophysiological data. All of these data provide the material for our study.

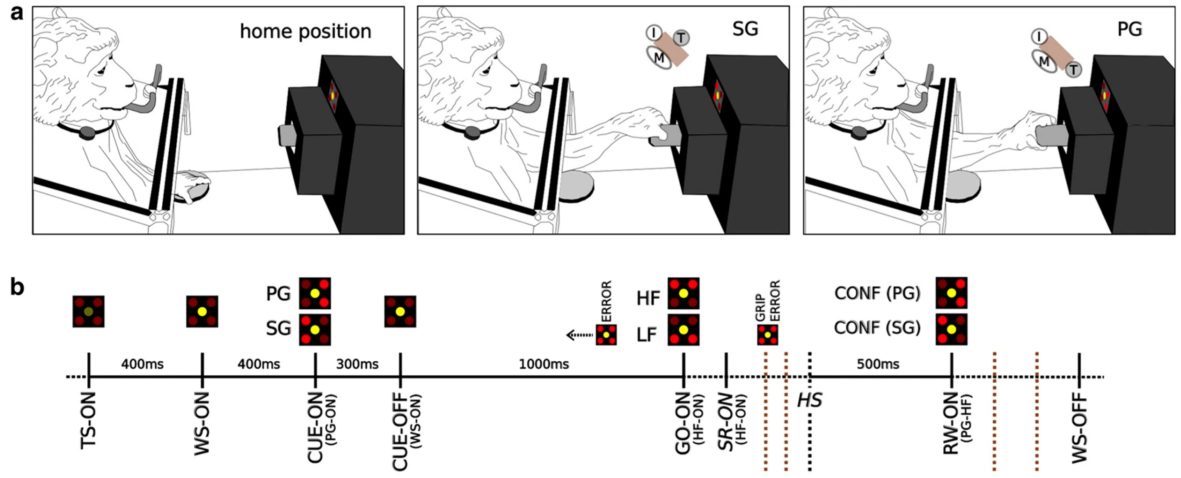

Figure 6.1: **Overview of the experimental design.** (a) Sketches of the monkeys performing the reach-to-grasp task. (b) The time axis of events and visual cues. Taken from [53].

The design of the experiment

In Refs. [86, 53], two monkeys were trained to grasp an object with different grips either a side grip (SG) or a precision grip (PG), depending on the position of the fingers when the monkeys hold the object, as shown in Fig.6.1 (a). Then the grips are further distinguished depending on

whether the object should be pulled using either a high or a low force (HF and LF, respectively). The instructions are given by the illumination of specific combinations of two LEDs. Specifically, the experiment is initiated by the monkeys deactivating the table switch (home position). This lights the WS-ON signal lights which are kept on for 400 ms to inform the monkeys that the trial has begun. Then the first cue (CUE-ON) is given, and after 300 ms it is turned off (CUE-OFF). A 1000 ms preparatory delay follows before the second cue (GO-ON) is given. Then the monkeys initiate the movement. The movement is composed of reaching, grasping, pulling and holding the object in the position window for 500 ms before rewarding juice is provided. What we focus on is the preparatory period (from CUE-OFF to GO-ON, around 1 s) when the beta power is elevated. So in the following, we mainly analyze the data during this period.

The recording session of monkeys L and N lasted 11:49 and 16:43 min in which they performed 204 and 160 trials, respectively. The trial types alternated randomly between trials, with 135 correct trials for monkey and 142 correct trials for monkey L as shown in Fig.6.2.

monkey	# trials	# error trials		# correct trials				
	total	total	grip	total	SG-LF	SG-HF	PG-LF	PG-HF
L	204	69	12	135	41	30	31	33
N	160	19	16	141	35	35	35	36

Figure 6.2: **Overview of the experimental trial.** Taken from [53].

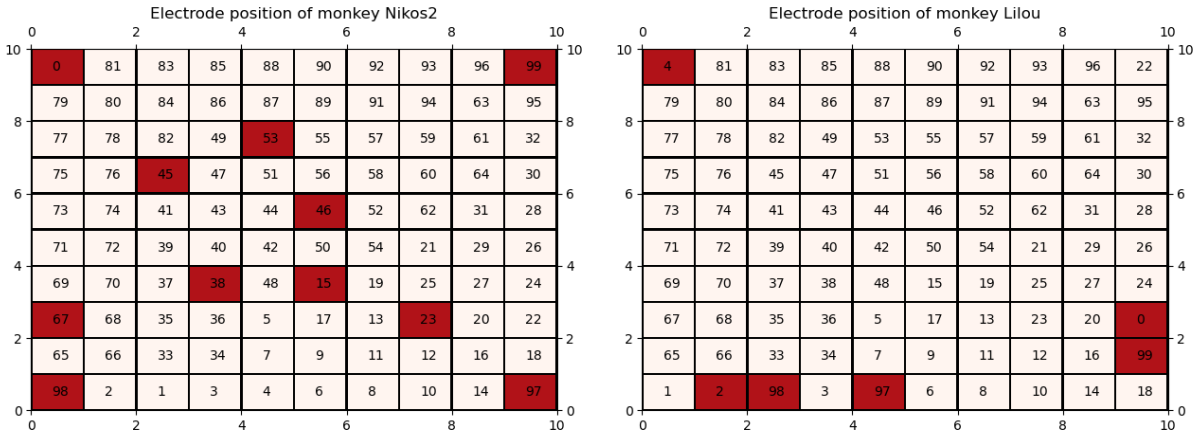

Figure 6.3: **Locations of the Utah arrays.** Monkey N (left), monkey L (right), the red channels are invalid channels.

The position maps of the electrode arrays for two monkeys are shown in Fig.6.3. The arrays are placed between the primary motor cortex (M1) and the dorsal or ventral premotor cortex (PMd or PMv) of the right hemisphere. Each electrode is 1.5 mm long with an inter-electrode distance of 400 μm. Besides 4 non-active electrodes, monkey L has 2 (electrode IDs: 2, 4) invalid electrodes and monkey has 7 (electrode IDs: 15, 23, 38, 45, 46, 53, 67) invalid electrodes (which are detected by abnormal signals). In order to better analyze the spatial characteristic of the

signals, we replaced the signal of each bad electrode with the mean signal of its effective nearest neighbors.

Spike waveform

The recording sessions include the spike unit waveforms. They can be used for spike sorting with a specific algorithm described in Ref. [53]. The statistics of the spike durations and spike amplitudes are shown in Fig.6.4. The spike duration can be used to classify the single unit as excitatory or inhibitory.

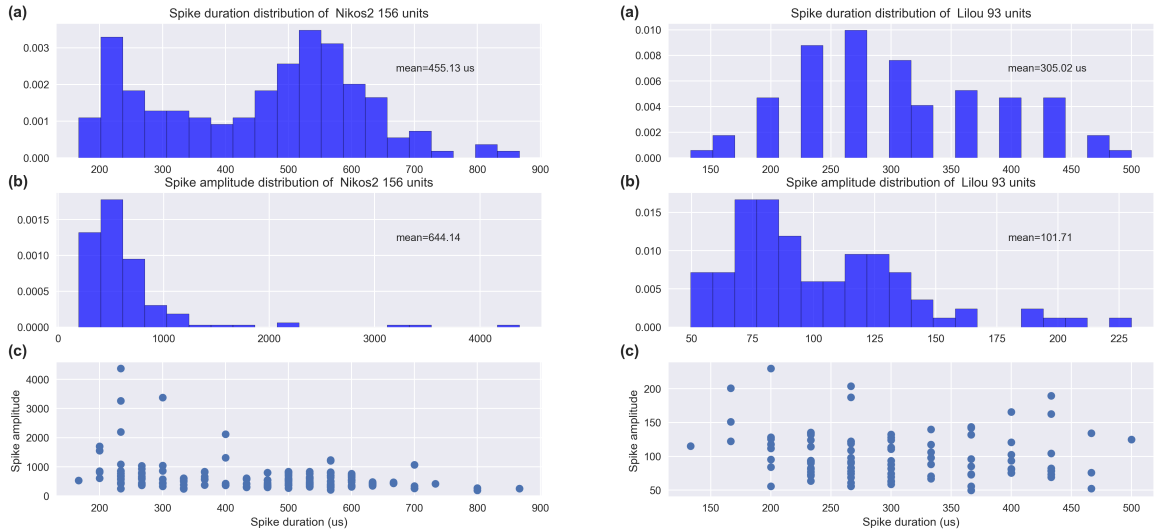

Figure 6.4: **Overview of the spike data for monkey N (left) and L (right).** (a) The distribution of spike durations. (b) The distribution of spike amplitudes. (c) The relationship between spike durations and spike amplitudes.

Firing rates of excitatory and inhibitory neurons

Following Ref. [169], we define spikes with a narrow width (shorter than 0.4 ms) as inhibitory neurons, whereas spikes with a broad width (longer than 0.41 ms) are considered to be excitatory neurons. For monkey L, there are 93 single units, 73 are inhibitory (their average firing rate is 16.23 Hz) and 12 are excitatory (the average firing rate is 12.26 Hz); for monkey N, there are 156 single units, 54 are inhibitory (their average firing rate is 13.70 Hz) and 97 are excitatory the average firing rate is 8.71 Hz (due to a small missing 0.1 ms interval in the unit classification, the sum of excitatory and inhibitory units does not exactly match the total number of single units). The statistics of the firing rate is obtained by convolving the spike trains with a *Gaussian* window as explained in Chapter.I. As shown in Fig.6.5, the units display large CVs (larger than 1) during the preparatory period. This means that although beta oscillations are prominent, the neurons do not fire periodically. Beta oscillations thus appear to be a collective phenomenon arising from the sparse synchronization [127] of different non-oscillating units.

Signal

Fig.6.6 exhibits the metadata in a temporal frame around TS-ON of trial 1 of electrode ID 7 for monkey N which includes the raw signals (sampled at 30 kHz, and broadly band-pass filtered to 0.3 Hz–7.5 kHz), LFPs (low-pass filtered at 250 Hz), spikes, and events.

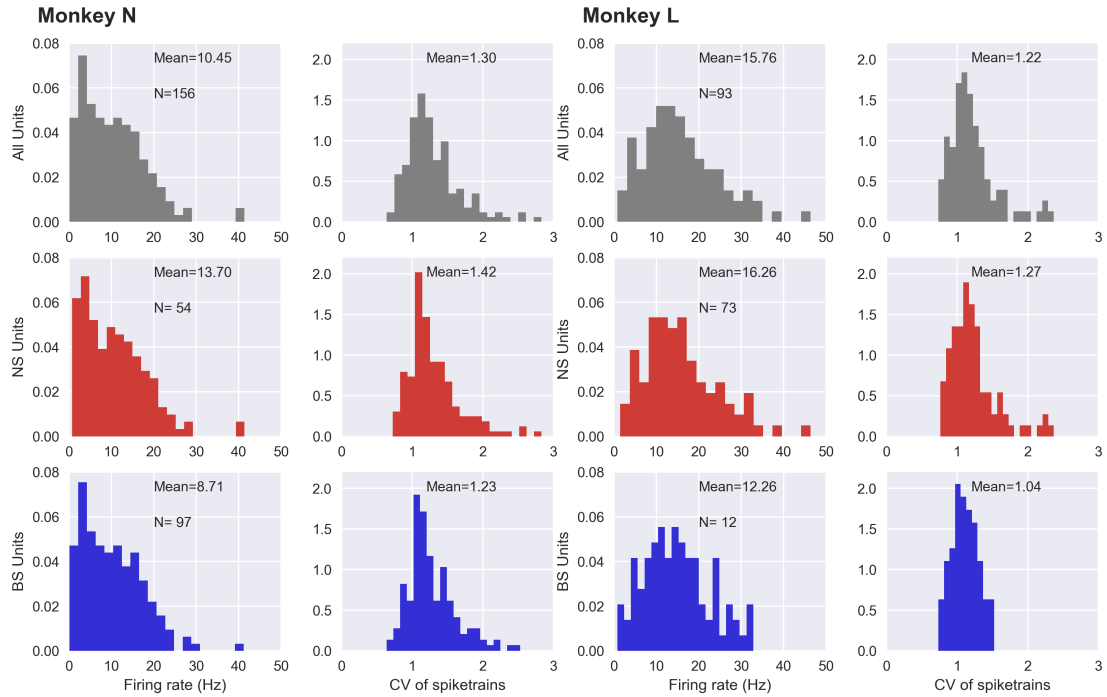

Figure 6.5: **The statistic of firing rates and CV of spiketrains for monkeys N (left) and L (right).** First row: all unit; second row: inhibition neurons with narrow spike width (NS units); third row: excitatory neurons with broad spike width (BS units).

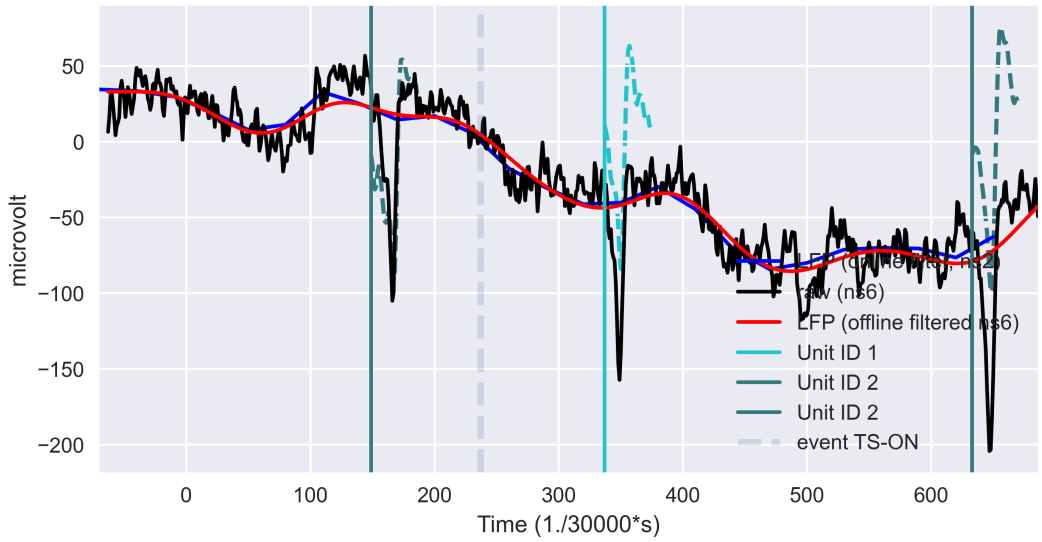

Figure 6.6: **Example of data presentation.** The data comes form monkey N (trial ID 1, electrode ID 7), raw signal (black), LFP (blue and red), spikes, and event (dash).

6.2 Analysis of experimental data

We analyze the LFP signals using the power spectrum, their auto- and cross-correlation, and the statistics of the beta bursts. We use an improved method for detecting traveling waves based on previous work [86, 85]. Illustrative results are presented below.

Power spectrum

As introduced before, the beta rhythm is one of the most prominent types of oscillation activity in the motor cortex. It is believed to relate to movement preparation. The LFP signals are modulated by the behavioral state of the monkey. Spectrograms can be used as a way of visualizing the change of a nonstationary signal's frequency content over time. Consistent with previous results, the beta oscillations are prominent during the movement preparation but attenuated during the movement execution for both monkeys (see Fig.6.7, the electrode-averaged, trial-averaged, time-resolved spectrograms).

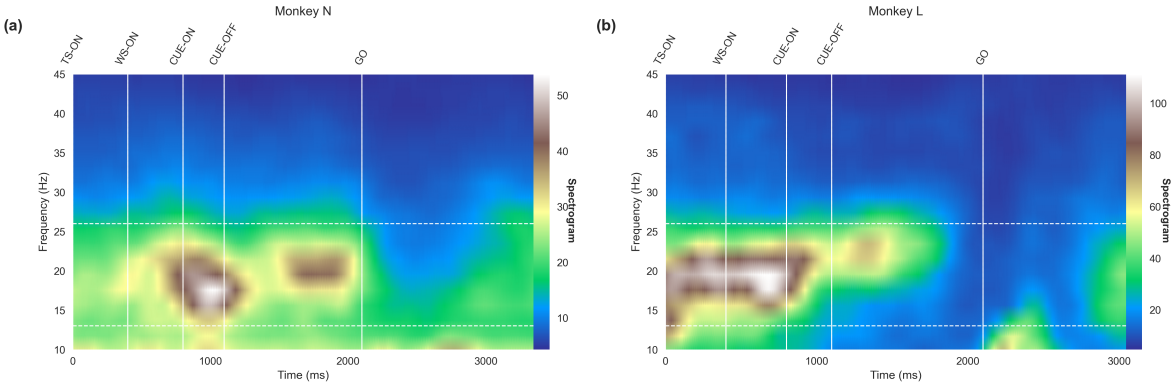

Figure 6.7: **The spectrograms of LFPs.** (a) Monkey N. (b) Monkey L, the data used from the whole period of the trials (from TS-ON to STOP), the spectrograms calculated as electrode-averaged, trial-averaged.

The power spectrum is used to assess the dominant frequencies in the LFPs. We use the Welch's average periodogram algorithm to calculate the power spectrum (the *psd* function of the Python package *scipy*, with the *Hanning* window, the length of each segment is $nperseg = 1024$, and sampling frequency $fs = 1kHz$). The spectrograms were calculated using *spectrogram* function of the Python package *scipy*, the length of each segment is $nperseg = 512$ and the number of points of overlap between segments is $noverlap = 500$.

Correlation

We use the spatiotemporal correlation to demonstrate how different LFPs are related to each other in space (Δd) and time (Δt). The correlation is defined by,

$$Cor(\Delta d, \Delta t) = \frac{1}{N_{\Delta d}} \sum_{Dis(m,n)=\Delta d} \frac{1}{N_{\Delta t}} \sum_{t=0,1...T-\Delta t} (I(m,t) - \bar{I}(m))(I(n,t+\Delta t) - \bar{I}(n))$$
$$(m, n = 1, \ldots, N) \tag{6.1}$$

where I is the LFP signal. m, n are the indices of the LFP signals, N ($N = 100$) is the total number of different LFP signals. $Dis(m, n)$ is the Euclidean distance between signal m and signal n, $N_{\Delta d}$ denotes the number of the signals when the distance difference $Dis(m, n)$ equals to Δd. $N_{\Delta t}$ denotes the number of time points with a time difference of Δt. T is the total duration of the signal.

Oscillatory data filtering

Our goal is to analyze the spatial arrangement of the oscillatory activity over the electrode arrays. To ensure that the data are properly displayed, the following procedures are applied as in Ref. [86]:

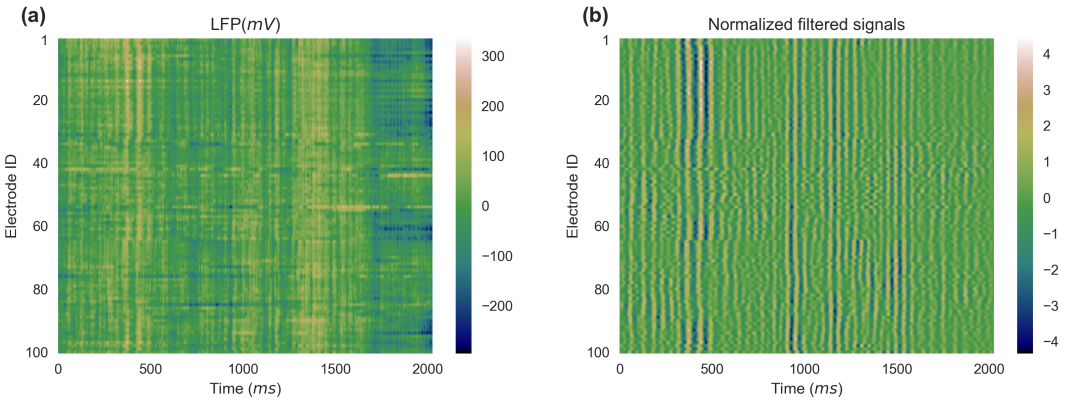

Figure 6.8: **Data Filtering process of LFPs.** (a) Original LFPs. (b) Filtered normalized signals, the data from monkey N (trial ID 1).

- First, we filter the LFP signals on each electrode (a third-order Butterworth filter, *filtfilt* function of the Python package *scipy*) to a specific frequency range (pass band: 13–30 Hz).
- Then, due to the different amplitude scales between electrodes, the LFP signal amplitude of each electrode is normalized using the z-scores. This allows one to assess the relative changes in amplitude between different electrodes.
- Next, the analytical signal $\mathscr{I}_{x,y}(t)$ (x, y are the coordinates of the channel in the electrode array) is obtained by applying the *Hilbert transform* function of the Python package on the normalized, filtered LFP at each electrode position (x, y). We retrieve the instantaneous signal amplitude $a_{x,y}(t)$ from $\mathscr{I}_{x,y}(t)$ by taking its module, and the instantaneous phase $\phi_{x,y}(t)$ by taking its argument (angle). Obtained maps $a_{x,y}(t)$ and $\phi_{x,y}(t)$ are used for beta burst detection and wave patterns detection, respectively.

Compared with the raw LFP signals, the filtered, and normalized ones are smoother (see in Fig.6.8) and are more convenient for performing spatial pattern recognition.

Beta burst determination

As previously introduced, the beta oscillations are transient during the movement preparatory period. To detect them, the beta burst threshold is determined in terms of percentiles of the

signal amplitude distribution following Ref. [156]. In our case, the threshold is set at the $75th$ percentile of the analytical amplitude distribution. The onset of a burst is defined as the time point at which the analytical amplitude exceeds the given threshold amplitude, its duration is obtained as the time point at which the amplitude falls below this threshold (see Fig.6.9(b), the sky blue areas correspond to beta bursts). We define the beta burst amplitude as the average amplitude over that beta burst duration.

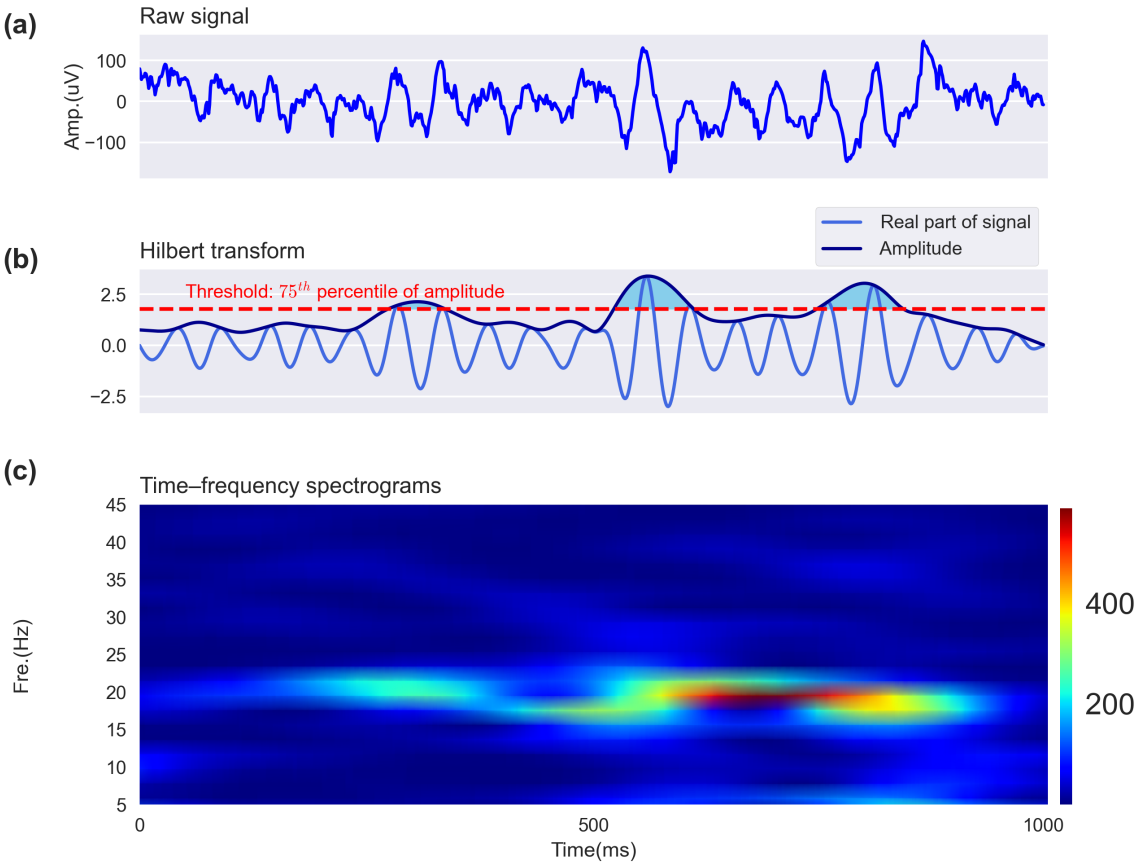

Figure 6.9: **Beta burst detection.** (a) Raw signal of monkey N (trial ID:1, electrode ID: 1). (b) The real part of the analytic signal (blue) and the amplitude of the analytical signal (dark blue). The threshold for beta burst is also shown (red dotted line). (c) Spectrograms of the signal shown in (a).

Detection of spatiotemporal patterns

We observed different types of waves (synchronized, planar, radial, spiral, random) on the basis of the phase map. To demonstrate the spatial organization of the oscillatory activity across the electrode arrays, we followed the method of identifying wave patterns as previously described in Ref. [86] with some modifications. Three additional maps (the *phase gradient* map $\Gamma_{xy}(t)$, the *directionality* map $\Delta_{xy}(t)$, and the *gradient coherence* map $\Lambda_{xy}(t)$) were constructed as defined in Ref. [86]. The *phase gradient* map $\Gamma_{xy}(t)$ and the *directionality* map $\Delta_{xy}(t)$ are used to

calculate the circular variances of phase and phase directionality which are then used to identify the synchronized waves and planar waves. The *gradient coherence* map $\Lambda_{xy}(t)$ is used to find the critical points. Then these classified critical points are used to distinguish radial and spiral waves. The remaining nonclassified patterns are defined as random waves (see Fig.6.12 for the steps of wave detection).

- Phase gradient map. For the electrode at position (x, y), its phase gradient is obtained as the average difference of the x-axis (or y-axis) of the phase map at its k nearest neighbors. We use $k = 2$ to obtain a smooth map that is convenient for the analysis (for the boundary electrodes, only the nearest neighbors are considered). The map of *phase gradients* is

$$\begin{aligned}\Gamma_{xy}(t) = \frac{1}{N_x} \sum_{x'=-k,\cdots,-1,1,\cdots,k} (\phi(x+x', y) - \phi(x, y)/|x'| \cdot e^{j\alpha}) + \\ \frac{1}{N_y} \sum_{y'=-k,\cdots,-1,1,\cdots,k} (\phi(x, y+y') - \phi(x, y)/|y'| \cdot e^{j\alpha})\end{aligned} \tag{6.2}$$

  where α denotes the angular direction between the electrode locations, N_x (N_y) is the number of neighbors along the x-axis (or y-axis).

  The phase speed is defined by

$$v(t) = \frac{2\pi f_\beta}{|\Gamma|} \tag{6.3}$$

  where f_β is the average frequency of the beta oscillation and $f_\beta = 21.5Hz$ which is obtained from the power spectrum of the metadata. $|\Gamma|$ is the average phase gradient. The inter-electrode distance is 400 μm.

- Phase directionality map. The vector of the phase gradient map $\Gamma_{xy}(t)$ is normalized to its unit length. It merely indicates the magnitude-independent direction of the local phase gradient. The *phase directionality* map is

$$\Delta_{xy}(t) = \frac{\Gamma_{xy}(t)}{|\Gamma_{xy}(t)|}. \tag{6.4}$$

- Gradient coherence map. In order to get a smoother map to distinguish complex waves, the *gradient coherence* map is defined as an average of the *directionality* map over its k-nearest neighbors, where N_{xy} is the number of its k-nearest neighbors,

$$\Lambda_{xy}(t) = \frac{1}{N_{xy}} \sum_{x',y' \in (-k,\cdots,-1,0,1,\cdots,k)} \Delta_{x+x', y+y'}(t). \tag{6.5}$$

- Circular variance of phases. Synchronized waves are commonly observed with identical phase angles and small random phase gradient directionalities. Therefore, the circular variance of phases σ_p (similar to an order parameter) is introduced in Ref. [86]as a measure to determine the similarity of the phase across the arrays. The synchronized degree

increases with $\sigma_p(t)$, $\sigma_p(t) = 1$ indicates that the electrodes are totally synchronized while $\sigma_p(t) = 0$ denotes that they are in a disordered state.

$$\sigma_p(t) = |\frac{1}{N} \sum_{x,y \in (1,\cdots,\sqrt{N})} e^{j\Phi_{x,y}(t)}| \in [0,1]. \tag{6.6}$$

N is the total number of electrodes.

- Circular variance of phase directionality. To measure how well phase gradients align across the arrays, the circular variance of the phase directionality is introduced in Ref. [86]. A perfect planar wave is observed when $\sigma_g(t) = 1$, meaning that all phase gradients point in the same direction. This measure is similar to the PGD measure defined in Ref. [84].

$$\sigma_g(t) = |N^{-1} \sum_{x,y \in (1,\cdots,\sqrt{N})} \Delta_{x,y}(t)| \in [0,1]. \tag{6.7}$$

N is the total number of electrodes.

Planar wave patterns are characterized by a non-zero phase gradient that points in the same direction at each electrode, and are thus well characterized by a large value of $\sigma_g(t) \geq 0.5$. Perfectly synchronized patterns exhibit the same phase at each electrode (large $\sigma_p(t) > 0.85$), and random phase gradient directionality (small $\sigma_g(t) < 0.5$).

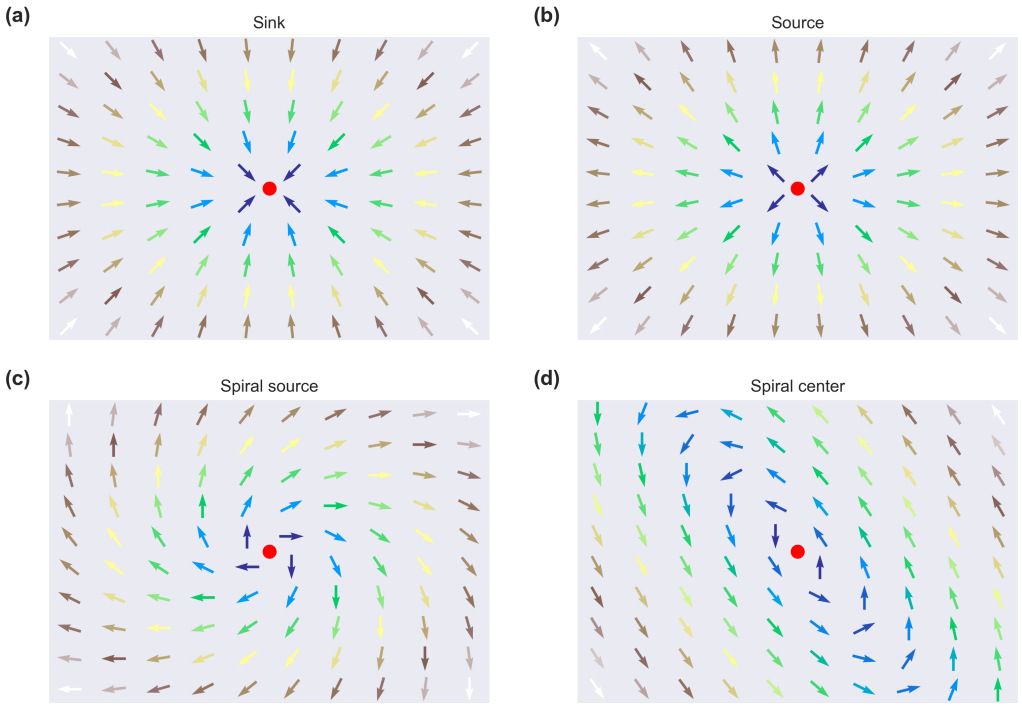

Figure 6.10: **Critical point example.** (a-b) Radial waves with sink or source point. (c-d) Spiral waves with source or center point.

- Critical point analysis. Complex waves are classified on the basis of critical points in the

local gradient coherence map. Minima, maxima, and saddle points can be distinguished by the direction of sign change in the local gradient coherence map [170]. The centers of spiral waves are required to show coherent positive or negative curl. It can be calculated by taking a line integral of the local gradient coherence map surrounding each point. Points around which this line integral equals nonzero multiples of 2π (the threshold we used is $\pm\pi$) are singularities and are the centers of spiral waves; if there is only one extremum and the line integral surrounding this critical point equals zero, we have a radial wave. Fig.6.10 shows vector fields for radial waves (a-b) and spiral waves (c-d). Otherwise, the pattern is classified as a random wave.

Fig.6.11 shows an example of the phases and phase gradients for different kinds of waves for monkey N. The planar wave is distinguished by non-zero phase gradients and almost identical phase gradient directions. The synchronized wave by the same phases and a random distribution of phase gradients. The radial wave by one critical point in gradient coherence map and non-zero phase gradients.

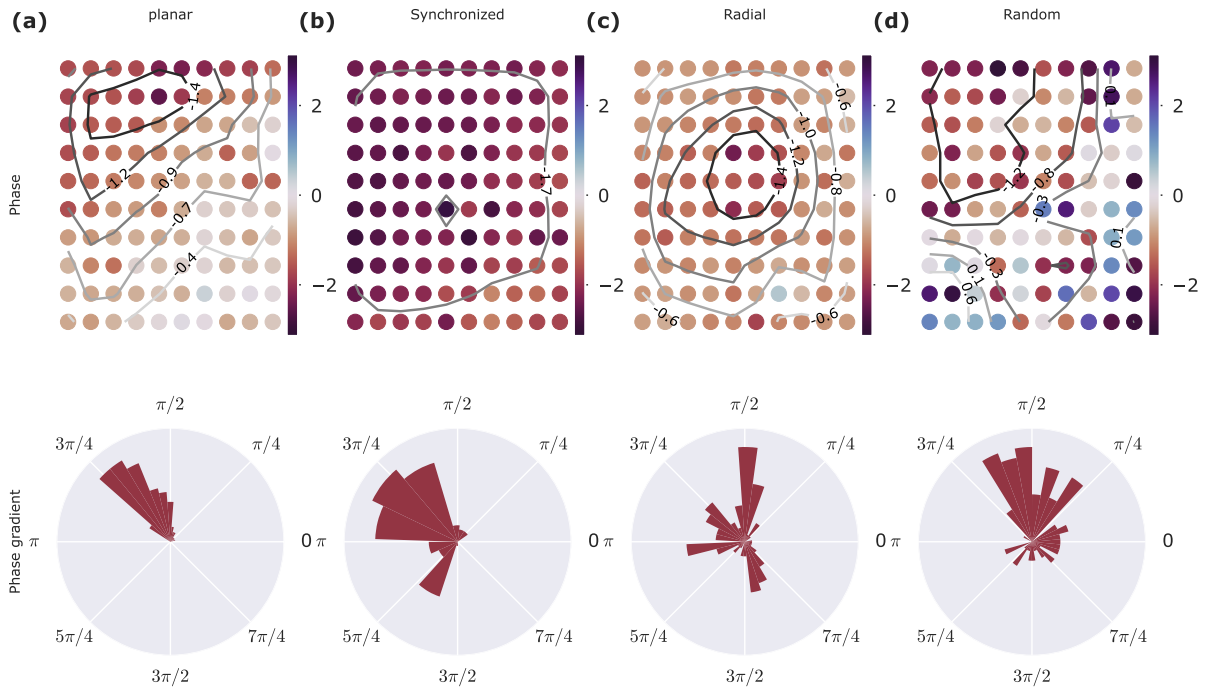

Figure 6.11: **Example of complex waves for monkey N.** The first row shown the phase and its isolines, the second row show the distribution of the phase gradient. (a) Planar wave. (b) Synchronized wave. (c) Radial wave. (d) Random wave.

Data treatment follows the workflow shown in Fig.6.12. It includes data filtering to extract the analytical phase and amplitude; the construction of the phase and phase gradient to obtain the vector map for the indexes used for wave classification; and the judgment rule of the different indexes to distinguish complex patterns.

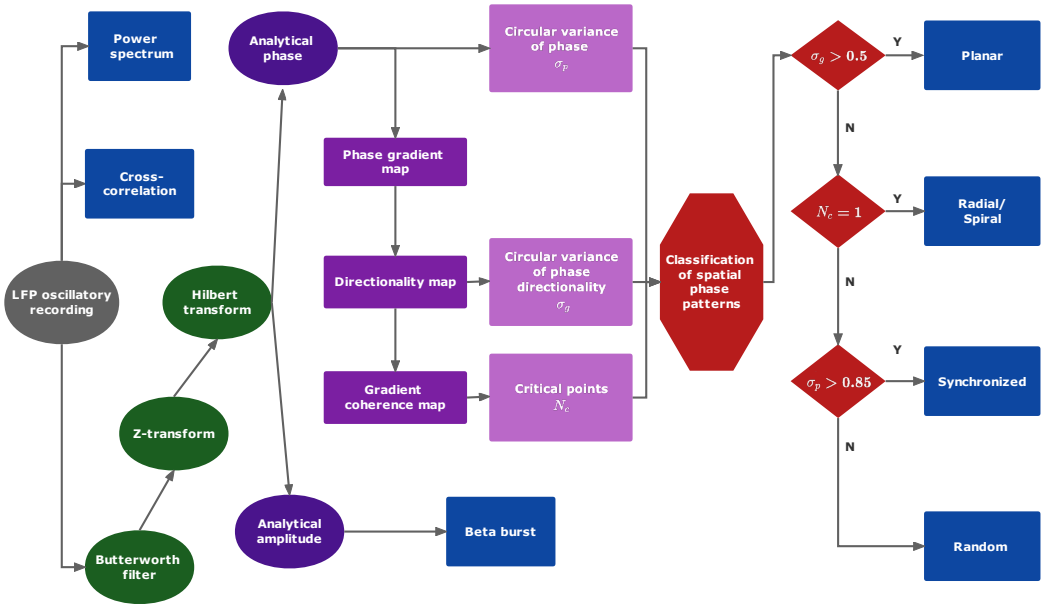

Figure 6.12: **Data flow diagram for the methodological framework.**

7 Mechanisms of generating beta oscillation

As discussed before, there are two different basic hypotheses on the origin of beta oscillations in the motor cortex. One is that they are as a reflection of inputs coming from basal ganglia and thalamic structures, the other is that they emerge within the neocortex as a consequence of internal dynamics. In the following, we will establish a network model that includes both these effects as the basis of beta oscillations. First, we introduce the network model and present the theoretical analysis of the model. Then, we will tie it with the experimental evidence, showing that our coupled network model is adequate for capturing the transient beta oscillation and propagating waves characteristics of beta oscillation in the motor cortex.

7.1 Description of the FAT dynamic network model

Modeling groups have aimed to bring light to the origin and the organization mechanism of the neural oscillatory activity for decades [171, 4]. The seminal work [62] introduced a simple description of neural network dynamics with a set of coupled mean-field equations of excitatory and inhibitory neuron populations. Dynamical systems analysis methods have shown that these equations exhibit multistability and limit cycles, where the frequency of the oscillation is a monotonic function of the stimulus strength. The combination of mathematical tractability and dynamical richness of rate models has promoted numerous studies of the synchronization

of spatially-coupled neural networks in the oscillatory regime [172, 173, 174, 175, 135]. Studies [126, 128, 129] have suggested that rhythms in the beta and gamma range arise from sparse synchronization [127] between excitatory (E) and inhibitory (I) neuronal populations with reciprocal interactions. The impact of structured connectivity and the influence of delay on sparse synchronization of spiking networks have been further studied in [176, 177, 178].

Ostojic *et al.* [64] proposed an "adaptive" firing rate model that accurately describes the dynamics of EIF spiking neurons. Building on this progress. Kulkarni *et al.* [66] more recently developed a "fitted adaptive timescale" (FAT) rate model which matches well the dynamics of EIF spiking neuron network. Kulkarni *et al.* [66] analyzed the dynamic regimes of the FAT model as the function of the synaptic coupling strengths, and further studied the dynamics of a chain of oscillatory E–I modules coupled by a distance-dependent long-range excitation. Here, we generalize the FAT rate model by taking into account distant-dependent delays and the kinetics of synaptic currents in a two-dimensional network. We also consider fluctuating and correlated in time external inputs with both global and local spatial components. The model successfully reproduces the transient beta oscillation and traveling waves of the recording data. Below, we will describe this network model in detail.

Network structure

With the aim of comparing with experimental data including its spatial patterns, we consider a two-dimensional network, similar to the multielectrode array used in the experiment as shown in Fig.7.1. In our model, different modules are connected by long-range excitatory couplings (see in Fig.7.1 (a)). The coupling strength takes a *Gaussian* form that decreases with the distance between modules (Fig.7.1(c)). It is described by

$$C(\mathbf{x}) = \frac{1}{Z}\exp(-|\mathbf{x}|^2/l^2), Z = \sum_{\mathbf{x}}\exp(-|\mathbf{x}|^2/l^2),$$
$$\sum_{\mathbf{x}} C(\mathbf{x}) = 1, \mathbf{x} = (x, y) \tag{7.1}$$

where $\mathbf{x} = (x, y)$ stands for the position in the array.

In order to reduce the impact of the boundary effects, we take the outermost layers (grey, fixed modules in Fig.7.1 (b)) to stay at a fixed value. The other modules (black, simulated modules) are simulated as described by Eq.7.2. Below, only the center parts (10×10, blue) are used for the analysis (Fig.7.1(b)).

We start by generalizing the FAT model used in the previous work [66], by considering two features that have not been taken into account in Ref. [66], namely recurrent inhibition between interneurons w_{II} and distant-dependent delay. The dynamics of the E-I modules locates at positions $\mathbf{x}$ of the two-dimensional square array are

$$\tau_E(I_E)\frac{dI_E}{dt}(\mathbf{x}, t) = -I_E(\mathbf{x}, t) + I_E^{ext}(\mathbf{x}, t) + I_{EE}^{syn}(\mathbf{x}, t) - I_{EI}^{syn}(\mathbf{x}, t),$$
$$\tau_I(I_I)\frac{dI_I}{dt}(\mathbf{x}, t) = -I_I(\mathbf{x}, t) + I_I^{ext}(\mathbf{x}, t) + I_{IE}^{syn}(\mathbf{x}, t) - I_{II}^{syn}(\mathbf{x}, t). \tag{7.2}$$

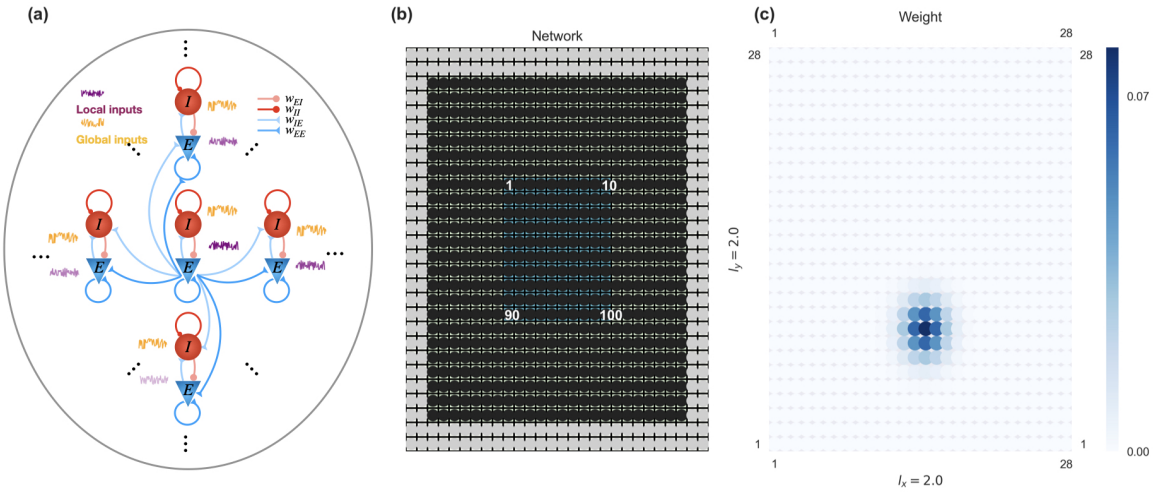

Figure 7.1: **Schematic structure of the simulation network.** (a) Schematic description of the network model with recurrent couplings between excitatory neurons and inhibitory neurons. The modules are connected by the long-range excitatory couplings. The fluctuating external inputs are separated into an identical global part (orange) on all modules and local parts (purple) different from module to module. (b) Two-dimensional network (grey: fixed modules; black: simulated modules; blue: modules are used for the analysis). (c) Coupling strength map of one module with its neighbors (connectivity range $l = 2$).

The recurrent synaptic currents between excitatory and inhibitory neurons are described by

$$I_{AE}^{syn}(\mathbf{x},t) = w_{AE}\sum_{\mathbf{y}} C(|\mathbf{x}-\mathbf{y}|)r_E(\mathbf{y},t-D|\mathbf{x}-\mathbf{y}|),$$
$$I_{AI}^{syn}(\mathbf{x},t) = w_{AI}r_I(\mathbf{x},t),\ A\in\{E,I\}. \tag{7.3}$$

In a spiking network, the stochastic component of the population depends on the number of neurons in the network. In order to take into account this stochastic component, the firing rate is described as one deterministic part depending on the mean current plus one stochastic term,

$$r_A = \Phi(I_A) + \sqrt{\Phi(I_A)/N_A}\xi, A\in\{E,I\} \tag{7.4}$$

where N_E, N_I are numbers of excitatory and inhibitory neurons in each module. Their relative proportion is $\frac{N_E}{N_I} = 4$; ξ is a *Gaussian* white noise which satisfies $<\xi(t)\xi(t')>=\delta(t-t')$.

The fluctuations of the external inputs are described as stochastic *Ornstein-Uhlenbeck* (O-U) processes, made up of local $\xi(\mathbf{x})$ and global ξ_g parts (see Fig.7.1(a)). The proportion between

them is controlled by c,

$$\begin{aligned} I_A^{ext} &= I_A^{ext,0} + \sigma_A^{ext}\eta, \quad \sigma_A^{ext} = w_A^{ext}\nu^{ext}, \ A \in \{E, I\}, \\ \tau_{ext}\frac{d\eta}{dt}(\mathbf{x}, t) &= -\eta(\mathbf{x}, t) + \sqrt{\tau_{ext}}[\sqrt{1-c}\ \xi(\mathbf{x}, t) + \sqrt{c}\ \xi_g(t)], \\ \langle \xi(\mathbf{x}, t)\xi(\mathbf{x}', t')\rangle &= \delta(t-t')\delta_{\mathbf{x},\mathbf{x}'}, \ \langle \xi_g(t)\xi_g(t')\rangle = \delta(t-t'). \end{aligned} \tag{7.5}$$

w_E^{ext}, w_I^{ext} are the synaptic coupling strengths of the external inputs into excitatory neurons and inhibitory neurons, respectively.

$$w_E^{ext} = w_{EE}, w_I^{ext} = 2w_{IE} \tag{7.6}$$

ν_{ext} is the amplitude of the external input fluctuations, τ_{ext} is the correlation time scale of O-U processes. The constant external inputs $I_E^{ext,0}, I_I^{ext,0}$ are chosen to impose the steady firing rates $r_E^s = 5Hz$,$r_I^s = 10Hz$, with

$$I_A^{ext,0} = I_A^s - w_{AE}r_E^s + w_{AI}r_I^s, A \in \{E, I\}. \tag{7.7}$$

7.2 Stability analysis of the FAT network model

Theoretical analysis is helpful for us to determine network states and oscillation frequencies. Here, we first analyze the different dynamical regimes of the network model. Then we calculate the power spectrum and correlation to help us determine the parameters that match well the experimental data.

Steady state

The steady state of the deterministic network is chosen such that the excitatory and inhibitory populations have the steady firing rates r_E^s, r_I^s. We consider first the limit when the number of the neurons in a module $N \to \infty$ to eliminate the intrinsic stochastic effect. The steady firing rates are

$$r_A^s = \Phi(I_A^s), A \in \{E, I\}. \tag{7.8}$$

In this situation, the synaptic currents are also steady as the synaptic couplings are fixed and the firing rates are steady,

$$I_{AB}^{syn}(\mathbf{x}, t) = I_{AB}^{syn,s} = w_{AB}r_B^s, A \in \{E, I\}, B \in \{E, I\}. \tag{7.9}$$

The external inputs are constant with $\sigma^{ext} = 0$ as described by Eq.7.7.

Bifurcation

The stability of the steady firing state can be assessed by imposing constant external currents and by computing the dynamics of small perturbations around the steady state. We proceed along similar lines to the analysis of stability in Chapter.I.

First, we linearize Eq.7.2 around the steady state with

$$I_A(\mathbf{x},t) = I_A^s + \delta I_A(\mathbf{x},t), A \in \{E,I\}. \tag{7.10}$$

We get the linear equations,

$$\begin{aligned}\tau_E(I_E^s)\frac{d\delta I_E}{dt}(\mathbf{x},t) &= -\delta I_E(\mathbf{x},t) + \delta I_{EE}^{syn}(\mathbf{x},t) - \delta I_{EI}^{syn}(\mathbf{x},t),\\ \tau_I(I_I^s)\frac{d\delta I_I}{dt}(\mathbf{x},t) &= -\delta I_I(\mathbf{x},t) + \delta I_{IE}^{syn}(\mathbf{x},t) - \delta I_{II}^{syn}(\mathbf{x},t).\end{aligned} \tag{7.11}$$

Then we perform the transformation

$$\delta I_A(\mathbf{x},t) = \delta\tilde{I}_A(\mathbf{q},\sigma)\exp(\sigma t + i\mathbf{q}\cdot\mathbf{x}), A \in \{E,I\}. \tag{7.12}$$

Substituting this expression into the linear equations to see how the perturbation evolves and using a vector notation $\mathbf{I} = (I_E, I_I)$ for the currents, we get the stability equation,

$$\tilde{L}_{EI}(\mathbf{q},\sigma)\cdot\delta\mathbf{I}(\mathbf{q},\sigma) = 0 \tag{7.13}$$

with the matrix

$$\tilde{L}_{EI}(\mathbf{q},\sigma) = \begin{pmatrix} 1+\sigma\tau_E(I_E^s) - \alpha C(\mathbf{q},\sigma) & w_{EI}\Phi'_I(I_I^s) \\ \\ -w_{IE}\,\Phi'_E(I_E^s)\,C(\mathbf{q},\sigma) & 1+\sigma\tau_I(I_I^s)+\gamma \end{pmatrix}. \tag{7.14}$$

The function $C(\mathbf{q},\sigma)$ is the *Fourier* transform of the coupling function with the propagation delay D taken into account,

$$C(\mathbf{q},\sigma) = \sum_{\mathbf{x}} \exp(-i\mathbf{q}\cdot\mathbf{x} - \sigma|\mathbf{x}|D)C(|\mathbf{x}|) \tag{7.15}$$

The determinant of the matrix $\tilde{L}_{EI}(\mathbf{q},\sigma)$ is given by $W(\mathbf{q},\sigma)$,

$$W(\mathbf{q},\sigma) = [1+\sigma\tau_E(I_E^s) - \alpha C(\mathbf{q},\sigma)]\,[1+\sigma\tau_I(I_I^s)+\gamma] + \beta\,C(\mathbf{q},\sigma) \;= 0 \tag{7.16}$$

with

$$\begin{aligned}\alpha &= w_{EE}\Phi'_E(I_E^s),\\ \beta &= w_{IE}w_{EI}\Phi'_E(I_E^s)\Phi'_I(I_I^s),\\ \gamma &= w_{II}\Phi'_I(I_I^s).\end{aligned} \tag{7.17}$$

When $\sigma = 0$, the growth rate vanishes. Which signals the real instability line. It is straightforward to show from Eq.7.16 that it occurs for,

$$\beta = (\alpha - \frac{1}{C(\mathbf{q},0)})(1+\gamma), \text{and } \beta = (\alpha-1)(1+\gamma) \text{ when } \mathbf{q} = 0. \tag{7.18}$$

The Hopf bifurcation line corresponds to the parameter for which, $\sigma = i\omega$, when the growth rate is purely imaginary. As above, it can be obtained in a parametric form, with α and β as functions of the oscillation frequency ω and the recurrent inhibition γ by separating the real and imaginary parts of $W(\mathbf{q}, \sigma)$ (Eq.7.16). By solving the resulting linear equations for α and β, we get

$$\alpha = \frac{\tau_I + (1+\gamma)\tau_E}{\tau_I} \frac{\mathrm{Re}[C(\mathbf{q}, i\omega)]}{|C(\mathbf{q}, i\omega)|^2} + \frac{\omega^2 \tau_E \tau_I - (1+\gamma)}{\omega \tau_I} \frac{\mathrm{Im}[C(\mathbf{q}, i\omega)]}{|C(\mathbf{q}, i\omega)|^2}, \tag{7.19}$$
$$\beta = \alpha(1+\gamma) + [\omega^2 \tau_E \tau_I - (1+\gamma)] \frac{\mathrm{Re}[C(\mathbf{q}, i\omega)]}{|C(\mathbf{q}, i\omega)|^2} - \omega[(1+\gamma)\tau_E + \tau_I] \frac{\mathrm{Im}[C(\mathbf{q}, i\omega)]}{|C(\mathbf{q}, i\omega)|^2}.$$

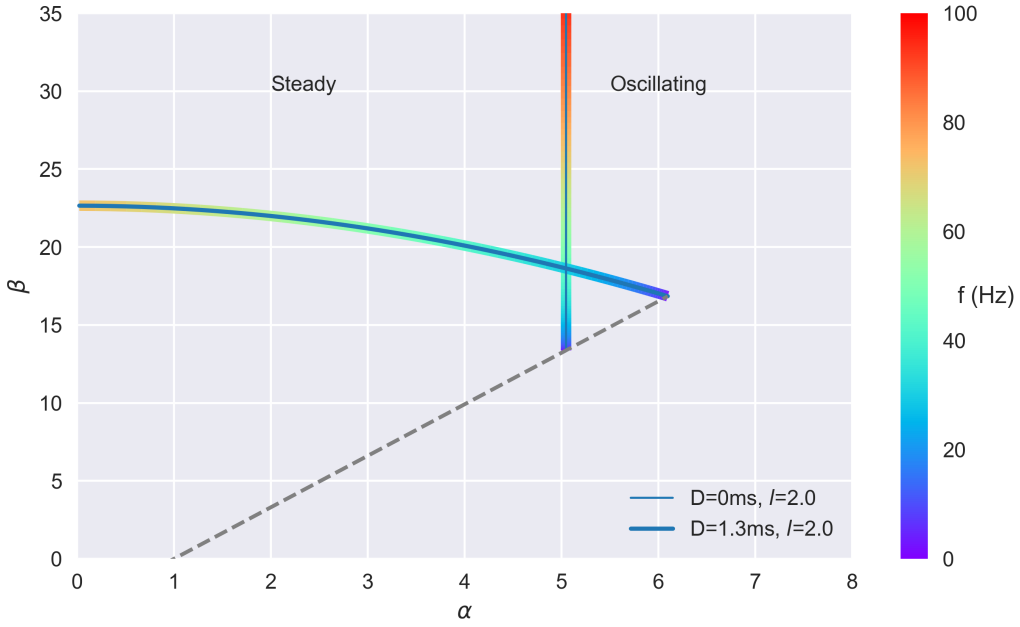

Figure 7.2: **The stability phase diagram of the network model with synaptic coupling strengths α and β.** The gray line is the "real instability" line, the colorful lines are the Hopf bifurcation lines for different D ($D = 0$: sky blue line, $D = 1.3ms$: dark blue line), the color corresponding to the oscillation frequency.

The stability diagram of the network model is shown in Fig.7.2. The colored lines are the bifurcation lines for different delay D. The oscillation frequency at each point is given by the vertical color bar on the right. If we want to keep the oscillation frequency around the beta range, the parameters have to be chosen near a narrow "tip area" (the area near the intersection of the Hopf line and real instability line). This appears as a biologically unrealistic "fine tuning" of parameters. In order to avoid it, we recall the works of [128, 176], which show that the kinetics of the synaptic currents play an important role in determining its oscillation frequency. Thus,

we take into account the kinetic kernels for the synaptic currents and replace Eq.7.3 by

$$I_{AE}^{syn}(\mathbf{x},t) = w_{AE}\int^{t} du S_E(t-u)\sum_{\mathbf{y}} C(|\mathbf{x}-\mathbf{y}|)r_E(\mathbf{y},u-D|\mathbf{x}-\mathbf{y}|)),$$
$$I_{AI}^{syn}(\mathbf{x},t) = w_{AI}\int^{t} du S_I(t-u)r_I(\mathbf{x},u). \tag{7.20}$$

S_E, S_I are the kinetic kernels of the synaptic currents with the normalization $\int dt\, S_A(t) = 1, A \in \{E, I\}$.

$$S_A(t) = \frac{\theta(t-\tau_l^A)}{\tau_d^A - \tau_r^A}\{\exp[-(t-\tau_l^A)/\tau_d^A] - \exp[-(t-\tau_l^A)/\tau_r^A]\}, A \in \{E, I\} \tag{7.21}$$

where τ_r^E, τ_r^I, τ_d^E, τ_d^I, τ_l^E, τ_l^I are the rise times, decay times and latencies of excitatory and inhibitory neurons for the synaptic currents. $\theta(t)$ denotes the *Heaviside* function, $\theta(t) = 1$ if $t > 0$ and 0 otherwise.

For the convenience of the simulation, we introduce supplementary variables $J_{EE}, J_{EI}, J_{IE}, J_{II}$. Then the Eq.7.20 can be rewritten as

$$\tau_d^E \frac{dI_{AE}^{syn}}{dt}(\mathbf{x},t) = -I_{AE}^{syn}(\mathbf{x},t) + J_{AE}(\mathbf{x},t),$$
$$\tau_r^E \frac{dJ_{AE}}{dt}(\mathbf{x},t) = -J_{AE}(\mathbf{x},t) + w_{AE}\sum_{\mathbf{y}} C(\mathbf{x}-\mathbf{y})r_E(\mathbf{y},t-\tau_l^E - D|\mathbf{x}-\mathbf{y}|)),$$
$$\tau_d^I \frac{dI_{AI}^{syn}}{dt}(\mathbf{x},t) = -I_{AI}^{syn}(\mathbf{x},t) + J_{AI}(\mathbf{x},t),$$
$$\tau_r^I \frac{dJ_{AI}}{dt}(\mathbf{x},t) = -J_{AI}(\mathbf{x},t) + w_{AI}r_I(\mathbf{x},t-\tau_l^I)\, A \in \{E, I\}. \tag{7.22}$$

This also allows one to easily obtain the expressions of the synaptic currents in terms of the module activities using Eq.7.13,

$$\delta\tilde{I}_{BA}^{syn}(\mathbf{q},\sigma) = w_{BA}C(\mathbf{q},\sigma)\tilde{S}_A(\sigma)\,\delta\tilde{I}_A(\mathbf{q},\sigma), A \in \{E, I\}, B \in \{E, I\} \tag{7.23}$$

where the functions $\tilde{S}_E(\sigma)$, $\tilde{S}_I(\sigma)$ are the *Laplace* transforms of $S_E(t)$ and $S_I(t)$ (Eq.7.21) with

$$\tilde{S}_A(\sigma) = \frac{\exp(-\sigma\tau_l^A)}{(1+\sigma\tau_r^A)(1+\sigma\tau_d^A)},\ A \in \{E, I\}. \tag{7.24}$$

In the presence of the synaptic currents with finite kinetics, the matrix (Eq.7.14) is replaced by

$$\tilde{L}_{EI}(\mathbf{q},\sigma) = \begin{pmatrix} 1+\sigma\tau_E(I_E^s) - \alpha\, C(\mathbf{q},\sigma)\tilde{S}_E(\sigma) & w_{EI}\,\Phi_I'(I_I^s)\tilde{S}_I(\sigma) \\ -w_{IE}\,\Phi_E'(I_E^s)\,C(\mathbf{q},\sigma)\tilde{S}_E(\sigma) & 1+\sigma\tau_I(I_I^s) + \gamma\tilde{S}_I(\sigma) \end{pmatrix}. \tag{7.25}$$

The determinant of the matrix $\tilde{L}_{EI}(\mathbf{q},\sigma)$ is

$$W(\mathbf{q},\sigma) = \left[1-\alpha\, C_l(\mathbf{q},\sigma)\,\tilde{T}_E(\sigma)\right]\left[1+\gamma\,\tilde{T}_I(\sigma))\right] + \beta\, C_l(\mathbf{q},\sigma)\,\tilde{T}_E(\sigma)\tilde{T}_I(\sigma) = 0 \tag{7.26}$$

where α, β, γ are given in Eq.7.17, and the notation $\tilde{T}_A(\sigma)$ is described by

$$\tilde{T}_A(\sigma) = \frac{\tilde{S}_A(\sigma)}{1+\tau_A(I_A^s)\sigma}, A \in \{E, I\}. \tag{7.27}$$

Following our previous calculation, we set $\sigma = i\omega$ in Eq.7.26. Separating the real and imaginary parts and solving for the α and β, the Hopf bifurcation line is obtained in parametric form,

$$\begin{aligned}
\alpha &= \frac{\mathrm{Im}\left\{C(\mathbf{q},i\omega)\left[\tilde{T}_I(i\omega)\tilde{T}_E(i\omega) + \gamma|\tilde{T}_I(i\omega)|^2\tilde{T}_E(i\omega)\right]\right\}}{|C(\mathbf{q},i\omega)|^2\,|\tilde{T}_E(i\omega)|^2\,\mathrm{Im}[\tilde{T}_I(i\omega)]}, \\
\beta &= \frac{\mathrm{Im}\left[C(\mathbf{q},i\omega)\tilde{T}_E(i\omega)\right]|1+\gamma\tilde{T}_I(i\omega)|^2}{|C(\mathbf{q},i\omega)|^2\,|\tilde{T}_E(i\omega)|^2\,\mathrm{Im}[\tilde{T}_I(i\omega)]}.
\end{aligned} \tag{7.28}$$

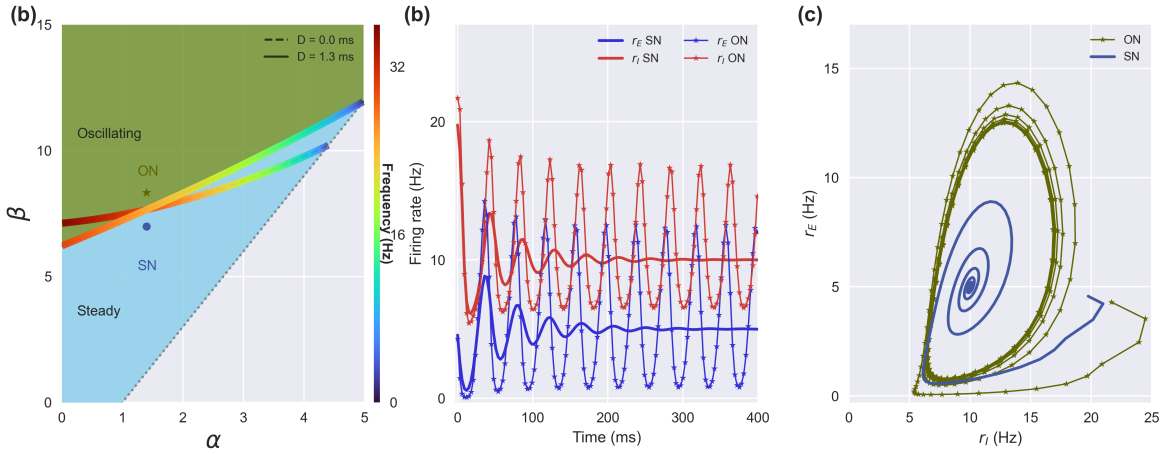

Figure 7.3: **The dynamic of the network model.** (a) The stability diagram of the network model with functions of α and β, the green area is the oscillating network regime, the blue area is the steady network regime, the colorful lines are the Hopf bifurcation lines for different D ($D = 0$: real line, $D = 1.3$ ms: dotted line), the color corresponds to the oscillation frequency. (b) show the traces of the r_E and r_I for the steady network (SN) and the oscillating network (ON) in (a). (c) Firing rates are plotted as r_E VS r_I. Parameters are: $N_E, N_I \to \infty$, $c = 1.0$, the other parameters correspond to SN and ON are given in Table.8.1.

When the kinetics of the synaptic currents are considered in our network model, the beta frequency is no longer limited to the "tip area" (see Fig.7.2 and Fig.7.3(a)). The colored lines are the bifurcation lines for different delay D, and the corresponding color is the oscillation frequency. It is obvious that the delay slows down the oscillation ($D = 1.3ms$: the solid colored line, $D = 0ms$: the dotted colored line). The theoretical analysis helps us in selecting appropriate parameters for the network to exhibit beta range oscillations. The evolution traces of r_E and r_I for the steady network (SN, real line) and the oscillating network (OS, star line) are shown

in Fig.7.3(b). The SN returns to fixed firing rates after a few oscillation cycles while the ON exhibits regular oscillations. A different representation is shown in Fig.7.3(c) by plotting r_E vs r_I (SN: blue, ON: green).

7.3 Theoretical analysis of power spectrum and correlation

The stochastic effects in the FAT network model have two sources as previously discussed: one comes from the fluctuation of the neuron population and the other one from fluctuating external inputs. We consider these stochastic effects by linearizing Eq.7.2 around the steady state and solving it in *Fourier* space. We define the *Fourier* transform

$$\delta I_A(\mathbf{x},t) = \int_{-\pi}^{+\pi}\int_{-\pi}^{+\pi}\frac{dq_x}{2\pi}\frac{dq_y}{2\pi}\int_{-\infty}^{+\infty}\frac{d\omega}{2\pi}\,\tilde{\delta I}_A(\mathbf{q},\omega)\exp[i(\mathbf{q}\cdot\mathbf{x}+\omega t)],\ A\in\{E,I\}. \tag{7.29}$$

Then we obtain

$$\tilde{L}_{EI}(\mathbf{q},i\omega)\cdot\tilde{\delta\mathbf{I}}(\mathbf{q},i\omega) = \mathbf{F}(\mathbf{q},i\omega). \tag{7.30}$$

The matrix $\tilde{L}_{EI}(\mathbf{q},i\omega)$ is given by Eq.7.25. The stochastic forcing term $F_A(\mathbf{q},i\omega)$ includes the two kinds of stochastic effects. It reads,

$$\begin{aligned} F_A(\mathbf{q},i\omega) &= \sigma_A^{ext}\tilde{\eta}(\mathbf{q},\omega)+ \\ &w_{AE}C(\mathbf{q},i\omega)\tilde{S}_E(i\omega)\sqrt{\frac{r_E^s}{N_E}}\,\tilde{\xi}_E(\mathbf{q},\omega) - w_{AI}\tilde{S}_I(i\omega)\sqrt{\frac{r_I^s}{N_I}}\,\tilde{\xi}_I(\mathbf{q},\omega),\ A\in\{E,I\}. \end{aligned} \tag{7.31}$$

Solution of the linear system (Eq.7.30) provides the expressions of the *Fourier* components of the currents. For the excitatory current, one obtains

$$\tilde{\delta I}_E(\mathbf{q},\omega) = \frac{1}{(1+i\omega\tau_E)}\frac{V_E(\mathbf{q},i\omega)}{W(\mathbf{q},i\omega)} \tag{7.32}$$

with $W(\mathbf{q},i\omega)$ given by Eq.7.26, and $V_E(\mathbf{q},i\omega)$ by the expression

$$V_E(\mathbf{q},i\omega) = F_E(\mathbf{q},i\omega)\left[1+\gamma\tilde{T}_I(i\omega)\right] - F_I(\mathbf{q},i\omega)w_{EI}\Phi_I'\tilde{T}_I(i\omega). \tag{7.33}$$

The fluctuating external inputs are separated into a global part ξ_g and a local part $\xi(\mathbf{x})$. So the *Fourier* components of the external inputs are

$$\tilde{\eta}(\mathbf{q},\omega) = \frac{\sqrt{\tau_{ext}}}{1+i\omega\tau_{ext}}\left[\sqrt{1-c}\,\tilde{\xi}(\mathbf{q},\omega)+\sqrt{c}(2\pi)^2\delta^2(\mathbf{q})\tilde{\xi}_g(\omega)\right] \tag{7.34}$$

with

$$\begin{aligned} \langle\tilde{\xi}(\mathbf{q},\omega)\tilde{\xi}^*(\mathbf{q}',\omega')\rangle &= (2\pi)^3\delta(\omega-\omega')\delta^2(\mathbf{q}-\mathbf{q}'), \\ \langle\tilde{\xi}_g(\omega)\tilde{\xi}_g^*(\omega')\rangle &= 2\pi\delta(\omega-\omega'). \end{aligned} \tag{7.35}$$

For the finite-size noise of the excitatory and the inhibitory populations, one has similarly,

$$\langle\tilde{\xi}_E(\mathbf{q},\omega)\tilde{\xi}_E^*(\mathbf{q}',\omega')\rangle = \langle\tilde{\xi}_I(\mathbf{q},\omega)\tilde{\xi}_I^*(\mathbf{q}',\omega')\rangle = (2\pi)^3\delta(\omega-\omega')\delta^2(\mathbf{q}-\mathbf{q}'). \tag{7.36}$$

The current-current correlation function is obtained by averaging the product of the currents (Eq.7.32) over the noises,

$$\begin{aligned}\langle\tilde{\delta I}_E(\mathbf{q},\omega)\tilde{\delta I}_E^*(\mathbf{q}',\omega')\rangle = 2\pi\delta(\omega-\omega')\{(2\pi)^2\delta^2(\mathbf{q}-\mathbf{q}')S_{EE}^N(\mathbf{q},\omega) \\ + [(1-c)(2\pi)^2\delta^2(\mathbf{q}-\mathbf{q}') + c(2\pi)^4\delta^2(\mathbf{q})\delta^2(\mathbf{q}')]S_{EE}^{ext}(\mathbf{q},\omega)\}.\end{aligned} \tag{7.37}$$

$S_{EE}^{ext}(\mathbf{q},\omega)$ is related to the external inputs,

$$S_{EE}^{ext}(\mathbf{q},\omega) = \frac{\tau_{ext}\left|\sigma_E^{ext} + (\gamma\sigma_E^{ext} - \sigma_I^{ext}w_{EI}\Phi_I')\tilde{T}_I(i\omega)\right|^2}{[1+(\omega\tau_{ext})^2][1+(\omega\tau_E)^2]|W(\mathbf{q},i\omega)|^2}. \tag{7.38}$$

$S_{EE}^N(\mathbf{q},\omega)$ describes the effect of finite-size noise,

$$\begin{aligned}S_{EE}^N(\mathbf{q},\omega) = \frac{1}{|W(\mathbf{q},i\omega)|^2}\left\{\frac{r_E^s}{N_E}w_{EE}^2\left|1+(\gamma-\frac{\beta}{\alpha})\tilde{T}_I(i\omega)\right|^2\left|C(\mathbf{q},i\omega)\tilde{T}_E(i\omega)\right|^2\right. \\ \left. + \frac{r_I^s}{N_I}\frac{w_{EI}^2\left|\tilde{S}_I(i\omega)\right|^2}{1+(\omega\tau_E)^2}\right\}.\end{aligned} \tag{7.39}$$

They provide the expression of the current-current correlation in real space,

$$\begin{aligned}\langle\tilde{\delta I}_E(\mathbf{x},t)\tilde{\delta I}_E(\mathbf{x}',t')\rangle = \int_{-\infty}^{+\infty}\frac{d\omega}{2\pi}\exp[i\omega(t-t')]\left\{c\,S_{EE}^{ext}(\mathbf{0},\omega)\right. \\ \left. + \int_{-\pi}^{+\pi}\int_{-\pi}^{+\pi}\frac{dq_x}{2\pi}\frac{dq_y}{2\pi}\left[(1-c)S_{EE}^{ext}(\mathbf{q},\omega) + S_{EE}^N(\mathbf{q},\omega)\right]\exp[i\mathbf{q}\cdot(\mathbf{x}-\mathbf{x}')]\right\}.\end{aligned} \tag{7.40}$$

The power spectrum is

$$S(\omega) = cS_{EE}^{ext}(\mathbf{0},\omega) + \int_{-\pi}^{+\pi}\int_{-\pi}^{+\pi}\frac{dq_x}{2\pi}\frac{dq_y}{2\pi}[(1-c)S_{EE}^{ext}(\mathbf{q},\omega) + S_{EE}^N(\mathbf{q},\omega)]. \tag{7.41}$$

As illustrated in Fig.7.3, without the stochastic effects, the network states either are at a steady state (SN) after a few oscillations or in an oscillating state (ON) with regular oscillations. None of these can account for the beta bump in the power spectrum seen in the experimental data. Fluctuating external inputs change the stability of the steady state as shown in Fig.7.4(a), which illustrates the stability diagram of the network model as the functions of I_E^{ext} and I_I^{ext} (the synaptic couplings are corresponding to SN in Table.8.1). If we choose the steady network (SN, blue point) as a basic state, the time-varying external inputs lead the SN to move along the black line and enter the oscillation area from time to time, causing the firing rate to wax and wane as shown in the graph of Fig.7.4(c). The corresponding theoretical and simulated power spectrum are shown in Fig.7.4(b). The inclusion of fluctuating external inputs creates a bump

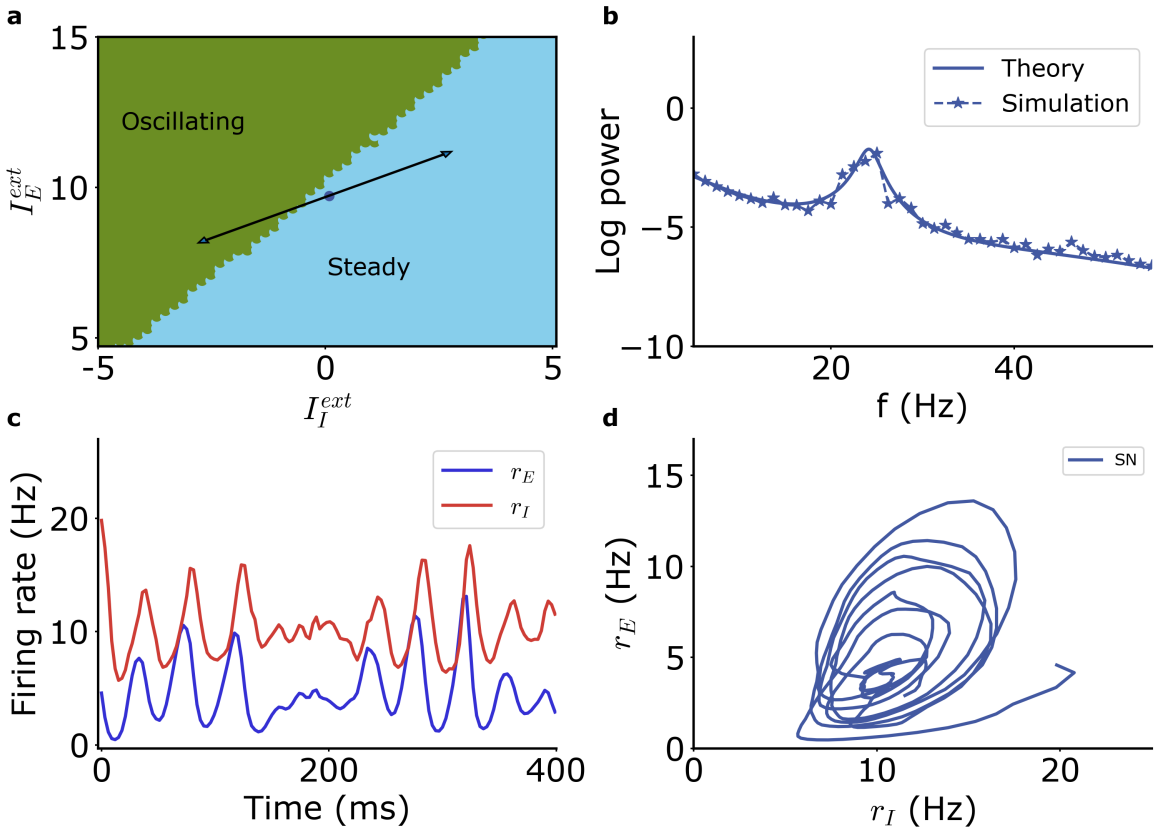

Figure 7.4: **The network model SN with external inputs.** (a) The stability diagram as functions of the external currents I_E^{ext}, I_I^{ext}. (b) The theoretical and simulated power spectrum of the network model with external inputs (simulation data in (c)). (c) The time traces of the firing rates r_E, r_I. (d) Same data as (c) but plotted as r_I Vs r_E. Parameters: $N \to \infty$, the other parameters are as SN in Table.8.1.

in the beta range on the power spectrum, which is consistent with experiment recordings. This encouraged us to compare other characteristics of the simulated network to experimental data.

7.4 The analysis of the parameters

Can this model account for other observed phenomena in the experimental data, such as sporadic beta bursts and complex waves? Where do these characteristics originate from? Here, we analyze the network model step by step based on these characteristics (frequency, correlation, beta burst, and waves) using both theoretical analysis and numerical simulations to see how the dynamics of the network model depend on different choices of the parameters.

In our model, the intrinsic finite-size noise is controlled by the number of neurons N in each module; the external inputs are defined by the correlation time τ_{ext}, the proportion between global and local noise c and the amplitude ν_{ext}. These parameters act together and by choosing them in an appropriate way, we will be able to account for beta oscillations in the motor cortex.

The theoretical expression for the power spectrum allows us to easily find the appropriate frequency range as a function of the essential parameters α (the strength of recurrent excitation), β (the strength of feedback inhibition through the disynaptic E-I loop) and γ (the strength of autoinhibition of interneurons) with different delay D and excitatory connectivity parameter l. We fixed $D = 1.3ms$ which corresponds to the speed of propagation along unmyelinated horizontal axons and $l = 2$ which corresponds to the typical range of excitatory connections. For convenience, we also fixed $\gamma = 0.87$ and just change α, β and other variables related to stochastic effects. We choose two points as base states for the network, one in the steady state (SN) and one in an oscillating state (ON) as shown in Fig.7.3 and investigate how the fluctuating external inputs affect the dynamic of the network model. For SN, we can also get the power spectrum from the analytical formula Eq.7.41. In the following, we show both the theoretical and simulated power spectrum for SN and only the simulated one for ON.

Fluctuating stochastic effects on frequency

We start by analyzing how the fluctuations in the model influence the spectral properties.

- Finite-size noise. First, we just assume that the stochastic effects only come from the number of neurons N without external inputs. Fig.7.5 depicts how the power spectrum changes with different N $(2 \times 10^3 - 2 \times 10^5)$ for SN and ON. For SN (Fig.7.5(a-b)), finite-size noise cannot account for the widened beta bump and also does not account for the power at low frequencies, even when the noise is large ($N \sim 2 \times 10^3$); for ON (Fig.7.5(c-d)), the finite-size noise is too small to strongly perturb its original regular oscillation, so the power spectrum is too spiky when compared with the experimental ones. It also displays an obvious second bump around $50Hz$ which is not seen in the experimental data. So intrinsic stochastic effects cannot account for the power spectrum observed in experimental data. This leads us to further consider the external inputs.

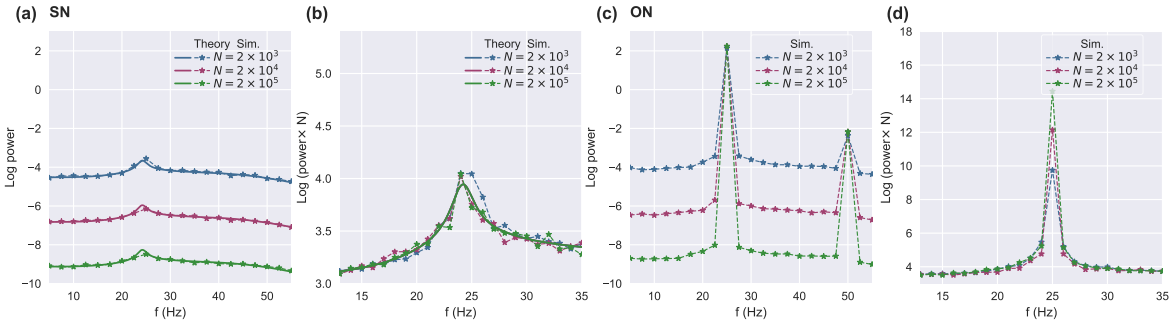

Figure 7.5: **Intrinsic finite-size effect on power spectrum for SN (a-b) and ON (c-d).** (a) The real lines are the theoretical results, the start lines are the simulation results for SN with $N = 2 \times 10^3$, blue; $N = 2 \times 10^4$, purple; $N = 2 \times 10^5$, green. (b) Same lines as (a) but normalized by N. (c, d) The simulated power spectrum for ON. The other parameters are corresponding to SN and ON in Table.8.1.

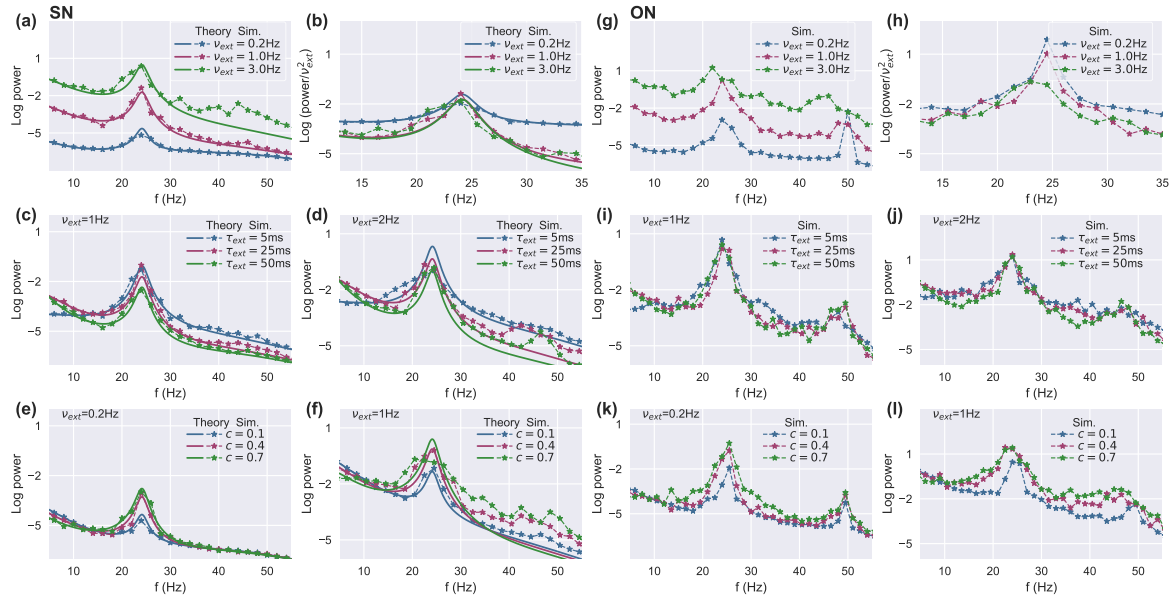

Figure 7.6: **How the external inputs (controlled by ν_{ext}, τ_{ext}, c) affect the power spectrum for SN (a-f) and ON (g-l).** (a-b, g-h) The influence of the external inputs amplitude ν_{ext}. (c-d, i-j) The influence of the external inputs correlation time τ_{ext}. (e-f, k-l) The influence of the external inputs fraction c. The other parameters are corresponding to SN and ON in Table.8.1.

- Fluctuating external inputs. The external inputs are characterized by their amplitude ν_{ext}, their correlation time τ_{ext} and the fraction c of global inputs. Fig.7.6 illustrates how they influence the power spectrum. The first row (Fig.7.6(a-b, g-h)) show how the amplitude of the external inputs ν_{ext} shapes the power spectrum. Fig.7.6(b, h) show the power spectrum as in Fig.7.6(a, g) but normalized by ν_{ext}^2. For SN (Fig.7.6(a-b)), the power spectrum becomes wider as the amplitude ν_{ext} increases. An intermediate level of noise is optimal: too little noise ($\nu_{ext} = 0.2Hz$, blue line) would not be sufficient to create

a bump in the power spectrum, whereas too much noise ($\nu_{ext} = 3Hz$, green line) would cause anharmonicity of beta oscillations (with a second bump around 50 Hz). In addition, significant power appears at low frequencies when ν_{ext} is suitably chosen (bigger than 0.2 Hz); for ON, the effect is opposite as compared to SN, a large ν_{ext} ($\nu_{ext} = 3Hz$, green line) destroys the original spiky power spectrum and makes it more similar to what is seen in the experimental data. The second row (Fig.7.6(c-d, i-j)) and third row (Fig.7.6(e-f, k-l)) show how the power spectrum depends on the external inputs correlation time τ_{ext} and on the fraction c with different fixed ν_{ext}, respectively. From the figures, we can see that τ_{ext} and c have a similar effect on SN and ON as ν_{ext} does.

In summary, a suitable power spectrum based on the essential parameters $\alpha, \beta, \gamma, D, l$ is primarily determined by the external inputs (amplitude ν_{ext}, correlation time τ_{ext} and fraction c). The intrinsic stochasticity coming from the number of neurons is insufficient to cause transient beta activity. We should moderately adjust the parameters related to external inputs to make the simulation currents comparable with recording signals.

The effect of the fraction c between the global part and the local part of the external inputs on the correlation between modules

As can be seen in Fig.8.5, the correlation between different modules decreases with distance, but there is still some degree of correlation (~ 0.5) at a long distance. Many factors influence the correlation in our model depending on its state. The correlation for SN is primarily affected by parameter c, which controls the fraction between the global noise (c) that makes the network synchronized and the local noise ($1 - c$) that has an inverse effect. Fig.7.7 (a-f) show the phase diagram of the evolution of the $I_E s$ for different c (0.1, 0.4, 0.7). The network becomes more and more synchronized as c increases. The best fit is obtained with recordings of monkey L when c is about 0.4. For ON (Fig.7.7 (g-l)), the network starts with highly synchronized oscillations. If the external inputs amplitude is small ($\nu = 0.2Hz$, Fig.7.7 (g-i)), the fraction c has a negligible effect on the correlation. When the external inputs amplitude is large enough ($\nu = 1.0Hz$, Fig.7.7 (j-l)), the situation is similar to SN.

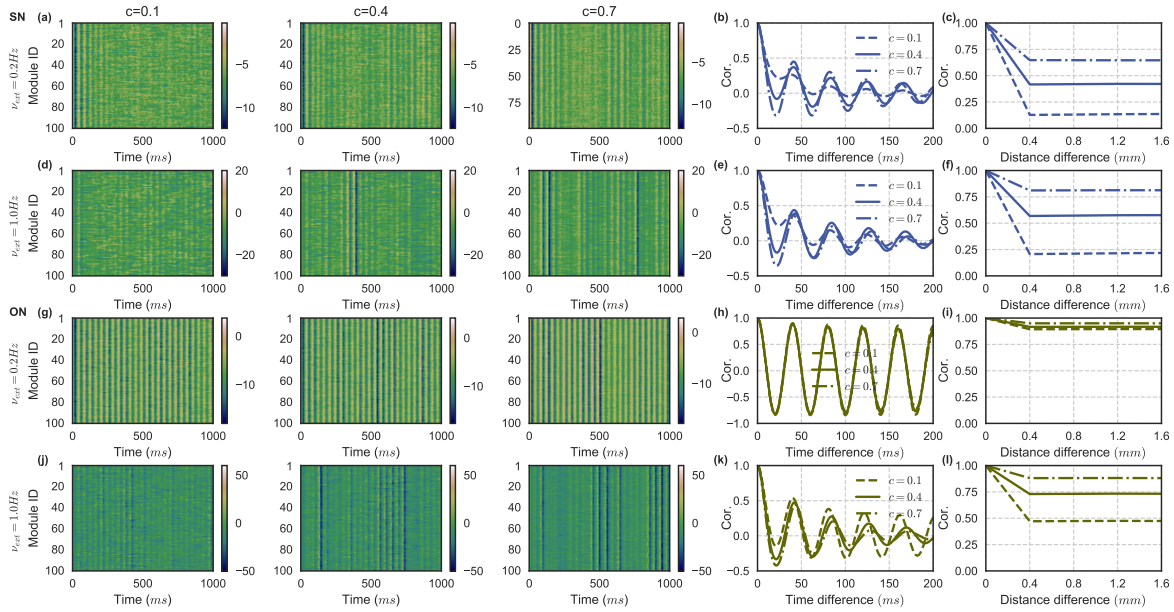

Figure 7.7: **The correlation with c for SN (a-f)) and ON (g-l).** (a, d, g, j) The phase diagram of the current trace for different c (0.1, 0.4, 0.7). (b, e, h, k) The autocorrelation. (c, f, i, l) The correlation with distance. The other parameters are corresponding to SN and ON in Table.8.1.

The influence of the external inputs on beta bursts

As previously stated, the fluctuating effects will change the stability of the network and cause occasional beta bursts. In our model, the beta burst duration mainly depends on the correlation time τ_{ext} of the external inputs.

Fig.7.8(a-b, f-g) show the spectra for different τ_{ext} for SN and ON. By comparing figures Fig.7.8(a) and Fig.7.8(b) (or Fig.7.8(f) and Fig.7.8(g) for ON), one sees that a larger τ_{ext} causes the beta bursts to continue for a longer time. The relationship between τ_{ext} and the beta burst duration is shown in Fig.7.8(c, h). They are seen to be positively correlated. Analysis of the experimental data shows that during the movement preparatory period, the burst duration is less than $100ms$. So this leads us to keep τ_{ext} smaller than $50ms$ in our model. Fig.7.8 (d, i), (e, j) show the distributions of the beta burst amplitudes and durations for different ν_{ext}. For SN and ON, ν_{ext} has little effect on the shape of the beta burst duration distribution, while it has a significant effect on the amplitude distribution for ON. Only large ν_{ext} can make the amplitude distribution similar to the experimental data (Fig8.3).

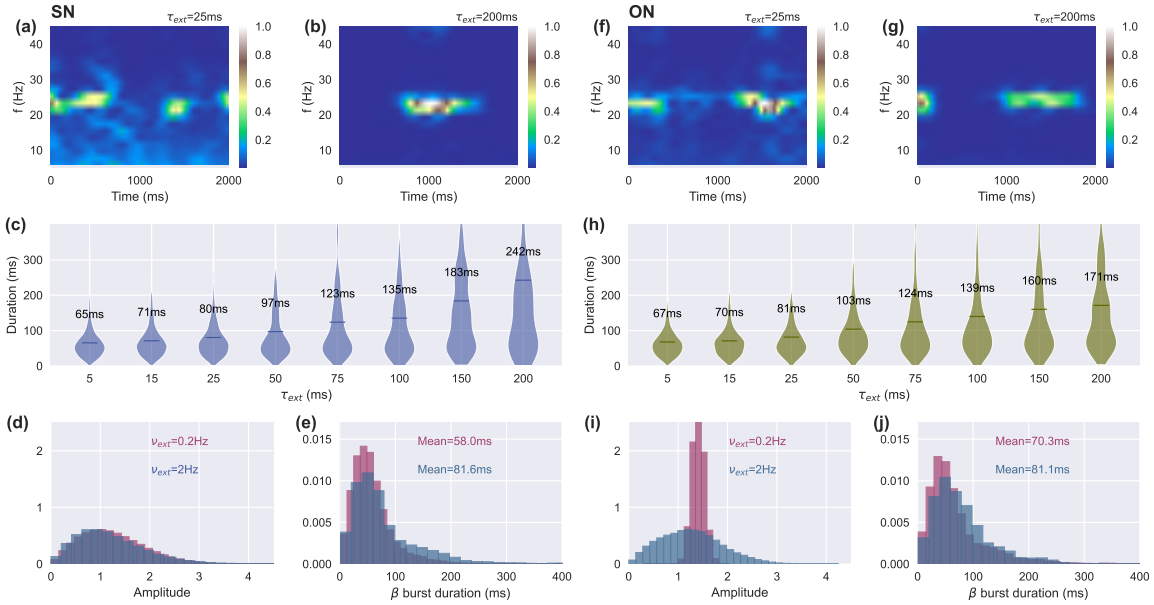

Figure 7.8: **External effect on the beta burst for SN (a-e) and ON (f-j).** The spectra for different τ_{ext}((a, f) $\tau_{ext} = 25ms$, (b, g) $\tau_{ext} = 200ms$). (c, h) The violin plot of the relationship between the τ_{ext} and the beta burst duration. (d, i), (e, j) The distribution of the amplitude and beta burst duration for different ν_{ext}. The other parameters are corresponding to SN and ON in Table.8.1.

In conclusion, the duration of beta burst mainly depends on the correlation time of the external inputs τ_{ext}. τ_{ext} should be less than $50ms$ to avoid the beta burst duration being too long.

The influence of the external inputs amplitude ν_{ext} on the waveform

The pioneering study [84] has shown that LFP beta oscillations in the motor cortex travel as planar waves, propagating at speeds around $30cm/s$. Later, several studies have shown that these signals also exhibit more complex patterns as radial waves, or spiral waves [86, 85]. In our model, we have found that traveling waves can be observed if we choose the network parameters near the Hopf bifurcation line. The external input amplitude will influence the proportion of planar waves. Fig.7.9 shows different wave type proportions and the distribution of planar wave speeds as one changes the external inputs amplitude ν_{ext}. For SN (see Fig.7.9(a)), the original network is in a relatively disordered state. As one increases the external input amplitude, it first increases the chance to make the network enter the oscillating phase and has a synchronizing effect. This increases the proportion of planar waves and also their speeds. While, above a certain amplitude ($\sim 2Hz$), large external inputs have a desynchronizing effect. This makes the network more desynchronized and thus the planar wave speeds also decrease. For ON (see Fig.7.9(b)), the original network is in a relatively synchronized oscillating state. Increasing the stochastic effects has no obvious influence on the proportion of planar waves but it acts as a desynchronizing effect that slows down the wave speeds.

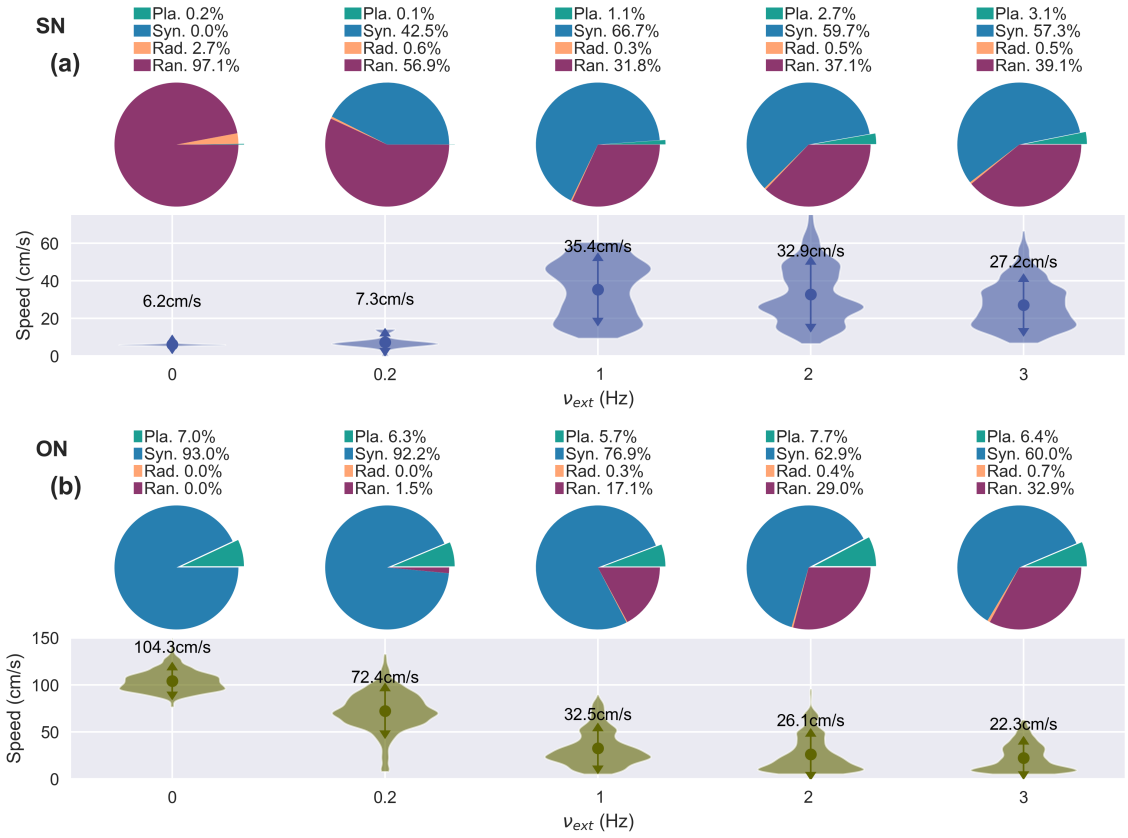

Figure 7.9: **The influence of the external inputs amplitude ν_{ext} on the wave kinds and the planar speed for SN (a) and ON (b).** Pla.(green), Syn.(blue), Rad.(orange), Ran.(purple) stand for planar wave, synchronized, radial wave, random, respectively. The point in the speed violin is the mean speed corresponding to the value shown, and the arrow is the standard deviation of the speed. The other parameters are corresponding to SN and ON in Table.8.1.

The influence of the excitatory connection range l on the wave directions

Studies have shown that the direction of planar waves at different location in the motor cortex has an orientational preference [84] which may reflect the underlying structure of the cortex. In the previous results, we used the same l for both axes in our network architecture and found no orientational preference in the direction, see Fig.7.10(a-c). To investigate the origin of this phenomenon, we choose different l for the range of excitatory connecting along the x-axis and y-axis (as shown in Fig.7.10(d)). The proportion of the wave direction is then found to have an obvious trend that is related to the anisotropy in l. We set $l_x = 1.0$ and $l_y = 2.0$, which indicates that connections have a longer range along the y-axis. Oscillations tend to be more synchronized along y-axis, and there are more planar waves propagating along the x-axis (Fig.7.10(f)). As compared with the isotropic case, the anisotropy of the connectivity strength has little effect on the proportion of wave types, but it dramatically influences the direction of planar waves.

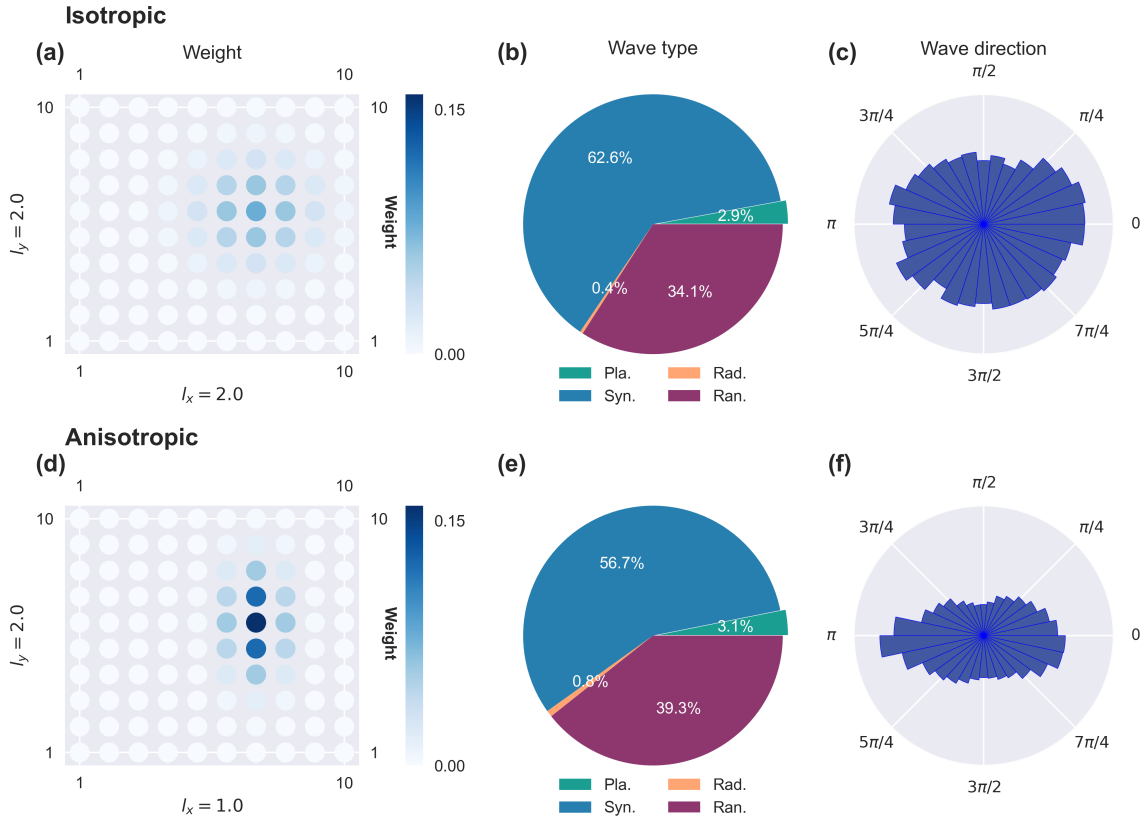

Figure 7.10: **Influence of connectivity anisotropy on planar wave propagation direction.** (a-c) Isotropic connectivity, (d-f) Anisotropic connectivity, (a, d) An example of the connectivity strength of module in position (7,6). (b, e) The wave kinds pie. (c, f) Distribution of propagation directions of planar waves. The other parameters are corresponding to SN and ON in Table.8.1.

8 Comparison with experimental data and simulations of the FAT network model

How do the simulation results compare with experimental data? We choose a network model in which each module has recurrent interaction between its excitatory and inhibitory populations. These local modules are connected by distance-dependent long range excitatory couplings. In addition, we consider external inputs which have two different components, one is local and different from module to module, and another one is global and the same for all modules. Through the above analysis, we know how every parameter shapes the dynamics of the model. To obtain simulation results that are comparable to recording data, first, we need to choose suitable synaptic coupling strengths α, β, γ to make the network exhibits beta oscillations when receiving fluctuating inputs. Then, we need to adjust the correlation time of the external inputs τ_{ext} to fit the beta burst durations. The fraction of global external inputs c mainly controls the correlation, and the amplitude of the external inputs ν_{ext} has a significant influence on the planar waves. These factors do not work alone but are linked together to account for the beta oscillations in our network model. Here, we choose two different sets of parameters (SN and SN', the corresponding parameters are given in Table.8.1) to compare with the two sets of data, SN corresponds to monkey L, and SN' corresponds to monkey N. Below, we consider the local excitatory currents as a proxy for the LFP in the recordings. Thus, the analysis results compare the LFPs for the monkey data to the excitatory currents I_E in the simulations.

8.1 Power spectrum

The average power spectrums of the LFPs during CUE-OFF to GO-ON for monkey L (purple) and monkey N (red) are shown in Fig.8.1(a) and Fig.8.2(a). The power spectrum is obtained by averaging across all electrodes (96 active electrodes) and all trials (135 trials for monkey N, 142 trials for monkey L). For both monkeys, an obvious bump between 13-30 Hz is seen in the power spectrum, while the peak frequency in the power spectrum is a little different, around $23Hz$, $20Hz$ for monkey L and monkey N, respectively.

The power spectra which are obtained from the simulation results of the network model SN and SN' are shown in Fig.8.1 (b) and Fig.8.1 (b).

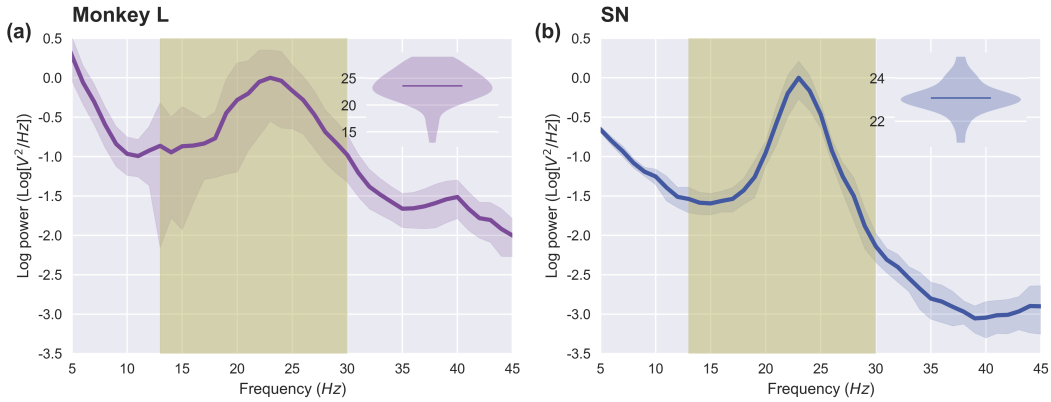

Figure 8.1: **Comparison of the power spectrum between monkey L (a) and the simulation of the network model SN (b).** The insert figure is the frequency distribution where the peak power spectrum occurs.

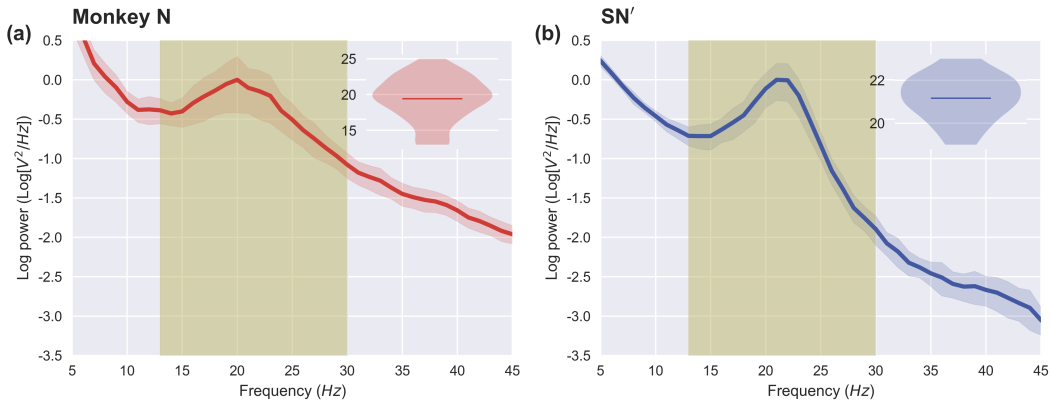

Figure 8.2: **Comparison of the power spectrum between monkey N (a) and the simulation of the network model SN′ (b).**

8.2 The statistics of the beta bursts

The statistical properties of the beta bursts for monkey L and the network model SN are showed in Fig.8.3. The average beta burst duration of monkey L is relatively short, around 60 ms (see in Fig.8.3(b)), while the simulated beta burst durations are a little longer, with an average value around 75 ms (see in Fig.8.3(e)). Fig.8.3(a, d) are the amplitude distributions of the analytical signals for monkey L and SN, the dark color corresponds to the beta burst amplitudes. The relationship between the beta burst amplitudes and the beta burst durations is shown in Fig.8.3(c, f) for monkey L and SN, respectively. The color bar corresponds to the density of the points. In general, the beta burst amplitudes and durations are positively correlated.

Fig.8.4 is the same figure as Fig.8.3 but for the comparison between monkey N and the network model SN'.

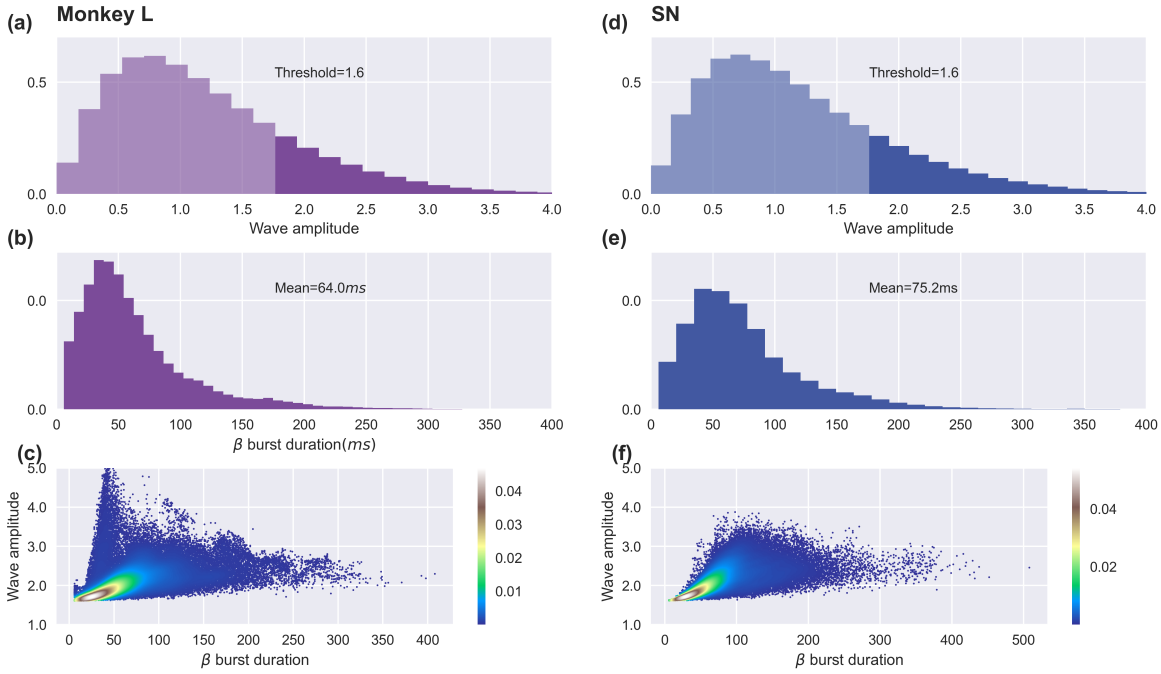

Figure 8.3: **Comparison of the beta bursts between monkey L (a-c) and the simulation of the network model SN (d-f).** (a, d) The distribution of the amplitudes. (b, e) The distribution of the beta burst durations. (c, f) Relationship between the beta burst amplitudes and the beta burst durations.

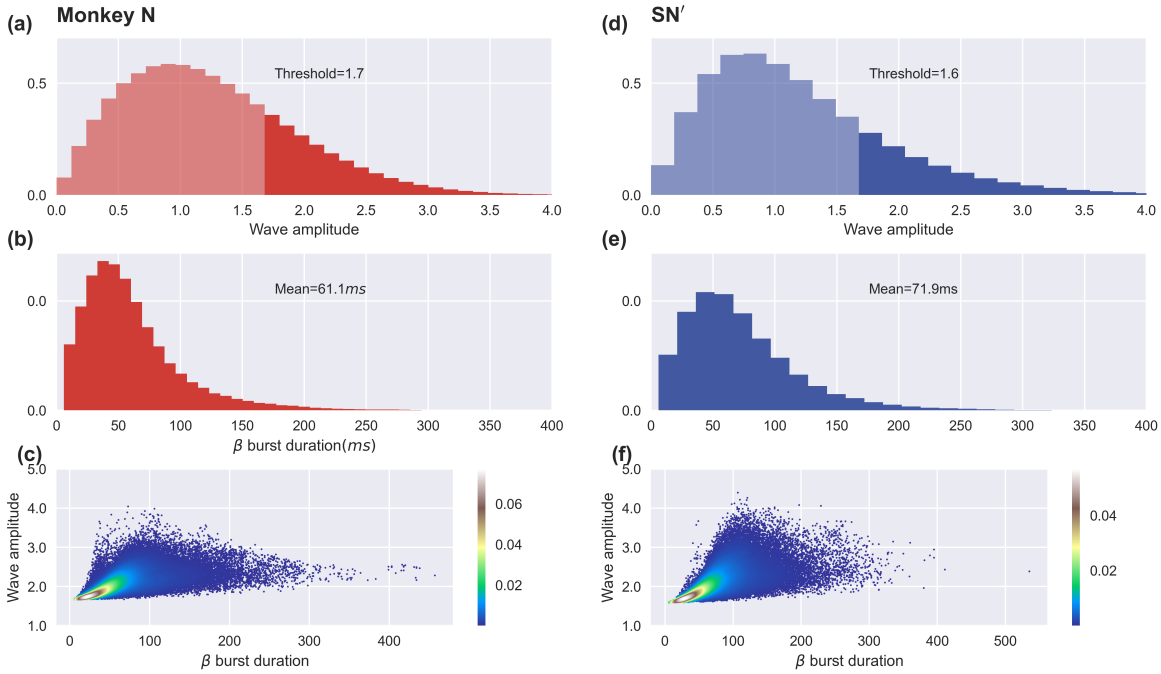

Figure 8.4: **Comparison of the beta bursts between monkey N (a-c) and the simulation of the network model SN′(d-f).** (a, d) The distribution of the beta burst amplitudes. (b, e) The distribution of the beta burst durations. (c, f) Relationship between the beta burst amplitudes and the beta burst durations.

8.3 Correlation

The comparison of the LFP correlations for monkey L and the simulation network SN is shown in Fig.8.5. Fig.8.5(a, d) are the correlation maps with distance and time difference. Fig.8.5(b, e) and Fig.8.5(c, f) show the autocorrelation and the correlation changes with distance. The tail of the correlation at long distance has a limiting value around 0.5 for monkey L, which means that the distant electrodes are relatively synchronized.

The comparison of correlation between monkey N and the network model SN' is shown in Fig.8.6.

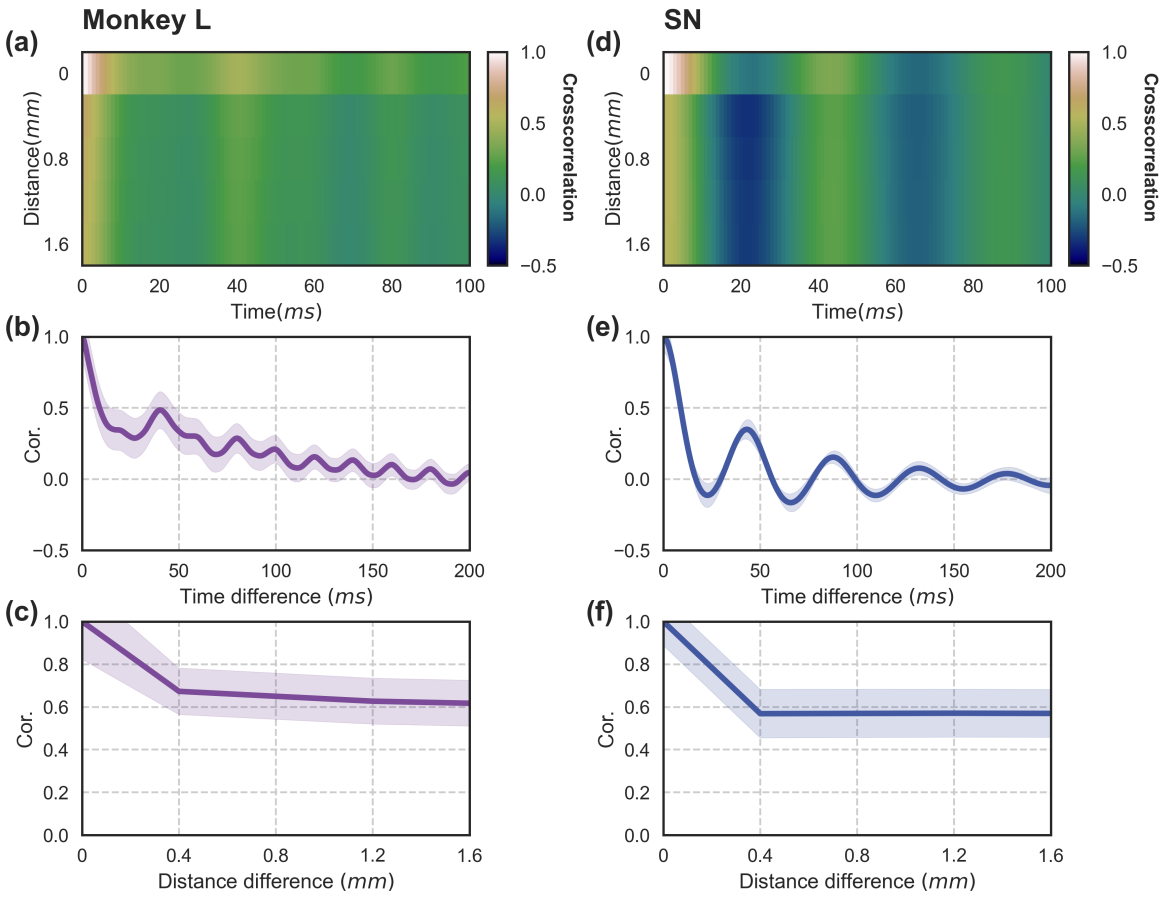

Figure 8.5: **Comparison of the correlation between monkey L (a-c) and the simulation of the network model SN (d-f).** (a, d) Correlation phase diagram as the function of the time difference and distance difference. (b, e) The autocorrelation. (c, f) The correlation with distance.

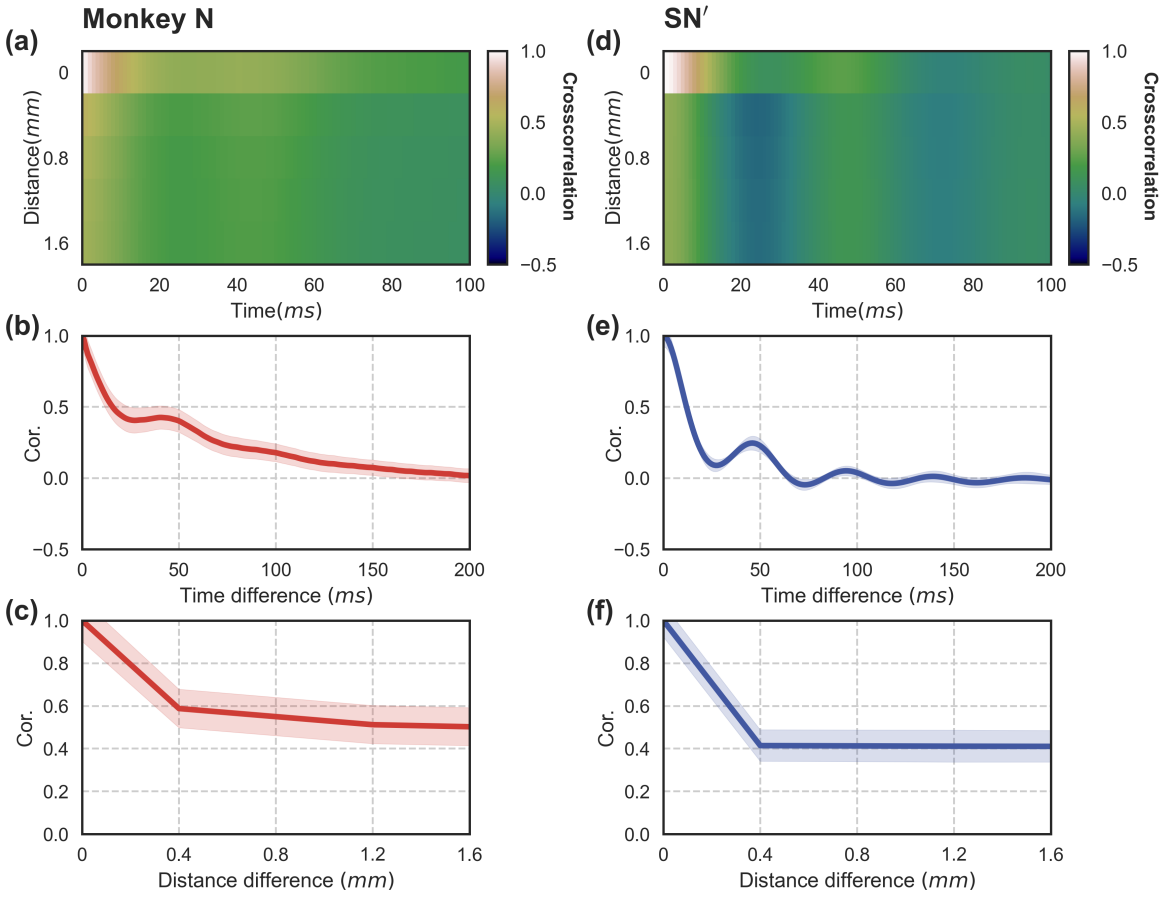

Figure 8.6: **Comparison of the correlation between monkey N (a-c) and the simulation of the network model SN′(d-f).** (a, d) Phase diagram of the correlation as the function of the time difference and distance difference. (b, e) The autocorrelation. (c, f) The correlation with distance.

8.4 Waves

Fig.8.7 depicts the statistics of the different waves. Fig.8.7 (a-d) are the phase maps and the distributions of the phase gradients for a planar wave and a radial wave for monkey L. The simulated waves of the model SN are shown in Fig.8.7(g-j). Fig.8.7(e, k) are the distributions of the planar wave speeds for monkey L and the network model SN. Both average speeds are around 30 cm/s. Fig.8.7 (f, l) are the proportions of the different waves. Complex waves are seen as in experimental data, while the proportions of the different wave types are slightly different.

The comparison of the waves for monkey N and the network model SN' is shown in Fig.8.8. One can also notice that the proportions of the different wave types vary between monkey N and monkey L. Compared with monkey L, monkey N has less synchronized waves (56.4% in monkey L while just 19.2% in monkey N), thus the planar wave speeds are slower.

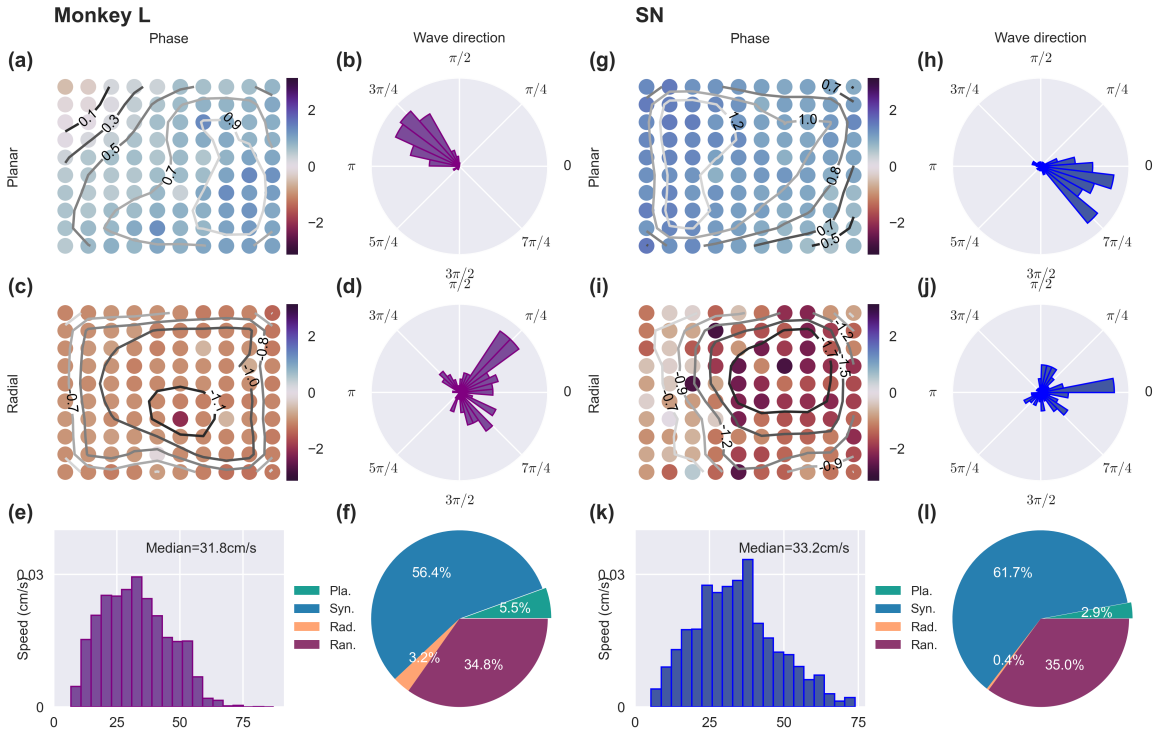

Figure 8.7: **Comparison of the wave between monkey L (a-f) and the simulation of the network model SN (g-i).** (a-b, g-h) Phase and the distribution of phase gradient of the planar wave (monkey L: LFPs, SN: excitatory currents I_E. (c-d, i-j) Same as (a-b, g-h) but for radial wave. (e, k) The distribution of the planar wave speed. (f, l) The proportion of the different kinds of waves.

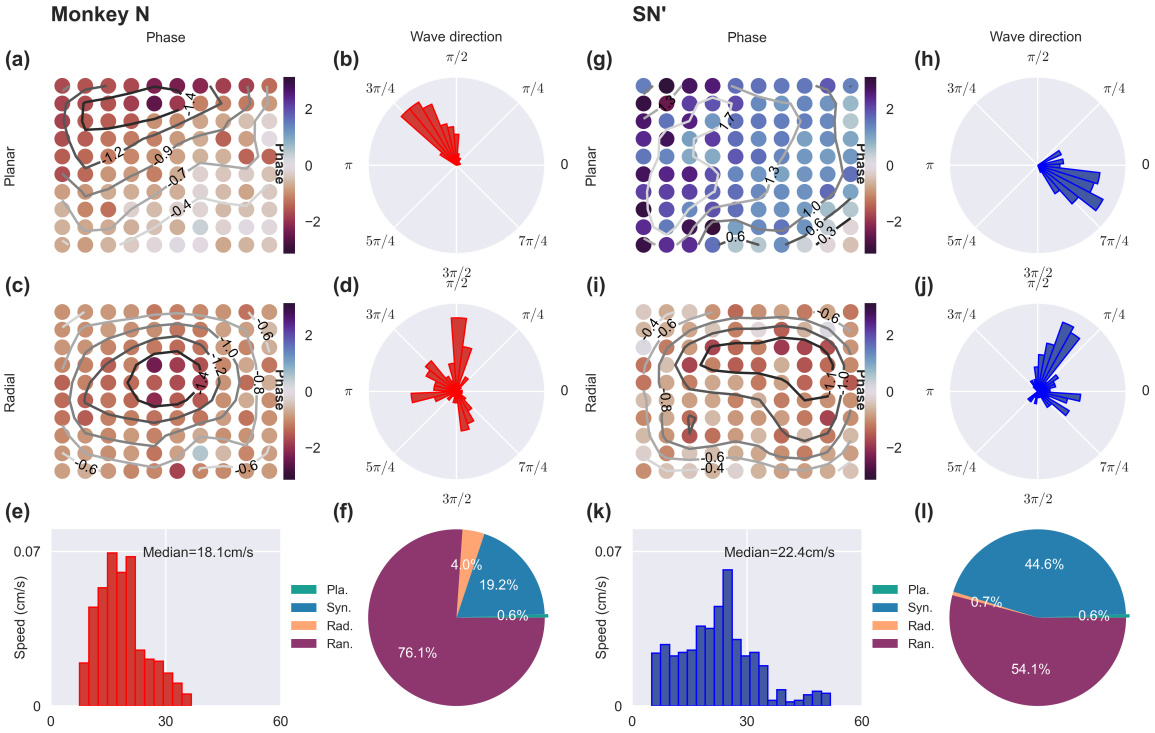

Figure 8.8: **Comparison of the wave between monkey N (a-f) and the simulation of the network model SN′ (g-i).** (a-b, g-h) The phase and the distribution of phase gradient of the planar wave. (c-d, i-j) Same as (a-b, g-h) but for radial wave. (e, k) The distribution of the planar wave speed. (f, l) Proportion of the different kinds of waves.

Parameters						
Symbol	Value				Unit	Definition
	SN	SN'	ON	SN_0		
r_E^s, r_I^s	5,10				Hz	Steady firing rates
I_E^s, I_I^s	-6.28,-3.62				mV	Currents at r_E^s, r_I^s
τ_E^s, τ_I^s	8.74,7.14				ms	Adaptive membrane time constant at r_E^s, r_I^s
$\Phi'_E(I_E^s), \Phi'_I(I_I^s)$	1.46,2.30					Firing rate gains at r_E^s, r_I^s
τ_r^E, τ_r^I	0.70				ms	Rise time of synaptic currents
τ_d^E, τ_d^I	3.50				ms	Decay time of synaptic currents
τ_l^E, τ_l^I	0.50				ms	Latency of synaptic currents
l	2					Excitatory connectivity range
N_E, N_I	16000, 4000					Neuron numbers in each E-I module
τ_{ext}	25				ms	Correlation time of external input fluctuations
ν^{ext}	2				Hz	External input amplitude fluctuations
$I_E^{ext,0}, I_I^{ext,0}$	9.72,0.08	6.12,0.08	13.72,0.08	5.72,0.08	mV	External currents
w_E^{ext}	0.96	1.12	0.96	1.20	mV·s	External input onto excitatory neurons synaptic coupling strength
w_I^{ext}	4.16	3.60	4.96	3.60	mV·s	External input onto inhibitory neurons synaptic coupling strength
w_{II}	0.87	0.87	0.87	0.87	mV·s	Recurrent synaptic coupling strength (I to I)
w_{IE}	1	1	1	1	mV·s	Recurrent synaptic coupling strength (E to I)
w_{EE}	0.96	1.12	0.96	1.20	mV·s	Recurrent synaptic coupling strength (E to E)
w_{EI}	2.08	1.80	2.48	1.80	mV·s	Recurrent synaptic coupling strength (I to E)
D	1.30	1.30	1.30	0	ms	Propagation delay between to nearest E-I modules
c	0.40	0.30	0.40	0.30		Proportion of global external inputs

Table 8.1: FAT network model parameter table.

Numerical methods

The network architecture is shown in Fig.7.1. The mathematical model is FAT network model. All equations are computed using a first-order Euler-Maruyama integration method programmed in C, with a time step $dt = 0.01ms$. Python programs were used for data analysis and to draw the figures. For model SN, ON, SN′, SN_0, the distributions and averages in all figures were obtained by performing 20 independent network simulations of 10 s of simulated time each.

CHAPTER III

Partial synchronization in the human cerebral cortex network

9 Introduction

9.1 Brain synchronization with cognitive functions

Neurons do not function alone, they are embedded in networks of functionally specialized brain regions, in which they influence each other through synaptic connections. One mechanism that is likely to be deeply involved in the communication within them is neural synchronization [179]. It refers to the oscillations of neuron activity within a specific band of frequencies that can become transiently phase-locked with that of another group of neurons between different brain regions, as it has been seen with assistance from electrophysiological recordings, such as electroencephalography(EEG), magnetoencephalography (MEG), electrocorticography (ECoG), and local field potentials(LFPs) [180]. Such transient phase locking can play a number of roles, including facilitating communication of information between the neural groups and even performing computational functions. As we introduced in Chapter.II, different rhythms have been shown to be associated with a variety of cognitive functions, such as perception, memory, attention, and consciousness. In addition, many cognitive dysfunctions such as schizophrenia, autism, anxiety and obsessive-compulsive disorders are related to neural synchronization [181].

Several synchronization regimes exist for intra- and inter-regional coordination of neural activity during cognition. One of the most-studied regimes is phase synchronization [179, 182]. It refers to the processes in which neurons oscillate with consistent relative phase angles at a common frequency. It is ubiquitously observed between spatially segregated cortical areas and it is thought to facilitate the integration of information across various regions in the brain including frontoparietal [183, 184, 185], frontotemporal [186, 187] and thalamocortical areas [188]. It is thought to serve various cognitive processes such as working memory [189, 183, 184, 185, 187, 186], memory retrieval [190], and selective attention [188]. Another dominant synchronization regime is cross-frequency phase-amplitude [191], which represents a process in which the amplitude of a high-frequency rhythm is modulated by the phase of a low-frequency rhythm. It is observed in or between various brain structures (temporal cortex, basal ganglia, medial-lateral prefrontal and frontoparietal areas). It is linked to numerous cognitive processes (selective attention, working memory, memory sequencing, abstract goal maintenance, and reward processing). For an overview of studies on synchronization, we refer the reader to Refs. [179, 181].

The cognitive processes do not involve the entire brain but rather arise from integrated processes of distributed but interconnected brain areas. So the association between interacting neurons and the neural network topologies is widely investigated [192, 193]. Although the extreme complexity of the brain (which consists of around 10^{11} neurons connected by around 10^{14} synapses) is daunting, efforts by a combination of computational neuroscience and experimental technology have made impressive progress. One can extract the network from electrophysiological recordings. Then, one can consider neural dynamics on the network nodes to represent cognitive activities. After that, one compare the network outputs with the measured data of

cognitive tasks to fit the model. Finally, one can use network dynamics to predict cognition and behaviors.

Brain networks can be derived from anatomical or physiological observations, resulting in structural and functional networks, respectively as we introduced in Chapter.I. The structural connectivity consist of anatomical connections linking a set of neural elements. It can be obtained by diffusion spectrum imaging (DSI). The structural connectivity is undirected and thought to be relatively stable. The brain network we introduced in Chapter.I is a structural network and exhibits various structural characteristics.

The node dynamics can be described by neuronal models at multiscales, from single neuronal models like the HH model, the FHN model, the LIF model to network models like firing rate model as we introduced in Chapter.I.

The researches have focused on structure-function relationships of brain networks, leading to a better understanding of how structural networks give rise to rich and flexible neural dynamics. In the following, we will introduce several partial synchronization mechanisms which are thought to be related to cognition based on the brain network.

9.2 Partial synchronization

Different from traditional synchronization, neuronal synchronization in brain networks involves only a subset of its total neurons due to the extreme complexity of the brain networks. It is in fact a partial synchronization [194]. Studies about partial synchronization can be classified into three classes which are chimera states, remote synchronization and cluster synchronization [195, 196]. They are depicted in Fig.9.1.

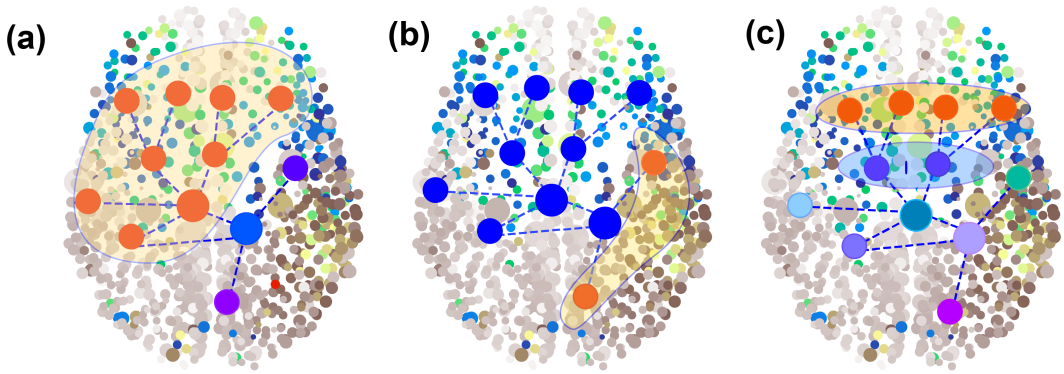

Figure 9.1: **Schematic illustration of partial synchronization.** The colors of nodes represent their dynamics. (a) Chimera state, nodes are divided into two parts, a coherent part (orange nodes in shadow area) and an incoherent part (nodes with different colors). (b) Remote synchronization, two orange nodes are synchronized while they are not directly connected. (c) Cluster synchronization, there are two clusters, the orange one and the blue one, where nodes in the same cluster are synchronized.

Chimera states (CS)

In Greek mythology, the *chimera* refers to a hybrid monster, which has the head of a lion, the body of a goat, and a tail of a dragon. Abrams and Strogatz [197] named *chimera state* the state of mixed synchronous and asynchronous behavior in a network of identical coupled oscillators. This is schematically represented in Fig.9.1(a) where the orange nodes are synchronized while the nodes with different colors are not. It was originally found by Kuramoto and Battogtokh [198]. Since then, an elaborate investigation of the existence, stability, and robustness of CS in a large variety of different systems are studied, such as chaotic systems [199, 200], high-dimensional systems [201, 202, 203, 204, 205], experimental systems [206, 207, 208, 209] and neural systems [210, 211, 212, 213]. A variety of coupling topologies have also been concerned when studying CS, such as globally coupled networks [209, 214, 215, 216, 217, 218], locally coupled networks [219, 220, 221, 222], complex networks [223, 224], and real brain networks [225, 226]. Recently, the involvement of the spatiotemporal dynamics has facilitated the new classifications of CS such as traveling chimera [227], chimera death [228] and multichimera [229]. There are many natural phenomena that show similarities with CS and may be linked to functional dynamics, such as the unihemispheric sleep found in mammals [230, 231] and even the first-night effect in human sleep [232]; ventricular fibrillation which is related to sudden cardiac death in humans exhibits spiral chimera states [233]; the possibility of synchronization in power distribution networks and social systems [203]. See Refs. [203, 6, 234] for a review of chimera states.

Remote synchronization (RS)

Remote synchronization [235] is characterized by the synchronization of pairs of nodes that are not directly connected via a physical link or any sequence of synchronized nodes, as shown in Fig.9.1(b). It has been experimentally observed among coupled analog electronic circuits [236, 237, 238]. RS is thought to be useful for information transfer. Recent studies have found that RS may lead to the emergence of cluster synchronization, global synchronization and more complex patterns [8, 239, 240, 241]. More recently, studies [242, 243] have shown remote propagation (where a signal is not successfully propagated to the neighbors of the source node but to its neighbors' neighbors) in neural networks.

According to the properties of oscillators in networks, homogeneous or inhomogeneous, the mechanisms for the appearance of RS can be considered in:

- RS in networks of homogeneous oscillators

Nicosia *et al.* [244] have found that RS can be observed in the network of homogeneous oscillators with symmetric topologies. Thus, symmetries of the network structure are fundamental for the emergence of this kind of remote synchronization. Gambuzza *et al.* [245] exploited symmetric topologies in designing strategies for the control of synchronization between groups of nodes in complex networks.

- RS in networks of inhomogeneous oscillators

RS was initially observed by Bergner *et al.* [235] in a star network of Stuart-Landau oscillators. The hub node is different from other leaf nodes due to parametric mismatch. The hub has a frequency set to 2.5, while the other leaf nodes have different but approximately the same

oscillation frequency around 1.0. This inhomogeneous parameter causes the hub node to synchronize leaf nodes but it is not entrained with them. Thus the hub node acts as a "transmitter". This star-like RS is not only confined to a star network but is also consistently observed in tree networks and complex networks with hubs [240, 238]. Sawicki *et al.* [246, 247] studied RS in multiplex networks, where a relay layer acts as a "transmitter".

Cluster synchronization

Cluster synchronization (see Fig.9.1(c)) denotes a network which can be decomposed into several clusters, in which the oscillators of the same cluster are synchronized to the same trajectory, but the oscillators of different clusters are not [8, 248, 249]. The appearance of cluster synchronization is related to the symmetries of network topology in complex networks. Recently, studies have shown that the emergence of cluster synchronization can be also found without symmetry when nodes receive the same total amounts of inputs from their neighboring nodes in different clusters [250]. Cluster synchronization has been experimentally demonstrated in a system of chaotic optoelectronic oscillators [251, 249].

These three kinds of partial synchronization are not completely independent of each other. For example, RS caused by the symmetric topology we introduced above can be considered as a particular case of cluster synchronization. Chimera state and cluster synchronization can be found simultaneously (Refs. [214, 252]), which have demonstrated that stable chimera states can emerge from two or more symmetry clusters (at least one stable and one unstable) that make up the entire fully symmetric network.

In the following, we will exploit chimera states and remote synchronization in the brain network to study the relationship between dynamics and structures.

10 Chimera states in the brain network

Previous studies of chimera states have mainly focused on phase oscillators. In recent years, many studies have drawn attention on neural systems. For example, Sakaguchi *et al.* [210] and Glaze *et al.* [211] investigated chimera states in coupled Hodgkin-Huxley neurons with different coupling topologies. Olmi *et al.* [253] studied chimera states on two symmetrically coupled populations of leaky integrate-and-fire neurons. Omelchenko *et al.* [254, 255] demonstrated that chimera states are robust with respect to perturbations of FitzHugh-Nagumo neurons. Hizanidis *et al.* [256] studied chimera states with Hindmarsh-Rose neuron models. Calim *et al.* [257] investigated the emergence of chimera states in nonlocal networks of Morris-Lecar neurons coupled via chemical synapses. Tian *et al.* [258] studied how electromagnetic induction influences the chimera states of neural networks with the time delay effects. Bansal *et al.* [225] and Huo *et al.* [229] used the neural mass models [62, 259, 260] to study the multi-scaled chimera state in brain networks.

In neural systems, Hizanidis *et al.* [261] studied chimera states on the modular neural network of C. elegans soil worm; Ramlow *et al.* [262, 263] analyzed the collective dynamics of FitzHugh-Nagumo neurons in an empirical structure, which was derived from diffusion-weighted magnetic resonance imaging with 90 cortical and subcortical regions (nodes); Bansal *et al.* [225] explored how large-scale brain architecture affects brain dynamics and functions by nine cognitive regions (obtained by stimulating 76 regions) with a neural mass model; Huo *et al.* [226] considered the diversity of dynamical patterns in the brain network with a case of adaptive coupling, and more recently, they studied chimera states with multiple spatial scales and revealed a positive correlation between the synchronization preference and the degree of symmetry of the connectivity of the region in the network [229]. They used a concept of effective symmetry to build the structural trees and dynamical hierarchical trees and found a close matching between them.

In the following, we consider FHN neurons on the brain network to study chimera states. We consider the brain network as a two-layered network with the left and right hemispheres of the cerebral cortex being different layers, respectively, and study how the properties of the network influence the dynamics of the network.

10.1 Introduction of the two-layered network model

Two-layered network structure

The brain network that we used consists of 998 nodes and 17865 links. Further analysis has shown that there are 9 isolated nodes that we are not interested in, so we removed them and there are 989 remaining nodes. In a macroscopic view, the brain network can be considered as the right and left hemispheres connected by the corpus callosum. In our network, the right hemispheric subnetwork has 496 nodes (from $i = 1$ to 496) with 8037 links between them, the average degree is $\langle k \rangle \approx 32.4$; the left hemispheric subnetwork has 493 nodes (from $i = 497$ to

989) with 7773 links between them, the average degree is $\langle k \rangle \approx 31.5$, and there are 2055 interconnecting links between these two hemispheres. The connection matrix of this brain network is shown in Fig.10.1(b). The clustering coefficients of the right and left hemispheres are 0.46 and 0.47, respectively. (see Fig.10.1(c, d)).

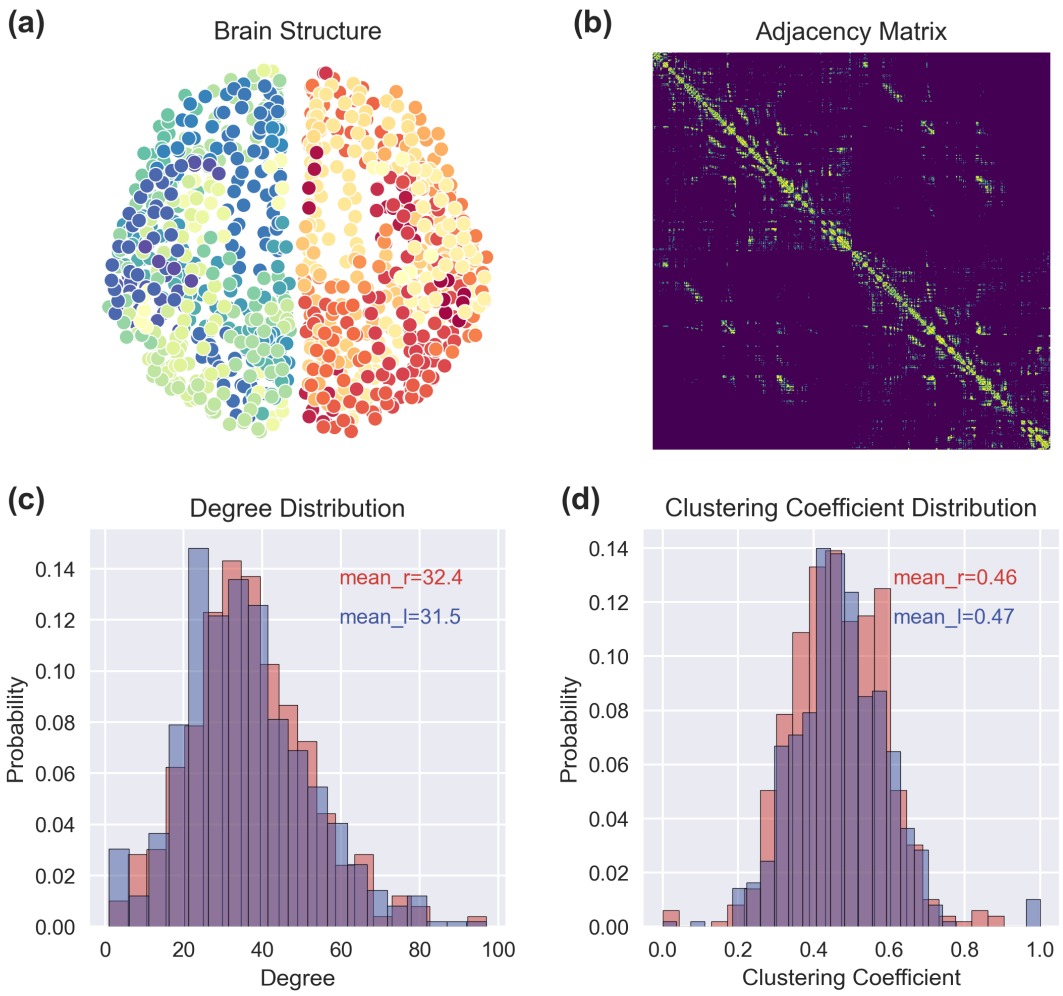

Figure 10.1: **Two-layered cerebral cortex network.** (a) 989 nodes distribute on the right and left hemispheres of the cerebral cortex network (496 nodes for the right hemisphere, 493 for the left hemisphere). (b) Connection matrix of the cerebral cortex network. (c) Degree distribution of the right (red) and left (blue) hemispheres of the cerebral cortex network, the average degree of the right and left hemispheres are 32.4, and 31.5, respectively. (d) Clustering coefficient distribution of the right (red) and left (blue)hemispheres of the cerebral cortex network, the average clustering coefficient of the right and left hemispheres are 0.46, and 0.47, respectively.

For simplicity and intuitiveness of the explanation, we use a schematic network to represent our real two-layered brain network as shown in Fig.10.8 where the lines stand for the couplings. We use real lines (l_{in}) and dotted lines (l_{out}) to distinguish the intra- and inter-couplings, the same name convention is used for the coupling strength λ_{in} and λ_{out}.

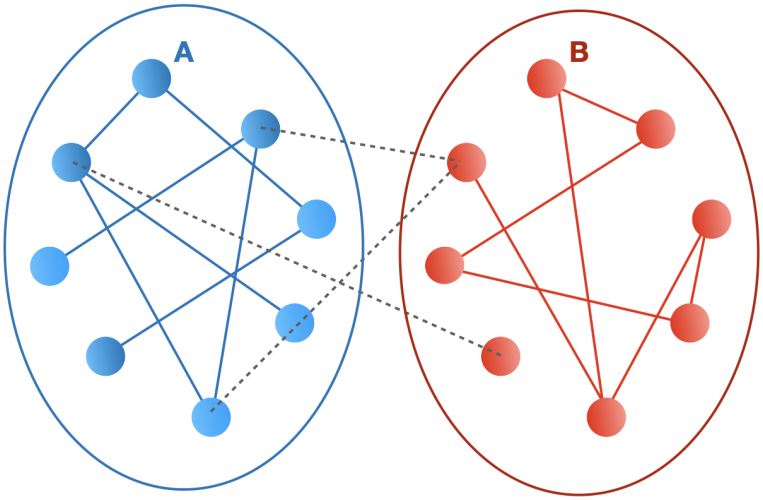

Figure 10.2: **Schematic figure of the two-layered brain network model.** Where A and B represent the two hemispheres, respectively, "circles" denote the nodes or neurons, and the real lines and the dotted lines represent the intra- and inter-couplings, respectively.

General dynamical description of the network

As we previously introduced, the communication within neurons mainly proceeds through two ways, one is through chemical synapses (which are slower) and the other one is through electrical synapses (which are faster). In most neural systems, these two types of synapses can be present independently or simultaneously. In the human brain, the communication between the left and right hemispheres has to go through the long corpus callosum and thus causes some time delays due to the limited speed of signal transmission and processing. Thus, we consider two different situations, one is a simple situation in which both synapses are effectively represented as electrical synapses; the other is a mixed situation in which the intra-connections are represented as electrical synapses while the longer inter-connections are represented as chemical synapses.

We use the FHN neurons to represent the behavior of each node in the network, for subnetworks A, B

- Network with electrical synapses

$$
\begin{aligned}
\epsilon\dot{u}_i^a &= u_i^a - \frac{(u_i^a)^3}{3} - v_i^a + \frac{\lambda_{in}}{k_{in,i}^a}\sum_{j=1}^{N} A_{ij}[d_{uu}(u_j^a - u_i^a) + d_{uv}(v_j^a - v_i^a)] \\
&+ \frac{\lambda_{out}}{k_{out,i}^a}\sum_{j=1}^{N}(AB)_{ij}[d_{uu}(u_j^b - u_i^a) + d_{uv}(v_j^b - v_i^a)], \\
\dot{v}_i^a &= u_i^a + a + \frac{\lambda_{in}}{k_{in,i}^a}\sum_{j=1}^{N} A_{ij}[d_{vu}(u_j^a - u_i^a) + d_{vv}(v_j^a - v_i^a)] \\
&+ \frac{\lambda_{out}}{k_{out,i}^a}\sum_{j=1}^{N}(AB)_{ij}[d_{vu}(u_j^b - u_i^a) + d_{vv}(v_j^b - v_i^a)],
\end{aligned}
$$

$$
\begin{aligned}
\epsilon\dot{u}_i^b &= u_i^b - \frac{(u_i^b)^3}{3} - v_i^b + \frac{\lambda_{in}}{k_{in,i}^b}\sum_{j=1}^{N} B_{ij}[d_{uu}(u_j^b - u_i^b) + d_{uv}(v_j^b - v_i^b)] \\
&+ \frac{\lambda_{out}}{k_{out,i}^b}\sum_{j=1}^{N}(AB)_{ij}[d_{uu}(u_j^a - u_i^b) + d_{uv}(v_j^a - v_i^b)], \\
\dot{v}_i^b &= u_i^b + a + \frac{\lambda_{in}}{k_{in,i}^b}\sum_{j=1}^{N} B_{ij}[d_{vu}(u_j^b - u_i^b) + d_{vv}(v_j^b - v_i^b)] \\
&+ \frac{\lambda_{out}}{k_{out,i}^b}\sum_{j=1}^{N}(AB)_{ij}[d_{vu}(u_j^a - u_i^b) + d_{vv}(v_j^a - v_i^b)].
\end{aligned} \tag{10.1}
$$

where $i = 1, 2, \cdots, N_a(N_b)$ is the index of the node, u_i^a (u_i^b) and v_i^a (v_i^b) represent the activator and inhibitor variables of FHN neurons, respectively. $k_{in,i}^a$ ($k_{in,i}^b$) and $k_{out,i}^a$ ($k_{out,i}^b$) are the intra- and inter-degrees of nodes i, respectively. A_{ij} (B_{ij}) and $(AB)_{ij}$ denote the intra- and inter-coupling matrices, respectively. ϵ is a small parameter characterizing the separation of slow and fast time scales and is fixed as $\epsilon = 0.05$. a is the excitable parameter, when $|a| > 1$, the neuron is in the excitable state; when $|a| < 1$, the neuron is in the oscillatory state [254, 212, 264]. Here we are interested in the oscillatory state, so we fix $a = 0.5$.

The relative coupling strength is represented by the rotational coupling matrix D, which takes into account both direct- and cross-couplings between u and v [254, 256, 212],

$$
D = \begin{pmatrix} d_{uu} & d_{uv} \\ d_{vu} & d_{vv} \end{pmatrix} = \begin{pmatrix} \cos\alpha & \sin\alpha \\ -\sin\alpha & \cos\alpha \end{pmatrix} \tag{10.2}
$$

where α is the coupling phase that represents the relative phase difference of interacting nodes.

- Network with electrical and chemical synapses

$$\begin{aligned}
\epsilon\dot{u}_i^a &= u_i^a - \frac{(u_i^a)^3}{3} - v_i^a + \frac{\lambda_{in}}{k_{in,i}^a}\sum_{j=1}^{N} A_{ij}[d_{uu}(u_j^a - u_i^a) + d_{uv}(v_j^a - v_i^a)] \\
&\quad + \frac{\lambda_{out}}{k_{out,i}^a}\sum_{j=1}^{N}(AB)_{ij}g_j(u_{th} - u_j^b), \\
\dot{v}_i^a &= u_i^a + a + \frac{\lambda_{in}}{k_{in,i}^a}\sum_{j=1}^{N} A_{ij}[d_{vu}(u_j^a - u_i^a) + d_{vv}(v_j^a - v_i^a)], \\
\epsilon\dot{u}_i^b &= u_i^b - \frac{(u_i^b)^3}{3} - v_i^b + \frac{\lambda_{in}}{k_{in,i}^b}\sum_{j=1}^{N} B_{ij}[d_{uu}(u_j^b - u_i^b) + d_{uv}(v_j^b - v_i^b)] \\
&\quad + \frac{\lambda_{out}}{k_{out,i}^b}\sum_{j=1}^{N}(AB)_{ij}g_j(u_{th} - u_j^a), \\
\dot{v}_i^b &= u_i^b + a + \frac{\lambda_{in}}{k_{in,i}^b}\sum_{j=1}^{N} B_{ij}[d_{vu}(u_j^b - u_i^b) + d_{vv}(v_j^b - v_i^b)].
\end{aligned} \tag{10.3}$$

with

$$g_j = g_{max}[\exp^{-(t-t_j^s-\tau)/\tau_d} - \exp^{-(t-t_j^s-\tau)/\tau_r}] \tag{10.4}$$

where g_{max} describes the maximal synaptic conductance between neurons, u_{th} denotes the synaptic reversal potential, τ is the time delay between connected neurons, t_j^s represents the synaptic spiking, τ_d and τ_r stand for the decay and rise time of the function and determine the duration of the response. We here take the parameters $g_{max} = 0.35$, $u_{th} = 0$, $\tau_d = 10$, and $\tau_r = 1$.

10.2 The measurement of chimera states

In order to clearly distinguish between coherent and incoherent parts, we introduce the average phase velocity as defined in Ref. [136],

$$\omega_i^a(\omega_i^b) = \frac{2\pi M_i}{\Delta T} \quad i = 1, 2, \cdots, N_a(N_b) \tag{10.5}$$

where ΔT is the time interval window used to measure the average phase speed of nodes when the system has evolved into a steady state. M_i is the measured firing number of node i during this time window, ΔT should be sufficiently large to contain enough firings M_i.

Several methods have been developed to measure chimera states. The most popular one is

by introducing the order parameter,

$$r(t)e^{i\Phi(t)} = \frac{1}{N}\sum_{j=1}^{N} e^{i\theta_j(t)} \tag{10.6}$$

where $r(t)$ represents the phase coherence of oscillators at time t. $\Phi(t)$ is the average phase of all oscillators. θ_j is the phase of the oscillator j. The network is completely synchronized when $r = 1$, disordered state when $r = 0$. For the network with two groups, if for one group $r \approx 1$ while for the other one $r \approx 0$, the network is in a chimera state.

Recently, Kemeth *et al.* [265] developed a more general way to distinguish chimera states. They extended the method to any type of dynamical system, not just limited to ensembles of phase oscillators as the order parameter did. They used the local curvature as a measurement for spatial coherence. For one dimensioned system, the local curvature of the observation is quantified by the second derivative, or more generally by the *Laplacian* $\mathbf{D}$ for any number of spatial dimensions,

$$\hat{\mathbf{D}}f = \Delta x^2 \mathbf{D}f = f(x + \Delta x, t) - 2f(x, t) + f(x - \Delta x, t) \tag{10.7}$$

where f represents the spatial data on a snapshot at time t. For a synchronous system, $|\hat{\mathbf{D}}| = 0$, while finite $|\hat{\mathbf{D}}|$ means that the system is asynchronous with fluctuations. In order to measure the relative size of spatially coherent regions, Kemeth *et al.* [265]considered the normalized probability density function g of $|\hat{\mathbf{D}}|$. For a fully synchronized system $g(|\hat{\mathbf{D}}| = 0) = 1$, while a totally unsynchronized system gives a value $g(|\hat{\mathbf{D}}| = 0) = 0$. A value between 0 and 1 of $g(|\hat{\mathbf{D}}| = 0)$ indicates the coexistence of coherence and incoherence and denotes a chimera state.

For a complex network, Kemeth *et al.* [265] took a threshold $\delta = 0.01D_m$ to neglect minor changes, which will not influence the qualitative outcome. D_m indicates the maximal value of $|\hat{\mathbf{D}}|$. The correlation measurement reads,

$$g_0(t) = \int_0^{\delta} g(t, |\hat{D}|)d(|\hat{D}|) \tag{10.8}$$

We use the average value $g_1 = \langle g_0(t)\rangle_t$ over a stable period to measure the synchronization of the system:

$$g_1 = \begin{cases} 0 & \text{unsynchronized state} \\ (0,1) & \text{chimera state} \\ 1 & \text{synchronized state} \end{cases} \tag{10.9}$$

10.3 Chimera states on the two-layered brain network

Can we find chimera states in this two-layered brain network model? If so, what requirements about the couplings should be satisfied for the emergence of chimera states? In order to answer these questions, in the following, we study how the coupling strengths, which are characterized

by parameters α, λ_{in}, λ_{out}, influence the dynamical behaviors of the network.

Different states on the two-layered brain network

Simulations showed that the brain network exhibits various dynamics when parameters are varied both with electrical synapses alone or with mixed electrical and chemical synapses. They can be divided into four typical states according to the dynamics of each hemisphere as shown in Fig.10.3 (Here, we just show the example of the network with electrical synapses, similar result hold for the mixed synapses network). The up row and down row represent the right hemisphere and the left hemisphere about the average phase speeds w_i at time t, respectively. The insets are the corresponding dynamics of u_i at the moment t.

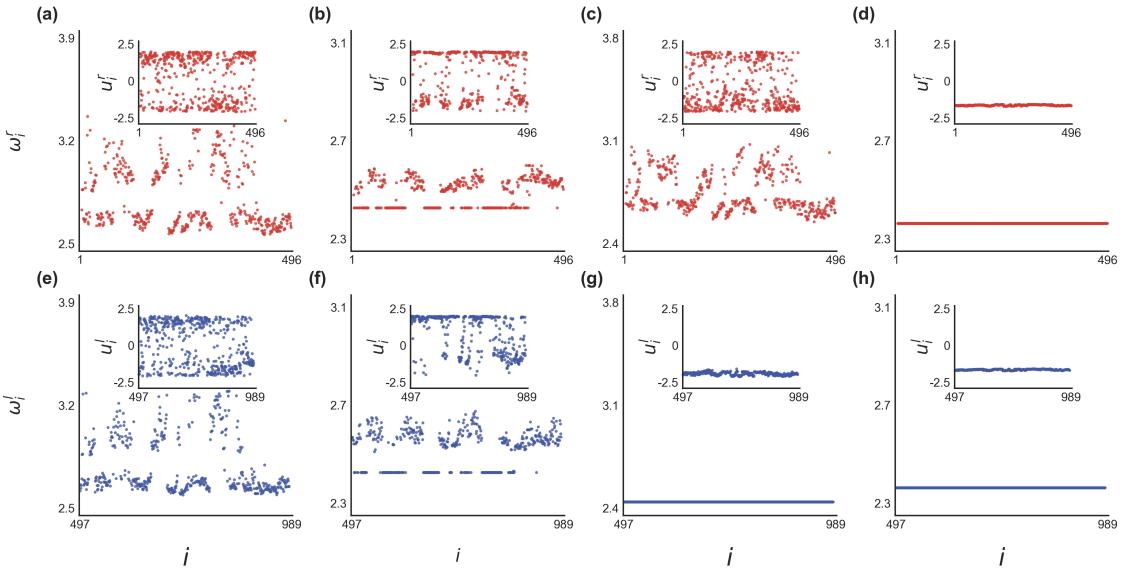

Figure 10.3: **Four typical states in the two-layered brain network.** The up and down panels represent the right and left hemispheres, respectively. The panels show the average phase speed w_i, and the insets are their corresponding dynamics of u_i at the moment t. (a, e) Unsynchronized state, with $g_1^r \approx 0$, $g_1^l \approx 0$. (b, f) Chimera state, with $g_1^r = 0.33$, $g_1^l = 0.32$. (c, g) Unihemispheric sleep-like state, with $g_1^r \approx 0$, $g_1^l \approx 1$. (d, h) Synchronized state, with $g_1^r \approx 1$, $g_1^l \approx 1$. The parameters for different states are given in Table.10.1.

Parameters			
Symbol / State	α	λ_{in}	λ_{out}
Synchronized state	$\frac{\pi}{2} - 0.1$	0.1	0.3
Chimera state	$\frac{\pi}{2} - 0.1$	0.1	1.8
Unihemispheric sleep-like state	$\frac{\pi}{2} - 0.1$	0.4	3.5
Unsynchronized state	$\frac{\pi}{2} - 0.1$	4.0	3.5

Table 10.1: **Parameters for four typical states on two-layered brain network**

For the first situation (Fig.10.3(a, e)), both ω_i^r and ω_i^l are randomly distributed, which means that both the right and left hemispheres are in an incoherent state, with $g_1^r \approx 0$, $g_1^l \approx 0$. We call this case an unsynchronized state. Different from the previous situation, a subset of oscillators

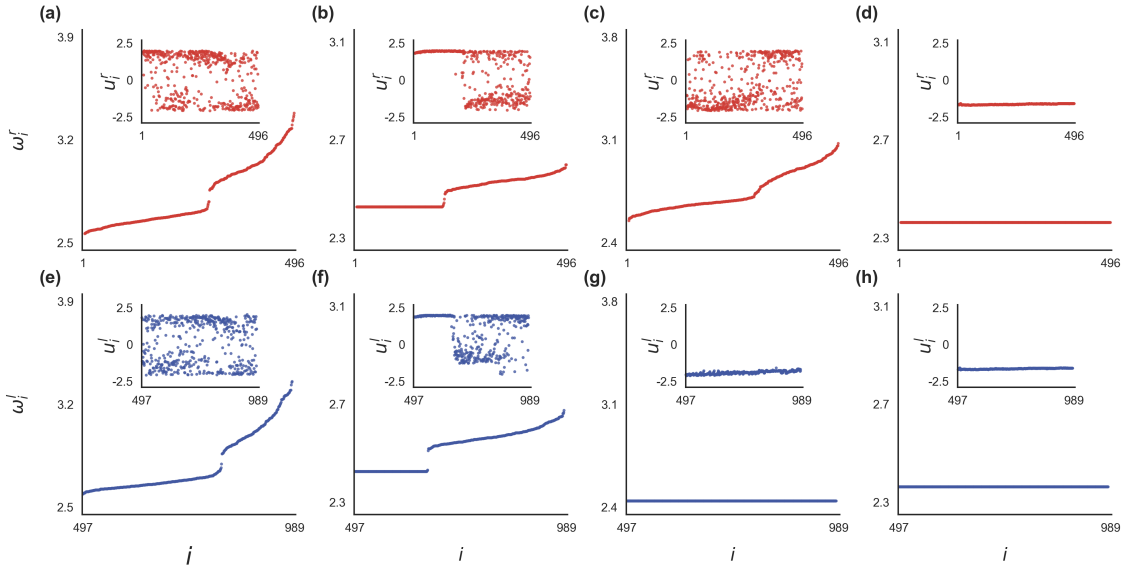

Figure 10.4: **Same figure as Fig.10.3 but with rearranging the nodes by their average phase velocities.**

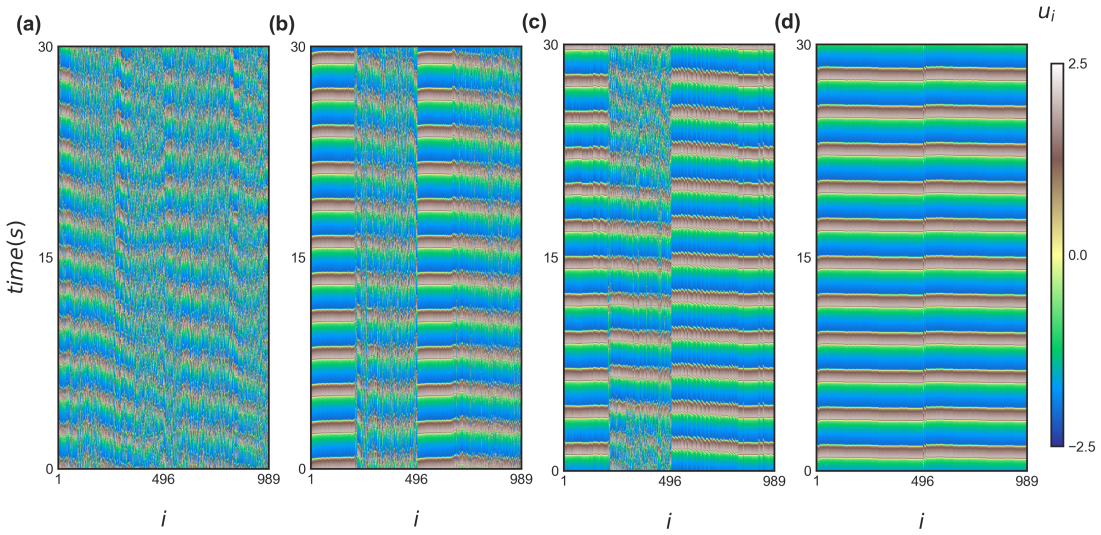

Figure 10.5: **The evolution of the u_i over time represents four typical states (corresponding to Fig.10.4).**

with exactly the same values of ω_i^r and ω_i^l are found in both hemispheres (Fig.10.3(b, f)), which means that parts of the nodes are synchronized while others are out of synchronization, so they are both in chimera states ($g_1^r = 0.33$, $g_1^l = 0.32$). A surprising result is shown in Fig.10.3(c, g), where the right hemisphere is an incoherent state with randomly distributed ω_i^r while the left hemisphere is in a totally coherent state with the same ω_i^l. This is similar to the *unihemispheric sleep* introduced before. We call it a unihemispheric sleep-like state with $g_1^r \approx 0$, $g_1^l \approx 1$. For convenience, the chimera state and the unihemispheric sleep-like state are called partially synchronized state. In Fig.10.3(d, h), both hemispheres are totally synchronized and we call this case a synchronized state ($g_1^r \approx 1$, $g_1^l \approx 1$).

When considering complex networks, it is hard to define space. Inspired by the previous work [223], we rearrange the nodes by the ascending order of ω_i, such that $i \geq j$ if $\omega_i \geq \omega_j$. Fig.10.4 shows the results corresponding to Fig.10.3, but with rearranging the order of nodes. It is significantly simpler to distinguish the characteristics of the different states. Therefore, we favor the use of the rearranged states in the following.

Fig.10.5 show the evolution of the u_i over time for different states shown in Fig.10.4.

By further comparison, we have found that in our simulation, the coupling strengths λ_{in}, λ_{out} are quite different for these four typical states. For the unsynchronized state (Fig.10.4(a, e)), $\lambda_{in} = 0.1$, $\lambda_{out} = 0.3$; the synchronized state (Fig.10.4(d, h)) has quite strong coupling strengths ($\lambda_{in} = 4.0$, $\lambda_{out} = 3.5$) when compared with the unsynchronized state; the coupling strengths for the chimera state (Fig.10.4(b, f)) are $\lambda_{in} = 0.1$, $\lambda_{out} = 1.8$, and are in an intermediate state; while, a dramatic increase of the λ_{out} accounts for the appearance of the unihemispheric sleep-like state (Fig.10.4(c, g)), with $\lambda_{in} = 0.4$, $\lambda_{out} = 3.5$.

We use λ_{in} and λ_{out} to stand for the intra- and inter-couplings within or between the right and left hemispheres. The different strengths may reflect some neurophysiological communication information. Firstly, the unsynchronized state with both weak λ_{in} and λ_{out} coupling strengths may indicate the absence of active brain functions. A typical situation corresponding to this state is the resting state of brain with random behaviors. Secondly, for chimera states with weak λ_{in} and relatively strong λ_{out}, the relatively strong λ_{out} may imply some communications between the two hemispheres of cerebral cortex, indicating that a normal functional state involves an ensemble of neurons distributed across different brain regions. Thirdly, relatively strong λ_{in} but very strong λ_{out} of the unihemispheric sleep-like state are beyond the couplings for a normal brain functional state. This may be launched by vigilance and thus is consistent with the first-night effect in human. Finally, the synchronized state with both very strong λ_{in} and λ_{out} represents an abnormal synchronization, which is well known for epileptic seizures.

In summary, the coupling strengths have an obvious influence on the states of the brain network. When the coupling strength parameters α, λ_{in} and λ_{out} are matched, the normal brain function state, chimera states may occur. In the following, we will study how the dynamics of the brain network depend on the coupling strengths.

The impact of the coupling strengths

There are three characteristic parameters related to the coupling strengths, the coupling phase α, the intra-coupling λ_{in} and the inter-coupling λ_{out}. We use g_1 (Eq.10.9) to stand for the

state of the network. Fig.10.6 show the phase diagrams of g_1 for the right (up) and left (down) hemispheres with electrical synapses, respectively. Fig.10.6(a, c), represent the values of g_1 in the parameter plane of λ_{in} and λ_{out} for fixed $\alpha = \pi/2 - 0.1$. One can see that the increase of λ_{in}, λ_{out} makes the network more coherent. Fig.10.6(b, d) shows how the network state changes with λ_{out} and α when fixed $\lambda_{in} = 3.0$. The network state is sensitive to the parameters so that the unsynchronized state, partially synchronized state and synchronized state are distributed in the phase diagram.

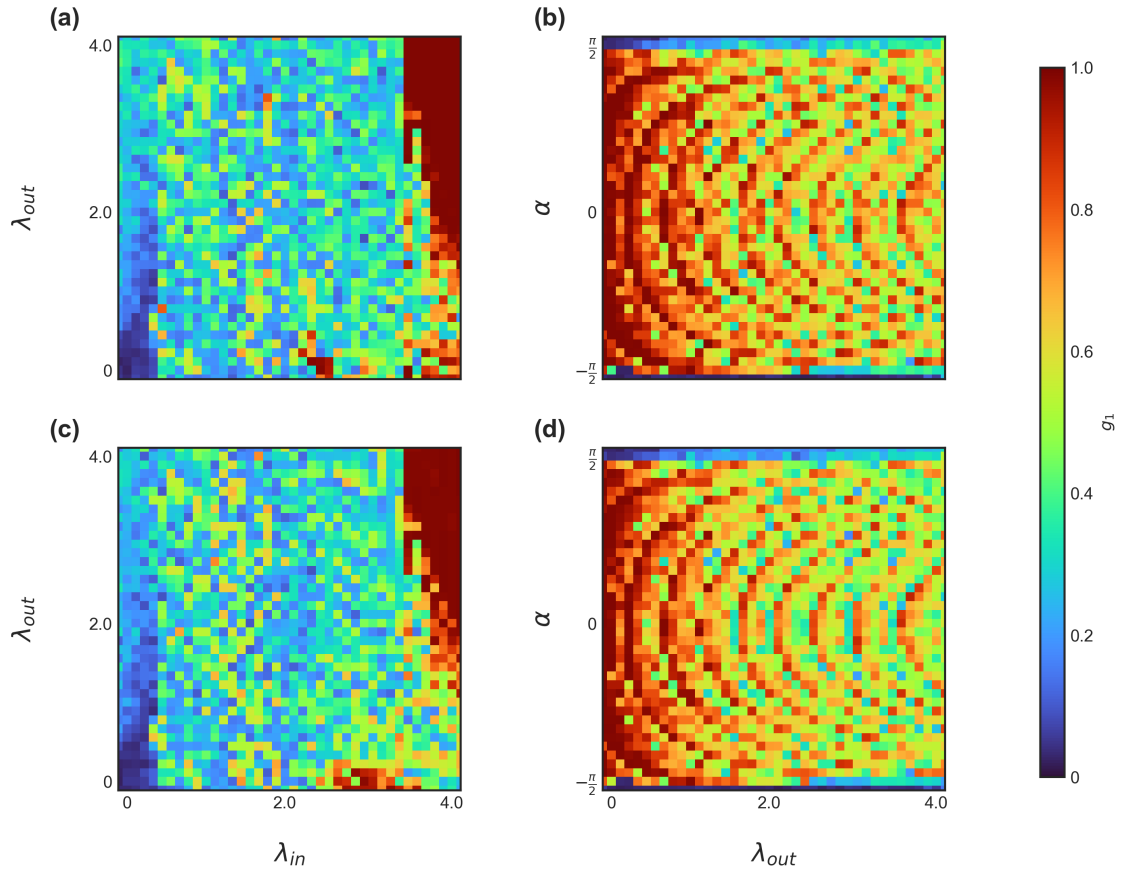

Figure 10.6: **Phase diagram of g_1 for the two-layered brain network with electric inter-coupling.** The up panels are for the right hemisphere and the down panels are for the left hemisphere. (a, c) The phase diagram of g_1 in the parameter plane of λ_{in} and λ_{out} for $\alpha = \pi/2 - 0.1$. (b, d) The phase diagram of g_1 in the parameter plane of λ_{out} and α for a fixed $\lambda_{in} = 3.0$.

Fig.10.7 shows the corresponding results when the inter-couplings are described by chemical synapses with $\tau = 0$ for the two-layered brain network. Comparing with the corresponding situation with electrical synapses only (Fig.10.6), one finds that the areas of synchronization (the red parts) in Fig.10.6 disappear. Instead, one sees more partial synchronized states, indicating that the chemical inter-coupling destroys the global synchronization. This is reasonable as a healthy person should not show the behavior of epileptic seizure characterized by global synchronization.

In sum, the real brain network has a special topology of community structure selected by

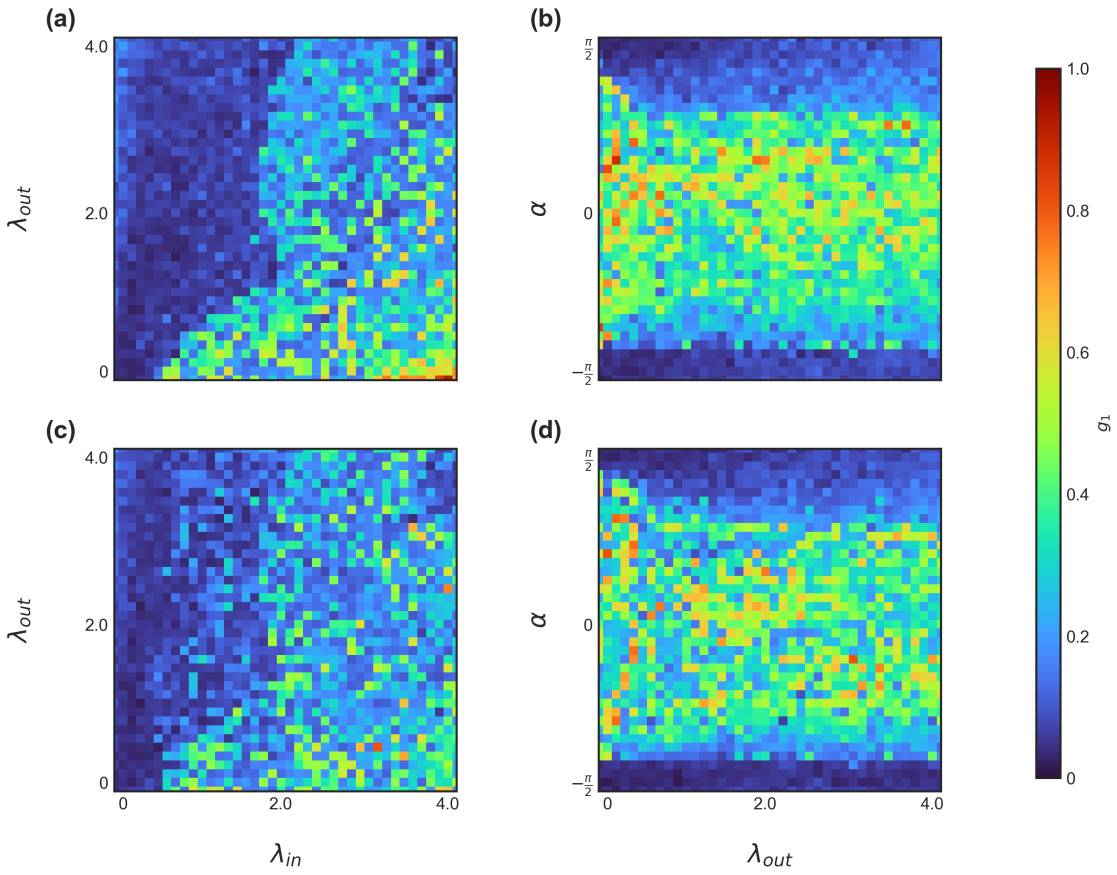

Figure 10.7: **Phase diagram of g_1 for the two-layered brain network with chemical inter-coupling.** The up panels are for the right hemisphere and the down panels are for the left hemisphere. (a, c) The phase diagram of g_1 in the parameter plane of λ_{in} and λ_{out} for $\alpha = \pi/2 - 0.1$. (b, d) The phase diagram of g_1 in the parameter plane of λ_{out} and α for fixed $\lambda_{in} = 3.0$.

nature. This structure is favorable to the diversity of brain dynamics.

10.4 Analysis of chimera states on general two-layered network

While the network of Fig.10.1 corresponds to a specific brain network, it is useful to consider a more general situation. For this purpose, we keep the characteristic features of Fig.10.1 but allow the key parameters such as the size N, the coupling strengths λ_{in} and λ_{out}, and the number of inter-coupling links l_{out} to vary and study how they shape the collective behavior of the network.

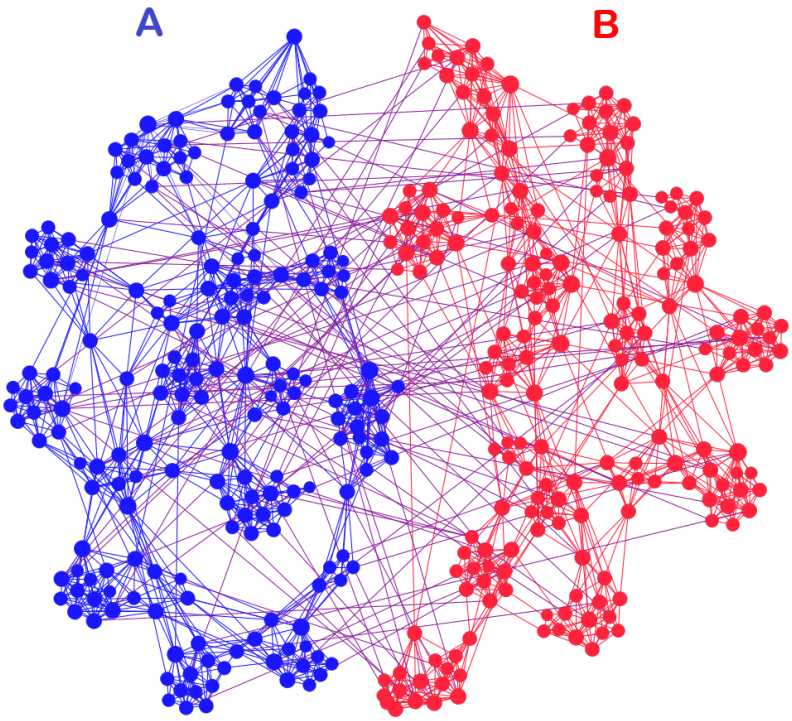

Figure 10.8: **A general model of brain network with size $N = 200$, average degree $\langle k \rangle = 10$, and clustering coefficient $C = 0.5$ in each subnetwork.** This is rewired from a random network by the algorithm of the rewiring approach introduced in Ref. [266].

As we introduced in Chapter.I, the brain network has a small-world property that is characterized by a high local clustering coefficient and a short path length between any (distant) pair of nodes due to the existence of relatively few long-range connections. This modular organization can support both segregated/specialized and distributed/integrated information processing. In this sense, a general model of brain network has to be a modular network, represented by a large clustering coefficient C. We here use the algorithm of the rewiring approach to generate this modular network from a random network [266]. In detail, we first start from two random subnetworks with size $N = 200$, average degree $\langle k \rangle = 10$, with a total network size $2N = 400$. We gradually increase the clustering coefficients C of the subnetworks to a larger value. Then, we

randomly add links between the two subnetworks A and B until the number of inter-connected links reaches l_{out}. Fig.10.8 shows the obtained network with $C = 0.5$, $l_{out} = 300$ which will be considered as the general model of brain network.

The general two-layered network show the diversity of dynamical behaviors (the unsynchronized state, chimera state, unihemispheric sleep-like state and synchronized state) that we found in the brain network as shown in Fig.10.9.

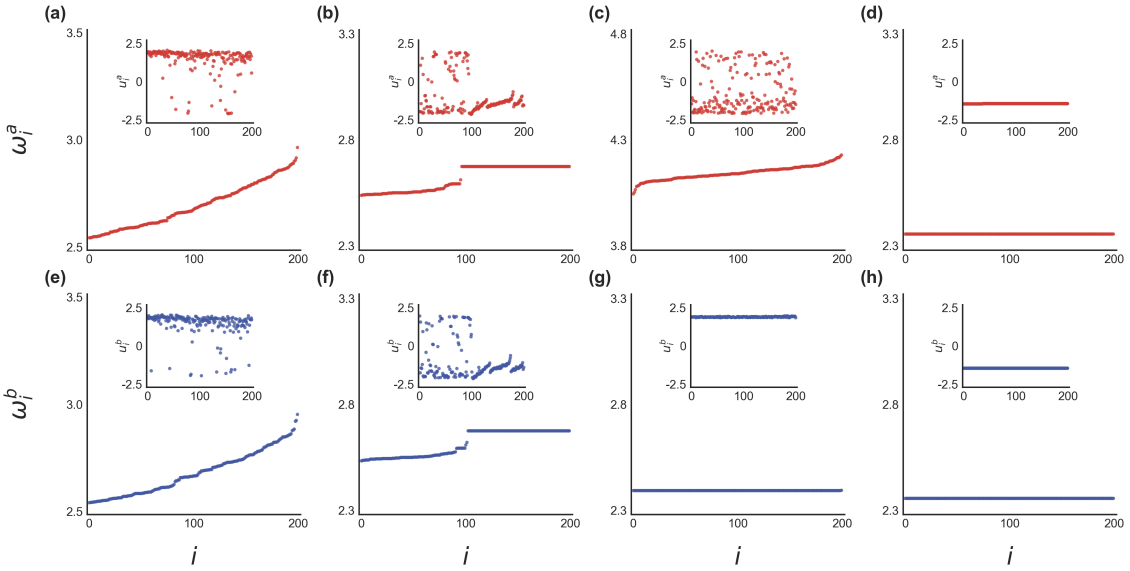

Figure 10.9: **Four typical states in the general two-layered network.** The up and down panels represent the subnetworks A and B, respectively. The panels show the average phase speed w_i, and the insets are their corresponding dynamics of u_i at the moment t. (a, e) Unsynchronized state. (b, f) Chimera state. (c, g) Unihemispheric sleep-like state. (d, h) Synchronized state. The parameters for different states are given in Table.10.2.

Parameters			
Symbol / State	α	λ_{in}	λ_{out}
Synchronized state	$\frac{\pi}{2} - 0.1$	0.2	0.5
Chimera state	$\frac{\pi}{2} - 0.1$	0.5	1.8
Unihemispheric sleep-like state	$\frac{\pi}{2} - 0.1$	0.5	2.5
Unsynchronized state	$\frac{\pi}{2} - 0.1$	1.0	3.0

Table 10.2: **Parameters for four typical states on the general two-layered network**

In the same way as we analyzed the brain network, we also study how the key parameters α, λ_{in}, λ_{out} and l_{out} influence the dynamics of this general network. Fig.10.10 show the phase diagram of g_1 for the general two-layered network with electrical connections.

From Fig.10.10(a, d), one sees that when the intra-coupling strength λ_{in} is small (around < 0.5) the number of inter-coupling links do not take effect. For larger λ_{in}, the increases of the

l_{out} makes the network more synchronized. Fig.10.10(b, e) show the phase diagram of g_1 with the function of λ_{in} and λ_{out} for fixed $\alpha = \pi/2 - 0.1$ and $l_{out} = 100$, one can see that λ_{out} has a similar effect as l_{out}. Fig.10.10(c, f) show the phase diagram of g_1 with the function of λ_{out} and α for fixed $\lambda_{in} = 0.6$ and $l_{out} = 100$, one can see that the network is sensitive to the change of α, and obvious arc-shapes bounder lines for the synchronized state can be observed.

Fig.10.11 shows g_1 for the same parameter panels of as those of Fig.10.10 but with chemical inter-connections. We can see that the involvement of the chemical connections broadens the partially synchronized state which is consistent with the brain network.

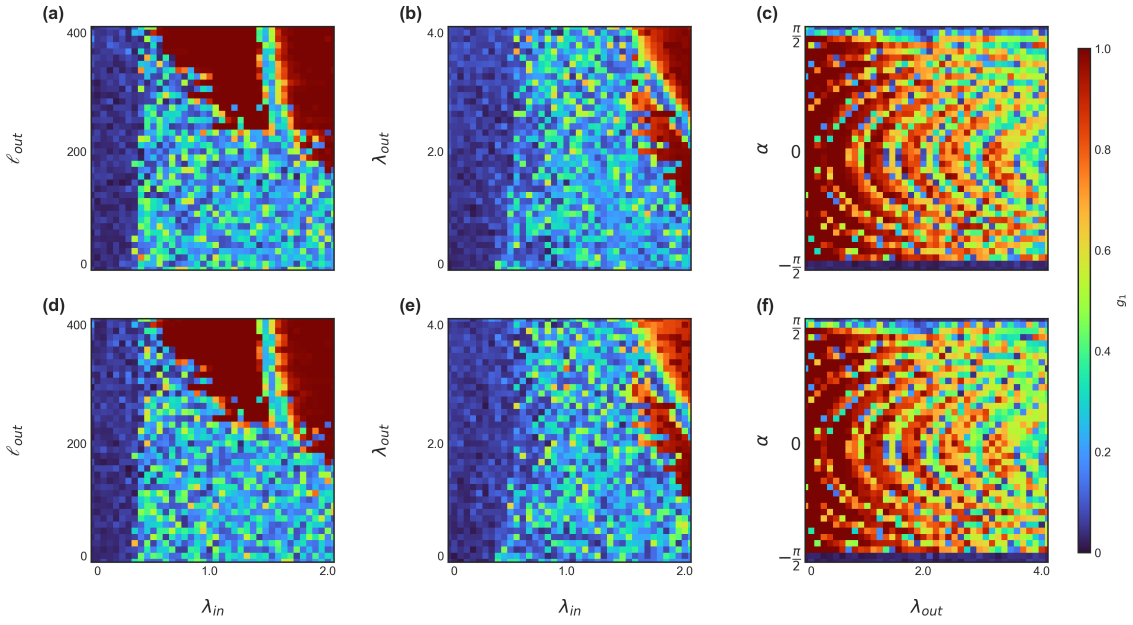

Figure 10.10: **Phase diagram of g_1 for the general two-layered network with electric inter-coupling.** The up panels are for the subnetwork A, and the down panels are for the subnetwork B. (a, d) The phase diagram of g_1 in the parameter plane of λ_{in} and l_{out} for $\alpha = \pi/2 - 0.1$ and $\lambda_{out} = 0.5$. (b, e) The phase diagram of g_1 in the parameter plane of λ_{in} and λ_{out} for fixed $\alpha = \pi/2 - 0.1$ and $l_{out} = 100$. (c, f) The phase diagram of g_1 in the parameter plane of λ_{out} and α for fixed $\lambda_{in} = 0.6$ and $l_{out} = 100$.

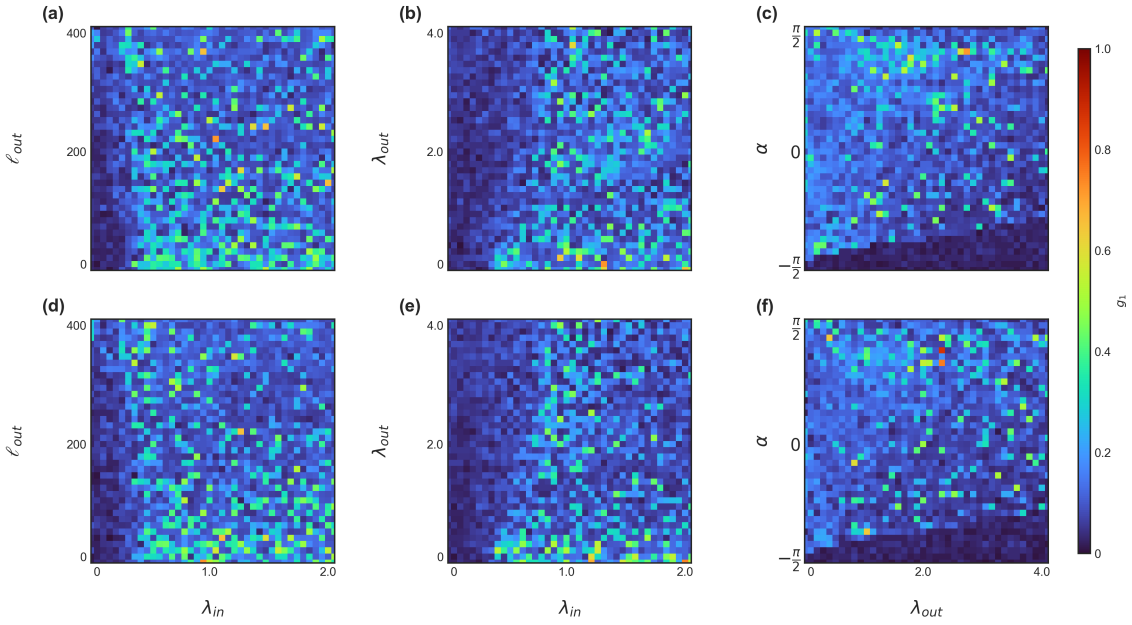

Figure 10.11: **Phase diagram of g_1 for the general two-layered network with chemical inter-coupling.** The up panels are for the subnetwork A, and the down panels are for the subnetwork B. (a, d) The phase diagram of g_1 in the parameter plane of λ_{in} and l_{out} for $\alpha = \pi/2 - 0.1$ and $\lambda_{out} = 0.5$. (b, e) The phase diagram of g_1 in the parameter plane of λ_{in} and λ_{out} for fixed $\alpha = \pi/2 - 0.1$ and $l_{out} = 100$. (c, f) The phase diagram of g_1 in the parameter plane of λ_{out} and α for fixed $\lambda_{in} = 0.6$ and $l_{out} = 100$.

The robustness of network size

Considering that the real cerebral cortex network that is modeled here (Fig.10.1) has a network size much larger than $N = 200$, it is necessary to discuss the robustness with variation of the size N in the general model of the human brain network. For this purpose, we here consider a case with $N = 1000$, average degree $\langle k \rangle = 50$, and $C = 0.5$. Fig.10.12 and Fig.10.13 show the phase diagram of g_1 for electrical inter-connections and chemical inter-connections, respectively. Comparing the corresponding panels of Fig.10.10, Fig.10.11 with $N = 200$ and of Fig.10.12, Fig.10.13 with $N = 1000$, respectively, we see that they are qualitatively similar to each other, confirming that the collective behaviors are robust to a change on network size.

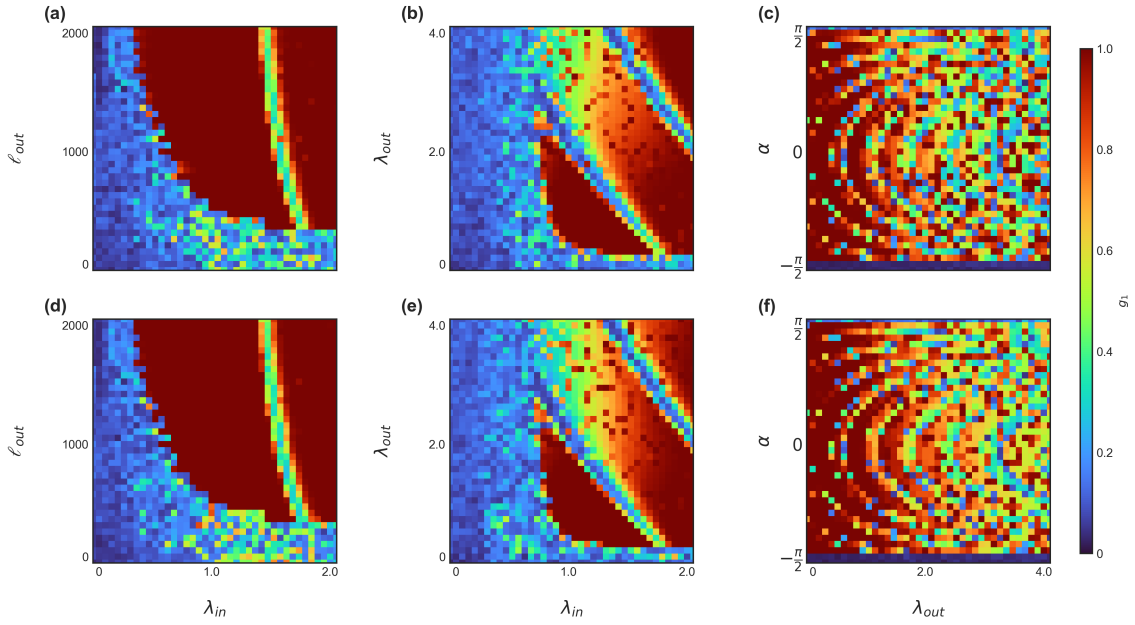

Figure 10.12: **Phase diagram of g_1 for the general two-layered network ($N = 1000$) with electric inter-coupling.** The up panels are for the subnetwork A, and the down panels are for the subnetwork B. (a, d) The phase diagram of g_1 in the parameter plane of λ_{in} and l_{out} for $\alpha = \pi/2 - 0.1$ and $\lambda_{out} = 0.5$. (b, e) The phase diagram of g_1 in the parameter plane of λ_{in} and λ_{out} for fixed $\alpha = \pi/2 - 0.1$ and $l_{out} = 500$. (c, f) The phase diagram of g_1 in the parameter plane of λ_{out} and α for fixed $\lambda_{in} = 0.8$ and $l_{out} = 500$.

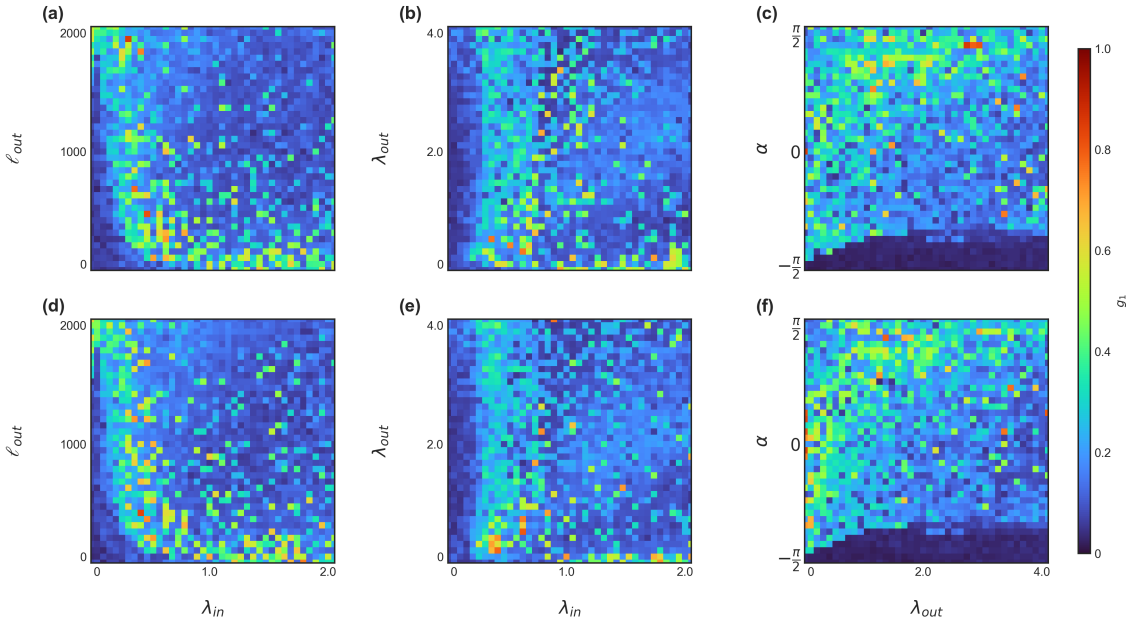

Figure 10.13: **Phase diagram of g_1 for the general two-layered network ($N = 1000$) with chemical inter-coupling.** The up panels are for the subnetwork A, and the down panels are for the subnetwork B. (a, d) The phase diagram of g_1 in the parameter plane of λ_{in} and l_{out} for $\alpha = \pi/2 - 0.1$ and $\lambda_{out} = 0.5$. (b, e) The phase diagram of g_1 in the parameter plane of λ_{in} and λ_{out} for fixed $\alpha = \pi/2 - 0.1$ and $l_{out} = 500$. (c, f) The phase diagram of g_1 in the parameter plane of λ_{out} and α for fixed $\lambda_{in} = 0.8$ and $l_{out} = 500$.

A brief explanation for the arc-shape borderline of synchronization

In the phase diagram of g_1 with λ_{out} and α in Fig.10.6, Fig.10.10 and Fig.10.12, there are obvious arc-shaped borderlines. In order to understand their origin, we propose a brief theoretical analysis.

For a synchronized state, we have $\delta_u \equiv u_j - u_i = 0$ and $\delta_v \equiv v_j - v_i = 0$, while for a unsynchronized state, both δ_u and δ_v evolve with time. Thus the synchronization borderlines distinguish the synchronized ad unsynchronized areas. The values of δ_u and δ_v for the points at the borderlines will be in between the two limits. In this sense, we may approximately assume that both δ_u and δ_v are non-zero and non-time dependent at the borderline of synchronization, i.e. non-zero constants. On the other hand, the total coupling from Eq.10.3 can be approximately written as:

$$y = (\lambda_{in} + \lambda_{out})[\cos(\alpha)\delta_u + \sin(\alpha)\delta_v] \tag{10.10}$$

The dynamics of the network is determined by the value of y. A constant y gives a line with networks in the same state. For a given y, with other parameters fixed, we get the relationship between λ_{out} and α shown in Fig.10.14, where the lines for three values of y are plotted. The λ_{out} vs α lines are arc-shaped, explaining the arc-shaped patterns in the parameter plane of λ_{out} and α of Fig.10.6, Fig.10.10 and Fig.10.12.

This also explains the relationship of λ_{in} and λ_{out} in Fig.10.6, Fig.10.10 and Fig.10.12, where

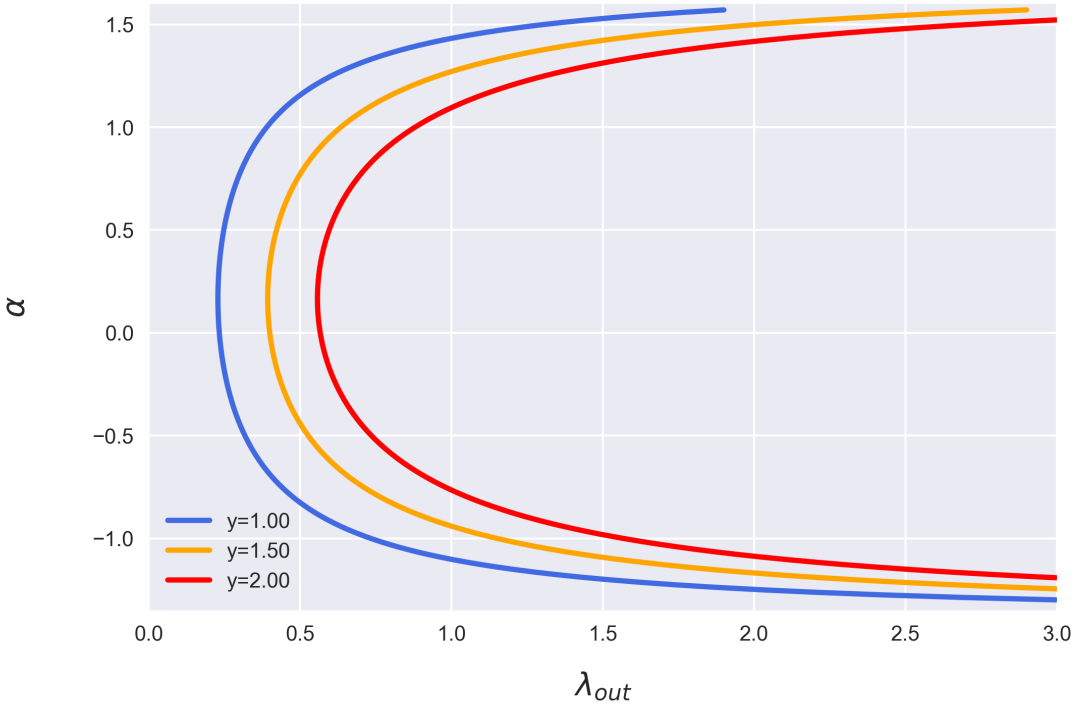

Figure 10.14: **The borderlines of synchronization in the parameter plane of λ_{out} and α.** The parameters are taken as $\delta_u = 3.0$, $\delta_v = 0.5$, $\lambda_{in} = 0.1$, and $\alpha \in (\pi/2, \pi/2)$. The three curves correspond to $y = 1.0$, 1.5 and 2.0, respectively.

an increase of λ_{in} corresponds to a decrease of λ_{out}.

11 Remote synchronization in the brain network

11.1 Introduction of RS in neural networks

Many experimental studies have revealed synchronous discharge of neurons distributed in different structures of the cerebral cortex, such as the hippocampal formation and thalamus [7, 267]. This phenomenon is known as zero time lag synchronization, which is the same as remote synchronization (RS). What is more, studies have shown that the synchrony of neuronal activity is not limited to short-range interactions within a cortical patch, but is observed across cortical regions, including interhemispheric areas [268]. For example, König *et al.* [269] have found long-range synchronization during gamma oscillations in the cat visual cortex, and Soteropoulos *et al.* [270] observed extensive oscillatory synchronization between the cerebellum and motor cortex during monkeys performing a precision grip task. As the axonal conduction delays among distant regions can amount to several tens of milliseconds, it is necessary to consider the effect of delay involved in the neuronal communication of neuronal systems. When axonal conduction delays are considered, Vicente *et al.* [271] have shown a network topology in which two populations of cells can become synchronized by a third mediating population.

Another way to reproduce the long-range synchronization in the brain network would be to take into account symmetry. Many studies have shown that the remote synchronization observed between cortical regions without apparent neural links is closely related to the underlying symmetry structure [244]. Recently, Vuksanovic *et al.* [272] have shown that remote synchronization between pairs of nodes not directly linked can also arise from the symmetry of the interactions in the resting-state functional networks. This symmetry can be defined by the size of shared neighborhoods of the synchronized nodes. A larger joint neighborhood positively correlates with a higher level of synchrony. In this mechanism, symmetric topologies are not sufficient to account for the appearance of remote synchronization, it results from the interaction between the structure and dynamics of the system.

Different from previous mechanisms in which remote synchronization is caused by time delay or symmetry, Vlasov *et al.* [240] have found that a hub node can drive synchronization of peripheral oscillators while remaining asynchronous itself in the brain network. They refer to this as “hub-driven remote synchronization".

In the following, we will study RS in the human cerebral cortex with homogeneous oscillators when considering the effect of time delay, and reveal the underlying structure and process for the emergence of RS.

11.2 Simulation of RS in the human cerebral cortex network

We study RS based on the structural network of the human cerebral cortex (Fig.10.1), which includes 989 nodes and 17,865 weighted links.

Dynamical description of the human cerebral cortex network

We use a simple oscillatory model, the Staurt-Landau model to represent the dynamics of the neural nodes. The Stuart-Landau model is the normal form of the Hopf bifurcation, which captures the essential features of the system near the bifurcation point [273]. The Hopf bifurcation widely appears in biological and chemical systems [274] and is often used to study oscillatory behavior and brain dynamics [174, 275, 276]. The Stuart-Landau model is defined as follows

$$\dot{u}_j = (\alpha + i\omega - |u_j|^2)u_j + \varepsilon \sum_{k=1}^{N} W_{jk}(u_k(t-\tau) - u_j(t)), \tag{11.1}$$

where $u \in \mathbb{C}$, $i = \sqrt{-1}$ is the imaginary unit, $j = 1, 2, \cdots, N = 989$ is the number of nodes, W_{jk} denotes the weighted connection matrix of the human cerebral cortex [38, 39]. $\sqrt{\alpha}$ and ω are the amplitude and natural frequency of the oscillator, respectively. ε is the coupling strength, and τ is the time delay. For the realization of numerical simulations, Eq.11.1 can be rewritten as

$$\begin{aligned} \dot{x}_i &= (\alpha - x_i^2 - y_i^2)x_i - \omega y_i + \varepsilon \sum_{j=1}^{N} W_{ij}(x_j(t-\tau) - x_i(t)), \\ \dot{y}_i &= \omega x_i + (\alpha - x_i^2 - y_i^2)y_i + \varepsilon \sum_{j=1}^{N} W_{ij}(y_j(t-\tau) - y_i(t)), \end{aligned} \tag{11.2}$$

where x_i and y_i represent the real and imaginary parts of u_i, respectively. Here, we fix $\alpha = 1.0$ and $\omega = 2.0$.

Appearance of RS in the human cerebral cortex network

According to Eq.11.1, the dynamics of the cerebral cortex network depend on the coupling strength ε and delay time τ. Fig.11.1(a) shows the behaviors of the nodes of the cerebral cortex when $\varepsilon = 0.1$ and $\tau = 0.5$. The different colors of the nodes represent the values of x at a moment t. Although the dynamics of most nodes are different from each other, there are some nodes with the same colors which means that they are synchronized. In order to more intuitively show the behavior of nodes, we pick the node $i = 189$ with its 40 neighbors as an example as shown in Fig.11.1(b). From Fig.11.1(b), we surprisingly find that 19 of the 40 leaf nodes are synchronized (red color) with each other but unsynchronized with the hub node, indicating that they form a cluster of RS.

Fig.11.1 shows the behavior of the human cerebral cortex network for a single snapshot, so the question is: is this RS phenomenon stable or occasional? To answer this question, we computed the Pearson's correlation coefficient matrix of all pairs of nodes over a period of time t as shown in Fig.11.2. From Fig.11.2, we see that some nodes are highly correlated (red color), which means that they are relatively stably synchronized.

To show it more clearly, we chose node $i = 189$ and its four synchronized leaf nodes as an example and show their dynamical evolution. Fig.11.3 shows the evolution of the hub node (real line) and its four arbitrary synchronized leaf nodes (dotted lines), Fig.11.3 (a) and Fig.11.3(b) represent the evolution of x and $\dot{x}$, respectively. At the beginning, these five nodes have different values. After a short time of evolution ($t > 70$), the four leaf nodes become synchronized but

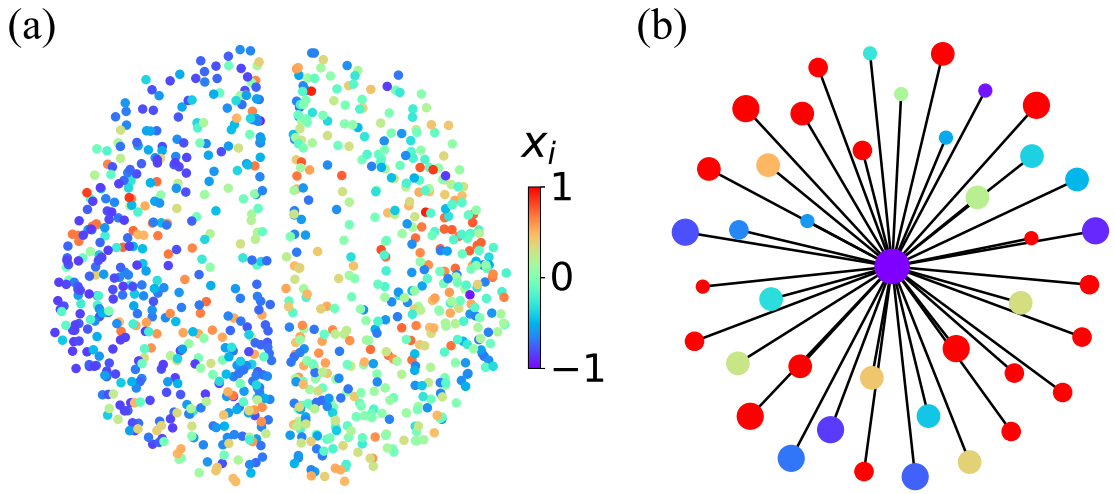

Figure 11.1: **RS in the human cerebral cortex network.** (a) The behaviors of all the 989 nodes on the network of the human cerebral cortex with $\tau = 0.5$ and $\varepsilon = 0.1$, where the color of nodes represents the value of x at a moment. (b) An example of RS for node $i = 189$ and its 40 neighboring nodes from (a).

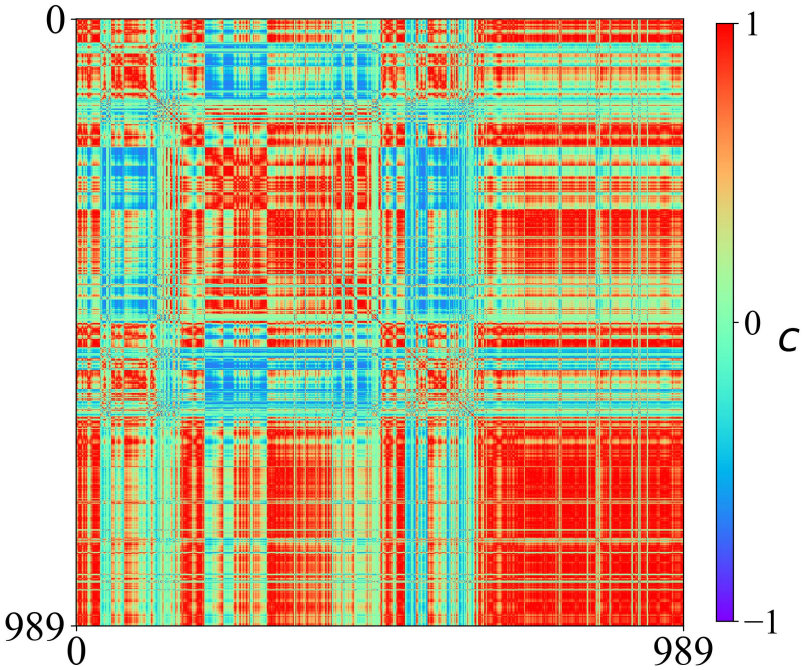

Figure 11.2: **Correlation matrix of the nodes.** Pearson's correlation coefficient among each pair of nodes when $\tau = 0.5$ and $\varepsilon = 0.1$. The red color means they are highly synchronized.

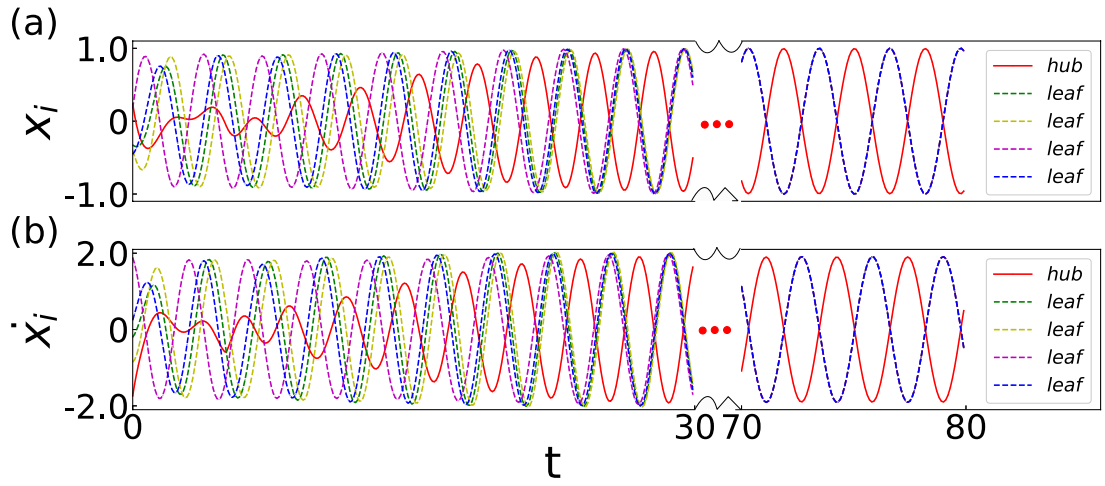

Figure 11.3: **The evolution of the hub node and four arbitrary synchronized leaf nodes in Fig.11.1(b).** The real line stands for the hub nodes, the dotted lines stand for the leaf nodes. (a) The evolution of x. (b) The evolution of $\dot{x}$.

unsynchronized with the hub node, further confirming that RS is stable.

Detection steps of RS in the cerebral cortex network

As introduced before, RS in networks of homogeneous oscillators comes from the symmetries of the network or from single star network. Is this consistent with our findings? To answer this question, we extract some RS structures in the cerebral cortex network. The steps are as follows. First, we simulate the node dynamics and calculate their correlation matrix. The correlation matrix is then used to find the nodes that have RS among their leaf nodes. If the synchronized leaf nodes are directly linked, we cut them and keep only the remaining nodes and their links.

By the above approach, Fig.11.4 shows six typical patterns of RS for $\tau = 0.5$ and $\varepsilon = 0.1$. Similar patterns of RS can also be found for other sets of parameters τ and ε. From Fig.11.4, it is clear that some RS patterns have star network structures (Fig.11.4(a, d), while some RS patterns include two or more hub nodes (Fig.11.4(b-c, e-f) (black nodes are hub nodes, green nodes are common leaf nodes, the other colors nodes are the leaf nodes, same color leaf nodes belong to one cluster). This finding may be significant as it is different from the paradigmatic pattern of RS with only one hub node analyzed in previous studies [235, 240].

11.3 A new mechanism for the emergency of RS

In order to better observe the characteristics of these RS patterns, we delete the other nodes, and just keep the nodes included in the RS patterns. Fig.11.5 show skeletons of the RS structures in the cerebral cortex network. We find that RS is observed not only in the network with one hub node, but that it is also observed in the network with more hubs (red nodes). Further analysis shows that RS patterns with more than one hub node, share the common structure that any two star networks are connected by some common leaf nodes (purple nodes).

To understand this mechanism, we present a new framework of RS as shown in Fig.11.6,

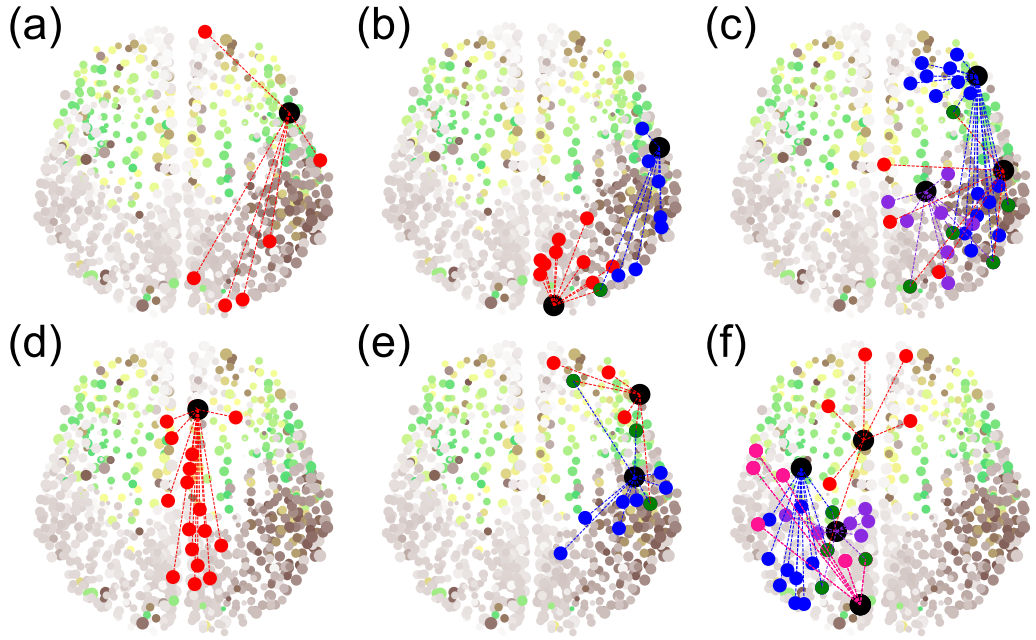

Figure 11.4: **Six example patterns of RS.** Each pattern is chosen by the conditions: there is no synchronization between the hub and its leaf nodes, and there are no direct links among the synchronous leaf nodes. The parameters are: $\tau = 0.5$, $\varepsilon = 0.1$.

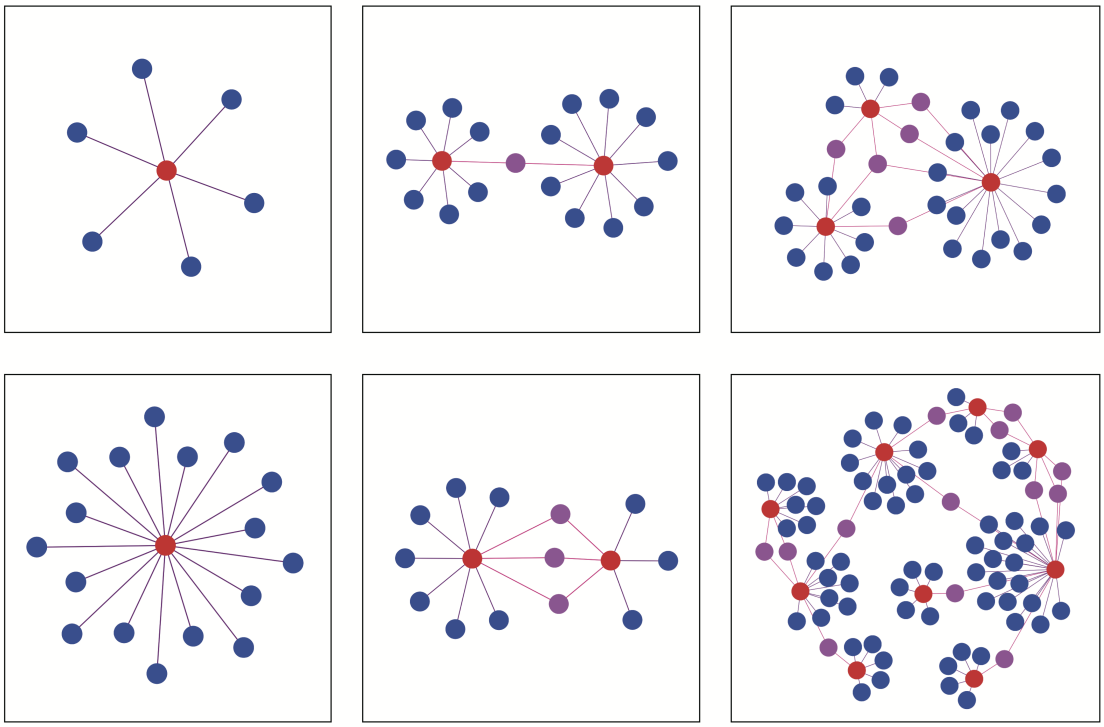

Figure 11.5: **The skeleton structures of RS patterns.** The red nodes are hub nodes, the purple nodes are common leaf nodes that link the single star networks, the blue nodes are leaf nodes.

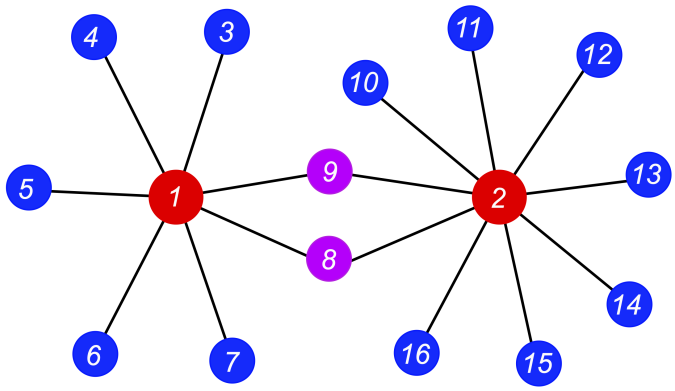

Figure 11.6: **A schematic figure of the new framework of RS.** The nodes with red, blue and pink numbers represent the hub, leaf and common leaf nodes, respectively.

where two single star networks are connected by their shared common leaf nodes (the nodes with red, blue and purple represent the hub, leaf and common leaf nodes, respectively).

In order to study this RS process more precisely, we introduce measures for RS. The most common measure for RS is the order parameter introduced before, which is defined as

$$r(t)e^{i\Phi(t)} = \frac{1}{N}\sum_{j=1}^{N} e^{i\theta_j(t)}, \tag{11.3}$$

where r and Φ are the module and argument of the mean field, respectively. θ_j is the phase variable of node j, defined as $\theta_j = \tan^{-1}(y_j/x_j)$. N is the number of nodes for consideration. The order parameter r is unity for synchronization, 0 for a totally random phase distribution, and in between 0 and 1, otherwise.

First, we study how the parameter coupling strength ε influences the emergence of RS. We calculate r for different combinations of nodes as we change ε. In detail, we let r_{l1} be the order parameter for the leaf cluster of hub node 1 in Fig.11.6 (the leaf nodes $3-7$); r_{l2} for the leaf cluster of hub node 2 (the leaf nodes $10-16$); r_l for all the leaf nodes (both the leaf nodes $3-7$ and $10-16$); r_{cl} for all the leaf nodes and common leaf nodes (the nodes $3-16$); and r for all the nodes (the nodes $1-16$).

Fig.11.7(a) shows how r_{l1}, r_{l2}, r_l, r_{cl}, r depend on ε when $\tau = 1.1$ for the schematic network (Fig.11.6). As ε increases, r_{l1}, r_{l2} are first to become close to 1 at a critical value $\varepsilon_{c1} = 0.125$, while the r and r_c and r_{cl} remain less than 0.5. This means that only the leaf nodes of hub nodes 1 and 2 become synchronized and they are unsynchronized with their hub nodes. So RS exists independently in each single star network. Then, the second critical transition appears around $\varepsilon_{c2} = 0.325$. When ε becomes larger than ε_{c2}, r_l and r_{cl} almost simultaneously arrive at

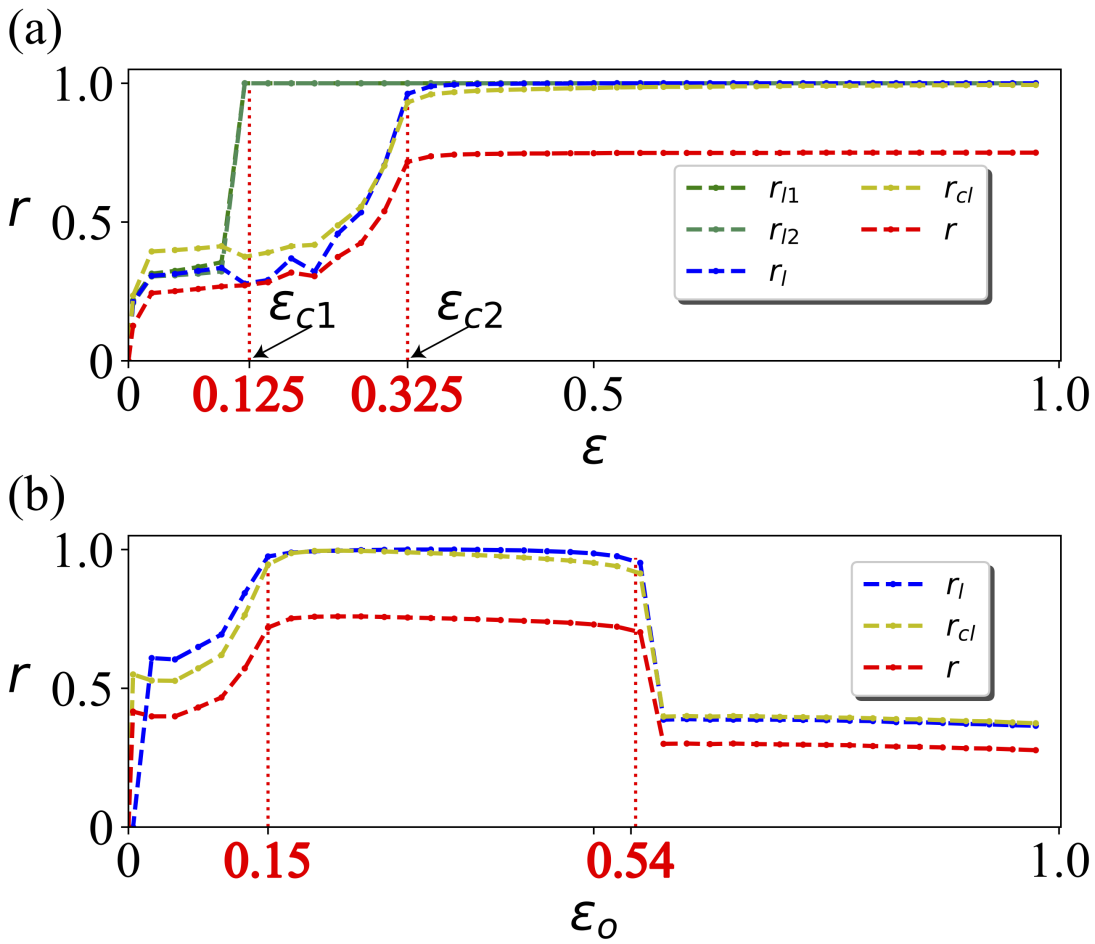

Figure 11.7: **Synchronization order parameters as a function of coupling strength.** (a) Dependence of the order parameters r_{l1}, r_{l2}, r_l, r_{cl} and r on the coupling strength ε. (b) Dependence of the order parameters r_l, r_{cl} and r on the coupling strength ε_0 of the two common nodes for fixing the other coupling strength as $\varepsilon = 0.4$. The parameter $\tau = 1.1$.

1, which means all leaf nodes including the common leaf nodes are synchronized. For the same ε value, r is still less than 1, so a bigger cluster of RS exists between all leaf nodes and hub nodes.

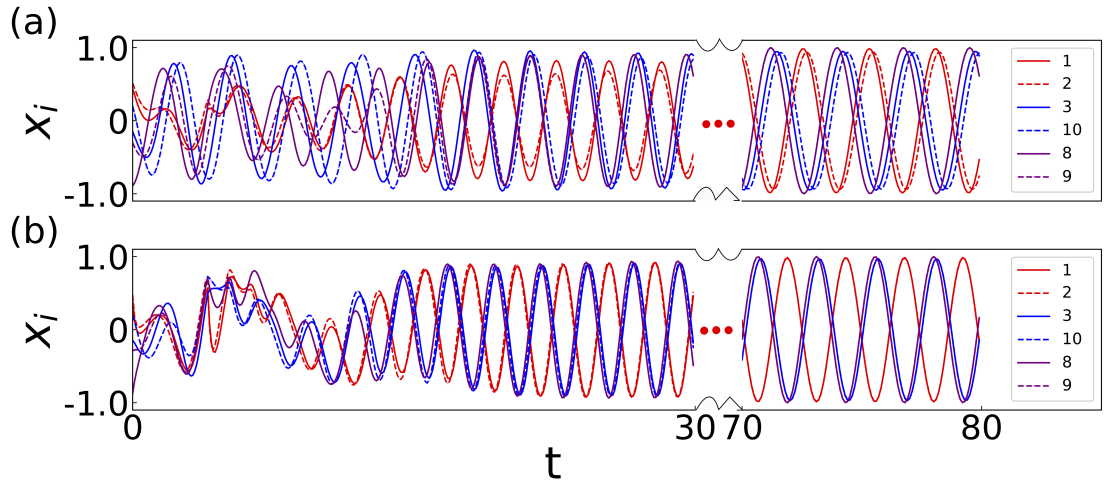

Figure 11.8: **Evolution of x_i for six typical nodes in Fig.11.6.** where the curves with "1" and "2" represent the behaviors of two hub nodes, "3" and "10" for two leaf nodes from the two leaf clusters, respectively, and "8" and "9" for the two common leaf nodes. (a) and (b) represent the cases of $\varepsilon = 0.275$ and 0.6, respectively.

In order to clearly explain the RS process, the evolution of x for some typical nodes for two different cases is shown in Fig.11.8. Specifically, we choose two hub nodes "1" and "2", two leaf nodes "3" and "10", two common leaf nodes "8" and "9" and show their evolutions when $\varepsilon = 0.275$ and $\varepsilon = 0.6$, respectively. When $\varepsilon = 0.275$ (Fig.11.8(a)), all of these six nodes are unsynchronized. When $\varepsilon = 0.6$ (Fig.11.8(b)), we can see the two hub nodes "1" and "2" are synchronized and the leaf nodes "3" and "10" are also synchronized, but the hub nodes are unsynchronized with the leaf nodes, indicating the emergence of RS when $\varepsilon > \varepsilon_{c2}$ in Fig.11.7.

In summary, the process of RS in a network with more than one hub node is as follows: first, the star network achieves RS independently, and they are not synchronized with one another. Then the common leaf nodes and all leaf nodes are synchronized resulting in two RS clusters gradually merging into a larger RS cluster.

Another interesting finding is that with increase of ε, the common leaf nodes and all leaf nodes become synchronized almost at the same time, so it is not clear whether the common leaf nodes take a role in this process. To answer this question, we fix the coupling strength ε for other links but just change the coupling strength that includes common leaf nodes ("8" and "9"). To distinguish, we call it ε_0. Fig.11.7(b) show how r_l, r_{cl} and r depend on ε_0 when the other coupling strengths are fixed at $\varepsilon = 0.4$. From Fig.11.7(b), we make three observations: (i) the synchronization order parameter r is less than both r_l and r_{cl} for the whole range of ε_0, indicating that the hub nodes cannot synchronize with the leaf nodes by increasing ε_0; (ii) there are two critical points for the r_l, r_{cl} and r when changing the ε_0. r_l and r_{cl} become approximately equal to 1.0 for $\varepsilon_0 > 0.15$, indicating that a synchronization between the two clusters has been induced by the common leaf nodes at $\varepsilon_0 \approx 0.15$; (iii) all the three curves jump down at the second critical point where $\varepsilon_0 > 0.54$. This indicates that a stronger ε_0 destroys RS. That is,

RS exists only for a middle range of ε_0 values. Therefore, we conclude that common leaf nodes do take a key role for RS in the framework of Fig.11.6.

In order to study how τ and ε influence the dynamics of the network, we show the phase diagrams for r_{l1}, r_l, r_{cl} and r of the network (Fig.11.6) with the functions of parameters τ and ε in Fig.11.9. In Fig.11.9, we have found that when $\tau = 0$ the network is completely synchronized no matter the value of ε, which is consistent with previous results that RS can be only observed with nonidentical oscillators. Further, we can see that for $\tau = 3.0$, the situation is almost the same as $\tau = 0$. This means that the effect is periodic in the value of τ. It corresponds to the oscillatory period of nodes which is about 3.0. It is obvious that the synchronized area in panel r is less than the other three panels of r_{l1}, r_l and r_{cl}, which thus guarantee the emergence of RS in such a network. By comparing Fig.11.9(a) and (b) for r_{l1} and r_l, we can see that the synchronized area for r_{l1} is clearly less than for that r_l, which means that RS in star networks is much easier than in more than one hub node networks.

11.4 A brief theoretical analysis of the process of RS

For the convenience of the theoretical analysis, we let $u_j = \rho_j e^{i\theta_j}$ and rewrite Eq.11.1 in polar coordinates,

$$\begin{aligned}
\dot{\rho}_i &= \alpha\rho_i - \rho_i^3 + \varepsilon \sum_{j=1}^{N} A_{ij}(\rho_j \cos(\theta_j(t-\tau) - \theta_i(t)) - \rho_i), \\
\dot{\theta}_i &= \omega + \varepsilon \sum_{j=1}^{N} \frac{\rho_j}{\rho_i} A_{ij} \sin(\theta_j(t-\tau) - \theta_i(t)),
\end{aligned} \tag{11.4}$$

where the weight matrix W_{ij} in the human cerebral cortex network is replaced by the adjacency matrix A_{ij} for the network of Fig.11.6.

Then we write the dynamic equations for leaf, common leaf and hub nodes, respectively. For leaf nodes, we have

$$\begin{aligned}
\dot{\rho}_i &= (\alpha - \rho_i^2 - \varepsilon)\rho_i + \varepsilon\rho_h \cos(\theta_h(t-\tau) - \theta_i(t)), \\
\dot{\theta}_i &= \omega + \varepsilon \frac{\rho_h}{\rho_i} \sin(\theta_h(t-\tau) - \theta_i(t)),
\end{aligned} \tag{11.5}$$

where ρ_h and θ_h represent the amplitude and phase of a hub node, respectively.

Similarly, for hub nodes, we have

$$\begin{aligned}
\dot{\rho}_h &= \alpha\rho_h - \rho_h^3 + \varepsilon \sum_{j=1}^{N} A_{hj}(\rho_j \cos(\theta_j(t-\tau) - \theta_h(t)) - \rho_h), \\
\dot{\theta}_h &= \omega + \varepsilon \sum_{j=1}^{N} \frac{\rho_j}{\rho_h} A_{hj} \sin(\theta_j(t-\tau) - \theta_h(t)).
\end{aligned} \tag{11.6}$$

And for common leaf nodes, it reads

$$\dot{\rho}_c = \alpha\rho_c - \rho_c^3 + \varepsilon\sum_{j=1}^{2} A_{cj}(\rho_j \cos(\theta_j(t-\tau) - \theta_c(t)) - \rho_c),$$
$$\dot{\theta}_c = \omega + \varepsilon\sum_{j=1}^{2} A_{cj}\frac{\rho_j}{\rho_c}\sin(\theta_j(t-\tau) - \theta_c(t)). \tag{11.7}$$

Next, we study the synchronization manifolds among leaf nodes, common leaf nodes and hub nodes. We first discuss the synchronization between the leaf nodes that come from the same cluster. From Eq.11.5, we have

$$\dot{\theta}_j - \dot{\theta}_i = \varepsilon\frac{\rho_h}{\rho_j}\sin(\theta_h(t-\tau) - \theta_j(t)) - \varepsilon\frac{\rho_h}{\rho_i}\sin(\theta_h(t-\tau) - \theta_i(t)). \tag{11.8}$$

It is obvious that $\theta_j = \theta_i$ and $\rho_j = \rho_i$ is a synchronization solution for Eq.11.8. To find the critical coupling strength ε_{c1} for this solution, we go back to the jacobian matrix of Eq.11.5 for the synchronization manifold. By simple operations, we find that the condition for two eigenvalues of the jacobian matrix to be negative is

$$\varepsilon_{c1} > \frac{\alpha - 3\rho_i^2}{1 + \frac{\rho_h}{\rho_i}\cos(\theta_h(t-\tau) - \theta_i(t))} \tag{11.9}$$

As $\alpha - 3\rho_i^2 < \alpha$, the critical value of ε_{c1} will be generally smaller than α. On the other hand, from Eq.11.9, we can see that the value of ε_{c1} depends on the time delay τ. These analytical results are consistent with the numerical results of Figs.11.7 and 11.9.

Then, we consider the synchronization between the hub and leaf nodes. From Eqs.11.5 and 11.6 we have

$$\dot{\theta}_h - \dot{\theta}_i = \varepsilon\sum_{j=1}^{N}\frac{\rho_j}{\rho_h}A_{hj}\sin(\theta_j(t-\tau) - \theta_h(t)) - \varepsilon\frac{\rho_h}{\rho_i}\sin(\theta_h(t-\tau) - \theta_i(t)). \tag{11.10}$$

We first consider a simple situation when $\tau = 0$, the jacobian matrix of the synchronization manifold $(\theta_h(t) - \theta_i(t) = 0)$ is

$$M = -\varepsilon\sum_{j=1}^{N}\frac{\rho_j}{\rho_h}A_{ij}\cos(\theta_h(t) - \theta_j(t)) - \varepsilon\frac{\rho_h}{\rho_i}\cos(\theta_h(t) - \theta_i(t)). \tag{11.11}$$

For the synchronization manifold of $\theta_h = \theta_i$, the eigenvalue of Eq.11.11 is always negative $(-\varepsilon(\sum_{j=1}^{N}\frac{\rho_j}{\rho_h}A_{ij} + \frac{\rho_h}{\rho_i}))$, indicating that the synchronization manifold is stable. Thus, we will not have RS for $\tau = 0$. This is consistent with our numerical simulations in Fig.11.9 and also consistent with the previous result that RS can be only observed in non-identical oscillators [235, 240, 239, 245, 244]. However, when $\tau \neq 0$, the solution will be complex. The synchronization manifold of $\theta_h = \theta_i$ cannot guarantee $\theta_j(t-\tau) - \theta_h(t) = 0$ and $\theta_h(t-\tau) - \theta_i(t) = 0$ in Eq.11.10. In this case, the eigenvalue of the jacobian matrix depends on time either positive or negative thus is unstable. According to the above analysis, we can see that $\tau \neq 0$ is the necessary condition

for RS in the identical oscillators of Eq.11.1. This result is consistent with the observations in Fig.11.7 and Fig.11.9.

Next, we discuss the synchronization between the leaf nodes and common leaf nodes. From Eqs.11.5 and 11.7, we have

$$\dot{\theta}_c - \dot{\theta}_i = \varepsilon \sum_{j=1}^{2} A_{cj} \frac{\rho_j}{\rho_c} \sin(\theta_j(t-\tau) - \theta_c(t)) - \varepsilon \frac{\rho_h}{\rho_i} \sin(\theta_h(t-\tau) - \theta_i(t)) \tag{11.12}$$

It is easy to see that $\theta_c = \theta_i$ and $\rho_c = \rho_i$ is generally not a synchronization solution of Eq.11.12. In this case, the eigenvalues of jacobian matrix depend on time and hub nodes, which is complex to give a solution.

Finally, we discuss the synchronization between the hub nodes and common leaf nodes. Doing a similar analysis as above, we find that $\theta_c = \theta_h$ and $\rho_c = \rho_h$ is not a synchronization solution. On the other hand, considering that the two common nodes "8" and "9" take the same role in the RS process of network Fig.11.6, we would like to treat them as a whole like a combined entity. In this sense, we may consider the common leaf nodes as a virtual "hub" node while the two real hub nodes "1" and "2" as virtual "leaf" nodes. Thus, RS between the two virtual "leaf" nodes can be induced by the new virtual "hub" node. This prediction is confirmed in Fig.11.8(b). Once the two hub nodes "1" and "2" are synchronized, Eq.11.10 will be the same for all the leaf nodes in the two leaf clusters of Fig.11.6 and thus result in RS for all the leaf nodes. This explains how the common leaf nodes induce RS for all the leaf nodes belonging to different clusters.

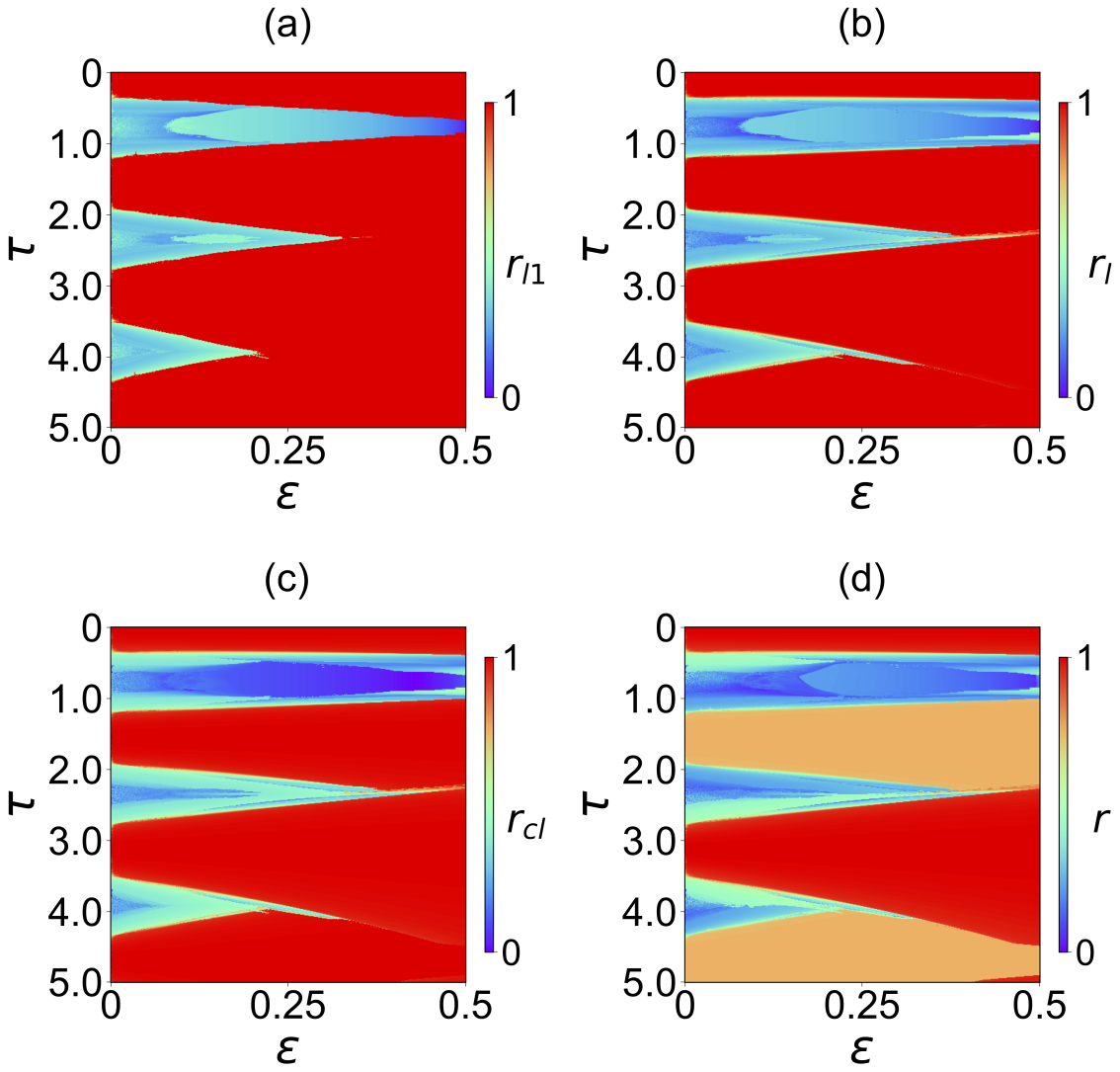

Figure 11.9: **Phase diagrams in the $\varepsilon - \tau$ plane for the case with the same coupling for all the links.** where (a)-(d) represent the values of $r_{\ell 1}$, r_ℓ, $r_{c\ell}$ and r, respectively.

CHAPTER IV

Conclusion and Perspectives

This thesis investigates neuronal activities such as oscillations, synchronization, and wave propagation using neuronal networks. The goal is to understand related brain functions and how the underlying mechanisms rely on the interaction of dynamics and structures. Specifically, first, we studied beta oscillations and beta propagating waves that are observed in the motor cortex of monkeys when they are trained to do a delayed reach-to-grasp task. Then, we introduced partial synchronization mechanisms such as chimera states and remote synchronization based on a human cerebral cortex network.

Neural rhythms are one of the most obvious features of neural dynamics. They are related to various brain functions and are a daily tool for the diagnosis of neurological dysfunction. Classic studies have shown that neural rhythms depend on neural structures and the behavioral state of the animal. Here, what I was interested in are beta oscillations, corresponding to the frequency band range $13 - 30Hz$, which are prominent during movement preparation.

First, we analyzed the experimental data of Ref.[53] when monkeys are trained to do a delayed reach-to-grasp task. An obvious beta bump in power spectrum is present during the movement preparation period. Moreover beta oscillations are sporadic and organized into complex waves (planar, radial, spiral waves). Then, in order to study the origin and characteristics of beta oscillations, we proposed a simple model of the motor cortex based on local excitatory-inhibitory neuronal populations coupled by longer range excitation. These modules also receive additional stochastic inputs from other neural structures. We separated the stochastic inputs into two parts: one that is local and varies from module to module, and the other one that is global and consistent across all modules. We have shown that this model can accurately reproduce the statistics of recording data when these external inputs are correlated on a short time scale ($25ms$) and the two different components of external inputs are appropriately weighted. The model reproduces the distribution of beta burst durations, the proportion of the different observed wave types,

and wave speeds. We have also provided a basic theoretical analysis of beta oscillations.

Debate exists regarding the origin of beta oscillations in the cortex. One hypothesis is that they are a reflection of inputs coming from basal ganglia and thalamic structures [161, 162, 163], the other is that they emerge within the neocortex as a consequence of internal dynamics [164, 165, 166]. In our model, we adopted the intermediate view, previously advocated by Sherman *et al.* [157], that beta oscillations are generated by recurrent interactions in the motor cortex but are strongly modulated by inputs from other structures. This needs to be tested in further experiments.

We proposed that external inputs have both local and global components. The existence of a global component appears consistent with the presence of global inhibition in the motor cortex during movement preparation [277]. In addition, considering the thalamo-cortical connectivity [278], the described diffused connectivity from calbindin-positive matrix neurons could be the source of our global inputs while core parvalbumin-positive neurons could be the source of our local inputs. This requires further experiments assessing the origin of synaptic inputs.

The propagating waves found in the motor cortex have an orientational preference [84] (anterior–posterior in primary motor cortex; mediolateral in dorsal pre-motor cortex) which may reflect the underlying structure of the cortex. So we considered anisotropic long-range connectivity. We have found that traveling waves are found to preferentially propagate along the axis where connectivity decays the fastest. This also needs to be tested in further experiments.

Traveling waves have been shown to carry information about the subsequent movement [84] and shape the dynamics of the movement itself [279, 280, 281, 282, 283]. However, it is unclear how the external inputs influence the beta oscillation and further reflect the functions. Further investigation of this important topic is required.

When the brain functions normally, some but not all neurons function together. Neurons are embedded in networks of functionally specialized brain regions, which reflects in fact a partial synchronization. Here we studied chimera states and remote synchronization based on the anatomy of human cerebral cortex. We focused on structure-function relationships of brain networks, leading to a better understanding of how structural features give rise to rich and flexible neural dynamics.

For chimera states in the human cerebral cortex network, we presented a two-layered brain network model of coupled neurons to study the collective patterns of the brain network. This model allowed us to find that the two-layered brain network may have different states such as chimera states in either one hemisphere or the whole network, reminiscent of both the unihemispheric sleep for some birds and marine mammals and the first-night effect for human beings. Further, we investigated the general two-layered network and studied how the structure parameters shape the dynamics of the network. We also considered the effect of delays due to the limited speed of signal transmission by distinguishing the inter- and intra-coupling as chemical synapse couplings and electrical synapse couplings, respectively.

Although this two-layered network can well explain the influence of the key parameters of structures on the rich patterns of the brain network, our model still has some limitations. For example, we treated the coupling between neurons as fixed constants but, in some cases, they

can vary in time due to synaptic platicity. Moreover, we used a single neuron model to represent the dynamics of a node. It perhaps could be better replaced by mean-field models such as the firing rate model or the neural mass model that we used to denote beta oscillations.

Remote synchronization is a potential mechanism used to account for the segregation and integration of the brain which is thought to take key roles in supporting the normal functions of the brain network. Based on the real network of the human cerebral cortex, we have shown that remote synchronization can be observed in systems of identical oscillators, provided that an appropriate time delay is considered. A new framework is presented to account for the emergence of remote synchronization in which a network with two hub nodes or more is connected by common leaf nodes. We have found that these common leaf nodes take a key role in inducing remote synchronization for the leaf nodes belonging to different leaf clusters.

Previous studies have shown that remote synchronization may be found in networks of homogeneous oscillators with symmetric topologies or in networks of inhomogeneous oscillators with a parametric mismatch. Here, we have shown a third possibility that seems to require an intricate interplay between structure and dynamics. However, the specific relationship of the phenomenon with the topological features of the network remains to be more fully investigated.

CHAPTER V

Appendix

A Analysis of single FAT module

For the interested reader, we detail the analysis of a single E-I module. The model is based on the recurrent coupling between an excitatory population and an inhibitory population as follows:

$$\begin{aligned}\tau_E(I_E)\frac{dI_E}{dt}(t) &= -I_E(t) + I_E^{ext}(t) + I_{EE}^{syn}(t) - I_{EI}^{syn}(t)\\ \tau_I(I_I)\frac{dI_I}{dt}(t) &= -I_I(t) + I_I^{ext}(t) + I_{IE}^{syn}(t) - I_{II}^{syn}(t)\end{aligned} \tag{A.1}$$

where τ_E, τ_I are the response time in this model, depending on the current as shown in Fig.4.4 (c). $I_{EE}^{syn}, I_{IE}^{syn}, I_{IE}^{syn}, I_{II}^{syn}$ are the recurrent currents between the excitatory and the inhibitory populations, I_E^{ext}, I_I^{ext} are the external inputs.

We consider the kinetic model for the synaptic currents,

$$I_{BA}^{syn} = w_{BA}\int^t du S_A(t-u) r_A(u), A \in \{E,I\}, B \in \{E,I\}, \tag{A.2}$$

$$S_A(t) = \frac{\theta(t-\tau_l^A)}{\tau_d^A - \tau_r^A}\{\exp[-(t-\tau_l^A)/\tau_d^A] - exp[-(t-\tau_l^A)/\tau_r^A]\}, A \in \{E,I\}. \tag{A.3}$$

S_E, S_I are the kinetic kernels of the synaptic currents, normalized such that $\int dt\, S_A(t) = 1, A \in \{E,I\}$; τ_r^E, τ_r^I, τ_d^E, τ_d^I, τ_l^E, τ_l^I are the rise times, decay times and latencies of the excitatory and the inhibitory of synaptic currents. $\theta(t)$ denotes the *Heaviside* function, $\theta(t) = 1$ if $t > 0$ and 0 otherwise. r_E, r_I, are the firing rates which are related to the currents by $r_A = \Phi(I_A), A \in \{E,I\}$, and which are shown in Fig. 4.4 (b). We also consider the stochastic component that comes from the finite number of neurons as in a spiking network. So the firing rate contains one deterministic part depending on the current plus one stochastic term,

$$r_A = \Phi(I_A) + \sqrt{\Phi(I_A)/N_A}\xi, A \in \{E,I\}. \tag{A.4}$$

N_E, N_I are the numbers of the excitatory and inhibitory neurons, with the proportion $\frac{N_E}{N_I} = 4$. ξ is a *Gaussian* white noise which satisfies $< \xi(t)\xi(t') >= \delta(t-t')$.

For the external inputs, the terms $I_E^{ext,0}, I_I^{ext,0}$ are chosen to impose the steady firing rates r_E^s, r_I^s,

$$I_A^{ext,0} = I_A^s - w_{AE}r_E^s + w_{AI}r_I^s, A \in \{E,I\} \tag{A.5}$$

The fluctuation term of the external inputs η are chosen as stochastic *Ornstein-Uhlenbeck* (O-U) processes,

$$I_A^{ext} = I_A^{ext,0} + \sigma_A^{ext}\eta, \quad \sigma_A^{ext} = w_A^{ext}\nu^{ext}, \ A \in \{E,I\} \tag{A.6}$$

$$\tau_{ext}\frac{d\eta}{dt}(t) = -\eta(t) + \sqrt{\tau_{ext}}\xi(t), < \xi(t)\xi(t') >= \delta(t-t') \tag{A.7}$$

where w_E^{ext}, w_I^{ext} are the synaptic coupling strengths of external inputs onto the excitatory neurons and the inhibitory neurons, respectively.

$$w_E^{ext} = w_{EE}, w_I^{ext} = 2w_{IE} \tag{A.8}$$

ν_{ext} is the amplitude of the external input fluctuations, τ_{ext} is the correlation time scale of the O-U processes.

A.1 The stability analysis

We first analyze the dynamic regimes of this model, following the method we introduced before. We linearize Eq.A.1 around the steady state,

$$I_A(t) = I_A^s + \delta I_A(t), A \in \{E, I\} \tag{A.9}$$

Then we get the linear equations,

$$\begin{aligned} \tau_E(I_E^s)\frac{d\delta I_E}{dt}(t) &= -\delta I_E(t) + \delta I_{EE}^{syn}(t) - \delta I_{EI}^{syn}(t), \\ \tau_I(I_I^s)\frac{d\delta I_I}{dt}(t) &= -\delta I_I(t) + \delta I_{IE}^{syn}(t) - \delta I_{II}^{syn}(t). \end{aligned} \tag{A.10}$$

We consider an exponential dependence in time of the currents

$$\delta I_A(t) = \delta \tilde{I}_A(\sigma)\exp(\sigma t), A \in \{E, I\}. \tag{A.11}$$

Using a vector notation for the currents $\mathbf{I} = (I_E, I_I)$, the perturbation evolves according to

$$\tilde{L}_{EI}(\sigma) \cdot \delta\mathbf{I} = 0 \tag{A.12}$$

with the matrix

$$\tilde{L}_{EI}(\sigma) = \begin{pmatrix} 1 + \sigma\tau_E(I_E^s) - \alpha\tilde{S}_E(\sigma) & w_{EI}\Phi_I'(I_I^s)\tilde{S}_I(\sigma) \\ \\ -w_{IE}\,\Phi_E'(I_E^s)\tilde{S}_E(\sigma) & 1 + \sigma\tau_I(I_I^s) + \gamma\tilde{S}_I(\sigma) \end{pmatrix}. \tag{A.13}$$

The functions $\tilde{S}_E(\sigma)$ and $\tilde{S}_I(\sigma)$ are the *Laplace* transforms of $S_E(t)$ and $S_I(t)$ (Eq.A.3) with

$$\tilde{S}_A(\sigma) = \frac{\exp(-\sigma\tau_l^A)}{(1 + \sigma\tau_r^A)(1 + \sigma\tau_d^A)}, A \in \{E, I\}. \tag{A.14}$$

The condition of existence of a non-trivial solution of Eq.A.12 determines the growth rate σ, namely,

$$W(\sigma) = \det[\tilde{L}_{EI}(\sigma)] = 0 \quad \Rightarrow \quad [1 - \alpha\tilde{T}_E(\sigma)][1 + \gamma\,\tilde{T}_I(\sigma)] + \beta\tilde{T}_E(\sigma)\tilde{T}_I(\sigma) = 0 \tag{A.15}$$

with

$$\tilde{T}_A(\sigma) = \frac{\tilde{S}_A(\sigma)}{1+\tau_A(I_A^s)\sigma}, A \in \{E, I\}, \tag{A.16}$$

$$\begin{aligned}\alpha &= w_{EE}\Phi'_E(I_E^s),\\ \beta &= w_{IE}w_{EI}\Phi'_E(I_E^s)\Phi'_I(I_I^s),\\ \gamma &= w_{II}\Phi'_I(I_I^s).\end{aligned} \tag{A.17}$$

The real instability line is obtained when the growth rate vanishes $\sigma = 0$,

$$\beta = (\alpha - 1)(\gamma + 1). \tag{A.18}$$

The Hopf bifurcation line corresponds to the parameter for which the growth rate is purely imaginary $\sigma = i\omega$. It can be obtained in parametric form, with α and β as functions of the frequency ω and of the recurrent inhibition γ by separating the real and imaginary parts of Eq.A.15. Solving the resulting linear equations for α and β we get

$$\begin{aligned}\alpha &= \frac{\mathrm{Im}[\tilde{T}_I(i\omega)\tilde{T}_E(i\omega) + \gamma|\tilde{T}_I(i\omega)|^2\tilde{T}_E(i\omega)]}{|\tilde{T}_E(i\omega)|^2\,\mathrm{Im}[\tilde{T}_I(i\omega)]},\\ \beta &= \frac{\mathrm{Im}[\tilde{T}_E(i\omega)]|1+\gamma\tilde{T}_I(i\omega)|^2}{|\tilde{T}_E(i\omega)|^2\,\mathrm{Im}[\tilde{T}_I(i\omega)]}.\end{aligned} \tag{A.19}$$

The dynamic regimes as functions of synaptic weights α, β are shown in Fig.A.1(a). The lines with different colored dotted lines are the bifurcation lines that distinguish the oscillating state regime (above the bifurcation line) from the steady state regime (below the bifurcation line) for different γ. The real lines are the real instability line defined as Eq.A.18. We chose two example points with oscillating (OS) and steady (SS) states for $\gamma = 2$ and show their traces with time in Fig.A.1(b). We can see that the SS module will stay at the steady state while the OS module will exhibit regular oscillations. Fig.A.1(c) shows the same traces as in (b) but plotted as r_E VS r_I.

A.2 Power spectrum and correlation

We consider the two types of stochastic effects, one coming from the finite-size of the neuron population and the other one from external inputs. We linearize Eq.A.1 around the steady state (Eq.A.9) and solve it in *Fourier* space. We define the *Fourier* transform

$$\begin{aligned}\delta I_A(t) &= \int_{-\infty}^{+\infty}\frac{d\omega}{2\pi}\delta\tilde{I}_A(\omega)\exp(i\omega t), A \in \{E, I\},\\ \xi(t) &= \int_{-\infty}^{+\infty}\frac{d\omega}{2\pi}\tilde{\xi}(\omega)\exp(i\omega t),\ <\tilde{\xi}(\omega)\tilde{\xi}^*(\omega')>= 2\pi\delta(\omega-\omega').\end{aligned} \tag{A.20}$$

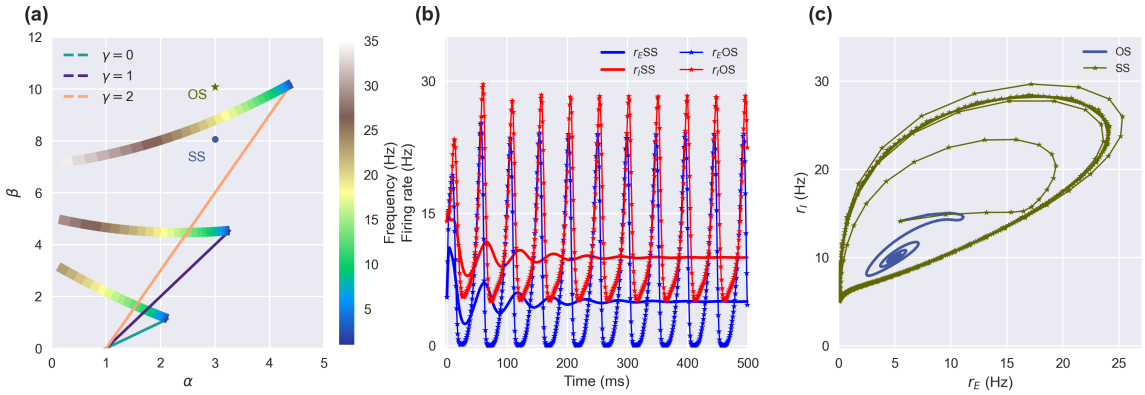

Figure A.1: **The dynamic of single FAT model.**(a) The stability phase diagram as function of synaptic weights α and β for different fixed γ (green, 0; purple, 1; orange, 2). (b) The firing rates of the excitatory (blue) and inhibitory (red) for the steady state (SS, real line) and oscillating state (OS, star line). (c) r_E VS r_I for the same data plot in (b). Parameters: SS : $w_{EE} = 2.06mV \cdot s$, $w_{EI} = 2.40mV \cdot s$, $w_{IE} = 1.00mV \cdot s$, $w_{II} = 0.87mV \cdot s$ OS: $w_{EE} = 2.06mV \cdot s$, $w_{EI} = 3.00mV \cdot s$, $w_{IE} = 1.00mV \cdot s$, $w_{II} = 0.87mV \cdot s$.

Then we obtain the equation

$$\tilde{L}_{EI}(i\omega) \cdot \tilde{\delta}\mathbf{I}(i\omega) = \mathbf{F}(i\omega). \tag{A.21}$$

We solve this equation and get the stochastic forcing term $F(i\omega)$,

$$F_A(i\omega) = w_{AE}\tilde{S}_E(i\omega)\sqrt{\frac{r_E^s}{N_E}}\,\tilde{\xi}_E(\omega) - w_{AI}\tilde{S}_I(i\omega)\sqrt{\frac{r_I^s}{N_I}}\,\tilde{\xi}_I(\omega) + \sigma_A^{ext}\tilde{\eta}(\omega),\ A \in \{E, I\}. \tag{A.22}$$

For the excitatory current,

$$\tilde{\delta I}_E(i\omega) = \frac{1}{(1 + i\omega\tau_E)}\frac{V_E(i\omega)}{W(i\omega)} \tag{A.23}$$

with $W(i\omega)$ and $V_E(i\omega)$ are given by

$$\begin{aligned} V_E(i\omega) &= F_E(i\omega)[1 + \gamma\tilde{T}_I(i\omega)] - F_I(i\omega)w_{EI}\Phi_I'\tilde{T}_I(i\omega), \\ W(i\omega) &= [1 - \alpha\tilde{T}_E(i\omega)][1 + \gamma\,\tilde{T}_I(i\omega)] + \beta\tilde{T}_E(i\omega)\tilde{T}_I(i\omega). \end{aligned} \tag{A.24}$$

The *Fourier* components of the external input fluctuations and the finite-size noise are

$$\begin{aligned} \tilde{\eta}(\omega) = \frac{\tilde{\xi}(\omega)}{1 + i\omega\tau_{ext}},\ \langle\tilde{\xi}(\omega)\tilde{\xi}^*(\omega')\rangle = 2\pi\delta(\omega - \omega'), \\ \langle\tilde{\xi}_E(\omega)\tilde{\xi}_E^*(\omega')\rangle = \langle\tilde{\xi}_I(\omega)\tilde{\xi}_I^*(\omega')\rangle = 2\pi\delta(\omega - \omega'). \end{aligned} \tag{A.25}$$

So the current-current correlation function is obtained as

$$\begin{aligned}\langle\delta\tilde{I}_E(i\omega)\delta\tilde{I}_E^*(i\omega')\rangle &= 2\pi\delta(\omega-\omega')S_{EE}(\omega)\\ &= 2\pi\delta(\omega-\omega')(S_{EE}^{ext}(\omega)+S_{EE}^{N}(\omega))\end{aligned} \tag{A.26}$$

$S_{EE}(\omega) = (S_{EE}^{ext}(\omega) + S_{EE}^{N}(\omega))$ is the power spectrum. $S_{EE}^{ext}(\omega)$ relates to the extend input noise part by the expression

$$S_{EE}^{ext}(\omega) = \frac{\left|\sigma_E^{ext} + (\gamma\sigma_E^{ext} - \sigma_I^{ext} w_{EI}\Phi_I')\tilde{T}_I(i\omega)\right|^2}{[1+(\omega\tau_{ext})^2][1+(\omega\tau_E)^2]|W(i\omega)|^2}. \tag{A.27}$$

$S_{EE}^{N}(\omega)$ relates to the finite-size noise part,

$$\begin{aligned}S_{EE}^{N}(\omega) = \frac{1}{|W(i\omega)|^2}\{&\frac{r_E^s}{N_E}w_{EE}^2|1+(\gamma-\frac{\beta}{\alpha})\tilde{T}_I(i\omega)|^2|\tilde{T}_E(i\omega)|^2\\ &+\frac{r_I^s}{N_I}\frac{w_{EI}^2|\tilde{S}_I(i\omega)|^2}{1+(\omega\tau_E)^2}\}.\end{aligned} \tag{A.28}$$

So the expression of the current-current correlation in real space is

$$\langle\delta\tilde{I}_E(t)\delta\tilde{I}_E(t')\rangle = \int_{-\infty}^{+\infty}\frac{d\omega}{2\pi}\exp[i\omega(t-t')]S_{EE}(\omega). \tag{A.29}$$

Fig.A.2 shows the traces of the currents of the steady state after adding the fluctuating inputs.

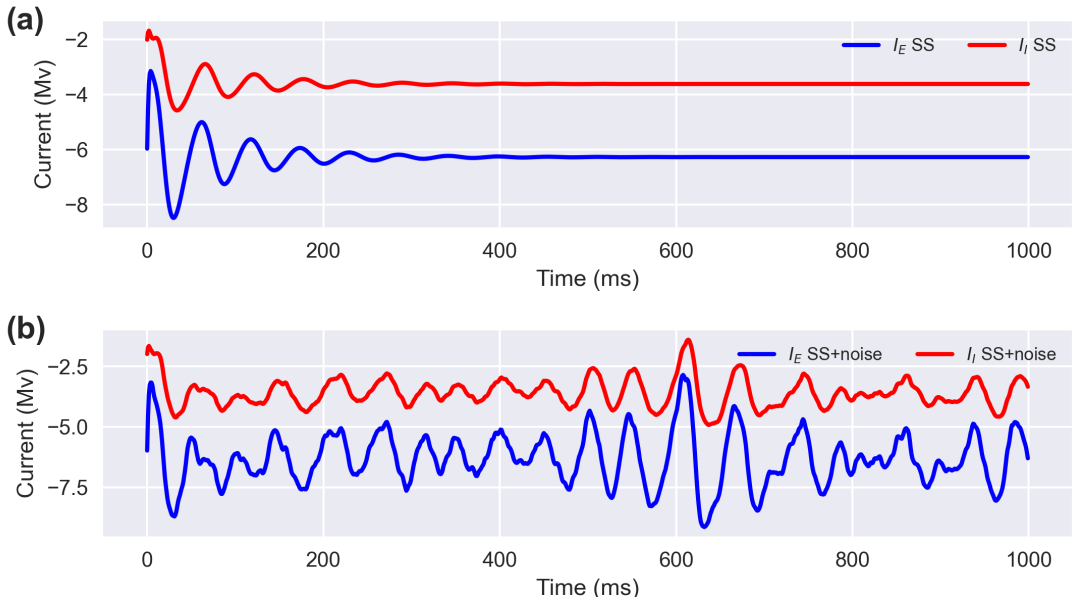

Figure A.2: **The currents traces (I_E, blue, I_I, red) of the FAT model.** (a) Steady State (SS) shown in Fig.A.1 (a). (b) SS With the external inputs, parameters are: $w_{EE} = 2.06mV \cdot s$, $w_{EI} = 2.40mV \cdot s$, $w_{IE} = 1.00mV \cdot s$, $w_{II} = 0.87mV \cdot s$, $N = 50000$, $\tau_{ext} = 25ms$, $\nu_{ext} = 0.2Hz$.

The power spectrum and the correlation of I_E from the analytical expression and the simu-

lation results are shown in Fig.A.3.

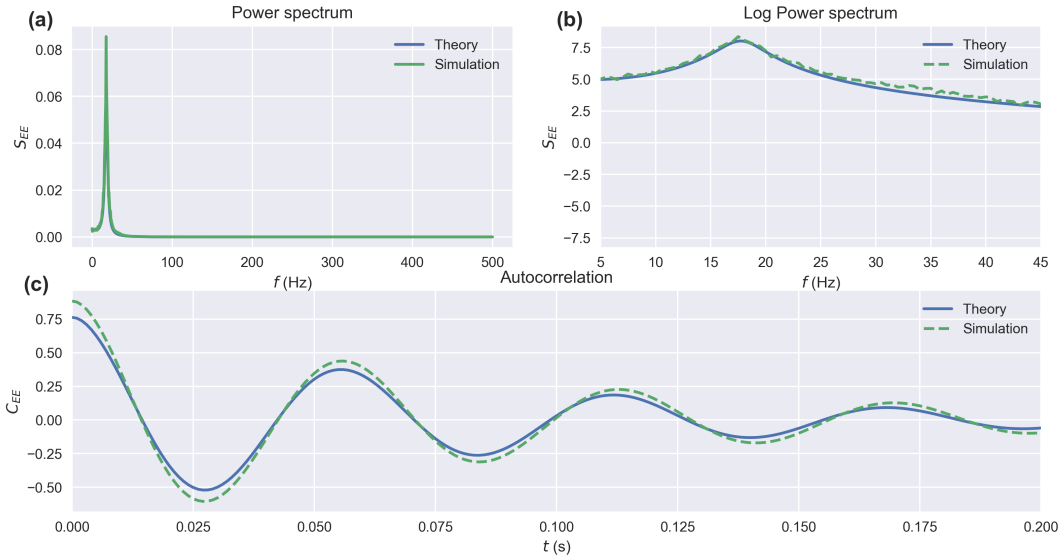

Figure A.3: **Power spectrum and correlation of I_E for the single FAT model with external inputs.** (a) Power spectrum. (b) Log plot of (a). (c) Autocorrelation, (theory, blue real line, simulation, green dot line).

B The effect of chemical synapse delay on chimera states

As introduced in Eq.10.3, when considering the chemical inter-connections, we also consider the effect of delay. It is reasonable because in the human brain, the communication between the left and right hemispheres has to go through the long corpus callosum and thus causes some time delay, due to the limited speed of signal transmission and processing. So, for longer inter-connections in our model, it is interesting to consider the effect of time delay.

Here we show the phase diagram of g_1 for the delay τ with the other parameters α, λ_{in}, λ_{out} and l_{out} (only for the general two-layered network). From Fig.B.1 and Fig.B.2, we see that the time delay increases the chimera states areas in the parameters panel. Interestingly, we have found that time delay effect makes an obvious borderline that distinguishes the chimera states and the unsynchronized states, which may be important for brain functions.

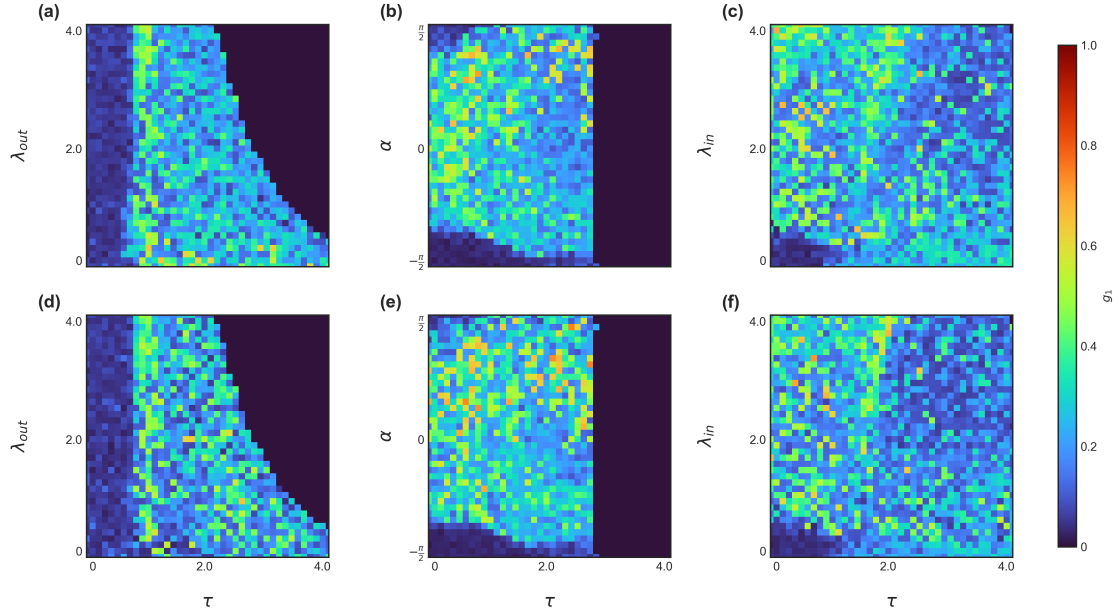

Figure B.1: **Phase diagram of g_1 for the two-layered brain network with time delay chemical inter-coupling.** The up panels are for the right hemisphere and the down panels are for the left hemisphere. (a, d) The phase diagram of g_1 in the parameter plane of τ and λ_{out} for $\alpha = \pi/2 - 0.1$ and $\lambda_{in} = 0.5$. (b, e) The phase diagram of g_1 in the parameter plane of τ and α for fixed $\lambda_{in} = 0.5$ and $\lambda_{out} = 2.0$. (c, f) The phase diagram of g_1 in the parameter plane of τ and λ_{in} for fixed $\lambda_{out} = 0.5$ and $\alpha = \pi/2 - 0.1$.

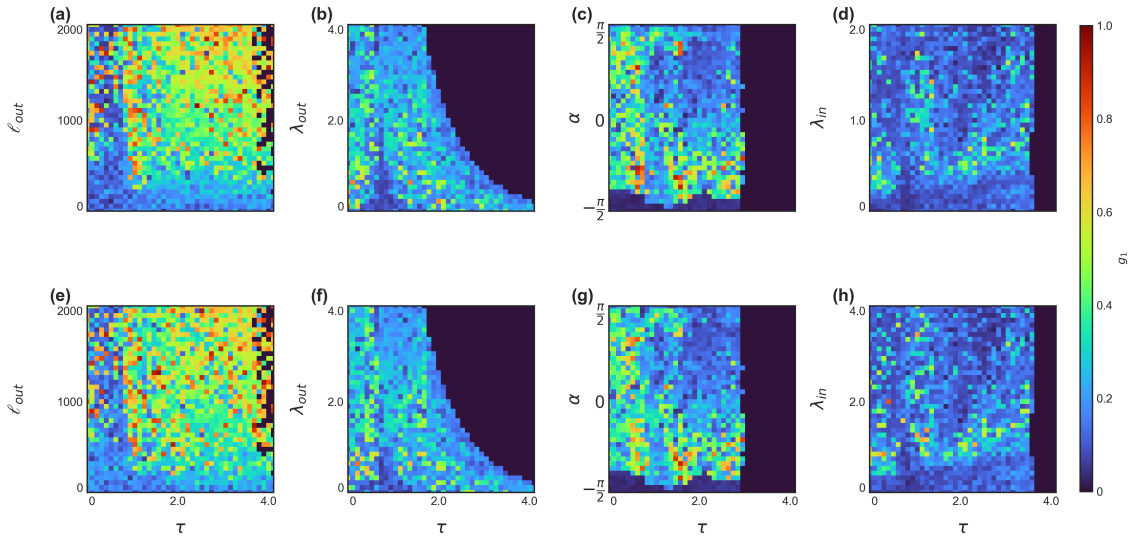

Figure B.2: **Phase diagram of g_1 for the general two-layered network ($N = 1000$) with time delay chemical inter-coupling.** The up panels are for the subnetwork A, and the down panels are for the subnetwork B. (a, e) The phase diagram of g_1 in the parameter plane of τ and l_{out} for $\alpha = \pi/2 - 0.1$, $\lambda_{in} = 0.1$ and $\lambda_{out} = 0.5$. (b, f) The phase diagram of g_1 in the parameter plane of τ and λ_{out} for fixed $\alpha = \pi/2 - 0.1$ $\lambda_{in} = 0.5$ and $l_{out} = 500$. (c, g) The phase diagram of g_1 in the parameter plane of τ and α for fixed $\lambda_{in} = 0.8$,$\lambda_{out} = 1.0$ and $l_{out} = 500$. (d, h) The phase diagram of g_1 in the parameter plane of τ and λ_{in} for fixed $\lambda_{out} = 0.5$,$\alpha = \pi/2 - 0.1$ and $l_{out} = 500$.

Bibliography

[1] Gyorgy Buzsaki and Andreas Draguhn. Neuronal oscillations in cortical networks. *Science*, 304(5679):1926–1929, 2004.

[2] Francisco Varela, Jean-Philippe Lachaux, Eugenio Rodriguez, and Jacques Martinerie. The brainweb: phase synchronization and large-scale integration. *Nature reviews neuroscience*, 2(4):229–239, 2001.

[3] Peter Uhlhaas, Gordon Pipa, Bruss Lima, Lucia Melloni, Sergio Neuenschwander, Danko Nikolić, and Wolf Singer. Neural synchrony in cortical networks: history, concept and current status. *Frontiers in integrative neuroscience*, 3:17, 2009.

[4] Lyle Muller, Frédéric Chavane, John Reynolds, and Terrence J Sejnowski. Cortical travelling waves: mechanisms and computational principles. *Nature Reviews Neuroscience*, 19(5):255–268, 2018.

[5] Andreas K Engel and Pascal Fries. Beta-band oscillations—signalling the status quo? *Current opinion in neurobiology*, 20(2):156–165, 2010.

[6] Soumen Majhi, Bidesh K Bera, Dibakar Ghosh, and Matjaž Perc. Chimera states in neuronal networks: a review. *Physics of life reviews*, 28:100–121, 2019.

[7] Roger D Traub, Miles A Whittington, Ian M Stanford, and John GR Jefferys. A mechanism for generation of long-range synchronous fast oscillations in the cortex. *Nature*, 383(6601):621–624, 1996.

[8] Louis M Pecora, Francesco Sorrentino, Aaron M Hagerstrom, Thomas E Murphy, and Rajarshi Roy. Cluster synchronization and isolated desynchronization in complex networks with symmetries. *Nature communications*, 5(1):1–8, 2014.

[9] Leonhard Euler. Solutio problematis ad geometriam situs pertinentis. *Commentarii academiae scientiarum Petropolitanae*, pages 128–140, 1741.

[10] Norman Biggs, E Keith Lloyd, and Robin J Wilson. *Graph Theory, 1736-1936*. Oxford University Press, 1986.

[11] Duncan J Watts and Steven H Strogatz. Collective dynamics of 'small-world'networks. *Nature*, 393(6684):440–442, 1998.

[12] Albert-László Barabási and Réka Albert. Emergence of scaling in random networks. *Science*, 286(5439):509–512, 1999.

[13] Albert-László Barabási, Réka Albert, and Hawoong Jeong. Mean-field theory for scale-free random networks. *Physica A: Statistical Mechanics and its Applications*, 272(1-2):173–187, 1999.

[14] Erzsébet Ravasz, Anna Lisa Somera, Dale A Mongru, Zoltán N Oltvai, and A-L Barabási. Hierarchical organization of modularity in metabolic networks. *Science*, 297(5586):1551–1555, 2002.

[15] Michelle Girvan and Mark EJ Newman. Community structure in social and biological networks. *Proceedings of the national academy of sciences*, 99(12):7821–7826, 2002.

[16] Mark EJ Newman. Fast algorithm for detecting community structure in networks. *Physical review E*, 69(6):066133, 2004.

[17] P Erodos. On random graphs i. *Publicationes Mathematicae (Debrecen)*, 6:290–297, 1959.

[18] Albert-László Barabási. Linked: The new science of networks, 2003.

[19] Reuven Cohen and Shlomo Havlin. Scale-free networks are ultrasmall. *Physical review letters*, 90(5):058701, 2003.

[20] Béla Bollobás and Oliver Riordan. The diameter of a scale-free random graph. *Combinatorica*, 24(1):5–34, 2004.

[21] Konstantin Klemm and Victor M Eguiluz. Growing scale-free networks with small-world behavior. *Physical Review E*, 65(5):057102, 2002.

[22] Béla Bollobás and Oliver M Riordan. Mathematical results on scale-free random graphs. *Handbook of graphs and networks: from the genome to the internet*, pages 1–34, 2003.

[23] Steven H Strogatz. Exploring complex networks. *Nature*, 410(6825):268–276, 2001.

[24] Misha Tsodyks, Tal Kenet, Amiram Grinvald, and Amos Arieli. Linking spontaneous activity of single cortical neurons and the underlying functional architecture. *Science*, 286(5446):1943–1946, 1999.

[25] Christof Koch and Gilles Laurent. Complexity and the nervous system. *Science*, 284(5411):96–98, 1999.

[26] Olaf Sporns. Structure and function of complex brain networks. *Dialogues in Clinical Neuroscience*, 15(3):247, 2013.

[27] Lucy Lee, Lee M Harrison, and Andrea Mechelli. The functional brain connectivity workshop: report and commentary. *Network: Computation in Neural Systems*, 14(2):R1, 2003.

[28] Barry Horwitz. The elusive concept of brain connectivity. *Neuroimage*, 19(2):466–470, 2003.

[29] Andrew A Fingelkurts, Alexander A Fingelkurts, and Seppo Kähkönen. Functional connectivity in the brain—is it an elusive concept? *Neuroscience & Biobehavioral Reviews*, 28(8):827–836, 2005.

[30] Ed Bullmore and Olaf Sporns. Complex brain networks: graph theoretical analysis of structural and functional systems. *Nature reviews neuroscience*, 10(3):186–198, 2009.

[31] Danielle Smith Bassett and ED Bullmore. Small-world brain networks. *The neuroscientist*, 12(6):512–523, 2006.

[32] David Meunier, Renaud Lambiotte, Alex Fornito, Karen Ersche, and Edward T Bullmore. Hierarchical modularity in human brain functional networks. *Frontiers in neuroinformatics*, 3:37, 2009.

[33] Mihail Bota, Hong-Wei Dong, and Larry W Swanson. From gene networks to brain networks. *Nature neuroscience*, 6(8):795–799, 2003.

[34] Olaf Sporns, Giulio Tononi, and Rolf Kötter. The human connectome: a structural description of the human brain. *PLoS computational biology*, 1(4):e42, 2005.

[35] John G White, Eileen Southgate, J Nichol Thomson, Sydney Brenner, et al. The structure of the nervous system of the nematode caenorhabditis elegans. *Philos Trans R Soc Lond B Biol Sci*, 314(1165):1–340, 1986.

[36] Daniel J Felleman and David C Van Essen. Distributed hierarchical processing in the primate cerebral cortex. *Cerebral cortex (New York, NY: 1991)*, 1(1):1–47, 1991.

[37] Claus-C Hilgetag, Gully APC Burns, Marc A O'Neill, Jack W Scannell, and Malcolm P Young. Anatomical connectivity defines the organization of clusters of cortical areas in the macaque and the cat. *Philosophical Transactions of the Royal Society of London. Series B: Biological Sciences*, 355(1393):91–110, 2000.

[38] Patric Hagmann, Leila Cammoun, Xavier Gigandet, Reto Meuli, Christopher J Honey, Van J Wedeen, and Olaf Sporns. Mapping the structural core of human cerebral cortex. *PLoS biology*, 6(7):e159, 2008.

[39] Christopher J Honey, Olaf Sporns, Leila Cammoun, Xavier Gigandet, Jean-Philippe Thiran, Reto Meuli, and Patric Hagmann. Predicting human resting-state functional connectivity from structural connectivity. *Proceedings of the National Academy of Sciences*, 106(6):2035–2040, 2009.

[40] J. H. (ed.) Byrne. Neuroscience online: An electronic textbook for the neurosciences. https://nba.uth.tmc.edu/neuroscience/m/index.htm, 1997.

[41] San-Qiang He, Richard P Dum, and Peter L Strick. Topographic organization of corticospinal projections from the frontal lobe: motor areas on the medial surface of the hemisphere. *Journal of Neuroscience*, 15(5):3284–3306, 1995.

[42] Jeffrey D Meier, Tyson N Aflalo, Sabine Kastner, and Michael SA Graziano. Complex organization of human primary motor cortex: a high-resolution fmri study. *Journal of neurophysiology*, 100(4):1800–1812, 2008.

[43] Roger N Lemon. Descending pathways in motor control. *Annu. Rev. Neurosci.*, 31:195–218, 2008.

[44] Terrence J Sejnowski, Christof Koch, and Patricia S Churchland. Computational neuroscience. *Science*, 241(4871):1299–1306, 1988.

[45] Wulfram Gerstner, Werner M Kistler, Richard Naud, and Liam Paninski. *Neuronal dynamics: From single neurons to networks and models of cognition*. Cambridge University Press, 2014.

[46] JE Darnell, H Lodish, A Berk, L Zipursky, P Matsudaira, and D Baltimore. Overview of neuron structure and function. In *Molecular cell biology*. WH Freeman and Company, 2000.

[47] Suzana Herculano-Houzel. The human brain in numbers: a linearly scaled-up primate brain. *Frontiers in human neuroscience*, page 31, 2009.

[48] James W Kalat. *Introduction to psychology*. Cengage Learning, 2016.

[49] Charles Scott Sherrington. On reciprocal innervation of antagonistic muscles. third note. *Proceedings of the Royal Society of London*, 60(359-367):414–417, 1897.

[50] Sanford L Palay. Synapses in the central nervous system. *The Journal of biophysical and biochemical cytology*, 2(4):193, 1956.

[51] Alberto E Pereda. Electrical synapses and their functional interactions with chemical synapses. *Nature Reviews Neuroscience*, 15(4):250–263, 2014.

[52] Yu Li, Lin Lin, Weisi Guo, and Hao Yan. Signal transmission through human body via engineered nervous system. In *GLOBECOM 2020-2020 IEEE Global Communications Conference*, pages 1–7. IEEE, 2020.

[53] Thomas Brochier, Lyuba Zehl, Yaoyao Hao, Margaux Duret, Julia Sprenger, Michael Denker, Sonja Grün, and Alexa Riehle. Massively parallel recordings in macaque motor cortex during an instructed delayed reach-to-grasp task. *Scientific data*, 5(1):1–23, 2018.

[54] Alan L Hodgkin and Andrew F Huxley. A quantitative description of membrane current and its application to conduction and excitation in nerve. *The Journal of physiology*, 117(4):500, 1952.

[55] Zhenyu Zhu, Rubin Wang, and Fengyun Zhu. The energy coding of a structural neural network based on the hodgkin–huxley model. *Frontiers in Neuroscience*, 12:122, 2018.

[56] Richard FitzHugh. Impulses and physiological states in theoretical models of nerve membrane. *Biophysical journal*, 1(6):445–466, 1961.

[57] Jinichi Nagumo, Suguru Arimoto, and Shuji Yoshizawa. An active pulse transmission line simulating nerve axon. *Proceedings of the IRE*, 50(10):2061–2070, 1962.

[58] Larry F Abbott. Lapicque's introduction of the integrate-and-fire model neuron (1907). *Brain research bulletin*, 50(5-6):303–304, 1999.

[59] Nicolas Fourcaud-Trocmé, David Hansel, Carl Van Vreeswijk, and Nicolas Brunel. How spike generation mechanisms determine the neuronal response to fluctuating inputs. *Journal of neuroscience*, 23(37):11628–11640, 2003.

[60] Srdjan Ostojic, Nicolas Brunel, and Vincent Hakim. Synchronization properties of networks of electrically coupled neurons in the presence of noise and heterogeneities. *Journal of computational neuroscience*, 26(3):369–392, 2009.

[61] Bruce W Knight. Dynamics of encoding in a population of neurons. *The Journal of general physiology*, 59(6):734–766, 1972.

[62] Hugh R Wilson and Jack D Cowan. Excitatory and inhibitory interactions in localized populations of model neurons. *Biophysical journal*, 12(1):1–24, 1972.

[63] Peter Dayan and Laurence F Abbott. *Theoretical neuroscience: computational and mathematical modeling of neural systems*. MIT press, 2005.

[64] Srdjan Ostojic and Nicolas Brunel. From spiking neuron models to linear-nonlinear models. *PLoS computational biology*, 7(1):e1001056, 2011.

[65] Nicolas Brunel, Frances S Chance, Nicolas Fourcaud, and Larry F Abbott. Effects of synaptic noise and filtering on the frequency response of spiking neurons. *Physical Review Letters*, 86(10):2186, 2001.

[66] Anirudh Kulkarni, Jonas Ranft, and Vincent Hakim. Synchronization, stochasticity, and phase waves in neuronal networks with spatially-structured connectivity. *Frontiers in computational neuroscience*, page 87, 2020.

[67] Moritz Augustin, Josef Ladenbauer, Fabian Baumann, and Klaus Obermayer. Low-dimensional spike rate models derived from networks of adaptive integrate-and-fire neurons: comparison and implementation. *PLoS computational biology*, 13(6):e1005545, 2017.

[68] Hiroki Sayama. *Introduction to the modeling and analysis of complex systems*. Open SUNY Textbooks, 2015.

[69] Jorge C Lucero. A theoretical study of the hysteresis phenomenon at vocal fold oscillation onset–offset. *The Journal of the Acoustical Society of America*, 105(1):423–431, 1999.

[70] György Buzsáki and Brendon O Watson. Brain rhythms and neural syntax: implications for efficient coding of cognitive content and neuropsychiatric disease. *Dialogues in clinical neuroscience*, 2022.

[71] Mario Tudor, Lorainne Tudor, and Katarina Ivana Tudor. Hans berger (1873-1941)–the history of electroencephalography. *Acta medica Croatica: casopis Hravatske akademije medicinskih znanosti*, 59(4):307–313, 2005.

[72] Xiao-Jing Wang. Neurophysiological and computational principles of cortical rhythms in cognition. *Physiological reviews*, 90(3):1195–1268, 2010.

[73] John D Green and Arnaldo A Arduini. Hippocampal electrical activity in arousal. *Journal of neurophysiology*, 17(6):533–557, 1954.

[74] Robert P Vertes. Hippocampal theta rhythm: A tag for short-term memory. *Hippocampus*, 15(7):923–935, 2005.

[75] Brian H Bland and Scott D Oddie. Theta band oscillation and synchrony in the hippocampal formation and associated structures: the case for its role in sensorimotor integration. *Behavioural brain research*, 127(1-2):119–136, 2001.

[76] György Buzsáki. Theta rhythm of navigation: link between path integration and landmark navigation, episodic and semantic memory. *Hippocampus*, 15(7):827–840, 2005.

[77] Jose L Cantero, Mercedes Atienza, Robert Stickgold, Michael J Kahana, Joseph R Madsen, and Bernat Kocsis. Sleep-dependent θ oscillations in the human hippocampus and neocortex. *Journal of Neuroscience*, 23(34):10897–10903, 2003.

[78] LI Aftanas and SA Golocheikine. Human anterior and frontal midline theta and lower alpha reflect emotionally positive state and internalized attention: high-resolution eeg investigation of meditation. *Neuroscience letters*, 310(1):57–60, 2001.

[79] Arianna Brancaccio, Davide Tabarelli, Marco Bigica, and Daniel Baldauf. Cortical source localization of sleep-stage specific oscillatory activity. *Scientific reports*, 10(1):1–15, 2020.

[80] Jerome N Sanes and John P Donoghue. Oscillations in local field potentials of the primate motor cortex during voluntary movement. *Proceedings of the National Academy of Sciences*, 90(10):4470–4474, 1993.

[81] Gert Pfurtscheller, Gunther Krausz, and Christa Neuper. Mechanical stimulation of the fingertip can induce bursts of β oscillations in sensorimotor areas. *Journal of clinical neurophysiology*, 18(6):559–564, 2001.

[82] Gert Pfurtscheller, Bernard Graimann, Jane E Huggins, Simon P Levine, and Lori A Schuh. Spatiotemporal patterns of beta desynchronization and gamma synchronization in corticographic data during self-paced movement. *Clinical neurophysiology*, 114(7):1226–1236, 2003.

[83] Thomas Gilbertson, Elodie Lalo, Louise Doyle, Vincenzo Di Lazzaro, Beatrice Cioni, and Peter Brown. Existing motor state is favored at the expense of new movement during 13-35 hz oscillatory synchrony in the human corticospinal system. *Journal of Neuroscience*, 25(34):7771–7779, 2005.

[84] Doug Rubino, Kay A Robbins, and Nicholas G Hatsopoulos. Propagating waves mediate information transfer in the motor cortex. *Nature neuroscience*, 9(12):1549–1557, 2006.

[85] Michael E Rule, Carlos Vargas-Irwin, John P Donoghue, and Wilson Truccolo. Phase reorganization leads to transient β-lfp spatial wave patterns in motor cortex during steady-state movement preparation. *Journal of neurophysiology*, 119(6):2212–2228, 2018.

[86] Michael Denker, Lyuba Zehl, Bjørg E Kilavik, Markus Diesmann, Thomas Brochier, Alexa Riehle, and Sonja Grün. Lfp beta amplitude is linked to mesoscopic spatio-temporal phase patterns. *Scientific reports*, 8(1):1–21, 2018.

[87] John R Hughes. Responses from the visual cortex of unanesthetized monkeys. In *International review of neurobiology*, volume 7, pages 99–152. Elsevier, 1964.

[88] Peyman Adjamian, Ian E Holliday, Gareth R Barnes, Arjan Hillebrand, Avgis Hadjipapas, and Krish D Singh. Induced visual illusions and gamma oscillations in human primary visual cortex. *European Journal of Neuroscience*, 20(2):587–592, 2004.

[89] Suresh D Muthukumaraswamy and Krish D Singh. Spatiotemporal frequency tuning of bold and gamma band meg responses compared in primary visual cortex. *Neuroimage*, 40(4):1552–1560, 2008.

[90] Andreas K Engel, Pascal Fries, Peter König, Michael Brecht, and Wolf Singer. Temporal binding, binocular rivalry, and consciousness. *Consciousness and cognition*, 8(2):128–151, 1999.

[91] Antoine Lutz, Lawrence L Greischar, Nancy B Rawlings, Matthieu Ricard, and Richard J Davidson. Long-term meditators self-induce high-amplitude gamma synchrony during mental practice. *Proceedings of the national Academy of Sciences*, 101(46):16369–16373, 2004.

[92] Georgia G Gregoriou, Stephen J Gotts, Huihui Zhou, and Robert Desimone. High-frequency, long-range coupling between prefrontal and visual cortex during attention. *Science*, 324(5931):1207–1210, 2009.

[93] Daniel Baldauf and Robert Desimone. Neural mechanisms of object-based attention. *Science*, 344(6182):424–427, 2014.

[94] György Buzsáki and Fernando Lopes da Silva. High frequency oscillations in the intact brain. *Progress in neurobiology*, 98(3):241–249, 2012.

[95] Jerome Engel Jr, Anatol Bragin, Richard Staba, and Istvan Mody. High-frequency oscillations: what is normal and what is not? *Epilepsia*, 50(4):598–604, 2009.

[96] Peter J Uhlhaas and Wolf Singer. High-frequency oscillations and the neurobiology of schizophrenia. *Dialogues in clinical neuroscience*, 2022.

[97] Peter Brown, Antonio Oliviero, Paolo Mazzone, Angelo Insola, Pietro Tonali, and Vincenzo Di Lazzaro. Dopamine dependency of oscillations between subthalamic nucleus and pallidum in parkinson's disease. *Journal of Neuroscience*, 21(3):1033–1038, 2001.

[98] Michael Cassidy, Paolo Mazzone, Antonio Oliviero, Angelo Insola, Pietro Tonali, Vincenzo Di Lazzaro, and Peter Brown. Movement-related changes in synchronization in the human basal ganglia. *Brain*, 125(6):1235–1246, 2002.

[99] Joseph Feingold, Daniel J Gibson, Brian DePasquale, and Ann M Graybiel. Bursts of beta oscillation differentiate postperformance activity in the striatum and motor cortex of monkeys performing movement tasks. *Proceedings of the National Academy of Sciences*, 112(44):13687–13692, 2015.

[100] RY Cho, RO Konecky, and Cameron S Carter. Impairments in frontal cortical γ synchrony and cognitive control in schizophrenia. *Proceedings of the National Academy of Sciences*, 103(52):19878–19883, 2006.

[101] Peter J Uhlhaas and Wolf Singer. Neural synchrony in brain disorders: relevance for cognitive dysfunctions and pathophysiology. *Neuron*, 52(1):155–168, 2006.

[102] Fernando Lopes Da Silva, Wouter Blanes, Stiliyan N Kalitzin, Jaime Parra, Piotr Suffczynski, and Demetrios N Velis. Epilepsies as dynamical diseases of brain systems: basic models of the transition between normal and epileptic activity. *Epilepsia*, 44:72–83, 2003.

[103] Roger D Traub, Richard Miles, and György Buzsáki. Computer simulation of carbachol-driven rhythmic population oscillations in the ca3 region of the in vitro rat hippocampus. *The Journal of Physiology*, 451(1):653–672, 1992.

[104] Carl Van Vreeswijk, LF Abbott, and G Bard Ermentrout. When inhibition not excitation synchronizes neural firing. *Journal of computational neuroscience*, 1(4):313–321, 1994.

[105] Xiao-Jing Wang and John Rinzel. Alternating and synchronous rhythms in reciprocally inhibitory model neurons. *Neural computation*, 4(1):84–97, 1992.

[106] X-J Wang and J Rinzel. Spindle rhythmicity in the reticularis thalami nucleus: synchronization among mutually inhibitory neurons. *Neuroscience*, 53(4):899–904, 1993.

[107] Xiao-Jing Wang and György Buzsáki. Gamma oscillation by synaptic inhibition in a hippocampal interneuronal network model. *Journal of neuroscience*, 16(20):6402–6413, 1996.

[108] Miles A Whittington, Roger D Traub, and John GR Jefferys. Synchronized oscillations in interneuron networks driven by metabotropic glutamate receptor activation. *Nature*, 373(6515):612–615, 1995.

[109] WALTER J Freeman. Relations between unit activity and evoked potentials in prepyriform cortex of cats. *Journal of neurophysiology*, 31(3):337–348, 1968.

[110] LS Leung. Nonlinear feedback model of neuronal populations in hippocampal cal region. *Journal of neurophysiology*, 47(5):845–868, 1982.

[111] Paul Tiesinga and Terrence J Sejnowski. Cortical enlightenment: are attentional gamma oscillations driven by ing or ping? *Neuron*, 63(6):727–732, 2009.

[112] Sheriar G Hormuzdi, Isabel Pais, Fiona EN LeBeau, Stephen K Towers, Andrei Rozov, Eberhard H Buhl, Miles A Whittington, and Hannah Monyer. Impaired electrical signaling disrupts gamma frequency oscillations in connexin 36-deficient mice. *Neuron*, 31(3):487–495, 2001.

[113] Derek L Buhl, Kenneth D Harris, Sheriar G Hormuzdi, Hanna Monyer, and György Buzsáki. Selective impairment of hippocampal gamma oscillations in connexin-36 knock-out mouse in vivo. *Journal of Neuroscience*, 23(3):1013–1018, 2003.

[114] Jun-nosuke Teramae and Dan Tanaka. Robustness of the noise-induced phase synchronization in a general class of limit cycle oscillators. *Physical review letters*, 93(20):204103, 2004.

[115] Michael Springer and Johan Paulsson. Harmonies from noise. *Nature*, 439(7072):27–28, 2006.

[116] Roberto F Galán, Nicolas Fourcaud-Trocmé, G Bard Ermentrout, and Nathaniel N Urban. Correlation-induced synchronization of oscillations in olfactory bulb neurons. *Journal of Neuroscience*, 26(14):3646–3655, 2006.

[117] Roberto F Galán, G Bard Ermentrout, and Nathaniel N Urban. Stochastic dynamics of uncoupled neural oscillators: Fokker-planck studies with the finite element method. *Physical Review E*, 76(5):056110, 2007.

[118] David J Tolhurst, J Anthony Movshon, and Andrew F Dean. The statistical reliability of signals in single neurons in cat and monkey visual cortex. *Vision research*, 23(8):775–785, 1983.

[119] William R Softky and Christof Koch. The highly irregular firing of cortical cells is inconsistent with temporal integration of random epsps. *Journal of neuroscience*, 13(1):334–350, 1993.

[120] P Heggelund and K Albus. Response variability and orientation discrimination of single cells in striate cortex of cat. *Experimental Brain Research*, 32(2):197–211, 1978.

[121] MW Oram, MC Wiener, R Lestienne, and BJ Richmond. Stochastic nature of precisely timed spike patterns in visual system neuronal responses. *Journal of neurophysiology*, 81(6):3021–3033, 1999.

[122] Albert Compte, Christos Constantinidis, Jesper Tegnér, Sridhar Raghavachari, Matthew V Chafee, Patricia S Goldman-Rakic, and Xiao-Jing Wang. Temporally irregular mnemonic persistent activity in prefrontal neurons of monkeys during a delayed response task. *Journal of neurophysiology*, 90(5):3441–3454, 2003.

[123] M Shafi, Y Zhou, J Quintana, C Chow, J Fuster, and M Bodner. Variability in neuronal activity in primate cortex during working memory tasks. *Neuroscience*, 146(3):1082–1108, 2007.

[124] Martin P Nawrot, Clemens Boucsein, Victor Rodriguez Molina, Alexa Riehle, Ad Aertsen, and Stefan Rotter. Measurement of variability dynamics in cortical spike trains. *Journal of neuroscience methods*, 169(2):374–390, 2008.

[125] Nicolas Brunel and Vincent Hakim. Fast global oscillations in networks of integrate-and-fire neurons with low firing rates. *Neural computation*, 11(7):1621–1671, 1999.

[126] Nicolas Brunel. Dynamics of sparsely connected networks of excitatory and inhibitory spiking neurons. *Journal of computational neuroscience*, 8(3):183–208, 2000.

[127] Nicolas Brunel and Vincent Hakim. Sparsely synchronized neuronal oscillations. *Chaos: An Interdisciplinary Journal of Nonlinear Science*, 18(1):015113, 2008.

[128] Nicolas Brunel and Xiao-Jing Wang. What determines the frequency of fast network oscillations with irregular neural discharges? i. synaptic dynamics and excitation-inhibition balance. *Journal of neurophysiology*, 90(1):415–430, 2003.

[129] Caroline Geisler, Nicolas Brunel, and Xiao-Jing Wang. Contributions of intrinsic membrane dynamics to fast network oscillations with irregular neuronal discharges. *Journal of neurophysiology*, 94(6):4344–4361, 2005.

[130] Camille de Solages, German Szapiro, Nicolas Brunel, Vincent Hakim, Philippe Isope, Pierre Buisseret, Charly Rousseau, Boris Barbour, and Clément Léna. High-frequency organization and synchrony of activity in the purkinje cell layer of the cerebellum. *Neuron*, 58(5):775–788, 2008.

[131] Michel Besserve, Scott C Lowe, Nikos K Logothetis, Bernhard Schölkopf, and Stefano Panzeri. Shifts of gamma phase across primary visual cortical sites reflect dynamic stimulus-modulated information transfer. *PLoS biology*, 13(9):e1002257, 2015.

[132] Lyle Muller, Alexandre Reynaud, Frédéric Chavane, and Alain Destexhe. The stimulus-evoked population response in visual cortex of awake monkey is a propagating wave. *Nature communications*, 5(1):1–14, 2014.

[133] Honghui Zhang and Joshua Jacobs. Traveling theta waves in the human hippocampus. *Journal of Neuroscience*, 35(36):12477–12487, 2015.

[134] Lyle Muller and Alain Destexhe. Propagating waves in thalamus, cortex and the thalamocortical system: experiments and models. *Journal of Physiology-Paris*, 106(5-6):222–238, 2012.

[135] Paul C Bressloff. Spatiotemporal dynamics of continuum neural fields. *Journal of Physics A: Mathematical and Theoretical*, 45(3):033001, 2011.

[136] Bjørg Elisabeth Kilavik, Manuel Zaepffel, Andrea Brovelli, William A MacKay, and Alexa Riehle. The ups and downs of beta oscillations in sensorimotor cortex. *Experimental neurology*, 245:15–26, 2013.

[137] Herbert Jasper and Wilder Penfield. Electrocorticograms in man: effect of voluntary movement upon the electrical activity of the precentral gyrus. *Archiv für Psychiatrie und Nervenkrankheiten*, 183(1):163–174, 1949.

[138] Wilder Penfield. Mechanisms of voluntary movement. *Brain: a journal of neurology*, 1954.

[139] JM Kilner, SN Baker, S Salenius, V Jousmäki, R Hari, and RN Lemon. Task-dependent modulation of 15-30 hz coherence between rectified emgs from human hand and forearm muscles. *The Journal of physiology*, 516(2):559–570, 1999.

[140] Venkatesh N Murthy and Eberhard E Fetz. Coherent 25-to 35-hz oscillations in the sensorimotor cortex of awake behaving monkeys. *Proceedings of the National Academy of Sciences*, 89(12):5670–5674, 1992.

[141] JJ Bouyer, MF Montaron, JM Vahnee, MP Albert, and A Rougeul. Anatomical localization of cortical beta rhythms in cat. *Neuroscience*, 22(3):863–869, 1987.

[142] Fabian Klostermann, Vadim V Nikulin, Andrea Annette Kühn, Frank Marzinzik, Michael Wahl, Alek Pogosyan, Andreas Kupsch, Gerd-Helge Schneider, Peter Brown, and Gabriel Curio. Task-related differential dynamics of eeg alpha-and beta-band synchronization in cortico-basal motor structures. *European Journal of Neuroscience*, 25(5):1604–1615, 2007.

[143] Stuart N Baker. Oscillatory interactions between sensorimotor cortex and the periphery. *Current opinion in neurobiology*, 17(6):649–655, 2007.

[144] Gert Pfurtscheller, A Stancak Jr, and Christa Neuper. Post-movement beta synchronization. a correlate of an idling motor area? *Electroencephalography and clinical neurophysiology*, 98(4):281–293, 1996.

[145] Alek Pogosyan, Louise Doyle Gaynor, Alexandre Eusebio, and Peter Brown. Boosting cortical activity at beta-band frequencies slows movement in humans. *Current biology*, 19(19):1637–1641, 2009.

[146] Alexandros G Androulidakis, Louise MF Doyle, Kielan Yarrow, Vladimir Litvak, Thomas P Gilbertson, and Peter Brown. Anticipatory changes in beta synchrony in the human corticospinal system and associated improvements in task performance. *European Journal of Neuroscience*, 25(12):3758–3765, 2007.

[147] Pieter R Roelfsema, Andreas K Engel, Peter König, and Wolf Singer. Visuomotor integration is associated with zero time-lag synchronization among cortical areas. *Nature*, 385(6612):157–161, 1997.

[148] Timothy J Buschman and Earl K Miller. Top-down versus bottom-up control of attention in the prefrontal and posterior parietal cortices. *Science*, 315(5820):1860–1862, 2007.

[149] Bijan Pesaran, Matthew J Nelson, and Richard A Andersen. Free choice activates a decision circuit between frontal and parietal cortex. *Nature*, 453(7193):406–409, 2008.

[150] Timothy J Buschman and Earl K Miller. Serial, covert shifts of attention during visual search are reflected by the frontal eye fields and correlated with population oscillations. *Neuron*, 63(3):386–396, 2009.

[151] Eberhard E Fetz. Volitional control of cortical oscillations and synchrony. *Neuron*, 77(2):216–218, 2013.

[152] Joachim Gross, Frank Schmitz, Irmtraud Schnitzler, Klaus Kessler, Kimron Shapiro, Bernhard Hommel, and Alfons Schnitzler. Modulation of long-range neural synchrony reflects temporal limitations of visual attention in humans. *Proceedings of the national Academy of Sciences*, 101(35):13050–13055, 2004.

[153] Cornelia Kranczioch, Stefan Debener, Alexander Maye, and Andreas K Engel. Temporal dynamics of access to consciousness in the attentional blink. *Neuroimage*, 37(3):947–955, 2007.

[154] Flavie Torrecillos, Gerd Tinkhauser, Petra Fischer, Alexander L Green, Tipu Z Aziz, Thomas Foltynie, Patricia Limousin, Ludvic Zrinzo, Keyoumars Ashkan, Peter Brown, et al. Modulation of beta bursts in the subthalamic nucleus predicts motor performance. *Journal of neuroscience*, 38(41):8905–8917, 2018.

[155] Simon Little, James Bonaiuto, Gareth Barnes, and Sven Bestmann. Human motor cortical beta bursts relate to movement planning and response errors. *PLoS biology*, 17(10):e3000479, 2019.

[156] Gerd Tinkhauser, Alek Pogosyan, Simon Little, Martijn Beudel, Damian M Herz, Huiling Tan, and Peter Brown. The modulatory effect of adaptive deep brain stimulation on beta bursts in parkinson's disease. *Brain*, 140(4):1053–1067, 2017.

[157] Maxwell A Sherman, Shane Lee, Robert Law, Saskia Haegens, Catherine A Thorn, Matti S Hämäläinen, Christopher I Moore, and Stephanie R Jones. Neural mechanisms of transient neocortical beta rhythms: Converging evidence from humans, computational modeling, monkeys, and mice. *Proceedings of the National Academy of Sciences*, 113(33):E4885–E4894, 2016.

[158] Peter Brown. Abnormal oscillatory synchronisation in the motor system leads to impaired movement. *Current opinion in neurobiology*, 17(6):656–664, 2007.

[159] Simon Little and Peter Brown. The functional role of beta oscillations in parkinson's disease. *Parkinsonism & related disorders*, 20:S44–S48, 2014.

[160] Abbey B Holt, Eszter Kormann, Alessandro Gulberti, Monika Pötter-Nerger, Colin G McNamara, Hayriye Cagnan, Magdalena K Baaske, Simon Little, Johannes A Köppen, Carsten Buhmann, et al. Phase-dependent suppression of beta oscillations in parkinson's disease patients. *Journal of Neuroscience*, 39(6):1119–1134, 2019.

[161] MM McCarthy, C Moore-Kochlacs, X Gu, ES Boyden, X Han, and N Kopell. Striatal origin of the pathologic beta oscillations in parkinson's disease. *Proceedings of the National Academy of Sciences*, 108(28):11620–11625, 2011.

[162] Yoshihisa Tachibana, Hirokazu Iwamuro, Hitoshi Kita, Masahiko Takada, and Atsushi Nambu. Subthalamo-pallidal interactions underlying parkinsonian neuronal oscillations in the primate basal ganglia. *European Journal of Neuroscience*, 34(9):1470–1484, 2011.

[163] Amin Mirzaei, Arvind Kumar, Daniel Leventhal, Nicolas Mallet, Ad Aertsen, Joshua Berke, and Robert Schmidt. Sensorimotor processing in the basal ganglia leads to transient beta oscillations during behavior. *Journal of Neuroscience*, 37(46):11220–11232, 2017.

[164] Mario Rosanova, Adenauer Casali, Valentina Bellina, Federico Resta, Maurizio Mariotti, and Marcello Massimini. Natural frequencies of human corticothalamic circuits. *Journal of Neuroscience*, 29(24):7679–7685, 2009.

[165] Gregor Thut and Carlo Miniussi. New insights into rhythmic brain activity from tms–eeg studies. *Trends in cognitive sciences*, 13(4):182–189, 2009.

[166] Isabella Premoli, Til O Bergmann, Matteo Fecchio, Mario Rosanova, Andrea Biondi, Paolo Belardinelli, and Ulf Ziemann. The impact of gabaergic drugs on tms-induced brain oscillations in human motor cortex. *Neuroimage*, 163:1–12, 2017.

[167] Robert Schmidt, Maria Herrojo Ruiz, Bjørg E Kilavik, Mikael Lundqvist, Philip A Starr, and Adam R Aron. Beta oscillations in working memory, executive control of movement and thought, and sensorimotor function. *Journal of Neuroscience*, 39(42):8231–8238, 2019.

[168] Rory G Townsend and Pulin Gong. Detection and analysis of spatiotemporal patterns in brain activity. *PLoS computational biology*, 14(12):e1006643, 2018.

[169] Paulina Anna Dąbrowska, Nicole Voges, Michael von Papen, Junji Ito, David Dahmen, Alexa Riehle, Thomas Brochier, and Sonja Grün. On the complexity of resting state spiking activity in monkey motor cortex. *Cerebral cortex communications*, 2(3):tgab033, 2021.

[170] Anthony E Perry and Min S Chong. A description of eddying motions and flow patterns using critical-point concepts. *Annual Review of Fluid Mechanics*, 19(1):125–155, 1987.

[171] Arkady Pikovsky, Michael Rosenblum, Jürgen Kurths, et al. A universal concept in nonlinear sciences. *Self*, 2:3, 2001.

[172] G Bard Ermentrout and Nancy Kopell. Multiple pulse interactions and averaging in systems of coupled neural oscillators. *Journal of Mathematical Biology*, 29(3):195–217, 1991.

[173] G Bard Ermentrout and David Kleinfeld. Traveling electrical waves in cortex: insights from phase dynamics and speculation on a computational role. *Neuron*, 29(1):33–44, 2001.

[174] Frank C Hoppensteadt and Eugene M Izhikevich. *Weakly connected neural networks*, volume 126. Springer Science & Business Media, 1997.

[175] Peter Ashwin, Stephen Coombes, and Rachel Nicks. Mathematical frameworks for oscillatory network dynamics in neuroscience. *The Journal of Mathematical Neuroscience*, 6(1):1–92, 2016.

[176] Demian Battaglia, Nicolas Brunel, and David Hansel. Temporal decorrelation of collective oscillations in neural networks with local inhibition and long-range excitation. *Physical review letters*, 99(23):238106, 2007.

[177] Demian Battaglia and David Hansel. Synchronous chaos and broad band gamma rhythm in a minimal multi-layer model of primary visual cortex. *PLoS computational biology*, 7(10):e1002176, 2011.

[178] Agostina Palmigiano, Theo Geisel, Fred Wolf, and Demian Battaglia. Flexible information routing by transient synchrony. *Nature neuroscience*, 20(7):1014–1022, 2017.

[179] Juergen Fell and Nikolai Axmacher. The role of phase synchronization in memory processes. *Nature reviews neuroscience*, 12(2):105–118, 2011.

[180] György Buzsáki, Costas A Anastassiou, and Christof Koch. The origin of extracellular fields and currents—eeg, ecog, lfp and spikes. *Nature reviews neuroscience*, 13(6):407–420, 2012.

[181] Shrey Grover, John A Nguyen, and Robert MG Reinhart. Synchronizing brain rhythms to improve cognition. *Annu. Rev. Med*, 72:29–43, 2021.

[182] Pascal Fries. Rhythms for cognition: communication through coherence. *Neuron*, 88(1):220–235, 2015.

[183] J Matias Palva, Simo Monto, Shrikanth Kulashekhar, and Satu Palva. Neuronal synchrony reveals working memory networks and predicts individual memory capacity. *Proceedings of the National Academy of Sciences*, 107(16):7580–7585, 2010.

[184] RF Salazar, NM Dotson, SL Bressler, and CM Gray. Content-specific fronto-parietal synchronization during visual working memory. *Science*, 338(6110):1097–1100, 2012.

[185] Rafael Polanía, Michael A Nitsche, Carolin Korman, Giorgi Batsikadze, and Walter Paulus. The importance of timing in segregated theta phase-coupling for cognitive performance. *Current Biology*, 22(14):1314–1318, 2012.

[186] Jonathan Daume, Thomas Gruber, Andreas K Engel, and Uwe Friese. Phase-amplitude coupling and long-range phase synchronization reveal frontotemporal interactions during visual working memory. *Journal of Neuroscience*, 37(2):313–322, 2017.

[187] Robert MG Reinhart and John A Nguyen. Working memory revived in older adults by synchronizing rhythmic brain circuits. *Nature neuroscience*, 22(5):820–827, 2019.

[188] Yuri B Saalmann, Mark A Pinsk, Liang Wang, Xin Li, and Sabine Kastner. The pulvinar regulates information transmission between cortical areas based on attention demands. *Science*, 337(6095):753–756, 2012.

[189] Paul Sauseng, Wolfgang Klimesch, Kirstin F Heise, Walter R Gruber, Elisa Holz, Ahmed A Karim, Mark Glennon, Christian Gerloff, Niels Birbaumer, and Friedhelm C Hummel. Brain oscillatory substrates of visual short-term memory capacity. *Current biology*, 19(21):1846–1852, 2009.

[190] Andrew J Watrous, Nitin Tandon, Chris R Conner, Thomas Pieters, and Arne D Ekstrom. Frequency-specific network connectivity increases underlie accurate spatiotemporal memory retrieval. *Nature neuroscience*, 16(3):349–356, 2013.

[191] Anatol Bragin, Gábor Jandó, Zoltán Nádasdy, Jamille Hetke, Kensall Wise, and Gy Buzsáki. Gamma (40-100 hz) oscillation in the hippocampus of the behaving rat. *Journal of neuroscience*, 15(1):47–60, 1995.

[192] Steven L Bressler and Vinod Menon. Large-scale brain networks in cognition: emerging methods and principles. *Trends in cognitive sciences*, 14(6):277–290, 2010.

[193] Timothy P Meehan and Steven L Bressler. Neurocognitive networks: findings, models, and theory. *Neuroscience & Biobehavioral Reviews*, 36(10):2232–2247, 2012.

[194] Carl van Vreeswijk. Partial synchronization in populations of pulse-coupled oscillators. *Physical Review E*, 54(5):5522, 1996.

[195] Zhenhua Wang and Zonghua Liu. Partial synchronization in complex networks: Chimera state, remote synchronization, and cluster synchronization. *Acta Physica Sinica*, 69(8):088902, 2020.

[196] Tianwei Wu, Xinhua Zhang, and Zonghua Liu. Understanding the mechanisms of brain functions from the angle of synchronization and complex network. *Frontiers of Physics*, 17(3):1–23, 2022.

[197] Daniel M Abrams and Steven H Strogatz. Chimera states for coupled oscillators. *Physical review letters*, 93(17):174102, 2004.

[198] Y Kuramoto and D Battogtokh. Coexistence of coherence and incoherence in nonlocally coupled phase oscillators. *NONLINEAR PHENOMENA IN COMPLEX SYSTEMS*, 5(4):380–385, 2002.

[199] Iryna Omelchenko, Yuri Maistrenko, Philipp Hövel, and Eckehard Schöll. Loss of coherence in dynamical networks: spatial chaos and chimera states. *Physical review letters*, 106(23):234102, 2011.

[200] Iryna Omelchenko, Bruno Riemenschneider, Philipp Hövel, Yuri Maistrenko, and Eckehard Schöll. Transition from spatial coherence to incoherence in coupled chaotic systems. *Physical Review E*, 85(2):026212, 2012.

[201] Mark J Panaggio and Daniel M Abrams. Chimera states on a flat torus. *Physical review letters*, 110(9):094102, 2013.

[202] Oleh E Omel'chenko, Matthias Wolfrum, Serhiy Yanchuk, Yuri L Maistrenko, and Oleksandr Sudakov. Stationary patterns of coherence and incoherence in two-dimensional arrays of non-locally-coupled phase oscillators. *Physical Review E*, 85(3):036210, 2012.

[203] Mark J Panaggio and Daniel M Abrams. Chimera states: coexistence of coherence and incoherence in networks of coupled oscillators. *Nonlinearity*, 28(3):R67, 2015.

[204] Jianbo Xie, Edgar Knobloch, and Hsien-Ching Kao. Twisted chimera states and multicore spiral chimera states on a two-dimensional torus. *Physical Review E*, 92(4):042921, 2015.

[205] Yuri Maistrenko, Oleksandr Sudakov, Oleksiy Osiv, and Volodymyr Maistrenko. Chimera states in three dimensions. *New Journal of Physics*, 17(7):073037, 2015.

[206] Aaron M Hagerstrom, Thomas E Murphy, Rajarshi Roy, Philipp Hövel, Iryna Omelchenko, and Eckehard Schöll. Experimental observation of chimeras in coupled-map lattices. *Nature Physics*, 8(9):658–661, 2012.

[207] Evgeny A Viktorov, Tatiana Habruseva, Stephen P Hegarty, Guillaume Huyet, and Bryan Kelleher. Coherence and incoherence in an optical comb. *Physical review letters*, 112(22):224101, 2014.

[208] N Lazarides, G Neofotistos, and GP Tsironis. Chimeras in squid metamaterials. *Physical Review B*, 91(5):054303, 2015.

[209] Joseph D Hart, Kanika Bansal, Thomas E Murphy, and Rajarshi Roy. Experimental observation of chimera and cluster states in a minimal globally coupled network. *Chaos: an interdisciplinary journal of nonlinear science*, 26(9):094801, 2016.

[210] Hidetsugu Sakaguchi. Instability of synchronized motion in nonlocally coupled neural oscillators. *Physical Review E*, 73(3):031907, 2006.

[211] Tera A Glaze, Scott Lewis, and Sonya Bahar. Chimera states in a hodgkin-huxley model of thermally sensitive neurons. *Chaos: An Interdisciplinary Journal of Nonlinear Science*, 26(8):083119, 2016.

[212] Changhai Tian, Hongjie Bi, Xiyun Zhang, Shuguang Guan, and Zonghua Liu. Asymmetric couplings enhance the transition from chimera state to synchronization. *Physical Review E*, 96(5):052209, 2017.

[213] Chang-Hai Tian, Xi-Yun Zhang, Zhen-Hua Wang, and Zong-Hua Liu. Diversity of chimera-like patterns from a model of 2d arrays of neurons with nonlocal coupling. *Frontiers of Physics*, 12(3):1–8, 2017.

[214] Lennart Schmidt and Katharina Krischer. Clustering as a prerequisite for chimera states in globally coupled systems. *Physical Review Letters*, 114(3):034101, 2015.

[215] Azamat Yeldesbay, Arkady Pikovsky, and Michael Rosenblum. Chimeralike states in an ensemble of globally coupled oscillators. *Physical review letters*, 112(14):144103, 2014.

[216] VK Chandrasekar, R Gopal, A Venkatesan, and M Lakshmanan. Mechanism for intensity-induced chimera states in globally coupled oscillators. *Physical Review E*, 90(6):062913, 2014.

[217] K Premalatha, VK Chandrasekar, M Senthilvelan, and M Lakshmanan. Impact of symmetry breaking in networks of globally coupled oscillators. *Physical Review E*, 91(5):052915, 2015.

[218] Arindam Mishra, Chittaranjan Hens, Mridul Bose, Prodyot K Roy, and Syamal K Dana. Chimeralike states in a network of oscillators under attractive and repulsive global coupling. *Physical Review E*, 92(6):062920, 2015.

[219] Carlo R Laing. Chimeras in networks with purely local coupling. *Physical Review E*, 92(5):050904, 2015.

[220] Bidesh K Bera and Dibakar Ghosh. Chimera states in purely local delay-coupled oscillators. *Physical Review E*, 93(5):052223, 2016.

[221] Bidesh K Bera, Dibakar Ghosh, and Tanmoy Banerjee. Imperfect traveling chimera states induced by local synaptic gradient coupling. *Physical Review E*, 94(1):012215, 2016.

[222] Rubao Ma, Jianxiong Wang, and Zonghua Liu. Robust features of chimera states and the implementation of alternating chimera states. *EPL (Europhysics Letters)*, 91(4):40006, 2010.

[223] Yun Zhu, Zhigang Zheng, and Junzhong Yang. Chimera states on complex networks. *Physical Review E*, 89(2):022914, 2014.

[224] Arturo Buscarino, Mattia Frasca, Lucia Valentina Gambuzza, and Philipp Hövel. Chimera states in time-varying complex networks. *Physical Review E*, 91(2):022817, 2015.

[225] Kanika Bansal, Javier O Garcia, Steven H Tompson, Timothy Verstynen, Jean M Vettel, and Sarah F Muldoon. Cognitive chimera states in human brain networks. *Science Advances*, 5(4):eaau8535, 2019.

[226] Siyu Huo, Changhai Tian, Ling Kang, and Zonghua Liu. Chimera states of neuron networks with adaptive coupling. *Nonlinear Dynamics*, 96(1):75–86, 2019.

[227] Jianbo Xie, Edgar Knobloch, and Hsien-Ching Kao. Multicluster and traveling chimera states in nonlocal phase-coupled oscillators. *Physical Review E*, 90(2):022919, 2014.

[228] Anna Zakharova, Marie Kapeller, and Eckehard Schöll. Chimera death: Symmetry breaking in dynamical networks. *Physical review letters*, 112(15):154101, 2014.

[229] Siyu Huo, Changhai Tian, Muhua Zheng, Shuguang Guan, Changsong Zhou, and Zonghua Liu. Spatial multi-scaled chimera states of cerebral cortex network and its inherent structure-dynamics relationship in human brain. *National science review*, 8(1):nwaa125, 2021.

[230] Neils C Rattenborg, Charles J Amlaner, and Steven L Lima. Behavioral, neurophysiological and evolutionary perspectives on unihemispheric sleep. *Neuroscience & Biobehavioral Reviews*, 24(8):817–842, 2000.

[231] Christian G Mathews, John A Lesku, Steven L Lima, and Charles J Amlaner. Asynchronous eye closure as an anti-predator behavior in the western fence lizard (sceloporus occidentalis). *Ethology*, 112(3):286–292, 2006.

[232] Masako Tamaki, Ji Won Bang, Takeo Watanabe, and Yuka Sasaki. Night watch in one brain hemisphere during sleep associated with the first-night effect in humans. *Current biology*, 26(9):1190–1194, 2016.

[233] Jorge M Davidenko, Arcady V Pertsov, Remy Salomonsz, William Baxter, and José Jalife. Stationary and drifting spiral waves of excitation in isolated cardiac muscle. *Nature*, 355(6358):349–351, 1992.

[234] Zhenhua Wang and Zonghua Liu. A brief review of chimera state in empirical brain networks. *Frontiers in Physiology*, 11:724, 2020.

[235] Andre Bergner, Mattia Frasca, Gregorio Sciuto, Arturo Buscarino, Eulalie Joelle Ngamga, Luigi Fortuna, and Jürgen Kurths. Remote synchronization in star networks. *Physical Review E*, 85(2):026208, 2012.

[236] Ludovico Minati. Experimental synchronization of chaos in a large ring of mutually coupled single-transistor oscillators: Phase, amplitude, and clustering effects. *Chaos: An Interdisciplinary Journal of Nonlinear Science*, 24(4):043108, 2014.

[237] Ludovico Minati. Remote synchronization of amplitudes across an experimental ring of non-linear oscillators. *Chaos: An Interdisciplinary Journal of Nonlinear Science*, 25(12):123107, 2015.

[238] Baris Karakaya, Ludovico Minati, Lucia Valentina Gambuzza, and Mattia Frasca. Fading of remote synchronization in tree networks of stuart-landau oscillators. *Physical Review E*, 99(5):052301, 2019.

[239] Lucia Valentina Gambuzza, Alessio Cardillo, Alessandro Fiasconaro, Luigi Fortuna, Jesus Gómez-Gardenes, and Mattia Frasca. Analysis of remote synchronization in complex networks. *Chaos: An Interdisciplinary Journal of Nonlinear Science*, 23(4):043103, 2013.

[240] Vladimir Vlasov and Angelo Bifone. Hub-driven remote synchronization in brain networks. *Scientific reports*, 7(1):1–11, 2017.

[241] Yong-Shang Long, Zheng-Meng Zhai, Ming Tang, and Ying-Cheng Lai. Metamorphoses and explosively remote synchronization in dynamical networks. *Chaos: An Interdisciplinary Journal of Nonlinear Science*, 32(4):043110, 2022.

[242] Zhenhua Wang and Zonghua Liu. Effect of remote signal propagation in an empirical brain network. *Chaos: An Interdisciplinary Journal of Nonlinear Science*, 31(6):063126, 2021.

[243] Qiwei Shen and Zonghua Liu. Remote firing propagation in the neural network of c.elegans. *Physical Review E*, 103(5):052414, 2021.

[244] Vincenzo Nicosia, Miguel Valencia, Mario Chavez, Albert Díaz-Guilera, and Vito Latora. Remote synchronization reveals network symmetries and functional modules. *Physical review letters*, 110(17):174102, 2013.

[245] Lucia Valentina Gambuzza, Mattia Frasca, and Vito Latora. Distributed control of synchronization of a group of network nodes. *IEEE Transactions on Automatic Control*, 64(1):365–372, 2018.

[246] I Leyva, I Sendiña-Nadal, R Sevilla-Escoboza, VP Vera-Avila, P Chholak, and S Boccaletti. Relay synchronization in multiplex networks. *Scientific reports*, 8(1):1–11, 2018.

[247] Jakub Sawicki, Julia M Koulen, and Eckehard Schöll. Synchronization scenarios in three-layer networks with a hub. *Chaos: An Interdisciplinary Journal of Nonlinear Science*, 31(7):073131, 2021.

[248] Michael T Schaub, Neave O'Clery, Yazan N Billeh, Jean-Charles Delvenne, Renaud Lambiotte, and Mauricio Barahona. Graph partitions and cluster synchronization in networks of oscillators. *Chaos: An Interdisciplinary Journal of Nonlinear Science*, 26(9):094821, 2016.

[249] Ben Cao, Ya-Feng Wang, Liang Wang, Yi-Zhen Yu, and Xin-Gang Wang. Cluster synchronization in complex network of coupled chaotic circuits: an experimental study. *Frontiers of Physics*, 13(5):1–11, 2018.

[250] Abu Bakar Siddique, Louis Pecora, Joseph D Hart, and Francesco Sorrentino. Symmetry- and input-cluster synchronization in networks. *Physical Review E*, 97(4):042217, 2018.

[251] Caitlin RS Williams, Thomas E Murphy, Rajarshi Roy, Francesco Sorrentino, Thomas Dahms, and Eckehard Schöll. Experimental observations of group synchrony in a system of chaotic optoelectronic oscillators. *Physical review letters*, 110(6):064104, 2013.

[252] Young Sul Cho, Takashi Nishikawa, and Adilson E Motter. Stable chimeras and independently synchronizable clusters. *Physical review letters*, 119(8):084101, 2017.

[253] Simona Olmi, Antonio Politi, and Alessandro Torcini. Collective chaos in pulse-coupled neural networks. *EPL (Europhysics Letters)*, 92(6):60007, 2011.

[254] Iryna Omelchenko, E Omel'chenko, Philipp Hövel, and Eckehard Schöll. When nonlocal coupling between oscillators becomes stronger: patched synchrony or multichimera states. *Physical review letters*, 110(22):224101, 2013.

[255] Iryna Omelchenko, Astero Provata, Johanne Hizanidis, Eckehard Schöll, and Philipp Hövel. Robustness of chimera states for coupled fitzhugh-nagumo oscillators. *Physical Review E*, 91(2):022917, 2015.

[256] Johanne Hizanidis, Vasileios G Kanas, Anastasios Bezerianos, and Tassos Bountis. Chimera states in networks of nonlocally coupled hindmarsh–rose neuron models. *International Journal of Bifurcation and Chaos*, 24(03):1450030, 2014.

[257] Ali Calim, Philipp Hövel, Mahmut Ozer, and Muhammet Uzuntarla. Chimera states in networks of type-i morris-lecar neurons. *Physical Review E*, 98(6):062217, 2018.

[258] Changhai Tian, Liang Cao, Hongjie Bi, Kesheng Xu, and Zonghua Liu. Chimera states in neuronal networks with time delay and electromagnetic induction. *Nonlinear Dynamics*, 93(3):1695–1704, 2018.

[259] Fabrice Wendling, Jean-Jacques Bellanger, Fabrice Bartolomei, and Patrick Chauvel. Relevance of nonlinear lumped-parameter models in the analysis of depth-eeg epileptic signals. *Biological cybernetics*, 83(4):367–378, 2000.

[260] Changsong Zhou, Lucia Zemanová, Gorka Zamora-Lopez, Claus C Hilgetag, and Jürgen Kurths. Structure–function relationship in complex brain networks expressed by hierarchical synchronization. *New Journal of Physics*, 9(6):178, 2007.

[261] Johanne Hizanidis, Nikos E Kouvaris, Gorka Zamora-López, Albert Díaz-Guilera, and Chris G Antonopoulos. Chimera-like states in modular neural networks. *Scientific reports*, 6(1):1–11, 2016.

[262] Teresa Chouzouris, Iryna Omelchenko, Anna Zakharova, Jaroslav Hlinka, Premysl Jiruska, and Eckehard Schöll. Chimera states in brain networks: Empirical neural vs. modular fractal connectivity. *Chaos: an interdisciplinary journal of nonlinear science*, 28(4):045112, 2018.

[263] Lukas Ramlow, Jakub Sawicki, Anna Zakharova, Jaroslav Hlinka, Jens Christian Claussen, and Eckehard Schöll. Partial synchronization in empirical brain networks as a model for unihemispheric sleep. *EPL (Europhysics Letters)*, 126(5):50007, 2019.

[264] Jakub Sawicki, Iryna Omelchenko, Anna Zakharova, and Eckehard Schöll. Delay controls chimera relay synchronization in multiplex networks. *Physical Review E*, 98(6):062224, 2018.

[265] Felix P Kemeth, Sindre W Haugland, Lennart Schmidt, Ioannis G Kevrekidis, and Katharina Krischer. A classification scheme for chimera states. *Chaos: An Interdisciplinary Journal of Nonlinear Science*, 26(9):094815, 2016.

[266] Beom Jun Kim. Performance of networks of artificial neurons: The role of clustering. *Physical Review E*, 69(4):045101, 2004.

[267] Diego Contreras, Alain Destexhe, Terrence J Sejnowski, and Mircea Steriade. Control of spatiotemporal coherence of a thalamic oscillation by corticothalamic feedback. *Science*, 274(5288):771–774, 1996.

[268] Eugenio Rodriguez, Nathalie George, Jean-Philippe Lachaux, Jacques Martinerie, Bernard Renault, and Francisco J Varela. Perception's shadow: long-distance synchronization of human brain activity. *Nature*, 397(6718):430–433, 1999.

[269] Peter König, Andreas K Engel, and Wolf Singer. Relation between oscillatory activity and long-range synchronization in cat visual cortex. *Proceedings of the national academy of sciences*, 92(1):290–294, 1995.

[270] Demetris S Soteropoulos and Stuart N Baker. Cortico-cerebellar coherence during a precision grip task in the monkey. *Journal of neurophysiology*, 95(2):1194–1206, 2006.

[271] Raul Vicente, Leonardo L Gollo, Claudio R Mirasso, Ingo Fischer, and Gordon Pipa. Dynamical relaying can yield zero time lag neuronal synchrony despite long conduction delays. *Proceedings of the National Academy of Sciences*, 105(44):17157–17162, 2008.

[272] Vesna Vuksanović and Philipp Hövel. Functional connectivity of distant cortical regions: role of remote synchronization and symmetry in interactions. *NeuroImage*, 97:1–8, 2014.

[273] Brian D Hassard, BD Hassard, Nicholas D Kazarinoff, Y-H Wan, Y Wah Wan, et al. *Theory and applications of Hopf bifurcation*, volume 41. CUP Archive, 1981.

[274] Steven H Strogatz. *Nonlinear dynamics and chaos: with applications to physics, biology, chemistry, and engineering*. CRC press, 2018.

[275] David Hansel, German Mato, and Claude Meunier. Phase dynamics for weakly coupled hodgkin-huxley neurons. *EPL (Europhysics Letters)*, 23(5):367, 1993.

[276] Alistair Steyn-Ross and Moira Steyn-Ross. *Modeling phase transitions in the brain*, volume 509. Springer, 2010.

[277] Ian Greenhouse, Ana Sias, Ludovica Labruna, and Richard B Ivry. Nonspecific inhibition of the motor system during response preparation. *Journal of Neuroscience*, 35(30):10675–10684, 2015.

[278] Edward G Jones. The thalamic matrix and thalamocortical synchrony. *Trends in neurosciences*, 24(10):595–601, 2001.

[279] Matthew T Kaufman, Mark M Churchland, Stephen I Ryu, and Krishna V Shenoy. Cortical activity in the null space: permitting preparation without movement. *Nature neuroscience*, 17(3):440–448, 2014.

[280] Jing Wang, Devika Narain, Eghbal A Hosseini, and Mehrdad Jazayeri. Flexible timing by temporal scaling of cortical responses. *Nature neuroscience*, 21(1):102–110, 2018.

[281] Andrew J Zimnik and Mark M Churchland. Independent generation of sequence elements by motor cortex. *Nature neuroscience*, 24(3):412–424, 2021.

[282] Hidehiko K Inagaki, Susu Chen, Margreet C Ridder, Pankaj Sah, Nuo Li, Zidan Yang, Hana Hasanbegovic, Zhenyu Gao, Charles R Gerfen, and Karel Svoboda. A midbrain-thalamus-cortex circuit reorganizes cortical dynamics to initiate movement. *Cell*, 185(6):1065–1081, 2022.

[283] Ludovica Bachschmid-Romano, Nicholas G Hatsopoulos, and Nicolas Brunel. Interplay between external inputs and recurrent dynamics during movement preparation and execution in a network model of motor cortex. *bioRxiv*, 2022.

RÉSUMÉ

Les oscillations corticales sont une caractéristique essentielle du cerveau et sont impliquées dans plusieurs fonctions perceptives et cognitives. La synchronisation et la propagation similaire à des ondes, de l'activité des populations neuronales, sont reliés aux fonctions corticales et au comportement. Dans cette thèse, je m' intéresse d'abord aux oscillations beta, des oscillations avec des fréquences entre $13Hz$ et $30Hz$, qui sont observées durant la préparation des mouvements. Je propose un modèle simple du cortex moteur fondé sur des populations locales de neurones excitateurs et inhibiteurs couplées à plus longues distances par des connexions excitatrices, qui reçoivent de plus des entrées fluctuantes en provenance d'autres régions cérébrales. Je montre que ce modèle reproduit de façon précise, les caractéristiques des oscillations beta et des ondes enregistrées expérimentalement, quand les entrées externes sont bien choisies. J'étudie ensuite différents modes d'activité dans lesquels seulement une partie seulement des neurones sont synchronisés, en utilisant la connectivité du cortex cérébral humain. Je mets en evidence plusieurs caractérisques structurales du réseau qui conduisent à une synchronisation partielle. Cela contribue à mieux comprendre comment la structure du réseau cérébral permet une dynamique neurale riche et flexible.

MOTS CLÉS

oscillations, synchronisation, ondes, neurosciences, réseau complexe

ABSTRACT

Cortical oscillations are an essential characteristic of the brain, which are involved in many perceptual and cognitive operations. The synchronization and the wavelike propagation of the activity of neuronal populations are cortical features that are related to functions and behaviors. In this thesis, first, I study beta oscillations, oscillations with frequencies between $13Hz$ and $30Hz$, which are observed during movement preparation. I propose a simple model of the motor cortex based on local excitatory-inhibitory neuronal populations coupled by longer range excitation and which receives fluctuating inputs from other cerebral structures. I show that the model accurately reproduces the features of beta oscillations and waves in recording data when external inputs are suitably chosen. Then, I investigate different patterns of activity when only a fraction of the neurons are synchronized, based on the anatomy of human cerebral cortex. I find that some particular features in the network structure lead to partial synchronization. This contributes to a better understanding of how the brain network structure gives rise to rich and flexible neural dynamics.

KEYWORDS

oscillations, synchronization, waves, neuroscience, complex network